National Library of Canada
Acquisitions and Bibliographic Services Branch
395 Wellington Street
Ottawa, Ontario
K1A 0N4

Bibliothèque nationale du Canada
Direction des acquisitions et des services bibliographiques
395, rue Wellington
Ottawa (Ontario)
K1A 0N4

Your file Votre référence

Our file Notre référence

NOTICE

The quality of this microform is heavily dependent upon the quality of the original thesis submitted for microfilming. Every effort has been made to ensure the highest quality of reproduction possible.

If pages are missing, contact the university which granted the degree.

Some pages may have indistinct print especially if the original pages were typed with a poor typewriter ribbon or if the university sent us an inferior photocopy.

AVIS

La qualité de cette microforme dépend grandement de la qualité de la thèse soumise au microfilmage. Nous avons tout fait pour assurer une qualité supérieure de reproduction.

S'il manque des pages, veuillez communiquer avec l'université qui a conféré le grade.

La qualité d'impression de certaines pages peut laisser à désirer, surtout si les pages originales ont été dactylographiées à l'aide d'un ruban usé ou si l'université nous a fait parvenir une photocopie de qualité inférieure.

Canada

ISBN 0-315-95950-9

Canada

UNIVERSITÉ D'OTTAWA
UNIVERSITY OF OTTAWA

To my parents .

ACKNOWLEDGEMENTS

I wish to express my sincere thanks to my research supervisor, Professor B.E. Conway, for his direction and guidance throughout the course of this work. Prof. Conway has always been available for discussions and help when I have had questions and problems in my studies and research. I am also very appreciative of the time he has spent and the patience he has demonstrated in the course of thesis correction. It was a privilege and honour for me to work with such a well-known, capable and understanding person.

I would like to thank my colleagues in this lab, Dr. L. Bai and Mr. S. Qian, with whom I co-authored several published papers and worked cooperatively in the present research project. Their help with the electrochemical experiments, especially in starting my work, is much appreciated.

Great acknowledgement is due to Cameco Corporation, Saskatoon, Canada, for their financial support that made this project possible. Thanks are also due to Dr. D.G. Garratt of Cameco Corporation for his personal interest in this work and for many perceptive discussions during its execution.

Acknowledgement is also due to The Electrochemical Society Inc. for the award of the Joseph W. Richards Summer Fellowship, 1992. The author is also grateful to the Ontario Government for partial financial support in the form of an Ontario Graduate Scholarship, 1992-1993.

I would like to thank Mr. J. McCaffery for taking the beautiful SEM pictures shown in this thesis. Grateful acknowledgement is also due to Mr. E. Kristoff who prepared the electrochemical glass cells for me which enabled many experiments to be conveniently conducted.

Finally, I am very grateful to my wife, Ming Yang, for her constant understanding, encouragement during the years, and for her hands-on help on some computer programming in this work.

PREFACE

It is necessary first to provide an outline of the work presented in this thesis. Five chapters and an appendix present the background information, and describe new methods developed during the course of this research project together with the results obtained and their interpretation.

Chapter I gives an introductory review on the origin of the project, and background of the topic of electrocatalysis. Adsorption behaviour of the overpotential-deposited H intermediate and kinetics of the H_2 evolution reaction have been of particular interest. Chapter II describes, in detail, the electrochemical systems, experimental techniques and electrochemical methods, used in the work. Chapter III provides a theoretical treatment and describes procedures for simulation of potential-relaxation transients for the H_2 evolution reaction. The basis of the initial potential-relaxation method for determination of double-layer capacitance is introduced. Chapter IV reports three sections of the experimental results. Part I is about electrocatalytic performance of Ni-Mo-Cd material as an H_2 cathode in a $KF \cdot 2HF$ melt and comparatively in $KOH \cdot 2H_2O$; Part II gives results on application of the initial potential-relaxation method to some practical systems for determining, *in situ*, the real surface-area of porous electrode materials. It is demonstrated how the rough surface area of the porous electrodes can be 'unfolded' electrochemically in solutions of increasing concentration of KOH; and Part III discusses effects of catalyst poisons on the adsorption behaviour of the H intermediate and the kinetic mechanisms of the HER at Pt electrodes both in KOH solutions and the $KF \cdot 2HF$ melt. Chapter V summarizes the conclusions drawn from the experimental results.

The procedures for the computer simulation of potential-relaxation transients are

described in the Appendix.

The work presented in this thesis work has been published or is in the process of publication, as follows:

1. "Problems in the determination of adsorption behaviour of intermediates in Faradaic reactions: distinction between double-layer and adsorption capacitance of electrocatalysts determined from fast potential-relaxation transients", P. Gu, L. Bai, L. Gao, R. Brousseau and B.E. Conway, *Electrochim. Acta*, **37**, No.12, 2145 (1992).
2. "The problem of in-situ real-area determination in evaluation of performance of rough or porous, gas-evolving electrocatalysts; Part I: Basis for distinction between capacitance of the double-layer and the pseudocapacitance due to adsorbed H in the H_2 evolution reaction at Pt", L. Bai, L. Gao and B.E. Conway, *J. Chem. Soc. Faraday Trans.*, **89(2)**, 235 (1993).
3. "The problem of in-situ real-area determination in the evaluation of performance of rough or porous, gas-evolving electrocatalysts; Part II: Unfolding of the electrochemically accessible surface of rough or porous electrodes: a case-study with an electrodeposited porous Pt electrode", L. Bai, L. Gao and B.E. Conway, *J. Chem. Soc. Faraday Trans.*, **89(2)**, 243 (1993).
4. "Determination of effective surface area of porous, gas-evolving electrocatalysts from potential-relaxation transients", L. Gao, *Interface*, **2**, No.3, 58 (1993).
5. "Adsorption and absorption of H in the H_2 evolution reaction, and the effects of co-adsorbed poisons", L. Gao and B.E. Conway, *Electrochim. Acta*, in press (1994).
6. "Electrolyte wetting effects in the comparative polarization behaviour of the H_2 evolution

reaction at Ni-Mo-Cd electrodes in KF·2HF and KOH·2H_2O melts", Lijun Gao, S.Y. Qian and B.E. Conway, *J. Appl. Electrochem.*, in press (1994).

7. "Poison effects of As_2O_3 on kinetic and adsorptive behaviours of the HER at Pt electrode", L. Gao and B.E. Conway, in course of preparation.

Papers presented at meetings:

1. "Procedure for separation of adsorption pseudocapacitance and 'unfolding' of the active real area of electrodes", B.E. Conway, L. Bai and L. Gao, 183rd meeting of The Electrochemical Society, Hawaii, May, 1993.
2. "Potential-relaxation transient studies on H_2 evolution on Ni-Mo-Cd and steel cathodes in KF·2HF and KOH·2H_2O electrolytes", B.E. Conway, L. Gao and L. Bai, 183rd meeting of The Electrochemical Society, Hawaii, May, 1993.
3. "Poisoning effects on adsorption and kinetic behaviours of H_2 evolution reaction (HER) at Pt electrode in alkaline solution", L. Gao, J. Barber and B.E. Conway, 184th meeting of The Electrochemical Society, New Orleans, October, 1993.

Reports

"Electrochemical characterization of the cathodic hydrogen evolution reaction from KF·2HF melts in F_2-production cells" : 17 quarterly reports to Cameco Inc., Saskatoon, Canada, B.E.Conway, S. Qian and L. Gao, from July 1989 to September 1993.

TABLE OF CONTENTS

CHAPTER III
THEORETICAL TREATMENT AND SIMULATION OF POTENTIAL-RELAXATION TRANSIENTS

CHAPTER IV
RESULTS AND DISCUSSION

CAPTIONS TO FIGURES

LIST OF TABLES

LIST OF SYMBOLS

α	exponent parameter
	transfer coefficient
β	barrier symmetry factor
γ	surface tension
η	overpotential
θ_H	surface coverage of H
θ_P	surface coverage of poison
σ	charge on the plate
τ	integration constant
Φ	Fermi level of metal
ϕ	electrode potential
$\Delta\phi$	absolute potential difference across the interface
ψ	contact angle
ω	impedance frequency
A	surface area of electrode
b	Tafel slope
c_i	concentration of reactant
C_1	Helmholtz capacitance
C_2	diffuse-layer capacitance
C_{dl}	double-layer capacitance
C_ϕ	pseudocapacitance

F	Faraday constant
g	interaction factor
$\Delta G^{0\neq}$	standard Gibbs chemical energy of activation
$\Delta \bar{G}^{0\neq}$	electrochemical Gibbs energy of activation
ΔG^{0}_{ads}	standard Gibbs energy of adsorption
i	current-density
i_0	exchange current-density
i_{corr}	corrosion current-density
$i_{t=0}$	current-density prior to interruption
IR	IR drop due to solution resistance
k_i	electrochemical rate constant
k_i'	rate constant including interaction factor
K	equilibrium constant
q_1	monolayer charge
R_F	Faradaic charge-transfer resistance
T	time constant
v_i	rate of individual step
X_H	lattice site fraction of H
Z'	real part of impedance
Z''	imaginary part of impedance

ABSTRACT

The industrial production of F_2 is through the electrolysis process from HF melt. The reaction of $HF \rightarrow F_2 + H_2$ includes the anodic production of F_2 and cathodic H_2 evolution. It is the latter process on which this thesis study has been concentrated. The objectives of the research were to characterize the polarization behaviour of the electrocatalyst material, a Ni-Mo-Cd composite, for the H_2 evolution reaction (HER) from the $KF \cdot 2HF$ melt, its comparison with that from the analogous $KOH \cdot 2H_2O$ hydrate melt, and the mechanism and kinetics of the HER.

It was found in the work described in this thesis that the high surface area of the electrodeposited material, Ni-Mo-Cd composite alloy, played an important role in its superior performance over a smooth surface electrode, e.g. mild-steel. The real, effective area of the electrode during the polarization process also varies in the different electrolyte solutions, as was observed through comparison between the $KF \cdot 2HF$ and $KOH \cdot 2H_2O$ melts. Contact angle measurements at the solid/melt/H_2 gas interphase and experimental *in situ* determinations of double-layer capacitance, C_{dl}, were carried out, and the effect of wettability and accessibility of electrolytes to the inner pores of the porous surface in association with the surface tension was discussed. The "unfolding" of the electrochemically accessible area of a porous Pt electrode in KOH electrolyte of increasing conductivity was demonstrated experimentally for the first time. The transmission-line model and constant phase element (CPE) concept were used in the interpretation of the a.c. impedance results.

A new method for *in situ* determination of C_{dl} was developed by means of analysis of initial (i.e. over short times of 2 to 100 μs) potential-relaxation transients in the HER. Its

effectiveness was examined in comparison with the results of other methods, e.g. cyclic voltammetry and a.c. impedance measurement, based on a well-known prototype system of Pt electrodes in KOH solutions.

A theoretical treatment was developed to describe the *full* potential-relaxation transient behaviour in terms of the roles of double-layer and H pseudocapacitance ($C_{\phi,H}$) relaxation processes. The representation of the experimental data through computer simulation provided rate constants and other parameters of the reaction. It is shown how the o.p.d. H coverage, θ_H, and the associated pseudocapacitance of the electrode can be quantitatively evaluated from the calculation involving rate constants.

The presence of catalyst poisons in the electrolytes has significant influence in the industrial electrolysis process. In the present work, the effects of As_2O_3 and $(NH_2)_2C{=}S$ as poisons for the HER on the kinetics and adsorption behaviour were quantitatively characterized. The effects on the HER were theoretically treated, taking account of poison coverage θ_P and a lateral interaction factor, g, at the electrode surface. Related θ_H, θ_P, g and $C_{\phi,H}$ quantities were evaluated from the experimental data obtained, for the HER, at the Pt electrode in $KF \cdot 2HF$ and KOH solutions.

CHAPTER I

INTRODUCTION

This Ph.D thesis is the result of research conducted on a project jointly supported by N.S.E.R.C and Cameco Corporation on a so-called N.S.E.R.C Cooperative Research and Development (CRD) grant. Accordingly, the subject has involved both fundamental electrode kinetic and adsorption studies, and a component of industrially oriented work of practical significance.

1.1 Background and Objectives of the Project

First it will be useful to give a brief outline of the origin of this research project and its general objectives. Elemental fluorine is required for preparation of UF_6 from uranium oxide ores for the purpose of obtaining pure or isotopically enriched uranium. In Canada this process had been operated for some years by Eldorado Resources Ltd. at their Port Hope plant which, in recent years, has been owned and operated by Cameco Corporation, the co-sponsor with N.S.E.R.C. of the present CRD project at University of Ottawa.

It is well known that, owing to the high electronegativity of fluorine and its position at the "bottom" of the electrochemical series, it can only be prepared by an electrolytic process or by means of an exotic reaction such as decomposition of XeF_4. The electrochemical route is by electrolysis of $KF \cdot 2HF$ melts at ca. 85°C, using a carbon anode and a mild-steel cathode in the commercial operation. The cathodic process, conjugate to the anodic one of F_2 production, is the evolution of molecular H_2 by discharge from the HF.

The operation of electrolysis cells for F_2 production is accompanied by a remarkably

large overvoltage at the anode, amounting to 6-8 V under operating conditions. The study and improvement of this behaviour, which leads to uneconomic power consumption in the commercial operation, was the subject of previous projects of this laboratory with Cameco Corporation and Eldorado Resources. The origins of the anode effect were examined and traced to (a) barrier-layer "CF" film formation and (b) a consequent formation of a F_2 gas-film barrier, with related sluggish F_2 bubble formation and detachment, connected with the contact angle of bubbles at the fluorinated carbon interface. A method leading to major improvement of the anode overvoltage behaviour was developed and reported in several papers arising from the previous work [1-3] in this laboratory. The physico-chemical basis of the improvement effect was also established in that work.

It was realized later that appreciable overvoltage effects were also associated with the cathode reaction, which had equal significance to those at the anode for the overall cell operation. Cathodic overvoltages at the H_2-evolving cathode can also rise to ca. 6 V under certain operating conditions (a so-called hyperpolarization effect). In the present project (work of Mr. Qian), the origin of this effect has been found to arise on account of (a) HF starvation locally at the electrode; (b) resulting local solidification of the melt in the electrode/melt boundary layer, and (c) a bubble-film barrier effect in the $KF \cdot 2HF$ melt due to unfavourable contact angle between H_2 bubbles and the melt/cathode interface, as was also found for F_2 bubbles at the C anode. This effect becomes more important when poison species such as As are present in the melt and become adsorbed at the surface. The overall work on this aspect has been reported in an original paper in course of publication [4].

Studies on alternative H_2-cathode materials, having improved electrocatalytic performance

over mild-steel, is also one of the objectives in the research project. Electrodeposited Ni-Mo-Cd composite electrodes, which are micro-porous, were found to have excellent electrocatalytic properties for the hydrogen evolution reaction (HER) in aqueous solutions, in terms of small Tafel slopes and high exchange current-densities [5]. The behaviour of such materials as electrocatalyst cathodes, and their resistance to corrosion in the KF·2HF melt, have been extensively studied during the course of the present Ph.D program.

1.2 Electrocatalysis in the Hydrogen Evolution Reaction (HER)

The hydrogen evolution reaction (HER) at cathodes is one of the reactions most frequently occurring in industrial cells, and thus naturally has been among the most intensively studied of electrochemical processes [6-19]. This reaction has also been extensively examined for reasons such as (a) elucidation of the mechanism of the HER as a prototype for heterogeneous electrochemical reaction kinetics of processes involving ion neutralization and atom transfer; (b) obtaining a systematic relation of the catalytic properties of various metals for the HER; (c) its relevance to many related important fields such as corrosion of metals, electrolytic hydrogenation of organic substances, etc., and (d) some more up-to-date reasons, such as efficient hydrogen production or use of hydrogen in fuel cells, seeking a prospect towards the so-called hydrogen economy. Finally it should be mentioned in (e), its role (in the case of d) in the supposed process of "cold fusion".

Traditional cathodes for industrial applications have long been iron or mild steel [20,21]. However, these materials do not withstand the more severe conditions of high caustic concentration and higher temperature which derive from the employment of most extreme conditions in commercial water electrolysis, and in membrane cells used in the chlor-alkali

industry at 95°C. Under similar circumstances, Ni and Ni-based alloys are mostly used to replace the above materials [22,23].

The search for new electrode materials is expected to be guided by the fundamental understanding of the factors governing the kinetic activity of such electrodes. In electrochemistry, this branch of the discipline is known as "electrocatalysis". It is the science devoted to the relationship between the properties of materials and their surfaces, and the electrode reaction rate at some defined potential. The objective of electrocatalysis as a science is to establish a predictive basis for the design and the optimization of electrocatalysts, exhibiting low overvoltage polarization behaviour and stability to corrosion.

In the case of hydrogen evolution, the theory of electrocatalysis on single individual metals was established about thirty years ago [24,25]. However, no decisive advances have been made since then from the point of view of the theory of composite materials. It is probably for this reason that a great deal of applied research has been conducted thus far, following the always convenient but empirical approach of "try and see". In one publication [26], it has been explicitly reported that more than 400 different materials have been tested in a few years with the purpose of finding the best one! However, a fundamental analysis was made by Parsons [27] on binary alloys with respect to improvement in kinetics of a reaction in relation to chemisorption energy of its intermediate(s), e.g. H.

1.3 Relations of Electrocatalysis to Catalysis

Electrode reactions always heterogeneously proceed at the interface of an electrode with an electrolyte. Electrocatalysts, i.e. catalysts for electrochemical reactions, can be defined here through a comparison with heterogeneous catalysts. The most significant difference between

chemical catalysis and electrocatalysis is based on the fact that the electrocatalytic reaction's rate is dependent on potential ($\Delta\phi$), while the rate of a chemical catalytic reaction cannot be so affected, except, e.g., analogously, by high pressure.

In the case of an heterogenous reaction, the Arrhenius equation [28] represents the catalytic rate according to

$$v = c\theta\frac{kT}{h}\exp[\frac{-\Delta G^{\circ\ddagger}}{RT}] \tag{1.1a}$$

where θ is the steady-state coverage by some adsorbed intermediate that is involved, or,

$$v = c(1-\theta)\frac{kT}{h}\exp[\frac{-\Delta G^{\circ\ddagger}}{RT}] \tag{1.1b}$$

for a step requiring a vacant surface site fraction, 1-θ. Or more generally

$$v = cf(\theta)\frac{kT}{h}\exp[\frac{-\Delta G^{\circ\ddagger}}{RT}] \tag{1.1c}$$

In the case of an electrocatalytic process, involving charge transfer, the rate is given [29] by:

$$v = \frac{i}{nF} = cf(\theta)\frac{kT}{h}\exp[\frac{-\Delta G^{\circ\ddagger}}{RT}]\exp[-\frac{\beta\Delta\phi F}{RT}] \tag{1.2}$$

where β is a barrier symmetry coefficient for the case where the reaction is a charge-transfer process. (There are other types of reactions, where the primary pre-electrochemical reaction is dissociative chemisorption as in fuel-cell processes, e.g. $HCOOH + 2M \rightarrow MH_{ads} + MCOOH_{ads}$, or $H_2 + 2M \rightarrow 2MH_{ads}$ followed by a potential-dependent charge transfer step). Both of these rates, v, contain, in their rate equations, a reactant concentration term, c; a factor $f(\theta)$, representing some function of the coverage of the electrode surface by adsorbed intermediates; Boltzmann's constant, k; Planck's constant, h; the gas constant, R, and the standard Gibbs chemical energy of activation, $\Delta G^{\circ\ddagger}$. Both expressions involve a dependence on temperature

(T) but only the electrochemical reaction rate expression involves a potential-dependent term, in which F represents Faraday's constant and $\Delta\phi$ represents formally the absolute metal-solution potential difference at the electrode/solution interface. Since the latter is never knowable at a given electrode, eqn.(1.2) is most conveniently recast in terms of the overpotential η defined (see following Section 1.4) as the difference of any ϕ value and that ϕ_{rev} for the same process when it is at equilibrium ($\eta=0$). η is normally measured against some convenient reference electrode, often (for the HER case) a reversible reference electrode involving the reaction itself.

1.4 Kinetic Aspects of Electrode Processes

Electrochemical rates v are measured as current-densities, which can be expressed in the following way:

$$i = nFv = \bar{k}_i nF(c_R)_s(1-\theta) \tag{1.3}$$

where $\bar{k}_i$, the electrochemical rate constant which, according to "absolute rate theory" [30], is given by

$$\bar{k}_i = \tau(\frac{kT}{h})\exp[\frac{-\Delta\bar{G}^{\circ\neq}}{RT}] \tag{1.4}$$

and τ is the so-called transmission coefficient (often taken as approximately unity); $\Delta\bar{G}^{\circ\neq}$ is an electrochemical standard Gibbs energy of activation; nF is the number of Coulombs involved (expressed in terms of Faradays) in the overall reaction proceeding at the rate v in mol s^{-1} cm^{-2}; $(c_R)_S$ is the concentration of the reactant molecule or ion at the outer Helmholtz plane and θ is the steady-state coverage of any intermediates that are adsorbed on the surface at a given potential as a result of the discharge of the reactant R. Other terms in the equation have their usual meanings. The Gibbs energy of activation is potential-dependent according to

$$\Delta\bar{G}^{\circ\neq} = \Delta G^{\circ\neq} + \beta F \Delta\phi \tag{1.5a}$$

$$= \Delta G^{\circ\neq} + \beta F (\Delta\phi_r + \eta) \tag{1.5b}$$

This equation is a relation between the electrochemical standard Gibbs energy of activation, $\Delta\bar{G}^{\circ\neq}$, and the chemical free energy of activation, $\Delta G^{\circ\neq}$, plus an additional term which is the electrical energy factor assisting reaction. The basic effect of voltage on rates originates from change of Fermi level of metals, Φ, ($\Phi_V = \Phi_{V=0} \pm$ eV). In eqn.(1.5), $\Delta\phi$ represents the absolute metal-solution potential difference at the electrode and η is the overpotential required to drive the reaction at a net current-density i beyond the reversible rate (net rate zero) at the reversible potential, $\Delta\phi_r$, i.e. $\eta = \Delta\phi - \Delta\phi_r$.

For a simple discharge process, eqns. (1.3), (1.4) and (1.5) can be combined to give a general expression for the net current-density, i, in the form of the so-called Butler-Volmer equation taking account of both the backward and forward components of the reaction rate (current-density):

$$i = i_f - i_b \tag{1.6a}$$

$$= i_0 [\exp(\frac{\beta F \eta}{RT}) - \exp(-\frac{(1-\beta) F \eta}{RT})] \tag{1.6b}$$

where i_f, i_b represent the current-densities of the forward and backward reactions, respectively, and i_0 is the so-called exchange current-density for $\eta=0$ which dynamically characterizes the reversibility of the reaction. In the case where the discharge step is rate-determining and produces an adsorbed intermediate, the exchange current-density is given by the following equations:

$$i_0 = Fk'_f c_i (1-\theta) \exp\left(\frac{\beta F \phi_r}{RT}\right) \tag{1.7a}$$

$$= Fk'_b c_j \theta \exp\left[-\frac{(1-\beta) F \phi_r}{RT}\right] \tag{1.7b}$$

where c_i and c_j are the concentrations of the reactants of the forward and backward steps and now potential-independent rate constants (k'_f, k'_b) are introduced. The fractional coverage by adsorbed intermediates and free site availability are represented by θ and 1-θ, respectively. At sufficiently high values of overpotential η, viz. $\frac{\beta F \eta}{RT} \gg 1$, eqn.(1.6) becomes

$$i = i_0 \exp\left(\frac{\beta F \eta}{RT}\right) \tag{1.8}$$

or

$$\eta = \left(\frac{RT}{\beta F}\right) \ln i - \left(\frac{RT}{\beta F}\right) \ln i_0 \tag{1.9}$$

This is a form of the well-known Tafel equation [6] commonly represented as:

$$\eta = a - b \log i \tag{1.10}$$

where a and b are given by

$$b = \frac{2.303 RT}{\beta F} \tag{1.11a}$$

and

$$a = -\left(\frac{RT}{\beta F}\right) \ln i_0 \tag{1.11b}$$

by comparison with eqn.(1.9).

At low values of overpotential η, viz. $\frac{\beta F \eta}{RT} \ll 1$, eqn.(1.6b) can be written, taking into consideration only the first term of the series expansion of the exponential, as

$$i = i_0 \frac{\eta F}{RT} \tag{1.12}$$

Ohm's law allows us then to define an equivalent Faradaic charge-transfer resistance, R_F, as $d\eta/di$ or

$$R_F = \frac{RT}{i_0 F} \tag{1.13}$$

which is important as one of the means for i_0 evaluation, to be considered later in this thesis, and as one of the bases of a.c. impedance analysis of kinetics of electrode processes.

The Tafel slope, b, and the exchange current-density, i_0, are the two fundamental parameters characterizing steady-state electrochemical polarization behaviour of an electrode reaction and thus of the effectiveness of electrocatalysis. Ideally, a combination of high i_0 and low b values is the condition required for optimizing cathode or anode performance, i.e., to minimize polarization at appreciable current-densities and thus provide "good electrocatalysis" in the process with minimum electrical power consumption.

However, i_0 and b values are usually mutually dependent quantities, e.g. both are closely related to the adsorption behaviour of the reaction intermediates adsorbed on the electrode surface, and the mechanism of the reaction and its rate-determining step.

The kinetically involved intermediates thus influence the exchange current-density of the process through their standard Gibbs energy of adsorption, and the Tafel slope through the potential-dependence of their coverage (see below).

1.5 The Steps in the Hydrogen Evolution Reaction (HER)

Cathodic H_2 evolution can take place from acid or alkaline aqueous solutions. The

overall reaction in acid solution is

$$2H_3O^+ + 2e \rightarrow H_2 + 2H_2O \qquad (1.14)$$

and in alkaline solutions, it is

$$2H_2O + 2e \rightarrow H_2 + 2OH^- \qquad (1.15)$$

Several reaction pathways are possible for the HER but on account of the previous work of many electrochemists, e.g. Butler, Frumkin, Bockris, Horiuti, Conway and Parsons, only two reaction paths are regarded now as likely to be involved even though, at the beginning of this century, a variety of reaction steps had been proposed as part of the overall process, including e.g. nucleation of bubbles.

In acidic solution, the reaction involves first the discharge of an hydrated proton at the electrode surface with formation of an adsorbed H atom at some site on the metal surface lattice:

$$M(e) + H_3O^+ \underset{k_{-1}}{\overset{k_1}{\rightleftharpoons}} MH_{ads} + H_2O \qquad (1.16)$$

The above step is common to all currently and previously considered reaction paths and it represents the process by which H is initially deposited onto an electrode surface.

The adsorption step must be followed by either an electrochemical-desorption step:

$$MH_{ads} + M(e) + H_3O^+ \underset{k_{-2}}{\overset{k_2}{\rightleftharpoons}} H_2 + H_2O + 2M \qquad (1.17)$$

or an heterogeneous chemical recombination step:

$$2MH_{ads} \underset{k_{-3}}{\overset{k_3}{\rightleftharpoons}} H_2 + 2M \qquad (1.18)$$

The steps (1.17) and (1.18) are alternative desorption paths, consecutive with respect to step

(1.16).

In alkaline solution, the mechanism is similar except that the proton donor is a water molecule rather than H_3O^+ and the conjugate base product is OH^- instead of H_2O:

$$M(e) + H_2O \underset{k_{-1}}{\overset{k_1}{\rightleftharpoons}} MH_{ads} + OH^- \qquad (1.19)$$

$$MH_{ads} + M(e) + H_2O \underset{k_{-2}}{\overset{k_2}{\rightleftharpoons}} H_2 + OH^- + 2M \qquad (1.20)$$

or

$$2MH_{ads} \underset{k_{-3}}{\overset{k_3}{\rightleftharpoons}} H_2 + 2M \qquad (1.21)$$

It has been noted in the literature, for alkaline solutions, that the activation energy of the steps (1.19) or (1.20) will not generally be the same, respectively, as those for (1.16) or (1.17), so that the mechanism in terms of which step is rate-determining of the HER in acidic and alkaline solution at a given metal will not generally be the same.

As can be seen from the two series of equations above, a multistep reaction is involved, for which it is assumed that there is always a "rate-determining step" (r.d.s.) which characterizes the kinetic behaviour of the reaction. A rate-determining step in a reaction sequence is the step having the smaller or smallest rate constant or, correspondingly, the highest Gibbs energy barrier. Often the rate-determining step is incorrectly referred to as the "slow step" in the reaction but, in the steady-state, all steps are proceeding at the same velocity. Through information obtained by means of the Tafel slope behaviour, coupled with results from the new potential-relaxation methods, and with a.c. impedance measurements, the adsorption behaviour of the overpotential-deposited (o.p.d.) H can be characterized and the rate-determining step more

easily identified.

1.6 Parameters Determining the Exchange Current-Density

The HER has been one of the first electrochemical reactions to be studied in a detailed kinetic way [31,32]. In the mechanistic studies of electrochemical reactions, an important concern is to find the dependence of standard rate constants or exchange current-densities, i_0, on the properties and chemical identity of the electrode metal, and the state and orientation of its surface. It was early noted [33] that there was a "periodic" relation of log i_0 to the properties of metals across the Periodic Table, such as lattice energy, electron work-function, Φ_M, etc. However, such correlations to Φ_M should not directly arise since the potential-dependent reaction rate constants cannot depend on the Φ_M due to the fact that the terms in Φ_M cancel out around the interfaces of the measuring circuit when potential is referred to the potential of a reference electrode [29] in experimental measurements.

It was shown by Butler [10] and by Horiuti and Polanyi [34], following Gurney's theory of electron transfer [35], that the activation energy for proton discharge at a metal producing the chemisorbed H intermediate, would depend on the adsorption energy $\Delta H_{ads,H}$ of the discharged H. The experimental relations of log i_0 values to $\Delta H_{ads,H}$, and indirectly to Φ_M, that were demonstrated by Conway and Bockris [36] and also by Ruetschi and Delahay [37] were rationalized by Parsons [25] on a theoretical basis that the log i_0 values for the steps in the HER should exhibit a "volcano" relation (Fig.1.1) when plotted against the standard Gibbs energy, $\Delta G^o_{ads,H}$, of adsorption of the H intermediate. The essential result of this analysis was that log i_0 value is determined by the product of two terms $(\theta_{H,r})^\beta$ $(1 - \theta_{H,r})^\beta$ where β is the barrier

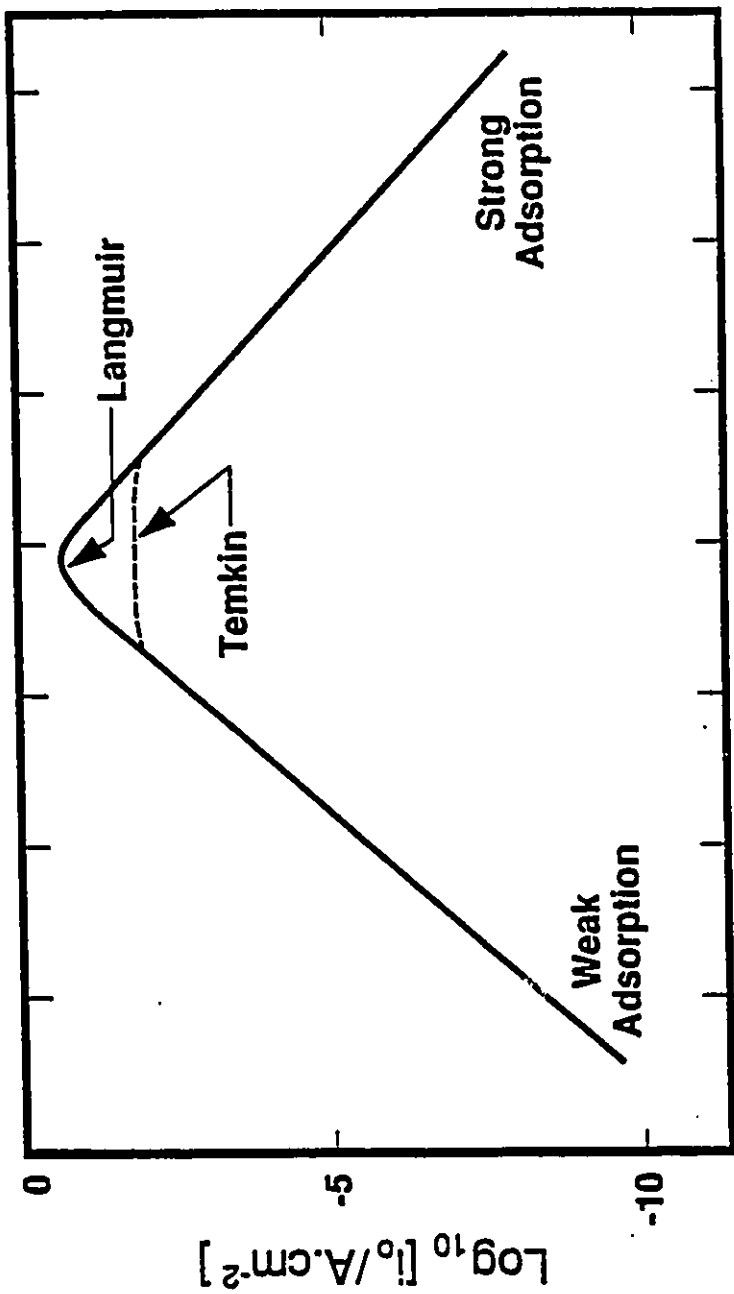

Fig. 1.1 Theoretical relation between log i_o values and standard Gibbs energy of chemisorption of H in the HER (from ref. [25]).

symmetry factor for the proton discharge step, and $\theta_{H,r}$ is the coverage by H at the reversible potential to which i_0 applies. For $\beta = 0.5$, the variation of log i_0 with $\Delta G^o_{ads,H}$ is symmetrical about $\Delta G^o_{ads,H} = 0$, with its maximum at this value corresponding to $\theta_H = 1 - \theta_H = 0.5$.

Physically speaking, this relation expresses the fact that for an overall process involving an adsorption step and a desorption step, kinetics will not be good if the surface is (a) extensively filled by a strongly adsorbed intermediate (since then discharge on the $1 - \theta$ fraction of the surface will tend to be slow) or alternatively (b), relatively empty, since then the desorption rate, determined by θ, will tend to be slow. Optimum conditions obviously arise when $\theta_H \approx 1 - \theta_H \approx 0.5$.

In a more recent examination of this matter, Trasatti [38] demonstrated that when log i_0 is plotted against the MH bond energy or the work function, (using a careful selection of more reliable log i_0 values for the HER for various metals together with better Φ values.), d- and sp-metals exhibit two distinct linear relationships (Fig.1.2). This type of plot is in good agreement with the form of Parsons' theoretical volcano plots expressed in terms of $\Delta G^o_{ads,H}$. The connection between these two types of plots (experimental and phenomenological, in terms of MH bond energy or Φ, and theoretical, in terms of $\Delta G^o_{ads,H}$) must arise because of a systematic relation between MH bond energies and Φ as was demonstrated in the paper of Conway and Bockris [36].

Of great importance is the nature of surface bonding of intermediates to the metal; this depends very much on the geometry and orientation of the crystal plane on which the chemisorption takes place, and on the orientation and symmetry of emergent orbitals (especially dsp hybrid orbitals at transition metal surfaces) at the metal surfaces as emphasised by Bond

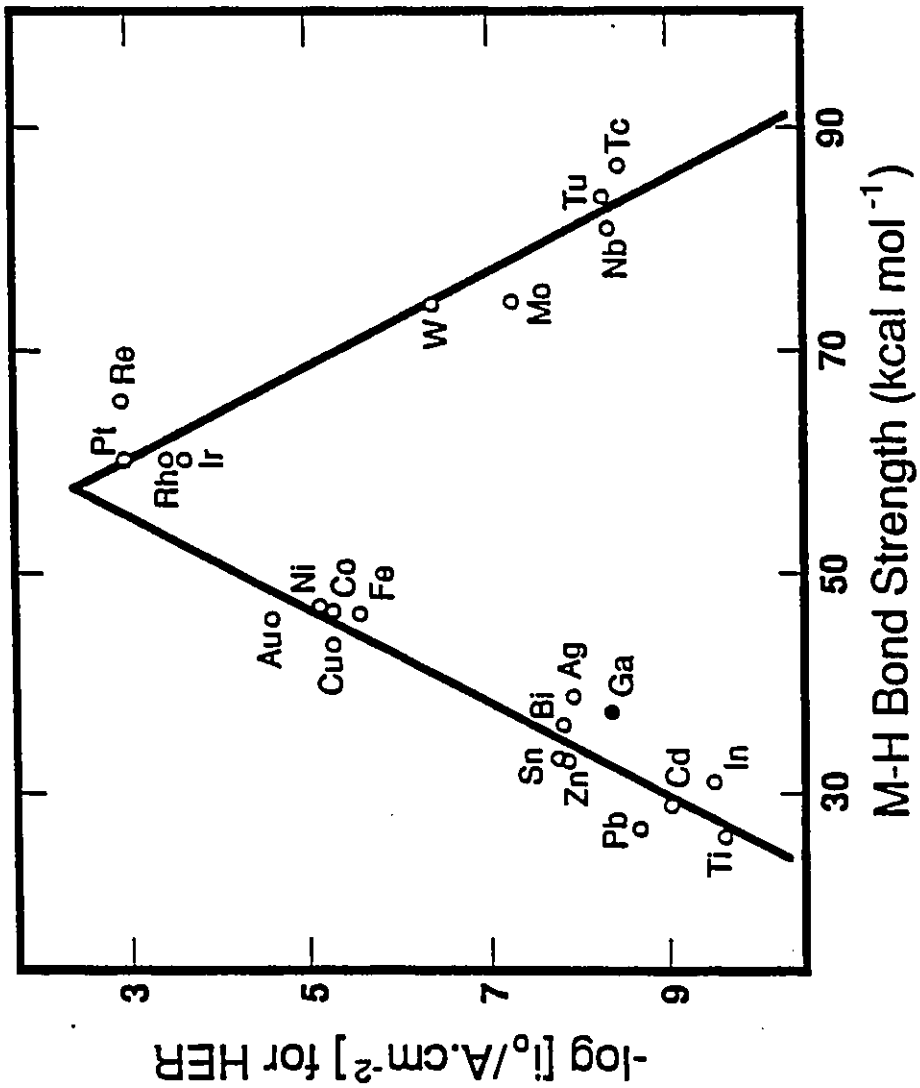

Fig. 1.2 Experimental "volcano"-shaped curve for kinetics (as log i_o) for hydrogen generation on metals (from ref. [38]).

[39]. He proposed a model of adsorption on group VIII metals [40], based on the assumption that the distributions of surface atomic orbitals may be calculated from bulk crystal theory, and that adsorption sites will arise where these orbitals overlap. These factors determine the geometry of coordination of the ad-species at the catalyst or electrocatalyst surface. Since that work [39], a great many papers have appeared on molecular-orbital calculations on bonding at surfaces, and surface states and electron-density distributions. Interesting modelling of local coordination situations at metal surfaces has been done on polyatomic clusters, e.g. as in the work by Messmer et al. [41].

If correlations do exist for simple metals, predictions are much more difficult for composite materials. The need to replace noble metals, which are often the best as catalysts, by cheaper and more available metals and alloys having improved electrode polarization behaviour, has led to the investigation of the electrocatalytic features of composite transition metal catalysts for the HER [42-45]. From a true catalytic point of view, what is looked for are so-called "synergetic effects", i.e., a complementary influence between two or more components so as to obtain a material the activity of which exceeds that of the pure components [46]. An important and perhaps surprising prediction made by Parsons [27] was that for a bimetallic catalyst with two *non-interacting* sites obtained by combining two metals with different adsorption energies, *no* enhancement of the activity is to be expected. However, electronic effects in homogenous alloys, related to d- and sp-band structures *can* lead to advantageous materials that have properties not directly related to those of their component metals, as has been found in a number of works [47,48]. Miles [49] suggested that a combination of two metals from the two branches of the volcano curve could result in enhanced activity [50], but this

implies, of course, that a direct correlation exists between composition and heat of hydrogen adsorption. The same approach was suggested by Jaksic [51] who showed that a combination of Ni or Co with Mo can result in a substantial enhancement of the activity for the HER [52].

These and other experimental observations have been examined in terms of the Brewer-Engel valance-bond model [53-56] for bonding in metals and intermetallic phases. The Brewer intermetallic bonding model is based on the Lewis acid-base interaction concept. If metals on the left half of the transition series, having empty or half-filled d-orbitals, are alloyed with metals of the right half of the transition series, having internally paired d-electrons, not available for bonding in the pure metal, an "internal charge transfer" will occur. The Brewer-Engel model is also concerned with the prediction of the particular mixture of d- and sp-electrons, which should be such that a configuration of lowest Gibbs energy is achieved for the alloy.

In the application of Brewer-Engel concepts of electronic-structure influence on the properties of transition metal alloys, it is not clear how these ideas predict improved catalytic activity for "Lewis base/acid" pairs of the metals in the alloys. Only on an empirical basis, from the observed experimental behaviour, are such effects indicated. A further complication is that the surface composition of alloys is rarely identical with bulk composition, so that concepts which properly apply to bulk properties cannot be expected to apply to surface behaviour due to the asymmetry of bonding in the surface and the geometry of emergent orbitals (*cf.* refs. [39,40]), as well as surface/bulk composition differences. The covalent or metal bonding in the bulk phase will discontinue at the surface, and form surface states due to dangling bonds. These surface states can be determining for the orientation and strength of binding of the adsorbed species at the surface. The surface structural factor, e.g. presence of various

single-crystal planes, defects and steps at the surface, is also important for catalytic activity [57], as will be discussed in a later section.

1.7 The Relationship Between the Tafel Slope, b, and the Isotherm for Adsorption of the Intermediate

Besides affecting the exchange current-density, H adsorption is also a determining factor in the value of the Tafel slope, b, through an adsorption isotherm factor. This is because (see eqns.(1.16-1.18)) the rate equation for the rate-determining step normally involves a function of coverage, $f(\theta)$, of the adsorbed intermediate. The reciprocal of the Tafel slope, b, can be expressed as follows:

$$\frac{1}{b} = \frac{d\log i}{d\eta} = \frac{d\log f(\theta_H)}{d\eta} + \frac{\beta F}{2.303RT} \qquad (1.22)$$

reciprocal Tafel slope — adsorption factor — charge-transfer factor

This equation reveals that the dependence of $log\ i$ on electrode overpotential, η, is related to both the adsorption factor and the charge-transfer factor which importantly includes β. It is important to indicate here that eqn.(1.22) offers also the possibility of a dual Tafel slope polarization behaviour for the same rate-determining step, i.e. if the adsorption factor becomes appreciable and constant in one particular potential range, or if it tends to zero in another, then two Tafel slopes can be observed depending on whether θ is « 1 or → 1.

For reaction mechanism studies, the importance of the Tafel slope and its dependence on the adsorption of intermediates has been emphasised in various works of Bockris [58,59], Parsons [60,61], Despić [62,63] and Conway [64-66].

When the proton-discharge step is rate-determining and θ_H « 1, the reciprocal of the

Tafel slope is determined mainly by the charge-transfer factor in eqn.(1.22). This situation is found to arise at mercury and also gold for the HER [59,67,68] since an experimental Tafel slope near 0.118 V is obtained at 298 K, as expected theoretically, taking $\beta \simeq 0.5$. However, when either of the desorption steps control the overall rate, e.g. (1.20) or (1.21) in alkaline and (1.17) or (1.18) in acidic solutions, θ_H can be appreciable and potential dependent. It is seen that a significant value of the adsorption factor must lead to reduced values of the Tafel slope; this is of great importance for electrocatalysis and is exemplified experimentally (0.030 V) at low overpotentials at Pt or (0.040 V) for some Ni-Mo composites in the HER [58,69-72]. Hence, proper elucidation of the rate-determining step and characterization of the electrocatalysis requires reliable experimental evaluation of the adsorption behaviour of the overpotential-deposited (o.p.d.) H in relation to Tafel slopes.

The possibility that the various steps proceed at comparable rates, rather than with a single r.d.s., has also been suggested and theoretical calculations have been carried out [73,74]. This would explain the curvature of the Tafel line observed in some cases [75]. A possibility of slow surface diffusion (or re-arrangement) of adsorbed intermediates:

$$M + H^+(aq) + e \rightarrow MH^{\bullet}_{ad} \qquad (1.23)$$

$$MH^{\bullet}_{ad} \rightarrow MH_{ad} \qquad (1.24)$$

has also been suggested. This would imply that the intermediate $H^{\bullet}_{ad}$ produced in step (1.23) may not be the catalytically active one. The existence of "inert" and "active" adsorbed hydrogen has recently been postulated on the basis of IR surface investigations [76]. For example, at Pt, the surface is already fully covered by strongly bound, underpotential-deposited (u.p.d.) H at the reversible potential and it is believed that this state of H is *not* the kinetically-involved

intermediate in the HER at more negative potentials.

It is the purpose of electrocatalysis to design materials capable of evolving hydrogen with low Tafel slope up to high current-densities, which should be achievable by appropriately modulating the M-H adsorption strength. This is precisely what is pursued when an elemental electrocatalyst (a metal) is alloyed with others, or combined with non-metals (such as oxides, etc.). The heat of adsorption of the intermediate is the most important parameter, which in turn will depend on the electronic and structural properties of the catalyst surface. Unfortunately, the *a priori* theoretical description of the surface bond is still insufficient for composite materials although important advances for pure metals have been made in recent years [27,36,38,77]; it is therefore necessary to have resource to experimental and conceptual correlations.

The Tafel slope b is an "intensive" quantity, i.e., in so far as it is not influenced by the surface area. Thus, the improvement of practical electrocatalytic behaviour (increase of current-density at a certain overpotential) by use of a porous electrode, such as an electrodeposited Ni-Mo-Cd composite electrode [5], is mainly because of the increase of the real, effective surface area of the material per apparent cm^2. When a change of Tafel slope arises, it must be the electronic and adsorption factors of the deposited composites that are responsible. Sometimes, Tafel slopes are found that are not regular values such as 118 mV (2.3RT/0.5F) or 30 mV (2.3RT/2F). Surface composition of the electrodes could be the major cause of this behaviour, as has been found experimentally with some binary transition metal alloy electrodes.

However, technical problems may arise in the measurement of Tafel plots in so far as that IR drop (originating from the solution resistance between the electrode surface and the Luggin capillary tip of the reference electrode) has to be corrected before the true Tafel slope

can be evaluated. However, in some types of electrocatalyst materials, the solution resistance is unknown *inside* the pores of the porous electrode, and this can lead to uneven distribution of electrode potentials and currents along the porous surface[1]. Another complication arises for the situation where part of the porous surface is not wetted by the electrolyte, as found with the KF·2HF melt during the work reported in this thesis. However, industrial interest is centered on the overall effectiveness of porous, high-area electrocatalyst materials. The practical electrocatalytic behaviour is usually characterized in terms of the achieved currents at certain voltages, or the required voltages under certain currents without quantitative reference to real current densities or Tafel slopes.

1.8 Evaluation of Real Surface Area of Electrodes

Knowledge of the real surface area is a prerequisite for the proper evaluation of the activity of an electrocatalyst material, especially when comparative data are required relative to other samples. It is quite difficult to determine real surface areas because there are no unique techniques applicable to all materials. Sometimes BET values are given, but the BET (dry) area may not correspond to the electrochemically accessible active (wet) one, especially if supported catalysts are used or inert components are part of an admixture [78]. Determinations based on double-layer capacitance (C_{dl}) are an obvious approach but can be ambiguous [79] because there exists no absolute reference for many materials and there is no potential at which the capacitance is the same even among different crystal faces of a given metal [80]. For porous materials,

[1] Under certain conditions of significant internal resistance in pores, these effects can lead to a doubling of the Tafel slope, as for porous fuel-cell electrodes [86].

traditional methods involving a.c. impedance or transients give results dependent on the time-domain of the response, but relative measurements for different samples of the same materials are acceptable. A procedure involving determination of the diffuse-layer capacitance was proposed by Parsons and Zobel [81], but is only easily applicable to interfaces of non-porous electrodes.

The best approach is normally an *in situ* determination based on voltammetry or charging curves, usually within the underpotential deposited hydrogen region [82,83] in the case of most noble metals. It is of course necessary to know the actual value of θ_H for absolute determinations, but the method is practicable on a relative basis. The method becomes absolute only in a few cases, in particular for Pt electrodes [84] for which the catalytic activity *per metal atom in a surface*, which is the parameter really needed to evaluate electrocatalytic effects, can be calculated.

It is essential to distinguish effects which arise just from real-area differences from other factors of more fundamental interest arising from the electrode kinetic difference of Tafel i_0 and slope b values due to surface and electronic properties [85] of the electrode metals. Because of the practical importance of the accessible real-area of many electrocatalyst materials [86,87], it is necessary to have ways of experimentally measuring the *in situ* "real-area" factor independently of the overall activity. Such evaluations, in the past, have suffered major uncertainty when electrochemical methods have been applied, due to the complicating effects of porosity on electrical response functions and the role of pore occupancy by evolved gases.

The practically measured real surface area is usually found to vary depending on the actual method used. For example, the commonly used BET method gives the real (dry) surface

area accessible to a gas phase and includes an area fraction which may not be wetted by an electrolyte in a real electrode/electrolyte solution system [2].

One of the major problems in *in situ* real surface area measurements is that there is no reliable method available to determine the real electrochemically active area pertinent to the *overpotential* regions where significant Faradaic currents are passing and the utilized surface area may, in fact, be changing during the electrode process. For example, in the process of metal plating, the surface area is usually continuously changing with time while in the H_2 evolution reaction at porous electrocatalysts, some fine pores may become filled by H_2 gas as the electrolysis proceeds.

As may be expected, the major difficulties in C_{dl} measurement in the overpotential region are associated with three problems: (i) the presence of the usually substantial continuous Faradaic current; (ii) the presence of the pseudocapacitance, C_ϕ [88], corresponding to the potential-dependence of adsorption of reaction intermediates and (iii) the influence of the porosity of the electrode on the distributed double-layer capacitance and resistance, related to the internal current-distribution [83].

These problems are treated in the present work (Chapter IV) by means of fast open-circuit potential-relaxation measurements, followed by interruption of the prior steady-state current. A prototype system was selected and quantitatively evaluated. The HER from KOH solution at a bright smooth Pt electrode and a porous plated one (platinized Pt) were examined comparatively. It is believed that this system provides the best example for illustrating treatments designed to overcome the above mentioned difficulties in C_{dl} measurements in the overpotential region, since the kinetics of the HER and its associated H-adsorption

pseudocapacitance at a Pt electrode have been well investigated previously [15,72]. In addition, the Pt electrode has the unique characteristic that its real electrochemical accessible surface area can be directly measured *in situ* reliably and accurately by means of slow cyclic-voltammetry from which the monolayer u.p.d. H charge can be precisely determined [89], and thus a true reference area evaluated.

The electrodeposited composite Ni-Mo-Cd electrode, that has been used as electrocatalyst material in a number of recent studies of the HER at high current-densities [5,72,90], is micro-porous in structure. The effective real-area has been examined comparatively in the present work in the $KF \cdot 2HF$ melt and the analogous $KOH \cdot 2H_2O$ hydrate melt at 85°C. The behaviour of a comparable smooth bulk alloy Ni-Mo electrode, which was prepared thermally as an homogeneous solid solution, was also examined as the reference for the real-area evaluation.

1.9 Surface Characterization

The properties of the electrocatalytic materials depend on the electronic structures and the orientations of their crystal surfaces. Well-defined single-crystal surfaces usually differ from corresponding polycrystal electrodes in their electrocatalytic performance. It is also desirable, where possible, to characterize the surfaces of the electrodes, i.e. the surface compositions of composite materials to assess the actual electrocatalytic activity. Surface analysis techniques, such as Scanning Electron Microscopy (SEM), X-ray Photoelectron and Absorption Spectroscopy, are required to identify the surface appearance and composition of porous materials (e.g. electrodeposited Ni-Mo-Cd electrodes) before and after the electrochemical measurements are made.

It is necessary to correlate the electronic and structural factors of the metals in characterizing the catalytic behaviours. The nature of the surface also depends on the orientation of surface structure, e.g. many catalytic features of single-crystal surfaces have been found [91-94], which are not recognized with polycrystalline surfaces. Upon formation of the surface, the coordination of surface atoms, interatomic distances, distance between adsorption sites, and surface energy will all depend on the plane exposed. Generally it is not the entire electrode surface, but only some individual elements, the so-called "active centres" that are believed to take part predominantly in the reactions; It is of great interest which of these surface elements, *viz* individual atoms, atomic groups, faces, edges, steps, angle of crystals, crystal lattice defects etc. are active, as has been demonstrated in various works [95-97].

In contrast to the strong efforts made to study the adsorption process, very little attention has been paid to investigate the influence of surface crystallography on the kinetics of the HER [98-100]. It was reported [99] that there is essentially no difference in H_2 evolution kinetics on Pt(100), Pt(111) and Pt(511) surfaces. This surprising lack of structural sensitivity, despite the differences in standard Gibbs energy of adsorption among these surfaces, was attributed to a compensation between the changes of ΔG^0_{ads} and the changes in the energy of repulsive lateral interaction between H atoms.

Work on the HER at single-crystal surfaces is outside the scope of this thesis, since major attention was on the study of polycrystalline Pt electrodes. However, it is believed that the behaviour of polycrystalline electrodes is determined by the combination of single-crystal domains at the surface. Investigations on single-crystals can provide a unique possibility for study of surface structural effects in a controllable way, and eventually for development of a

predictive base in electrocatalysis.

Surface characterization includes also the study of the modification of a surface under cathodic load or after some pretreatment. The effect of corrosion on the electrode composite should be considered (as is studied in the present work on the long-term performance of Ni-Mo-Cd electrocatalyst materials in the KF·2HF melt). The modification of surface behaviour during the polarization by the adsorbed intermediates, can also be evaluated by electrochemical techniques by obtaining information on the kinetic parameters and the state of adsorption of intermediates, especially if digital acquisition of open-circuit potential relaxation transients and a.c. impedance techniques are used [15,101].

1.10 Interfacial Structure and Double-Layer Capacitance

In this thesis, substantial attention has been devoted to the measurement of double-layer capacitance at the electrode interface, in relation to the determination of real surface area, and the distinction between the double-layer capacitance and the pseudocapacitance arising from adsorbed intermediates. It is necessary here, in relation to material which follows in other chapters, to depict some models of interfacial structure and the associated concepts of the double-layer capacitance [102].

The electrochemical metal/solution interface behaves electrically as a capacitor, involving very high fields (10^6 - 10^7 V cm^{-1}) between the separated charges on the metal and, as ions, in the solution. The charge separation due to ion charge on the solution side together with electron charges or holes on the electrode side, leads to what is called the "double-layer" having a capacitance, C_{dl}.

The simplest model of the distribution of ions at interfaces was proposed by Helmholtz [103], who regarded the behaviour of the double-layer of charges on the surface and those in solution as approximating to that of a parallel-plate condenser. Later, Gouy [104] and Chapman [105] pointed out that the thermal distribution of ions should be considered, which would depend on the exponential of their electrostatic energy at various locations in the interphase, in comparison with *RT*. This distribution is analogous to that considered for counter-ions around a given ion in the Debye-Hückel theory of electrolyte solutions. The mathematical treatment was based on the assumption that the ions were point charges. Stern [106] recognised that the ions have finite size, determined by their hydration radii, so that the inner region of the double-layer has an effective average thickness and a characteristic capacitance corresponding to the "Helmholtz" layer. The latter combines with the diffuse layer capacitance according to a series addition given by eqn.(1.25)

$$\frac{1}{C_{dl}} = \frac{1}{C_1} + \frac{1}{C_2} \qquad (1.25)$$

where C_{dl} is the total measurable double-layer capacitance, C_1 is the Helmholtz capacitance and C_2 the diffuse-layer capacitance. Since C_1 and C_2 are additive in a series combination, the contribution from the *smaller* one then determines the overall value of C_{dl}. C_2 is dependent on the electrolyte concentration, as described in the Gouy-Chapman and Stern treatments [106]. High concentration of electrolytes, e.g. 1.0M, diminishes the influence of C_2 upon the overall capacitance C_{dl}.

Grahame [107] further refined the model by taking into account the different distances of closest approach of anions (positive to the p.z.c.) and hydrated cations (negative to the p.z.c.)

to the electrode metal surface. In this way, he distinguished an inner Helmholtz plane (for anion contact) and an outer Helmholtz plane (for cation contact).

More detailed models of the double-layer were later developed by Bockris [108], Watts-Tobin [109], and others. For example, they considered a sheet of solvated ions, a first layer of water molecules on the electrode surface and the contact specific adsorption of anions and neutral molecules, as depicted in Fig.1.3. The potential distribution across the interphase is shown in Fig.1.3 with ϕ_M representing the potential in the metal. Through the Helmholtz layer the potential drops to ψ_1, and beyond, ψ_s is the potential of bulk solution, which is usually referred to the potential of a reference electrode in the practical electrochemical measurement circuit, excluding the IR drop from the solution resistance. The potential difference ψ_1-ψ_s is the potential drop across the diffuse layer. It should be mentioned that it is the potential difference ϕ_M - ψ_1 that is involved in the rate equations.

The magnitude of the double-layer capacitance is measurable by modulation or transient techniques since the charge on the capacitance is related to the applied potential across the double-layer. Double-layer charging is a non-Faradaic process, while electron-charge transfer through the double-layer, i.e. when C_{dl} behaves as a leaky condenser, is a Faradaic process. Normally the magnitude of C_{dl} is about 20 ~ 40 μF cm^{-2}, depending on whether the electrode is at a potential negative or positive to the potential of zero charge, and can vary noticeably with applied potential.

The pseudocapacitance, C_ϕ, arising from the deposition of adsorbed intermediates on electrodes is, wherever applicable, unavoidably measured simultaneously with the C_{dl} by electrochemical techniques. However, as will be shown later, the time-response of C_{dl} to

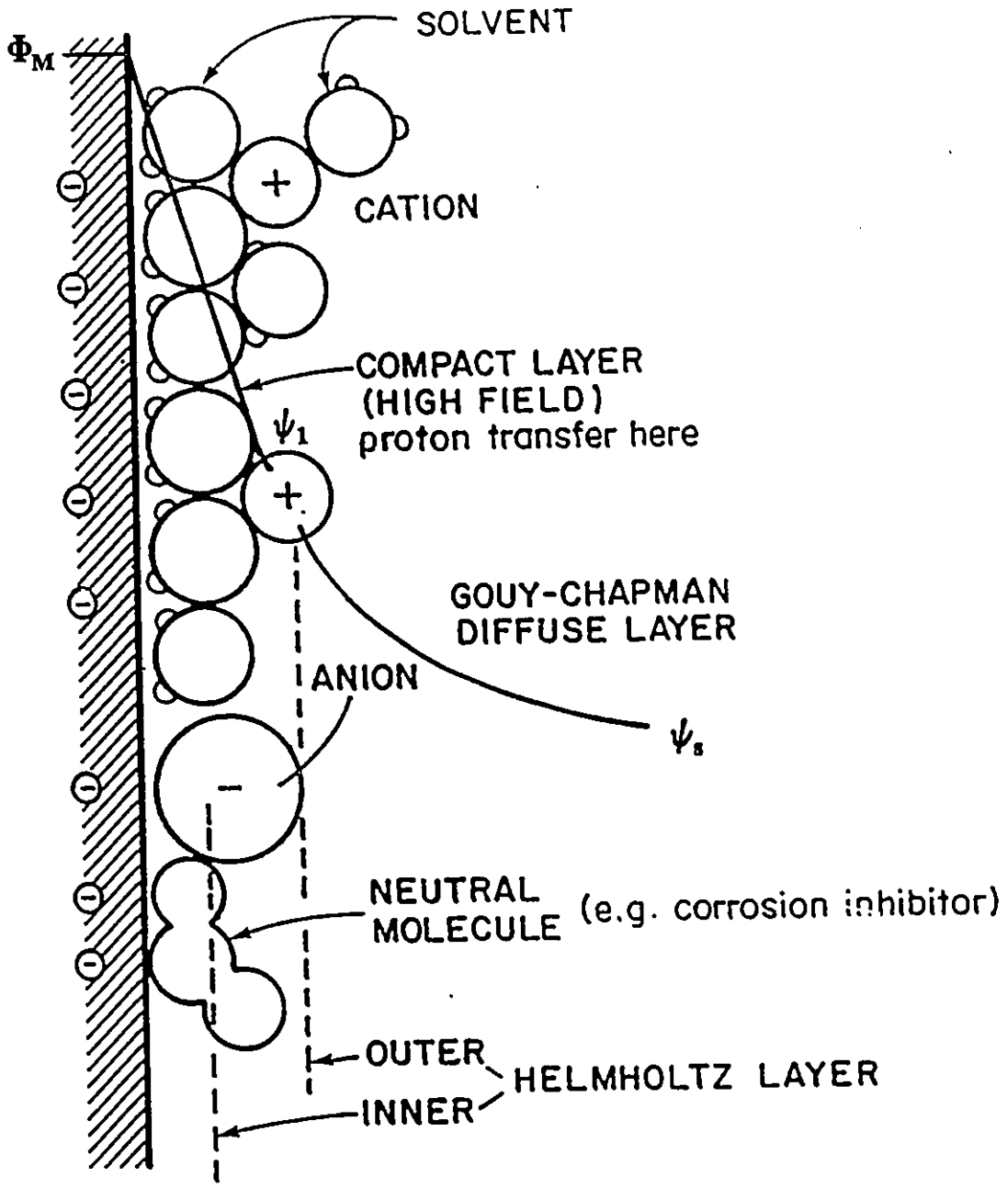

Fig.1.3 Schematic diagram of the double-layer interphasial region at an electrode across which the microscopic processes of proton and electron transfer occur in the HER with the assistance of the potential drop over the inner, compact layer (from ref. [108]).

potential modulation arises over much higher frequencies than those for C_ϕ; hence a distinction is possible. The pseudocapacitance is found experimentally to be potential-dependent, as defined by $C_\phi = dQ/d\eta = q_1 d\theta/d\eta$, and is normally much larger in magnitude than C_{dl} except as θ or $1-\theta \rightarrow 1$. This is a useful feature of the C_ϕ behaviour. In the above equation for C_ϕ, q_1 is the charge for a monolayer of the adsorbed intermediate species; for H at Pt $q_1 \approx 210\ \mu C\ cm^{-2}$.

The present research project introduces, amongst other things, a new treatment for analysis of fast potential-relaxation curves (time range 1μs - 1ms) in order to measure the high-frequency component of the electrode's capacitance consisting primarily of the C_{dl} contribution. The influence of the pseudocapacitance associated with the adsorbed H intermediate has been elucidated quantitatively, as will be described later.

The electrode's capacitance, as measured by means of a.c. impedance and also by a potential-relaxation technique, together with a theoretical kinetic simulation developed in this laboratory, enables the coverage by the intermediates involved in the kinetics of the HER at different metals, to be determined as a function of overpotential, η.

1.11 Distinction Between U.P.D. and O.P.D. Adsorbed H Intermediate

In the above sections, the adsorption of u.p.d and o.p.d species, e.g. H, has been mentioned several times. It is necessary to clearly define these terms here. At potentials more negative than the hydrogen reversible potential, the adsorbed H intermediate is involved kinetically in the electrolytic H_2 evolution reaction (*cf.* eqns.(1.16-1.18)). Species adsorbing at such potentials are referred to as the "overpotential deposited" (o.p.d.) H, the coverage, θ_H, of which can be evaluated as a function of overpotential, by integration of the C_ϕ vs η profile.

The o.p.d. H species are deposited in excess of any coverage by strongly chemisorbed species (the so-called underpotential deposited (u.p.d.) species) that may already be present at the reversible potential, $\theta_{H,\eta=0}$, e.g. as at Pt. This so-called "underpotential deposition" of H adatoms occurs by direct Faradaic reaction from solution, at potential more positive than the H^+/H_2 reversible potential ($\eta=0$) (Fig.1.4). The coverage by these strongly bonded u.p.d. adatoms can be directly measured experimentally at noble metals by means of charging curves [110,111], a.c. impedance [112-114] or cyclic-voltammetry [115,116] methods, because such measurements are not interfered with by any continuous Faradaic currents due (in this case) to cathodic H_2 evolution.

Several theoretical works [70,117-119] on u.p.d. H have indicated the probability [120-124] that the u.p.d adatoms are not necessarily the species that participate as intermediates in the kinetics of the HER since a full monolayer of strongly chemisorbed H is already present at platinum at the reversible potential. Since there is no interference by large currents due to a continuous Faradaic process in the case of u.p.d., not only can the small currents ($1 \sim 25\ \mu A\ cm^{-2}$) associated with the formation of u.p.d. H be easily detected and quantitatively measured, but also various current response peaks due to multiple-state adsorption at electrodes can be resolved (see Fig.1.4) with excellent sensitivity.

Major attention has been concentrated on the investigation of the behaviour of the o.p.d. H intermediate for the HER at Pt and other Ni alloy materials in the present work. The coverage, θ_H, and the associated pseudocapacitance, C_ϕ, in relation to overpotential, η, can be obtained through approximations (simulation treatments) by theoretical kinetic equations to the experimental data.

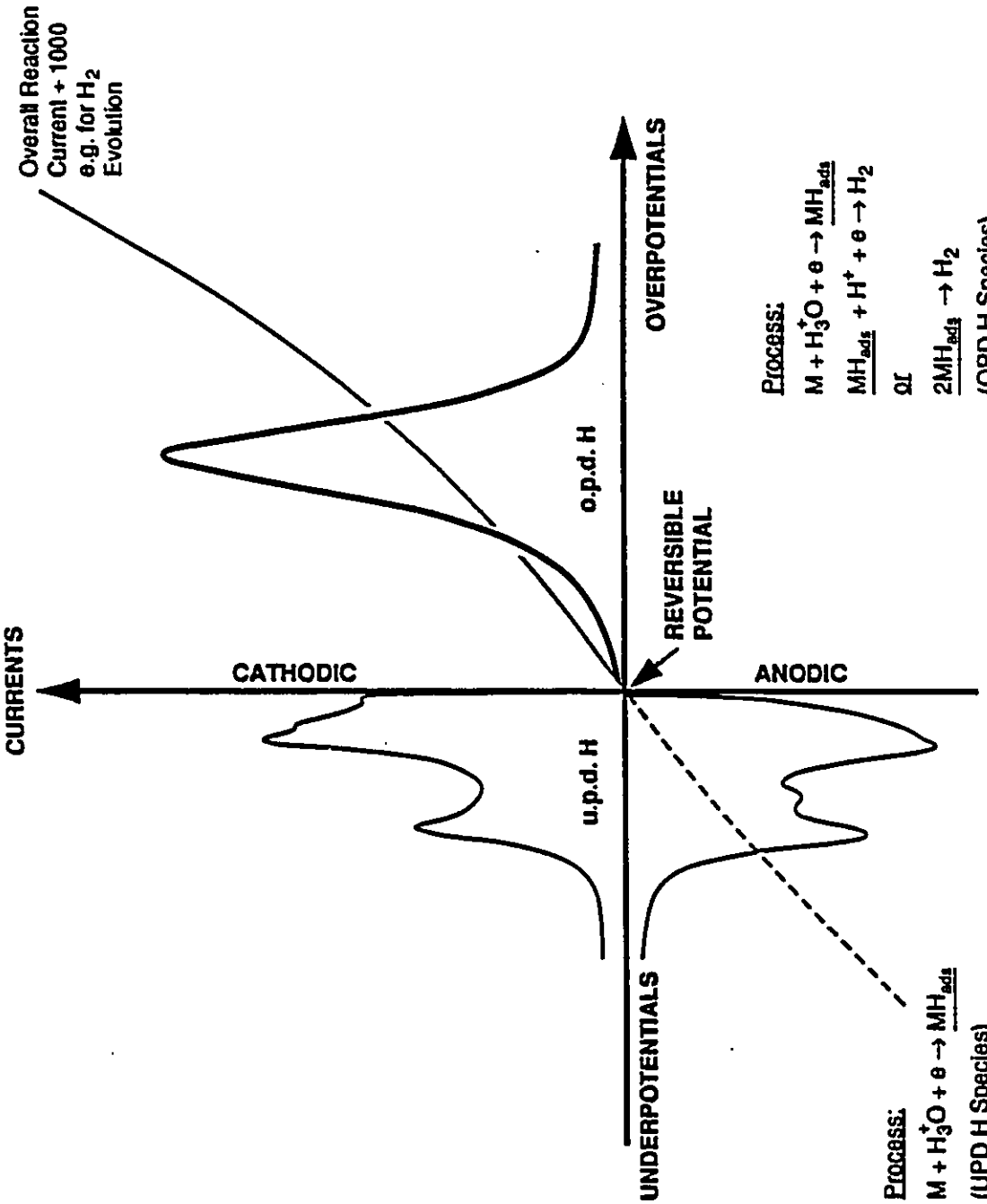

Fig.1.4 Relation between u.p.d. currents for H adsorption and desorption, and overall H_2 evolution currents negative to the reversible potential.

1.12 The Role of Metal Hydrides or Absorbed H in Electrocatalysis

It appears that in generating the highly active surface of Ni alloys by electrodeposition, e.g. of Ni-Mo-Cd electrodes, which takes place with cathodic co-evolution of H_2 and hence codeposition of H, some kind of hydride phase is formed having desirable electrocatalytic properties, in particular low Tafel slopes that are as important as high exchange current-densities for minimizing overpotential [5] at appreciable practical currents. The surface region hydride may be similar to the 2-dimensional surface hydride (strongly chemisorbed H at full site coverage) at metals, e.g., Pt, Rh, which exists already at or below the reversible hydrogen potential; thus the HER occurs at Pt or Rh on an already completed chemisorbed H film. On the other hand, previous work on Ni electrodes indicates [125-127] that full coverage by atomic H is not attained at the reversible hydrogen potential, but a 3-dimensional hydride can develop on cathodic polarization and give rise to a surface having good electrocatalytic properties for the HER. On open-circuit, this hydride phase formed during cathodic polarization can undergo decomposition, leading to visible evolution of H_2 [5]. The role of the metal hydride phase in electrocatalysis can be attributed to the modification of electronic structure of the metal, which is favourable for the interaction of intermediates with the metal surface. The involvement of the penetrated H into the metal lattice will consequently change the location of such metals or alloys on the "volcano" curve in Fig.1.2 in terms of *in situ* H adsorption energy at the H-*absorbed* electrode in contact with solution [128].

The study of H sorption into metals has been a topic of major fundamental and technological interest for many years [129]. The properties of metal hydrides of various kinds have been known for a long time and characterized in some detail [130-132]. Practically, the

role of H sorption into Ferrous metals and alloys is of major importance in embrittlement during corrosion. New interest in metal hydrides has arisen recently with respect particularly to the development of rechargeable hydride anodes for high energy-density batteries, e.g. employing the Ni_5La alloy [133] and multi-component transition metal alloys [134,135]. It is also a major aspect of the frequently and publicly discussed "cold-fusion" process [136] amongst D atoms sorbed in Pd. Earlier work on H sorption into Pd [137,138] is also closely relevant.

The influence of poisons such as arsenic, thiourea etc. on the H sorption into transition metals has been examined in a variety of works [139,140]. The presence of such poisons can enhance the entry of H into a metal during the H_2 evolution processes or under conditions of corrosion in the absence of O_2. It is believed that the strongly adsorbed poisons competitively occupy the surface sites which are otherwise taken by the chemisorbed H intermediate. It is the "driving force" determined by the surface coverage, θ_H, of the metal by adsorbed H that promotes the sorption of H into metals.

1.13 Effects of Poisons on the Kinetic and Adsorption Behaviour of the HER

The presence of poison species usually greatly influences the electrocatalytic behaviour of electrodes. Two kinds of substances are generally "poisons": the first are inorganic species, e.g. S[141-143], As[144-146], CO[147,148] etc., which are present as impurities in the electrolytes or as an intermediate formed during the reaction itself (e.g. CO in oxidation of HCOOH); the second are metallic species [149], e.g. Pb, Hg or Fe, Ni and Cu etc., which can arise e.g. as a result of corrosion of the cell hardware in industrial electrolyses. Organic impurities can sometimes also act as poisoning inhibitors for hydrogen evolution [150].

The effect of poisons can depend on the nature of the cathode. If the main impurity is metal ions, e.g. Fe^{3+}, it is expected to have negligible effects on mild-steel, while it can result in activation at Ni or Ti cathodes [26,151] leading to a composite catalyst film on the surface.

Poisoning effects become reduced or insignificant if the cathode surface is very rough and porous (e.g. platinized Pt, electrodeposited Ni-Mo-Cd composite electrode, etc.) [152] simply because the internal active surface is much larger than the diffusion front. Thus, porosity offers a kind of simple physical boundary of limited accessibility, whose features depend on the morphology of the inner electrode surface layer. Another reason could be that the real area of the porous surface is so large that a trace amount of poison will only cover a small fraction of the catalytic sites and thus has a negligible influence on the overall rate of electrode process.

From a general heterogenous catalysis point of view, poisons, e.g. sulphur, arsenic, are usually considered to deactivate catalytic reactions [153,154] through irreversible adsorption of poison compounds on metals. Taking the example of sulphur, its adsorption at the metal surface can be characterized by determining the chemisorption energy or the strength of bonding. The electronic structure of sulphur is $3s^2 3p^4$; therefore bonding involves s and p orbitals, usually their lone pairs. Bond formation with transition elements involves mainly their d-orbitals. Maxted [155] suggested that sulphur compounds chemisorb on transition metals by forming bonds in which unshared electrons in the sulphur atom are donated into the d-orbitals of the metal. According to Schultze and Koppitz [156], when a species S^z comes in close contact with a metal M, a charge transfer of electrons is possible (depending on the chemical nature of the adsorbent and adsorbate): $M + S^z \rightarrow M\text{-}S^{z+} + e$. This charge transfer can, however, be only partial, resulting in a partial charge-transfer "adsorption valency", which depends on the difference of

electronegativities between the metal substrate and the adsorbate.

It has been reported that different adsorbed species are involved in sulphur chemisorption [157]. In fact, electrooxidation of adsorbed sulphur on Pt catalysts occurs at two different electrochemical potentials. According to the experimental conditions, reducible PtS_2 or nonreducible PtS monolayers can be created [158]. Under reduction conditions, essentially independent of the starting sulphur compound (e.g. thiourea or H_2S), the adsorption on the surface is typically dissociative, leaving a reduced sulphur atom strongly bonded to the surface [154]. The adsorption of sulphur is also surface-structure sensitive, i.e. it usually chemisorbs at sites of high coordination on the metal surface, as was found in gas-phase surface chemistry [159,160].

The adsorbed sulphur has various influences on the adsorption of other reactants. In the case of chemisorbed hydrogen on metals, sulphurization of the metal results in a decrease of the hydrogen adsorption capacity or coverage by H and a decrease of the hydrogen binding energy [142]. However, studies with olefinic compounds have shown that the adsorption energy was increased by sulphurization of metals [161,162]. The sulphur acts as an electron acceptor compound and decreases, through its adsorption, the electron density of the unpoisoned metallic surface area and promotes the adsorption of the olefinic compounds through the high electron density region (π-orbitals) of the double bond.

The kinetics of the HER are sensitively influenced by adsorption of catalyst poisons such as arsenic, thiourea, etc. [163] which decrease the coverage of the o.p.d. H intermediate as found in the present work. Poisons usually raise the overpotential at a given current-density or correspondingly diminish currents at given overpotentials. Adsorbed poisons will not only

competitively occupy available adsorption sites but can also interact with the H atoms already covering the surface [147].

It is also known [139,140,163-167] that adsorption of catalyst poisons promotes the cathodic sorption of H into host transition-metal lattices such as Fe, Pd and Ni. The sorption involves diminished adsorption of H and its transfer to a sub-surface state, followed by diffusion into the bulk. It is the chemical potential gradient across the surface, determined by the 2-dimensional coverage, θ_H, that drives the diffusion across the boundary and thence continuously into the bulk metal until 3-dimensional saturation or phase formation occurs.

In the present thesis work, the effects of trace amount of poisons, e.g. $(NH_2)_2C{=}S$ and As_2O_3, on the state of H adsorption in the HER at Pt electrodes was extensively investigated by means of the potential-relaxation method and associated theoretical simulations by means of the kinetic "rate equations" approach (see Chapter IV).

1.14 Objectives of the Research

As indicated in the introduction, the project arose from some well defined problems encountered in the behaviour of anode and cathode electrodes for the process of electrolytic F_2-production from KF·2HF melts, employed industrially.

The following objectives emerged from knowledge of the types of problems involved, especially at the H_2-evolving cathode.

1) To study and characterize the high polarization potentials (overvoltages) that arise at the mild-steel cathodes at which H_2 is evolved from the KF·2HF melt, the so-called "hyperpolarization effect". To investigate its origin in relation to HF consumption in the melt.

2) To develop alternative electrocatalytic materials for the cathode, and characterize H_2 evolution behaviour at them.

3) Some cathode materials being porous composites (Ni-Mo-Cd), to develop a method for *in situ* determination of their real, electrochemically accessible surface areas per apparent cm^2; also to characterize their corrosion resistance in the melt.

4) To show how the results applied to a porous electrode in (3) depend materially on the conductivity of the electrolyte.

5) To examine the wetting behaviour of the $KF \cdot 2HF$ melt at electrode metals by means of contact angle goniometry and use of rotated cone electrodes.

6) To examine, comparatively, the electrode-kinetic and double-layer capacitance behaviour of electrodes in a $KOH \cdot 2H_2O$ hydrate melt *vis à vis* the $KF \cdot 2HF$ melt, also in relation to wetting effects characterized in (5). (The $KOH \cdot 2H_2O$ melt is the aquo-system analogue of $KF \cdot 2HF$, for the HF solvent system).

7) Based on the method in (3), extended to recording of *full* potential-relaxation transients, to determine practically and theoretically, by means of simulation calculations, the conditions for which kinetic parameters can be obtained and H adsorption behaviour determined by the potential transient method and to make practical applications of the procedure.

8) To examine both experimentally and kinetically the effect of arsenic and thiourea poisons on the HER in terms of H coverage and the kinetics of the partial reaction steps. In this aspect of the work, to compare behaviour deduced from the potential-relaxation method with those from the use of impedance spectroscopy and cyclic voltammetry techniques.

CHAPTER II

EXPERIMENTAL

2.1 Electrochemical Systems

2.1.1 Electrodes

2.1.1.1 Electrodeposited Ni-Mo-Cd Electrodes

A composite Ni-Mo-Cd electrocatalyst was prepared and investigated as an alternative to the mild-steel cathode employed industrially. The Ni-Mo-Cd was plated (see below) on a mild-steel rod. This electrode was used in studies of the reaction of H_2 evolution (HER) from a KF·2HF melt as used industrially. The construction of the electrode used is shown in Fig.2.1, which illustrates how it was designed to be sealed in Teflon, since the HF melt is corrosive to the glass which is usually used for mounting conventional electrodes. To avoid changes of the effective area caused by possible permeation of the melt along any crevices, the mild-steel rod (diameter = 5.1 mm) was designed to be a little larger than the hole in the Teflon (diameter = 4.9 mm) to keep the contact as tight as possible. Inside the Teflon cylinder was a stainless-steel cylinder provided with a thread near its bottom for electrical contact. The cone-shaped mild-steel electrode was designed to be used as a rotating electrode, which was found to be very effective for spinning off the gas bubbles generated at the electrode during the polarization which, in the KF·2HF melt, adhere strongly to the electrode surface. The surface area exposed at the tip of the electrode was 0.28 cm^2.

The electrodeposition of Ni-Mo-Cd proceeds easily on a mild-steel substrate. The electrode was pre-treated before each experiment by freshly polishing its surface using #1200 grit then #2400 silicon-carbide sandpaper. The polished surface was then washed in distilled

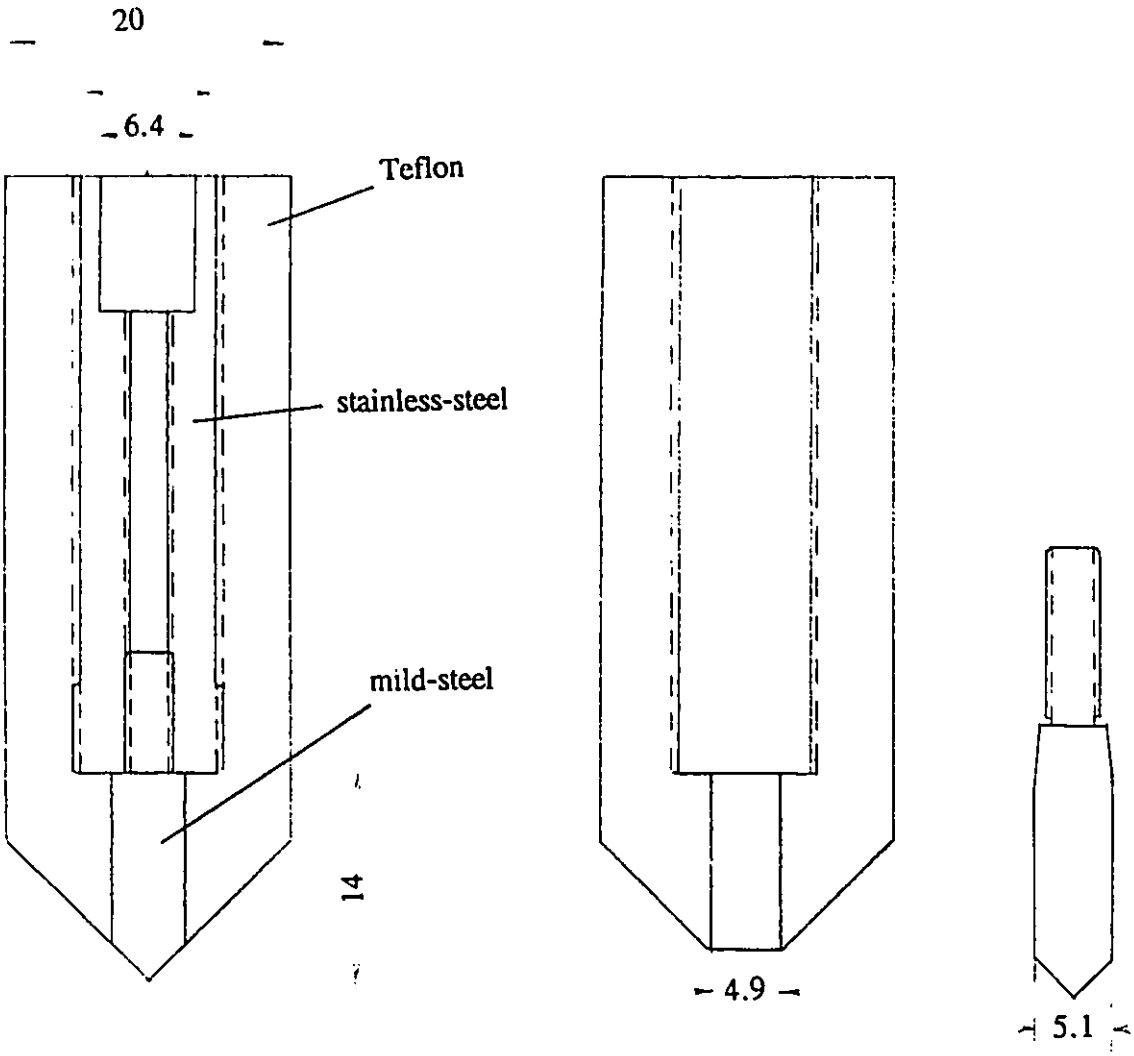

Fig.2.1 Diagram of the design of the cone-shaped rotating electrode.

water and dried before being transferred to a methanol ultrasonic bath to remove possible organic contaminants other than methanol. The methanol solvent being highly volatile, enabled the electrode to be then dried in air. The deposition method is described in ref. [5], based on a patented procedure [168]. It consists of three steps of deposition from three plating solutions. The compositions of the plating solutions and procedures involved are listed below:

Watts Nickel:

$NiSO_4 \cdot 6H_2O$	(1.14 M)
$NiCl_2 \cdot 6H_2O$	(0.19 M)
Boric acid	(0.48 M)
Dodecyl sodium sulphate	(1.04×10^{-3} M)

Adjust pH to 3 by addition either of $NiCO_3$ or H_2SO_4.

Intermediate Layer:

$Na_2MoO_4 \cdot 2H_2O$	(0.012 M)
$NiCl_2 \cdot 6H_2O$	(0.040 M)
$Na_4P_2O_7 \cdot 10H_2O$	(0.125 M)
$NaHCO_3$	(0.74 M)
NaCl	(0.17 M)
$Na_3C_6H_5O_7 \cdot 2H_2O$	(0.034 M)
$CdCl_2 \cdot 2H_2O$	(3.1×10^{-4} M)
KSCN	(1.2×10^{-3} M)

On the day of plating, add 0.025 M of hydrazine sulphate (do not heat the solution) and 1 millilitre of ammonia liquor to the solution. Adjust pH to 8, filter solution.

Final Layer:

$Na_2MoO_4 \cdot 2H_2O$	(0.028 M)
$NiCl_2 \cdot 6H_2O$	(0.040 M)
$Na_4P_2O_7 \cdot 10H_2O$	(0.125 M)
$NaHCO_3$	(0.74 M)
NaCl	(0.17 M)
$CdCl_2 \cdot 2H_2O$	(3.1×10^{-4} M)
KSCN	(2.0×10^{-3} M)

On the day of plating, add 0.025 M of hydrazine sulphate (do not heat the solution) and adjust pH to 8, then filter solution.

The plating procedure was then followed using the above prepared solutions. The electrode was rotated at 2000 r.p.m (Analytical Rotator, Pine Instrument Company) during the plating process in order to spin off the simultaneously generated H_2 gas. A cylinder of Pt gauze was used as the counter electrode. A reference electrode was unnecessary since the plating was under galvanostatic control. The empirical procedures are described in the following paragraphs.

A. Pretreatment

- Standard cleaning and pickling procedures for steel
- Transfer wet sample directly to Watts bath and immediately begin plating

B. Watts Bath

- Plate sample for 10 minutes at 77.5 mA cm^{-2} (at 53°C)
- Reduce current density to 38.8 mA cm^{-2} and plate for an additional 40 minutes
- Rinse sample for 2 minutes in running distilled water

- Rinse sample in NH_4Cl/NH_4OH solution for 7 minutes

C. Ni-Mo-Cd (Intermediate)

- Plate at 116.4 mA cm^{-2} for 15 minutes at room temperature and allow the temperature to rise to 34°C
- Rinse sample for 2 minutes in running distilled water
- Rinse in NH_4Cl/NH_4OH solution for 7 minutes
- Transfer wet sample to the final plating bath

D. Ni-Mo-Cd (Final)

- Plate at 116.4 mA cm^{-2} for 30 minutes at room temperature and allow the temperature to rise to 34°C
- Rinse sample for 2 minutes in running distilled water
- Rinse sample in methanol and blow in dry air
- Store plated material in sealed plastic bag

The resulting composite electrode was examined under the Scanning Electron Microscope (SEM); its surface appearance was "cauliflower-like", with regions micro-porous in structure as shown in Fig.2.2a. The coating layer looks compact and fine. The deposited sample was then sliced vertically with the cut edge exposed. Fig.2.2b shows the SEM picture of this section plane. There are three layers in this deposit: the dark bottom part is the steel substrate, the middle layer is composed of the under-layer of electrodeposited Watts nickel and the top "cauliflower" layer is the Ni-Mo-Cd composite deposit. From the scale shown in this picture, it can be seen that the thickness of the total deposited layer is about 20 μm of which ca. 10 μm is from the contribution of the middle nickel layer. Of course, only the surface of the top region

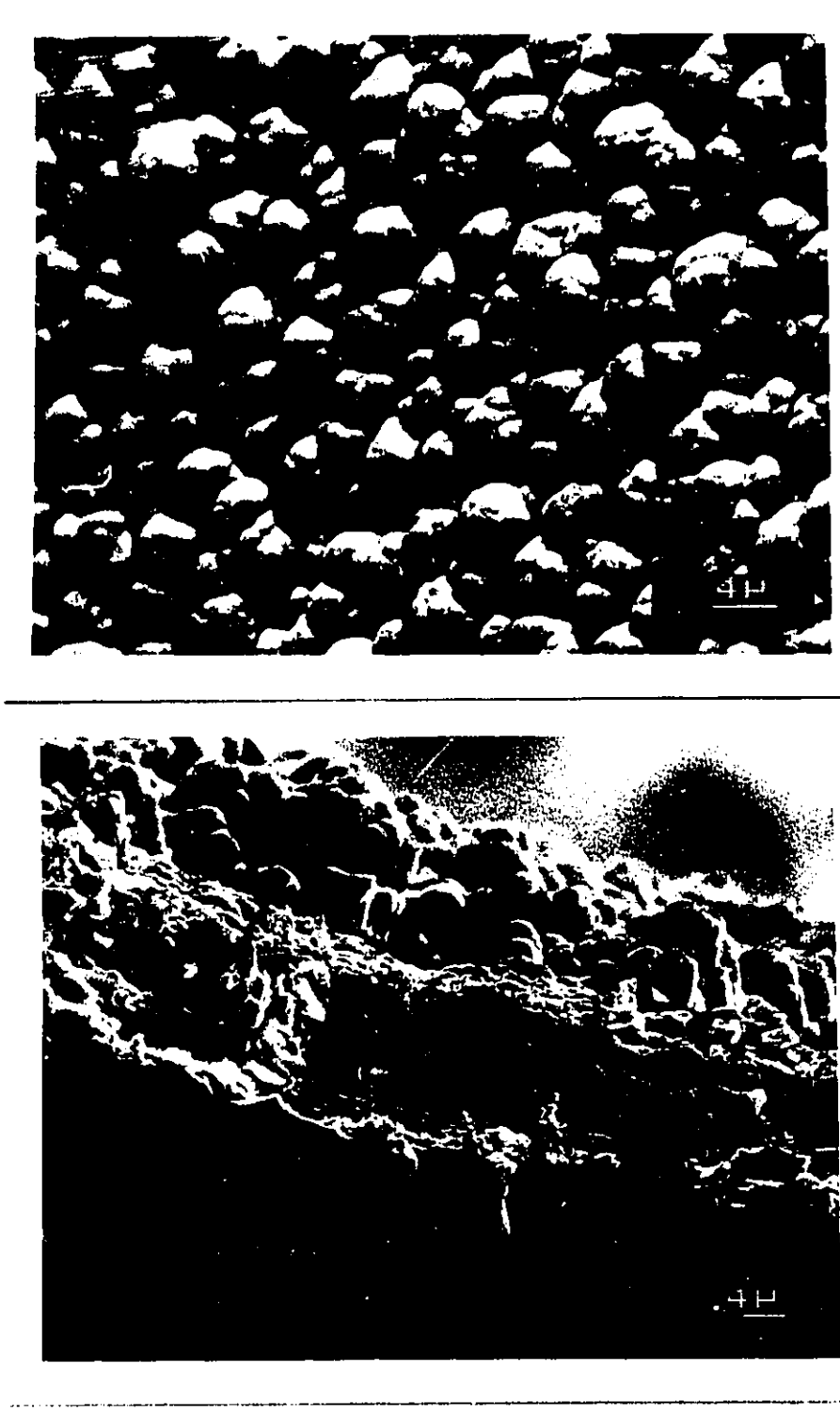

(a)

(b)

Fig.2.2 SEM pictures of the electrodeposited Ni-Mo-Cd electrode. (a) top view; (b) sectional view.

of the alloy layer and its pores that are exposed to the solution, function as the electrocatalyst, both through its rough, high real area and its electronic and adsorptive properties. The mean composition of the alloy surface region was determined by X-ray emission analysis, giving the following atomic percentages: 88% Ni, 11% Mo and 0.25% Cd.

2.1.1.2 Ni-Mo Bulk Alloy Electrodes

A smooth surface, bulk Ni-Mo composite alloy electrode was employed in several experiments for comparison. It was designed and prepared similarly to the composite electrode in a conical shape with the Ni-Mo alloy cylinder being mounted into the Teflon tube with a machined conical tip exposed. The binary alloys were metallurgically prepared by Aremco Products Inc. in the composition range where homogeneous solid solutions of the two elements are found (up to 19 atom percent Mo). The surface-region compositions of these alloys were examined by X-ray emission analysis, and 6 atomic percent of Mo was found. The polishing and cleaning procedures were similar to those used for the mild-steel electrodes, i.e. the electrode was polished by using fine carbide sandpapers and washed in methanol solution before the electrochemical experiments were commenced. The geometric surface area of the electrode was determined as 0.27 cm^2.

2.1.1.3 Bright Pt Electrodes

Smooth, bright polycrystalline Pt electrodes were made from Pt wire of 99.99% purity and 0.45 mm in diameter, supplied by Johnson Matthey Inc., USA. The electrode preparation procedures were: (a) initial "degreasing" of the Pt electrode by refluxing in acetone for 12 h; (b) flame-welding of the Pt electrode to a long piece of Ag wire to provide an electrical contact;

(c) sealing into pre-cleaned soft-glass tubing (15 cm) leaving ca. 1.5 - 2.5 cm of Pt wire extending beyond the end of the glass-tube. The apparent surface area of the Pt electrodes was measured geometrically and found to be in the range of 0.2 - 0.4 cm^2, differing from one electrode to another. The real surface area was calculated from the electrochemical u.p.d. H charges associated with the cyclic voltammetry peaks [115,170], assuming the monolayer charge for u.p.d. H at the Pt surface is 210 $\mu C\ cm^{-2}$.

When not in use, the Pt electrodes were stored in concentrated pure H_2SO_4 and, before using, were thoroughly washed and soaked again in "Milli-Pore" distilled water.

2.1.1.4 Platinized Pt Electrodes

The porous, platinized Pt electrode used as a model for examining the behaviour of porous electrode structures was prepared by electrodeposition of Pt from a 2% chloroplatinic acid (H_2PtCl_6) solution on to a bright Pt wire substrate [171] mounted in a glass-tube as described above for the case of the bright Pt electrode. The geometric surface area was 0.195 cm^2 and all apparent current-densities in the experiments are reported relative to this value. The electrode was plated with Pt from the 2% H_2PtCl_6 solution in 2 M aqueous HCl with 0.02% of added $Pb(OAc)_2$, using a current-density of 30 mA cm^{-2}. As is known [172], the presence of 0.02% lead acetate has a dramatic effect in promoting even deposition of finely divided platinum black and maintaining long life of the electrode.

Fig.2.3 shows an SEM picture of the platinized Pt surface. Under large image enlargement (Fig.2.3c), the granular particles are clearly visible, and the micro-porous structure of the deposit is revealed.

After platinization the electrode was stored in "Milli-Pore" distilled water.

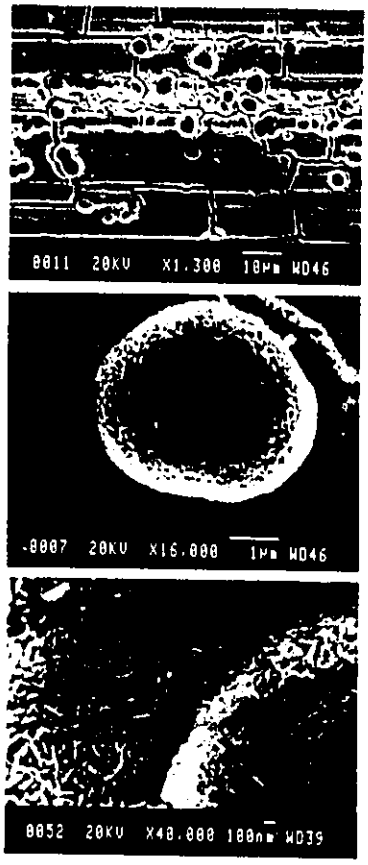

Fig.2.3 SEM micrographs of the plated Pt electrode at three magnifications: (a) x 1,300; (b) x 16,000; (c) x 40,000

2.1.1.5 Reference Electrodes

Potentials of working electrodes are usually referred to the potential of a reference electrode immersed in the same solution under study. There are three kinds of reference electrodes that were involved in the different electrochemical systems examined in the present work. The conventional hydrogen reference electrode (at platinized Pt) was used in the aqueous solutions; an Fe/FeF_2 reference electrode was employed in the $KF \cdot 2HF$ melt and a Hg/HgO reference electrode was selected for the experiments in the $KOH \cdot 2H_2O$ hydrate solution. According to the properties of the solution or melt, these reference electrodes were selected for compatibility since they are thermodynamically reversible (non-polarizable electrodes) and stable with time at constant potential in the experiments. They were also designed to fit conveniently the construction of the cells.

(i) Hydrogen Reference Electrode

The reversible hydrogen electrode, $H^+/H_2(Pt)$, (RHE) is one of the most commonly used reference electrodes in electrochemical experiments [172]. It is normally made of platinized Pt gauze using the plating process as described in Section 2.1.1.4. The Pt gauze was of 99.99% purity and 100 mesh, supplied by Johnson Matthey Inc. H_2 gas was continuously bubbled into the reference compartment of the cell. The RHE was mostly used in the alkaline solutions in the present work. The potential of the RHE was found very stable in all the experiments.

(ii) Mercuric Oxide Reference Electrode

For alkaline solutions, the employment of a Hg/HgO reference electrode is convenient and it was used in the $KOH \cdot 2H_2O$ hydrate. Orange HgO powder was of analytical grade purity, supplied from BDH Chemicals Canada Ltd. The mercury used for the electrode was of high

purity (99.9999%), obtained from Aldrich Chemical Company, Inc. A Ag wire was connected, to a Pt contact, to the liquid mercury to provide electronic contact and extended out to the external electrical circuit. The reference electrode was specially designed for the acrylic cell (see below) which was alkali and acid resistant. The electrode potential of Hg/HgO relative to the RHE is unable to be reliably calculated, since the activities of OH^- and H_2O are unknown in this high KOH concentration as $KOH \cdot 2H_2O$ (about 28 M, without considering the activity factor). However, the potential is experimentally available from measurements of the relative potential of Hg/HgO vs RHE in the same solution over a long period of time, and it was found that $V_{HgO/Hg}$ vs $V_{RHE} = - 0.91$ V. This corresponds to the solution-independent reaction $HgO + H_2 \rightarrow Hg + H_2O$. The potential of this reference electrode was found very stable during the experiments.

(iii) Iron Fluoride Reference Electrode

It is not realistic to use a RHE electrode as a reference in the $KF \cdot 2HF$ melt because the HF content can be quickly diminished by passage of the flowing H_2 gas in the reference compartment. Accordingly, an Fe/FeF_2 reference electrode was used in this melt, made of pure Fe wire immersed in the melt for over 2 hours until its potential was established at a stable value. The FeF_2 is formed on the Fe substrate from the reaction of the melt with the pure Fe. Again, since the potential of this electrode is not available by means of theoretical calculations in the case of the $KF \cdot 2HF$ melt, experimental measurement of the potential was made relative to a RHE in the same melt. It was found that $V_{Fe/FeF2}$ vs $V_{RHE} = 0.17$ V, and its value was also very stable under the experimental conditions at 85°C.

2.1.1.6 Counter Electrodes

A Pt gauze, having a large surface area and prepared in the same manner as the Pt wire electrode, was used as the counter-electrode in the aqueous solution work. It was set in a separate compartment of the electrochemical cell, to avoid migration of anodically generated O_2 to the main compartment. The large surface area of the Pt gauze minimizes the Faradaic current-density of the oxygen evolution process at the counter electrode during polarization experiments in $KOH \cdot 2H_2O$. However, in the $KF \cdot 2HF$ melt, a graphite counter electrode (anode) had to be used in the work, as is operated in industry for electrolytic F_2 production. The graphite, having a large specific surface area was provided by Cameco Inc. It was set in the counter-electrode compartment of the acrylic cell, for reasons similar to those already mentioned above.

2.1.2 Electrochemical Cells

2.1.2.1 Acrylic cell

Since regular glass electrochemical cells cannot be used for experiments in $KF \cdot 2HF$ melts due to the etching reaction of HF with the glass, cells made of an acrylic plastic were therefore fabricated and used. Acrylic is transparent (compared to Teflon) and resistant to acid and alkaline solution and to HF; therefore it was selected as the cell material for containing the $KF \cdot 2HF$ melt at the 85°C experimental temperature. It consisted of two compartments for the working and counter electrodes, with a small opening between the two compartments at the bottom of the cell. The Fe/FeF_2 reference electrode, made of pure iron wire, was sealed into a Teflon tube with the tip situated close to the working electrode. The top of the cell was covered with an acrylic plate in order to avoid unnecessary evaporation of HF during

experiments. Purging by N_2 or H_2 gases was not necessary since it was found that the solubility of O_2 in the melt was very small, and in addition, any bubbling would cause disturbance that would enhance evaporation of HF. A picture of the cell and electrodes under polarization is shown in Fig.2.4, in which H_2 evolution can be observed at the tip of the mild-steel electrode.

2.1.2.2 Glass Cell

A conventional three-compartment cell, as shown in Fig.2.5, was used in the comparative aqueous solution work and specially designed for rotating electrodes. The cup attached on top of the cell was made to contain water so that when the "cap" of the rotating electrode was immersed in the water, the main compartment of the cell became sealed off from air. The reference electrode compartment was separate but connected to the working electrode compartment by a Luggin capillary in the usual way. In each experiment, the electrode was adjusted close to the tip of the Luggin capillary in order to minimize the "IR" drop in solution. The counter electrode compartment was isolated from the main compartment by a wetted glass stopcock which is conductive through the electrolyte at the rough surface between the stopcock's key and barrel. This allows current to pass between the working and counter electrodes but prevents migration of oxygen from the counter to the main compartment.

All the glass components of the cell, prior to the experiments, were thoroughly cleaned by soaking in concentrated sulfuric acid, rinsing in distilled water and finally washing with the electrolyte solution.

Solutions in the main compartment were deoxygenated by bubbling a slow stream of H_2 for the cathodic polarization experiments (potential-relaxation, Tafel and a.c impedance experiments) or of N_2 for anodic experiments (cyclic voltammetry). H_2 gas was continuously

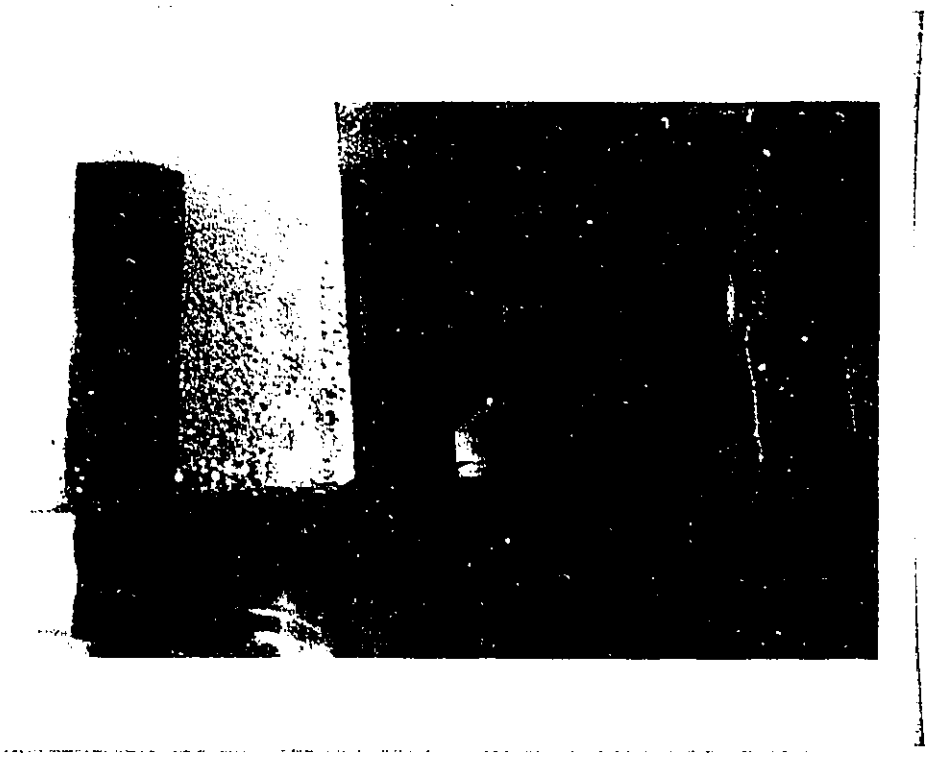

Fig.2.4 Photographic picture of the electrochemical system with the mild-steel cathode (cone-shaped), the graphite anode presented in the $KF \cdot 2HF$ melt which is contained in the acrylic cell.

Fig.2.5 Photographic picture of the 3-compartment glass cell.

bubbled into the reference electrode compartment.

2.1.2.3 Gas lines

Electrolytic grade H_2 and N_2 gases, used for the hydrogen reference electrode and for deoxygenation (outgassing) of the solutions, were further treated in conventional purification trains [171] before use, to remove any traces of O_2 since the latter is chemically reactive and electrochemically reducible.

Hydrogen gas was passed through a gas train consisting of $Mg(ClO_4)_2$ as a drying agent, molecular sieve (BDH type 4A), an oven containing Cu turnings and palladized asbestos at 623 K, and finally activated charcoal traps.

Nitrogen gas was passed through an identical gas purification train except that only Cu turnings were used in the oven for removal of O_2. The metallic surface of the Cu turnings was periodically regenerated by passage of H_2 through the oven.

2.1.3 Electrolyte Melt and Solutions

2.1.3.1 KF·2HF Melt

In order to prepare the pure KF·2HF melt, the purest commercially available KF·HF (99+%, from Johnson Matthey Company) and 99.9% HF (from Matheson Gas Products, Canada) were used for making the melt. A special non-metal, non-glass system was prepared by using Teflon tubes and valves. A two litre high-density polyethylene bottle was set up as the reaction tank which was mounted on an electronic read-out balance (Sartorius B61000) so that the quantity of the added HF could be monitored accurately during the course of the preparation. The HF was added slowly by controlling the Teflon valve, with the melt being stirred by means

of a Teflon propeller so that KF·HF and HF could be reacted thoroughly in a controlled manner.

The phase diagram of the KF/HF components is indicated in Fig.2.6 from which it is seen that the melting point of the system sharply increases below the composition KF:1.87HF. The practical operating temperature was around 85°C in the experiments, maintained by an air-heated thermostat oven. The composition of the melt was taken as KF·2HF (41% HF) with a melting point of 71.7°C [176]. The evaporation or electrochemical consumption of HF during the polarization causes a change of composition and correspondingly the melting point of the mixture, as was found in the experiments [4] leading to the major contribution to the so-called "hyperpolarization effect" in the cathode reaction (see Section 4.I.2).

The specific conductivity of the melt is shown in Fig.2.7 [177]. Its conductivity arises from proton hopping, like the proton conductance mechanism in acid or alkaline aqueous solutions [178,179], *viz.*

$$F\text{-}H + F^- \rightarrow F^- + HF \rightarrow FH + F^- \rightarrow F^- + HF \ldots \text{etc.} \qquad (2.1)$$

Such a process can continue in the solid state as is known e.g. for proton transport in ice [180].

Since the KF·2HF melt is a non-aqueous electrolyte, little solvation energy is available to dissociate the HF bond unlike the situation when it is in aqueous solutions. The strong H bond between HF and H (H-F···H) would further tend to minimize dissociation. Therefore, only a very small additional fraction of free ions would be expected in the melt arising from the self-dissociation, $2HF \rightleftharpoons H_2F^+ + F^-$, analogous to that in H_2O ($K_w = 10^{-14}$).

The "acidity" of the KF·2HF melt may be considered in relation to analogy with the aquo-system. Like H_2O, autoprotolysis in HF ($3HF \rightleftharpoons H_2F^+ + FHF^-$) is weak. The pH of

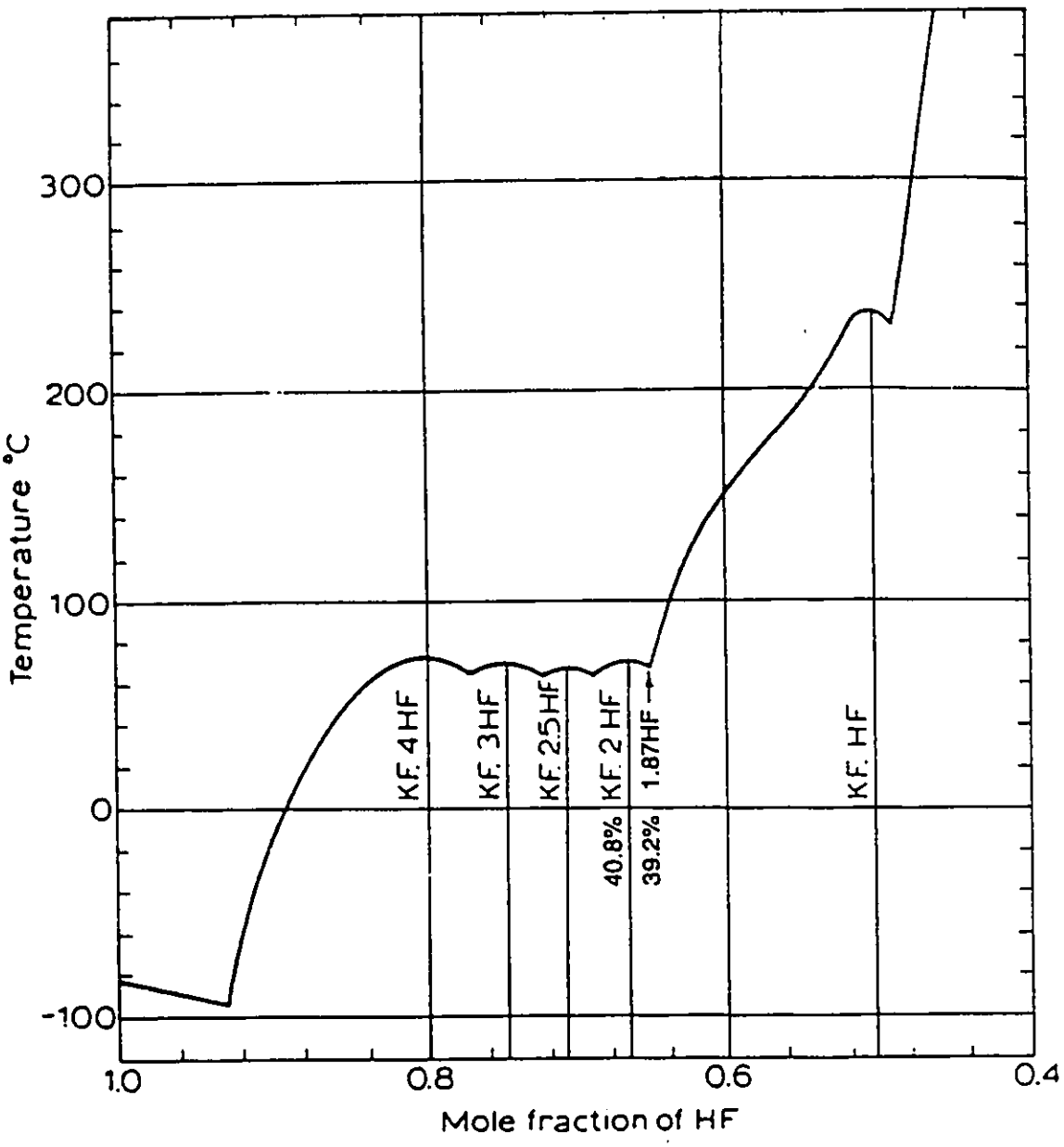

Fig.2.6 Melting point vs composition diagram for the KF/HF system.

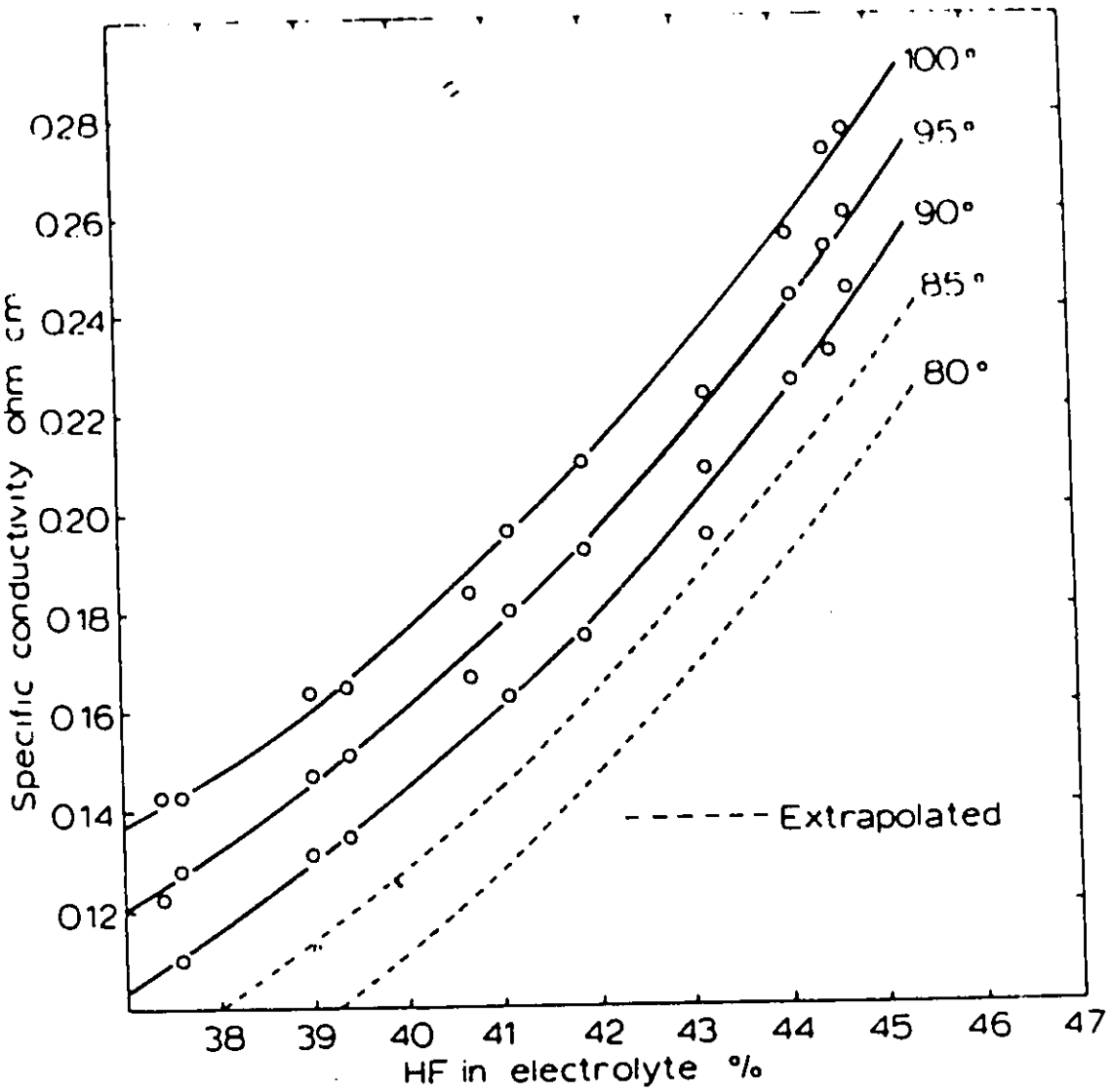

Fig.2.7 Specific conductivity of the KF/HF system.

the system is represented by $-\log[H_2F^+]$. Corresponding to KOH in the aquo-system, KF in HF is therefore an "alkaline" solution, i.e. the KF·2HF melt is to be regarded as an alkaline system.

Trace amounts of impurities can be present in the melt. Metal ion impurities, e.g. Fe^{3+}, Cu^{2+}, which can come from the hardware of the HF cylinder during the melt preparation, could have catalytic effects on the cathodic polarization through deposition processes. However, pre-polarization using a platinized Pt electrode for a long time, e.g. 2 hours, effectively eliminates the influence of metal ion impurities. The presence of trace amount of H_2O (max. 0.1%) in the melt will also cause some complexity in the electrode processes. In order to reduce the moisture content, small amounts of P_2O_5 were added in some experiments to the melt, which, it was supposed, would absorb the water without generating any new reactive products. In this way, the influence of H_2O can be effectively diminished as was found from the results of cyclic voltammetry experiments (see Section 4.III.4).

2.1.3.2 Aqueous Electrolyte Solutions

Various concentrations of KOH solutions were made up from BDH "Aristar" grade KOH and Milli-Pore distilled water as solvent (Milli-Pore Ultra-Pure Water System, Milli-Q UV Plus); the resistivity of the water was measured and found to be 18.2 MΩ cm, a value indicating that there were almost no impurity ions present. Since high-purity reagents were used, it was found unnecessary to pre-electrolyze the solutions for the purpose of further purification.

0.5M H_2SO_4 solutions used in some of the work were prepared from BDH "Aristar" grade acid, which, in earlier work, had been found to be of sufficiently high purity for the purposes of the experiments as judged by sensitive cyclic voltammetry results obtained at Pt electrodes [181].

2.1.4 Activation of Pt Electrodes Used in Cathode Polarization Studies

In the present work, following the purification procedure mentioned above, it was found that deactivation could occur at Pt after a period of cathodic polarization. This is due to accumulation of poison species from residual organic impurities or traces of heavy metal ions in the solution, notwithstanding the use of high-purity water [114,182,183]. However, an anodic activation procedure applied prior to each polarization and potential-relaxation measurement gave excellent reproducibility and consistently high i_0 values [72], and time effects associated with slow impurity adsorption or deposition were able to be avoided. In experiments where poison species, e.g. thiourea and As_2O_3, were added into the solution, anodic activation served to enhance the desorption process of the strongly adsorbed poisons on the surface through oxidation of those species (see Chapter IV).

The point-by-point activation procedure for Pt was as follows: before each adjustment of the cathodic polarization current and the following interruption of the current for potential-relaxation measurements, an anodic potential of +1.1 V (vs. RHE) in alkaline solutions was applied to the working electrode for 5 s. The potential was then switched to the required cathodic value and 4 s was allowed for stabilization before data were collected.

It is known [89,115] that at +1.1 V at Pt, surface oxidation, but not O_2 evolution, occurs; moreover, successive potential sweeps between 0.05 and 1.5 V gave identical surface-process current profiles which meant that the state of the Pt electrode was excellently reproducible over that potential region and a clean surface had been attained.

2.2 Solution Resistance "IR" Corrections

In many experiments in interfacial electrochemistry, the measurement of the relative potential drop between an electrode and the solution side of the electrical double-layer is of primary importance. However, when a net current, I, is passed across such an interface, a potential-sensing probe placed near the electrode surface measures a finite potential drop, IR, in the solution near the electrode, in addition to the desired interfacial potential difference:

$$V_{obs} = V + IR_s \tag{2.2}$$

where V_{obs} is the observed potential, V is the real potential and R_s is the resistance of solution between the tip of the potential-sensing probe (the Luggin capillary) and the working electrode. The experimental error due to this "IR drop" becomes significantly large when appreciable currents are passed [184,185], depending on the conductance of the solution, as is well known.

In the present work, all Tafel plots were corrected for this effect of the solution resistance, R_s; the latter was determined by the current interruption method with digital recording of the potential-relaxation transients made by means of a Nicolet digital oscilloscope, Model 310. Currents were interrupted by means of a fast vacuum mercury relay, controlled by a suitably debounced micro-switch which gave a clear interruption of current without noise or "ringing" in the potential transient.

A typical potential-relaxation curve (Fig.2.8) consists of two components: (i) a steep, almost instantaneous and linear drop due to elimination of IR_s as $I \rightarrow 0$, and (ii) an exponential, dominating component due to the Faradaic process at the interface. Using the fastest available horizontal sweep rate of the oscilloscope, i.e. 1 μs per point, the potential difference at the time of interruption, $\Delta V_{t=0}$, which is the drop due to solution resistance, V_{IR}, can then be measured.

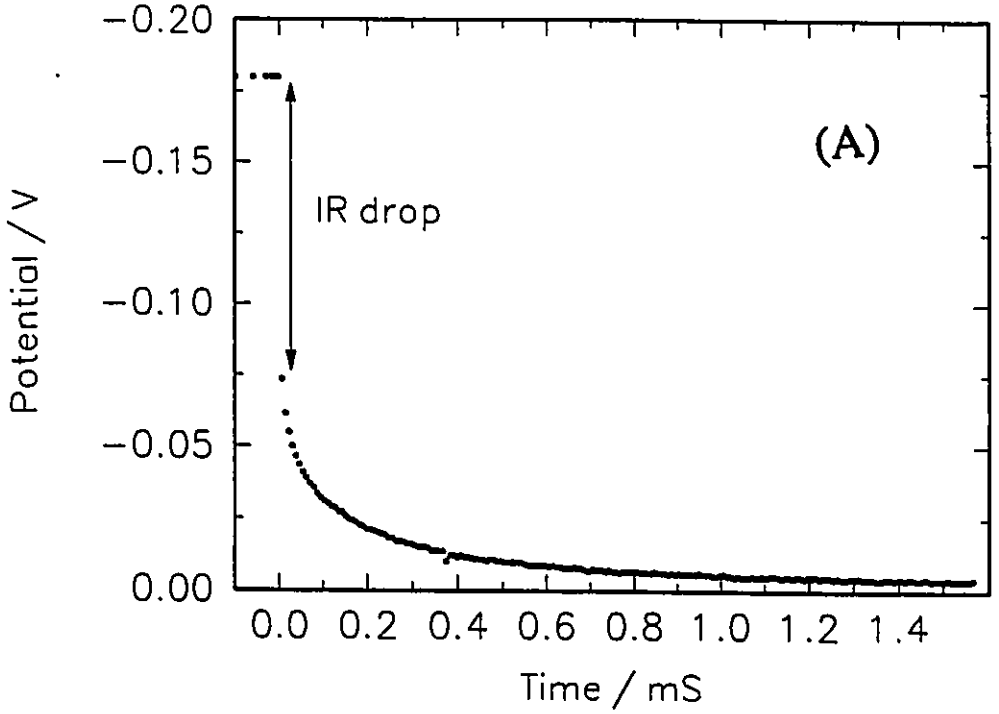

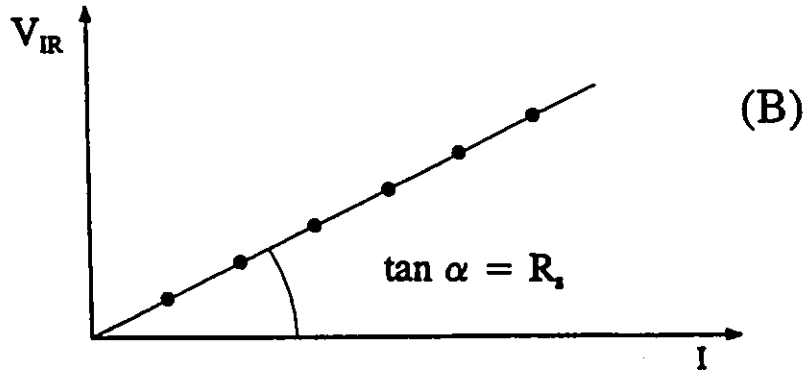

Fig.2.8 (a) A typical potential-relaxation curve (η - t relation).
(b) Relation of V_{IR} vs I.

By measuring the "length" of the linear component, V_{IR}, and the current, I, prior to its interruption, the value of R_s can be determined from the slope of the V_{IR} vs I plot.

The solution resistance could also be measured by means of a.c. impedance using a Solartron Frequency Analyzer. The R_s can then be obtained from the intercept on the real (Z') axis of the complex plane plot at the high frequency response end.

The results of measurements by the two methods were in good agreement. *I*R drop corrections, based on these measured resistances, were applied in all the polarization experiments, especially at appreciable I's.

Complications arise when porous electrodes and/or problems of wetting of such an electrode by the electrolyte melt are involved in the measurements. Solution resistance inside the pores of the electrodes cannot be precisely determined since currents inside the pores are unevenly distributed, especially when the porous surface is not totally wetted by the melt. Small H_2 bubbles occupying in the pores of the porous electrode will also contribute to the difficulty in R_s determination. The effectively measured resistances would probably vary according to the potential applied. However, the R_s could usually be determined satisfactorily and *in situ* over various potential regions by utilizing the two methods mentioned above.

2.3 Contact Angle Measurements in Relation to Bubble Adhesion

In the course of the work on H_2 evolution from KF·2HF melts, it became necessary to consider the wetting characteristics of various electrode materials by the melt.

Contact angle is one of the measurements of adhesion in wetting of a solid surface by a liquid and is used to calculate adhesion tension. A Goniometer (Model 100, Kruss) was used to measure the contact angles of H_2 bubbles at the electrodeposited Ni-Mo-Cd electrode in the

$KF \cdot 2HF$ and $KOH \cdot 2H_2O$ melts. The H_2 bubbles were generated *in situ* cathodically and could be viewed individually through the optical goniometer.

The melts were contained in an acrylic, transparent cell which was mounted in a chamber with controlled temperature. The gas/melt/electrode interphase was viewed through a microscope with rotatable reticules. The contact angle was measured from the aligned tangent of a fiducial hair to the bubble profile at its baseline of contact with the electrode substrate. All the setup was placed on an optical bench enabling the assembly to be smoothly adjusted. The microscopic view of the bubble at the electrode surface was recorded photographically by a placed Polaroid camera.

2.4 Electrochemical Measurement Techniques

2.4.1 Tafel Measurements

Measurements of steady-state currents, resulting from controlled but variably applied potential, provide useful information on the overall kinetics of the electrode process of interest (in this case, cathodic H_2 evolution). The general form of the log i vs η relation, commonly called a Tafel plot, and its slope(s), provides information about the reaction mechanisms. The exchange current-densities derived from extrapolation of the linear part of the Tafel plots to zero overpotential, which characterize the kinetics of the electrode process at equilibrium, are explicitly related to the standard rate constants of the reactions.

All the Tafel plot measurements made in the course of this work utilized an automated, computer-controlled, data acquisition system and employed software developed in previous years in this Laboratory.

An HP217 (9000 series) computer-controlled, HP-IB-compatible digital-analog converter (Kepco, Model SN488-122) was used to supply the desired potential to the external control input of a Potentialstat (Model HA-301, Hokuto Denko Ltd.). This D/A converter gave 13 bit resolution over $\pm$ 1 V or $\pm$ 10 V, which corresponds to a minimum potential increment of 0.2 mV and 2.4 mV, respectively. The current resulting from the applied potential was monitored by means of an HP-IB-compatible digital multimeter (Keithley, Model 195A).

The computerized experimental setup allowed convenient use of staircase and rectangular potential programs for steady-state polarization measurements. The current data were acquired every 4 seconds at the programmed overpotentials. In the experiments involving activation of the Pt electrode, the potential could be set in the anodic direction for a required time (e.g. 5 seconds at +1.1 V in alkaline solutions). Data could be displayed simultaneously on the computer screen and stored later on a disc. The Tafel measurements were plotted using an HP 7470A Plotter.

Note that the potential data acquired through the computer are the directly observed values. The actual overpotentials applied at the metal/solution interface in steady-state polarization measurements have to be obtained by *I*R correction, using eqn.(2.2).

2.4.2 Potential-Relaxation Transient Measurements

Open-circuit potential-relaxation transients were recorded following the interruption of currents by means of a vacuum mercury module (AMF Potter and Brumfield, Model JMF 2-2000-71) controlled by a suitably debounced micro-switch, which gave a clean interruption of current in a very short time (which should be less than 1 μs) with no noise being introduced at the commencement of the potential transient. Before the interruption of current, similar

experimental conditions were maintained as those for the Tafel measurements under steady-state polarization conditions. The potential vs time relaxation transients were recorded digitally by means of the Nicolet digital oscilloscope (Model 310).

In most experiments, two or three oscilloscopes were operated in tandem to cover a total of 6 or 7 decades of time change, starting in the μs region. The oscilloscopes were simultaneously triggered from the signal of the mercury relay when the current was interrupted. Steady-state current-densities were monitored prior to the interruption of currents. Since each digital oscilloscope can record 4000 data points, the horizontal sweep rates were typically set at 1 μs/point for the first oscilloscope, 500 μs/point for the second and 200 ms/point for the third one, depending on the electrochemical system under study (it was found that it took longer times for porous electrodes to relax to the equilibrium potentials (see Chapter IV). It is very important that full-range potential-relaxation transients be recorded in order to make kinetic simulations of the experimental data, i.e. transients for which the potential relaxes down to or near the reversible potential.

The data acquired from the oscilloscope were stored on the disk and then treated using in-house prepared software in QuickBasic on an IBM PC. Data on different time-scales were joined smoothly into one full curve. Very clean η-t relaxation transients were obtained from the careful measurements described above. The potential transient figures were plotted by means of AXUM software and printed out using a HP LaserJet III printer.

Much desired information can be obtained from the potential-relaxation measurements. The double-layer capacitance of the electrode can be conveniently obtained from use of a fitting procedure for the initial region of the potential-relaxation transient (in the range of 1 μs - 1 ms,

depending on the system). The fitting was realized by the nonlinear regression method operated by means of STATGRAPH software. Parameters could then be obtained from the fitting of the $\eta(t)$ curve so that $(d\eta/dt)_{t=0}$ could be calculated. From the obtained $(d\eta/dt)_{t=0}$ and the initial current $(i_{t=0})$ prior to interruption, C_{dl} could be easily evaluated (see Section 3.3) from $-C_{dl}(d\eta/dt)_{t=0} = i_{t=0}$.

The full potential-relaxation behaviour is determined by the equations of the HER which involve the rate of electron production, or Faradaic current, and the rate of production of MH, the adsorbed H intermediate (see Section 3.2). The two rate equations are stiff ordinary differential equations, which can be solved numerically using the STFODE subroutine from SANDIA [186], kindly supplied to us from the University of Sherbrooke [187]. The simulation of the experimental transients was realized using a non-linear least-squares technique (NLSQ), the program for which was originally developed by Macdonald [188]. Substantial modifications were made to the programs in order for them to be used in the present work, especially with regard to the rate equations which take into account lateral interactions and coverage by a poison (Chapter IV, Part 3), an important aspect of the present work. The program was implemented in VS FORTRAN language and run on the CMS mainframe system at University of Ottawa. More detailed discussion of the procedures will be given in the Appendix.

2.4.3 Cyclic Voltammetry

The technique of cyclic voltammetry [115,116], or CV, involves the procedures of sweeping the potential linearly between two limits, under the control of a potentiostat, at a constant sweep-rate, s, and recording the current response. The dynamic current-density vs potential profile can provide uniquely detailed information about a particular surface process,

such as underpotential deposition (u.p.d.) of H and surface oxide formation. In the present work, interest was mainly centered on the measurement of the monolayer charge for the underpotential deposition of H at Pt, which provides a precise basis for determining electrode surface area by taking (see Chapter I) $q_l = 210\ \mu C\ cm^{-2}$. Poison effects on the u.p.d. H adsorption were also quantitatively investigated (Chapter IV) by means of the CV technique.

Standard instruments for CV measurements were used consisting of the following components: (a) a function generator (Model HB-104, HD Ltd., Japan) which provides a linearly-varying, time-dependent input potential to a potentiostat; (b) a potentiostat (Model HA-301, HD Ltd., Japan) which controls potentials and monitors current responses; (c) a digital oscilloscope (Nicolet 310) which records V vs *i* profiles in two channels; and (d) a low-frequency filter which is used to eliminate electronic noise (the 60 Hz city electricity noise). Continuous read-out of the potential was available on a digital multimeter (Pacal Dana model 4002). Data recorded from the oscilloscope could be stored on the disks, and treated on the IBM PC with the developed softwares and the CV then plotted using AXUM software.

2.4.4 A.C. Impedance Measurements

The system used for impedance measurements consisted of a Solartron 1255 Frequency Response Analyser in conjunction with a PARC M273 Potentiostat, controlled by ZPLOT software (Scribner Associates Inc.).

The solartron affords a rapid and accurate means of measuring a system's frequency response to various input signals. It consists basically of a programmable sinusoidal generator and an analyzer. The generator provides an output signal of known amplitude (A) (10 mV in the present case) and frequency (ω) in the form A sin ωt. This signal is applied to the

electrochemical system to be tested, through the potentiostat.

The response of the electrochemical system to its input signal has a fundamental a.c. component in the form of R sin ($\omega t+\psi$). In simple terms, this means that response of the system has an amplitude, R, different from the input amplitude, A, and a phase-angle change, ψ. The function of the analyser is to accept the electrochemical system's response to the stimulus signal of the generator using a correlation process, resolving it in terms of R and ψ, or as real and imaginary components of the overall impedance for plotting in the complex plane. Relations of phase-angle and log |Z| the impedance vector, to log ω can also be analyzed and displayed simultaneously.

The frequency range was typically set from 6.5 x 10^4 to 0.2 Hz. A short integration time was selected in using the Solartron 1255 FRA, so that only about 50 s was required to complete the full range of frequency scan. Therefore, any effects due to deactivation during the passage of d.c. current were minimized and were actually negligible. Reasonably good reproducibility of the impedance spectra was confirmed by sweeping the frequency from high to low ('LOG DOWN') and from low to high values ('LOG UP') in the scan.

The impedance spectra were fitted by means of a complex, non-linear, least-squares immitance fitting program, LEVM [188] and treated using ZSIM software based on equivalent circuit models.

CHAPTER III

THEORETICAL TREATMENT AND SIMULATION OF POTENTIAL RELAXATION TRANSIENTS

3.1 Introduction

In order to derive information on surface coverage, θ_H, by the adsorbed o.p.d. H intermediate in the HER and the associated pseudocapacitance[1], $C_\phi = q_1 \, d\theta_H/d\eta$, steady-state methods are not useful nor is cyclic voltammetry applicable. The required information can only be derived from non-steady-state transients, e.g. potential-relaxation following current interruption or a.c. modulation at potentiostatically controlled potentials. These two methods have therefore been employed complementarily in much of the experimental work described in this thesis.

The method of recording the time-course of potential-relaxation on open-circuit, following interruption of a polarizing current of an electrode reaction, provides data leading to information on the interfacial capacitance, and the adsorption behaviour of the intermediate involved in an electrode reaction. In cases where steady-state coverage by one or more adsorbed intermediates is appreciable, a potential dependence of the coverage by such intermediates arises, i.e. an adsorption pseudocapacitance (see Section 1.8), C_ϕ, is generated [117,118]. The method's principal value lies in the provision of a procedure that enables determination of the latter quantity over an appreciable range of overpotentials where substantial continuous Faradaic currents for the reaction were previously passing. Thus, information on the kinetically

---

[1] C_ϕ is also known as C_P defined as the pseudocapacitance (*cf. refs.* [72,85]). Here C_ϕ is referred as a steady-state quantity (see eqn.(3.9)), different from the transient pseudocapacitance, $C_{\phi,t}$ and the operational pseudocapacitance, $C_{\phi,b}$ (*cf. ref.* [15]).

significant, *overpotential-deposited* (o.p.d.) species is obtained, complementary to data that can be derived (for the case of some noble metals) for the underpotential deposited species, below the reversible potential, by means of cyclic voltammetry or charging curves. Related information on the o.p.d. species may be obtained from a.c. impedance measurements conducted under potentiostatic control of the overpotential [101,189-191]. Recently, the first method has been developed in depth in this lab [14,15,72,82] by means of digital data acquisition and computer processing of information from potential-relaxation experiments, applied to evaluation of the behaviour of o.p.d. H in the HER, as further extended in the present work.

When the electrode is polarized, the current across the interface will charge the capacitance and pass through the reaction resistance. Upon interruption of the current, charge will continue to flow across the interface, discharging the capacitance by passing through the reaction resistance, R_F (Chapter I). At the real electrochemical electrode/solution interface, this process involves the continuing electron transfer from the metal to the reactive solution species in the double-layer, for example, H_3O^+, while the external current is zero. Reaction is still transiently taking place, thus the recording of potential-relaxation at the electrode provides information from which data such as kinetic rate constants, interfacial capacitances, and information on the state(s) of chemisorbed intermediates can be deduced. The principle of this method originates from Armstrong and Butler's paper published in 1933 [192], applied to the determination of the *double-layer* capacitance at Hg.

A general treatment of potential-relaxation behaviour for several mechanisms of the HER was initially based in earlier work from this lab on the simple decay rate relation - C $d\eta/dt = i_f$ [193,194], where i_f is the potential-dependent current-density for the Faradaic process

represented kinetically by the Tafel equation. In that treatment, the decay rate was related to the behaviour of a simple "RC" equivalent circuit for the electrode process and assumptions were made by relating the potential-dependence of the steady-state Tafel current to that involved in the experimental transients.

In the present work, a different and more complete approach [82,83,90] is presented in which the kinetic equations for steps in the HER are solved numerically for open-circuit potential-relaxation conditions without any restrictive conditions or representation of the process in terms of arbitrary equivalent circuits. The theoretically calculated η-t relations, using the rate equations (described below), are related to the experimental data by means of an non-linear least squares fitting procedure, which successfully generates rate constants and the parameters C_{dl}, C_{ϕ} and θ etc., necessarily required for the understanding of o.p.d. H adsorption behaviour.

In the following sections, the theoretical treatment of the potential-relaxation behaviour in terms of kinetic rate equations for the HER will be introduced. The procedure of simulation of the experimental potential-relaxation transients by means of the automatic computer-controlled least-squares fitting procedure will also be described and discussed. The roles, which the kinetic parameters, e.g. rate-constants k, C_{dl}, etc. play in determining the potential-relaxation and adsorption behaviour, are investigated through theoretical simulations and graphical illustrations.

A new method for determination of double-layer capacitance at potentials where appreciable continuous Faradaic currents are passing, is proposed in terms of fitting the initial stages of the potential-relaxation transient; the reliability of this procedure is tested by means of a real electronic hardware circuit and by other means of examination, based on theoretically generated potential-relaxation curves.

3.2 Kinetic Equations for Potential-Relaxation Transients Involving the HER

3.2.1 Theoretical Treatment

The steps of the HER have been discussed in Chapter I of this thesis. In alkaline solutions, the HER proceeds via well known steps, viz. electrosorption of H (Volmer reaction) followed by the "atom-ion" electrodesorption of H (Heyrovsky reaction) and/or by desorption recombination (Tafel reaction) (see also eqns.(1.19-1.21)):

Step 1:
$$M(e) + H_2O \underset{k_1}{\overset{k_1}{\rightleftharpoons}} MH_{ads} + OH^- \qquad (3.1a)$$

Step 2:
$$MH_{ads} + M(e) + H_2O \underset{k_2}{\overset{k_2}{\rightleftharpoons}} H_2 + OH^- + 2M \qquad (3.1b)$$

or

Step 3:
$$2MH_{ads} \underset{k_3}{\overset{k_3}{\rightleftharpoons}} H_2 + 2M \qquad (3.1c)$$

No *a priori* assumptions are made about the mechanism or which step is rate-limiting. When the adsorption behaviour of H obeys a Langmuir isotherm in the steps above (Frumkin or Temkin adsorption isotherms will also be considered in Chapter IV about poisoning effects on the adsorption behaviour and kinetics of the HER), the net rates of individual steps (v_1, v_2, v_3 /mol cm^{-2} s^{-1}) are dependent only on the overpotential, η, and the fractional coverage, θ, by the adsorbed intermediate "MH". Taking β nominally as 0.5 for the charge-transfer steps 1 and 2, one has:

$$v_1 = k_1 (1-\theta) \exp [F\eta/2RT] - k_1 \theta \exp [-F\eta/2RT] \qquad (3.2a)$$

$$v_2 = k_2 \theta \exp [F\eta/2RT] - k_2 (1-\theta) \exp [-F\eta/2RT] \qquad (3.2b)$$

$$v_3 = k_3 \theta^2 - k_3 (1-\theta)^2 \qquad (3.2c)$$

Here, the surface concentrations of reagent (H_2O or H_3O^+) are formally absorbed into the forward rate constants, while k_2 and k_{-3} include pressure of H_2. The Faradaic current is proportional to the rate of electron production, r_0, which is equal to the sum of v_1 and v_2 , thus

$$i_f / F = r_0(\theta,\eta) = v_1 + v_2 \tag{3.3}$$

Likewise, $d\theta/dt$ is proportional to r_1, the rate of production of MH_{ad} :

$$(q_1/F)\ (d\theta/dt) = r_1(\theta,\eta) = v_1 - v_2 - 2v_3 \tag{3.4}$$

where q_1 is the hypothetical monolayer charge per cm^2 for the o.p.d. intermediate, H, corresponding to $\theta_H=1$. Since v_3 is defined as the rate of hydrogen (H_2) production in step 3, or half the rate of consumption of adsorbed H in that step, the consequence is that a coefficient two appears in eqn.(3.4)

On opening the circuit, the potential difference across the interface must be reduced by diminution of the charge on each "plate" of the double-layer capacitor. For a cathodic reaction, each electron being transferred from the metal to the solution side of the interface reduces the charge, σ, on each plate. Consequently, the rate of reduction of this charge is equal to the Faradaic current and eqn.(3.5) then follows as:

$$i_f = -d\sigma/dt = (-d\sigma/d\eta)\ (d\eta/dt) = - C_{dl}(d\eta/dt) \tag{3.5}$$

For the parallel-plate model assumed here, C_{dl} will be potential independent. A more complete theory would take into account the fact that C_{dl} is often potential dependent, e.g. near or through the zero-charge potential region, but this need not be pursued here. Bringing eqn.(3.2) and eqn.(3.5) into eqns.(3.3) and (3.4), and making the substitution $B = \exp[F\eta/2RT]$, we have

$$d\eta/dt = -F/C_{dl}\ [k_1(1-\theta)B - k_{-1}\theta B^{-1} + k_2\theta B - k_{-2}(1-\theta)B^{-1}] \tag{3.6}$$

and

$$d\theta/dt = F/q_1 [k_1(1-\theta)B - k_{-1}\theta B^{-1} - k_2\theta B + k_{-2}(1-\theta)B^{-1} - 2k_3\theta^2 + 2k_{-3}(1-\theta)^2] \quad (3.7)$$

The rate constants are not all independent but are constrained by the equilibrium condition, at $\eta = 0$, for the net reaction, and thus must obey eqn.(3.8):

$$k_1k_2 / k_{-1}k_{-2} = k_1^2k_3 / k_{-1}^2k_{-3} = 1. \quad (3.8)$$

Therefore, only four out of the six rate constants are independent in the eqns.(3.6) and (3.7).

Eqns.(3.6) and (3.7) are two "stiff" differential equations which do not have analytical solutions. However, they can be solved numerically using the STFODE subroutine [186], which has been employed for solving stiff equations. The overpotential transients, $\eta(t)$, thus obtained, may be compared directly with the appropriate experimental transient, and the rate constants can be derived by seeking the best agreement between the calculated transients for various rate constant values and the experimentally observed $\eta(t)$ behaviour. The simulation of the potential-relaxation transients was realized employing the FORTRAN program implemented on the CMS mainframe computer at University of Ottawa. A full-range $\eta(t)$ curve, i.e. with η falling to 0 for the equilibrium condition, has to be recorded in the experiment and used in the simulation. This is particularly important in order to obtain information on the pseudocapacitance, since the discharge of the adsorbed intermediate H usually occurs over the long time region (>1 ms) and at low overpotentials (below -150 mV) [82] (see below).

Usually, the polarization is at steady-state just before the circuit is opened. Therefore the value of $\eta(0)$ (i.e. η at t=0) is defined as the initial condition for solution of the differential equations and is the overpotential at which the system was held prior to the transient (solution resistance IR drop has been compensated). The initial value of θ is the corresponding steady-state value, obtained by inserting $\eta(0)$ into eqn.(3.4), setting eqn.(3.4) equal to zero and solving

for θ:

$$d\theta_{ss} / dt = v_1 - v_2 - 2v_3 = 0 \qquad (3.9)$$

The steady-state adsorption pseudocapacitance is defined according to the treatment by Gileadi and Conway [118], as the product of the monolayer charge, q_1, and the derivative of coverage with overpotential, eqn.(3.10):

$$C_{\phi,ss} = q_1 (d\theta_{ss} / d\eta_{ss}) \qquad (3.10)$$

All the reported values of coverage, θ, and pseudocapacitance, C_ϕ, in this thesis are referred to the steady-state quantities.

By providing the rate constants, the solutions of eqns.(3.6) and (3.7) can be numerically obtained using the appropriate software. A resulting computed arbitrary η - t relationship[2] is shown in Fig.3.1a for three initial overpotentials -0.4, -0.3 and -0.2 V, taking $k_1 = 10^{-9}$, $k_{-1} = 10^{-8}$, $k_2 = 10^{-10}$, $k_3 = 10^{-10}$ mol cm^{-2} s^{-1}, $C_{dl} = 25$ μF cm^{-2}, $q_1 = 210$ μC cm^{-2} which are typical values for the HER behaviour at Pt and Ni-based electrocatalysts. Fig.3.1b shows the corresponding coverage and pseudocapacitance calculated from the same set of rate constants. It can be seen that the potential-relaxation curves are comprised mainly of two regions. The early stage, in the short time region (1 μs - 10 ms), is associated with the discharge of the double-layer capacitance; as the consequence, eqn.(3.5) controls the process. The overpotential falls slowly with log t and θ does not change significantly from its initial, steady-state value. After certain time τ, however (further discussion later), the overpotential falls approximately linearly with log t but θ still remains almost unchanged. In the longer time region (10 ms -

[2] The purpose of this calculated example is simply to provide an illustration of the type of potential-relaxation behaviour to be expected, provided that θ_H and $C_{\phi(H)}$ are significant.

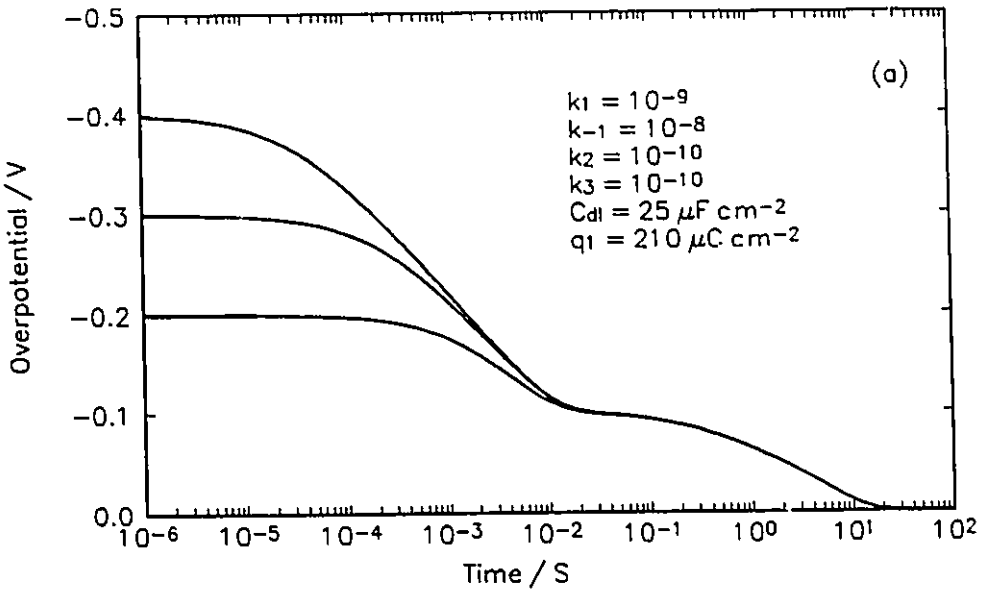

Fig.3.1 (a) Theoretical calculation of potential-relaxation transients. Parameters are shown in the Figure, which are typical values for the HER mechanism at Pt or Ni.

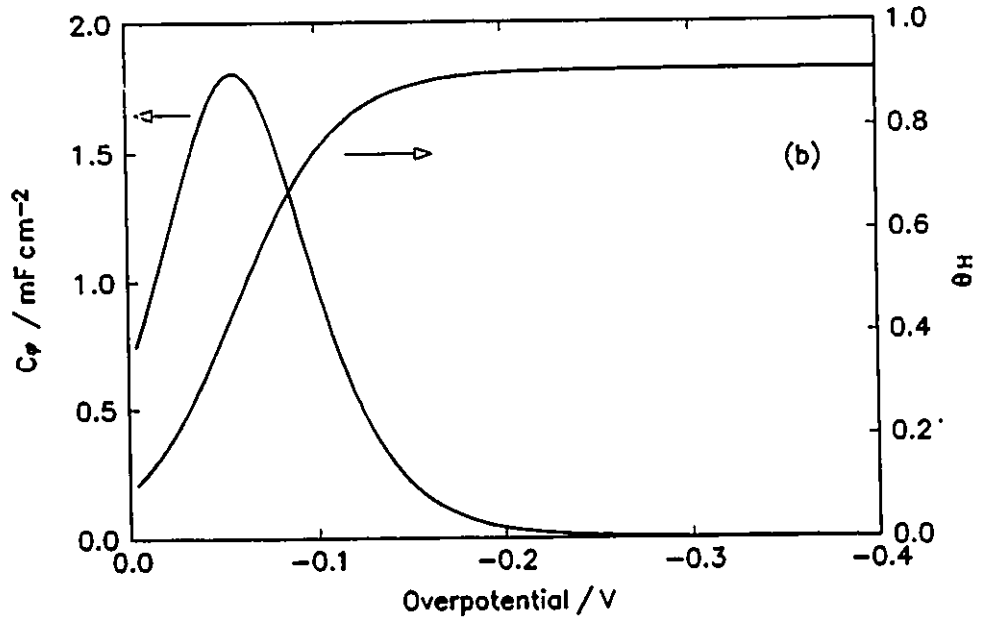

Fig.3.1 (b) Dependence of steady-state coverage and pseudocapacitance on overpotential, calculated from parameters shown in Fig.3.1a.

> 100 s), an arrest appears which is due to the discharge of the pseudocapacitance arising from the adsorbed intermediate H. The overpotential begins to level off and then finally decays to zero. Correspondingly, the coverage, θ, by the adsorbed H decreases dramatically (see Section 3.2.2 below), which means the pseudocapacitance changes significantly according to the definition of eqn.(3.10). A peak of maximum pseudocapacitance appears in the low overpotential region (Fig.3.1b) with its values in the range of mF cm^{-2}, which are thus much larger than that of the double-layer capacitance.

3.2.2 Physical Processes Associated with the Potential-Relaxation Transients

In order to provide a basis for discussion of the significance of the results presented in the previous section, it will be necessary to outline briefly the mechanisms and physical processes which are involved in potential-relaxation following current interruption.

In the case of electrode surfaces at which there is insignificant surface coverage by an electroactive adsorbed intermediate, e.g. H, i.e. normally when the rate constant for the step of desorption for the adsorbed H is substantially greater than that for the initial discharge step producing it, as with the HER at Hg and Au, the course and the time scale of the potential-relaxation transient is determined simply by the "RC time constant" of the parallel combination of the double-layer capacitance and the potential-dependent Faradaic resistance corresponding to the parameters of the Tafel relation for the electrode process [192]. For such a condition, i.e. $C=C_{dl}$, $C_\phi \approx 0$, and the slope $[-d\eta/d \log(t)]$ of the transient in log time is numerically equal to the Tafel slope $[d\eta/d \log(i)]$ of the steady-state polarization relation (*cf.* ref.[90]).

The open-circuit relaxation of overpotential in the HER in alkaline solution over the

potential range where C_ϕ is appreciable, takes place [118] by a mixed, coupled anodic/cathodic process in which: a) self-discharge of C_{dl} takes place and b) the non-equilibrium coverage (θ_H) by H relaxes to its equilibrium value. The processes involved in the latter change are represented by:

$$MH_{ads} + OH^- \rightleftharpoons M + H_2O + e \qquad [I]$$

$$MH_{ads} + H_2O + e \rightarrow M + H_2 + OH^- \qquad [II]$$

where the latter step, II, is simply the continuation of the rate-controlling process in the overall reaction. However, discharge of C_{dl} must still occur and takes place in a much shorter time scale than that for the H desorption as shown in the treatment of Harrington and Conway [15], referred to above. Disposal of the charge on C_{dl} must result in a small generation of adsorbed H which will be removed at lower potentials through the coupled process [I], [II], together with any H present at coverage θ_H corresponding to the steady-state kinetics of the overall reaction. An arrest plateau arises in the $\eta(t)$ transient when processes [I] and [II] "buffer" the declining potential in time in the case when θ_H is significant, as found in ref.[72] (see also Fig.3.1a).

The situation when recombination desorption, *viz.*

$$2MH_{ads} \rightarrow 2M + H_2 \qquad [III]$$

is the rate-controlling step must be different from that for the other cases since no charge is consumed in step [III]. Then, in addition to a small generation of adsorbed H through the reverse of step [I] from discharge of C_{dl}, step [III] continues with the potential being determined by quasi-equilibrium in [I] according to

$$\theta_H / (1 - \theta_H) = K_1 \exp [F\eta/RT] \qquad (3.11)$$

(or some other electrosorption isotherm) as θ_H declines due to continuation of process [III]. In

the case of either processes [I], [II] or [I], [III], an arrest arises in the potential-relaxation transient corresponding to discharge of the adsorption-pseudocapacitance of H, C_ϕ, but the initial potential decay rate will be determined principally by the C_{dl} [82,83,90], as will be discussed below and in section 3.3 (also *cf.* ref.[90])

From the theoretical calculation discussed in Section 3.2.1, it is seen that an explicit correlation can be found by numerical analysis between the individual kinetic parameters and the potential-relaxation transients, or the steady-state coverage and pseudocapacitance. Influence of these kinetic parameters on the behaviour of potential-relaxation will thus be examined by varying each individual parameter while keeping the others unchanged.

3.2.3 Effect of Values of Parameters

3.2.3.1 k_{-1}

Fig.3.2a shows the effect of changing the k_{-1} value in this way while taking $k_1 = 10^{-9}$, $k_2 = 10^{-10}$, i.e. changing the ratio k_1/k_{-1} (k_{-2} can be known from eqn.(3.8), here the second step is rate limiting), $k_3 = 10^{-11}$ mol cm^{-2} s^{-1}, $C_{dl} = 25$ μF cm^{-2} and $q_1 = 210$ μC cm^{-2}. As k_{-1} is increased from 2×10^{-9} to 2×10^{-7}, the discharge of the double-layer capacitance remains uninfluenced, while the plateau region (Fig. 3.2a) appears earlier and increases in height. This is because the effect of the back-reaction of the first step becomes increasingly important in the relaxation process so that H desorption in the reverse of step 1 is dominant at the interface as the k_{-1} value increases. This Figure provides evidence that the height of the plateau or arrest appearing already at shorter times in the overall time range of the potential-relaxation curve is an important indication of the significance of the rate constant of the back-reaction in the first step.

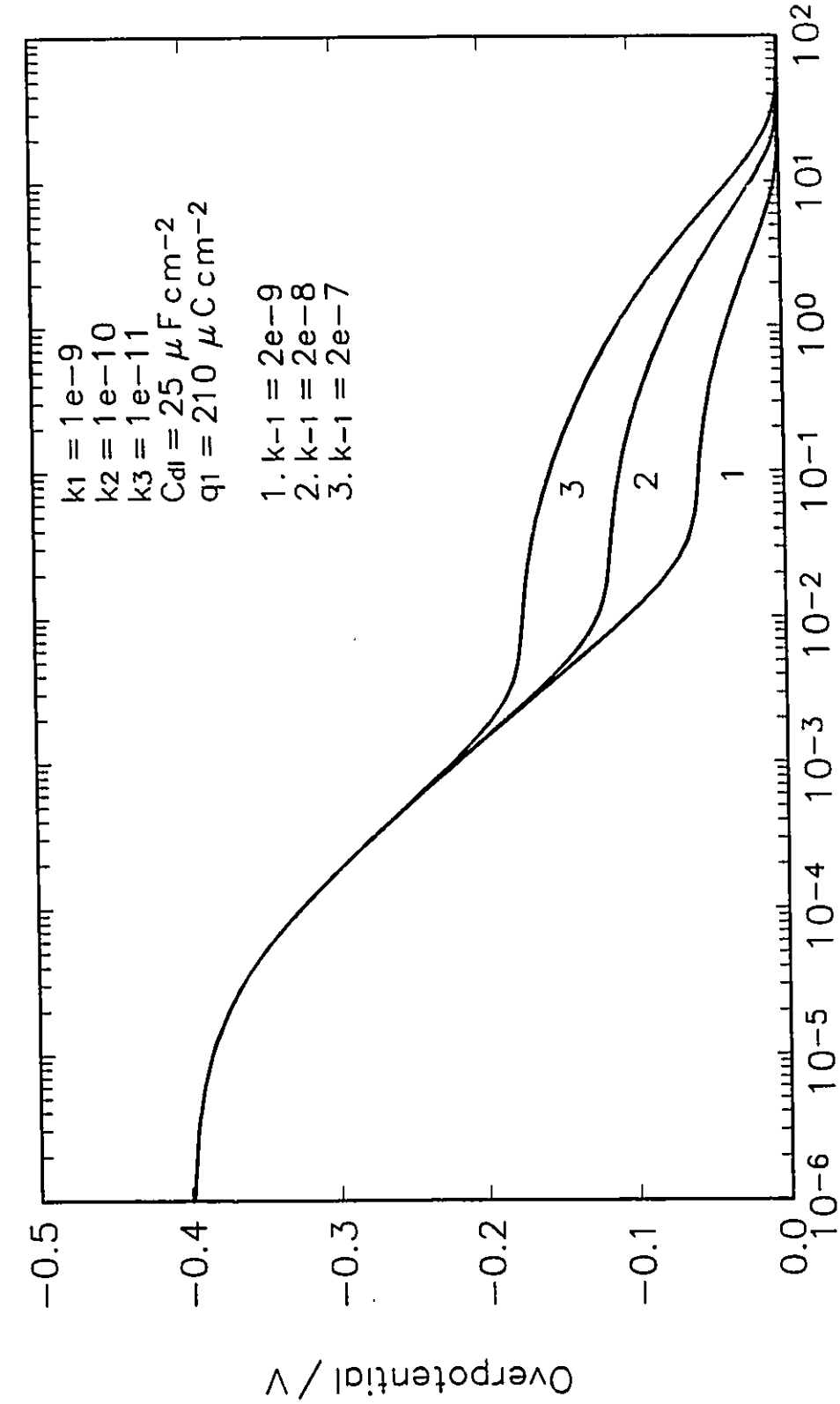

Fig.3.2 **(a) Effect of changing k_1 on calculated potential-relaxation transients. Parameters are shown in the Figure.**

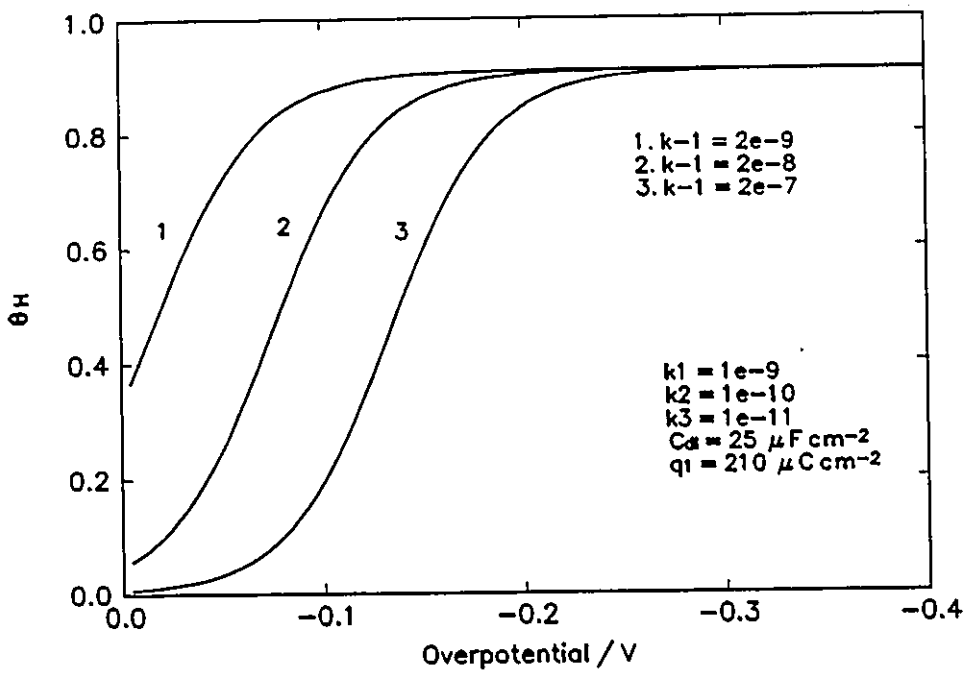

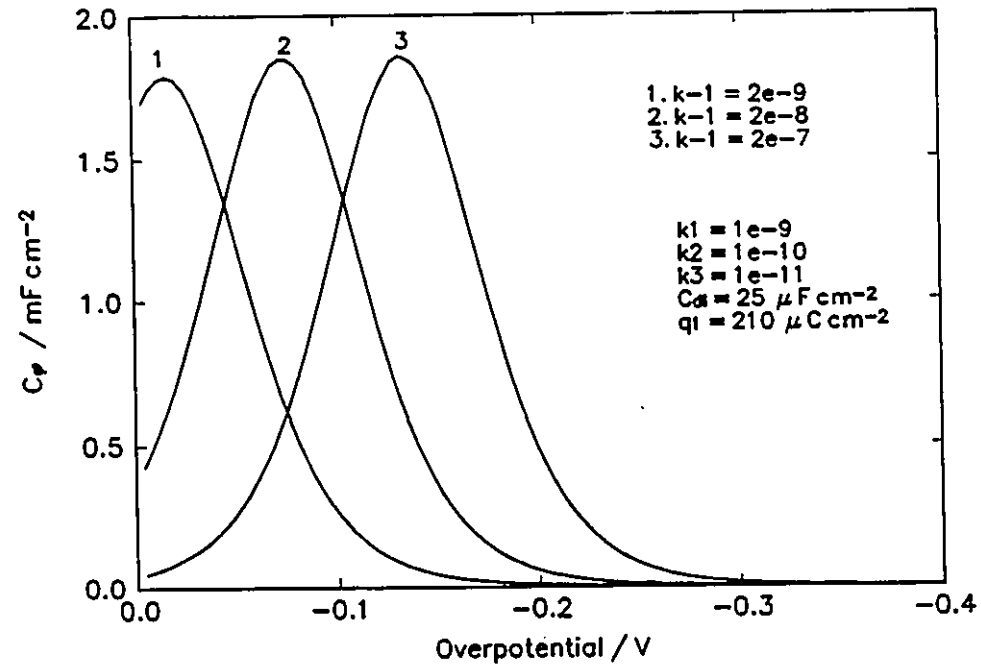

Fig.3.2 (b) The relation of θ_H vs η calculated from the parameters shown in the Fig.3.2a.

(c) The relation of C_ϕ vs η calculated from the parameters shown in the Fig.3.2a.

Fig.3.2b shows the corresponding θ vs η plot, calculated using the same set of parameters as for Fig.3.2a. The coverage values at equilibrium (η = 0) vary with the change of k_1 as they are dependent on the $K_1 = k_1/k_{-1}$ value shown in eqn.(3.11). In fact, η for the maximum θ scales with log K_1. When k_{-1} increases, values of η for a given coverage shift increasingly to a higher overpotential region; this means that with larger k_{-1} values higher overpotentials are required to approach the same extent of coverage with the smaller k_1 value. Fig.3.2c shows the corresponding relations of pseudocapacitance vs overpotential: the peaks of C_ϕ shift to higher overpotentials with increasing k_{-1}, which is a result corresponding to the derivatives of the θ - η curves in Fig.3.2b, (recalling the definition $C_\phi = q_1(d\theta/d\eta)$). Additionally, the maximum scale of C_ϕ, and the θ_H values attained, depend [85] on the ratio k_2/k_1 (see below).

3.2.3.2 k_2

Fig.3.3a illustrates a series of potential-relaxation transients calculated for increasing values of k_2, while other parameters $k_1 = 10^{-9}$, $k_{-1} = 2 \times 10^{-8}$, $k_3 = 10^{-11}$ mol cm^{-2} s^{-1}; $C_{dl} = 25$ μF cm^{-2} and $q_1 = 210$ μC cm^{-2} remain unchanged. For larger k_2, the decay of overpotential begins earlier. Curve 3 shows a transient which decays so fast that the arrest becomes insignificant. This is because the exchange current-density is determined by the rate-limiting step 2, so an increase of exchange current-density due to increased (rate-limiting) k_2 will lead to more rapid relaxation of overpotentials. A facile electrochemical desorption step, of course, more rapidly reduces the coverage of the H intermediate, leading to rapid discharges of both the double-layer capacitance and pseudocapacitance in the potential-relaxation process.

An intriguing result arises from curve 4 ($k_2 = 10^{-7}$, Fig.3.3a), insofar as the arrest in the relaxation curve appears to be longer than that in curve 3 which arises from a smaller k_2 value.

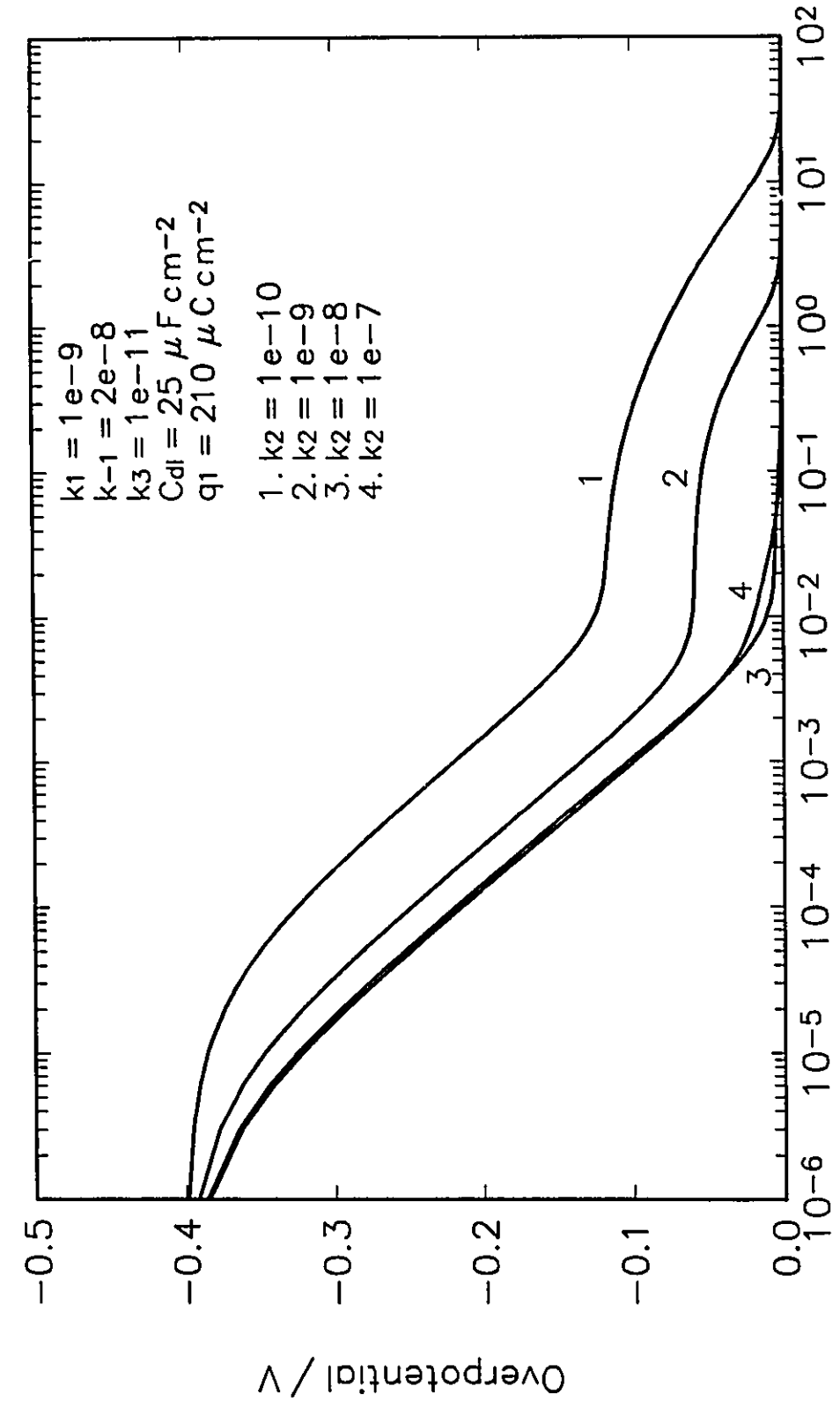

Fig.3.3 **(a) Effect of changing k_2 on calculated potential-relaxation transients. Parameters are shown in the Figure.**

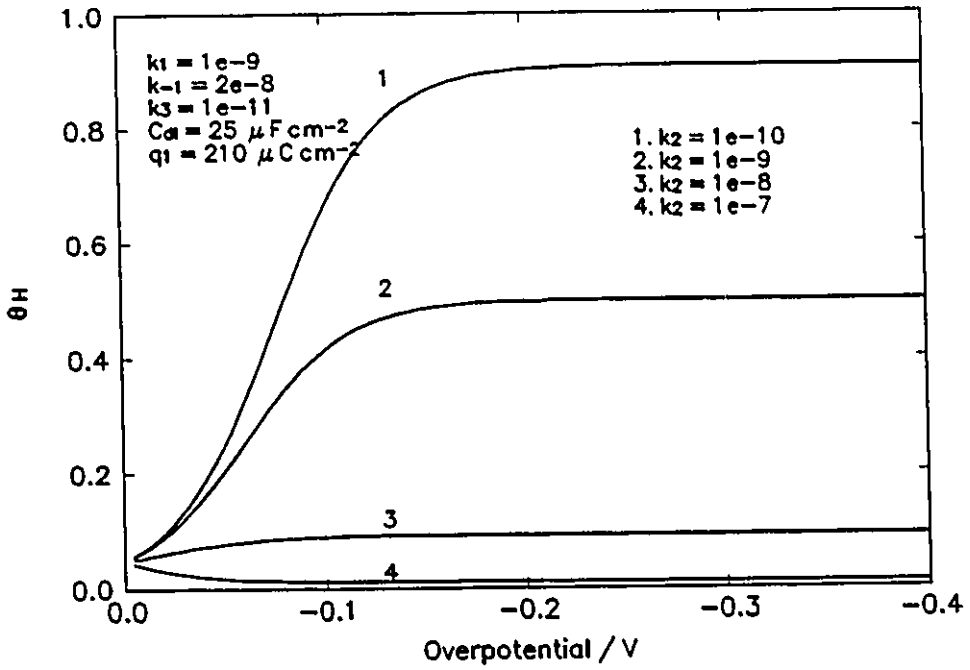

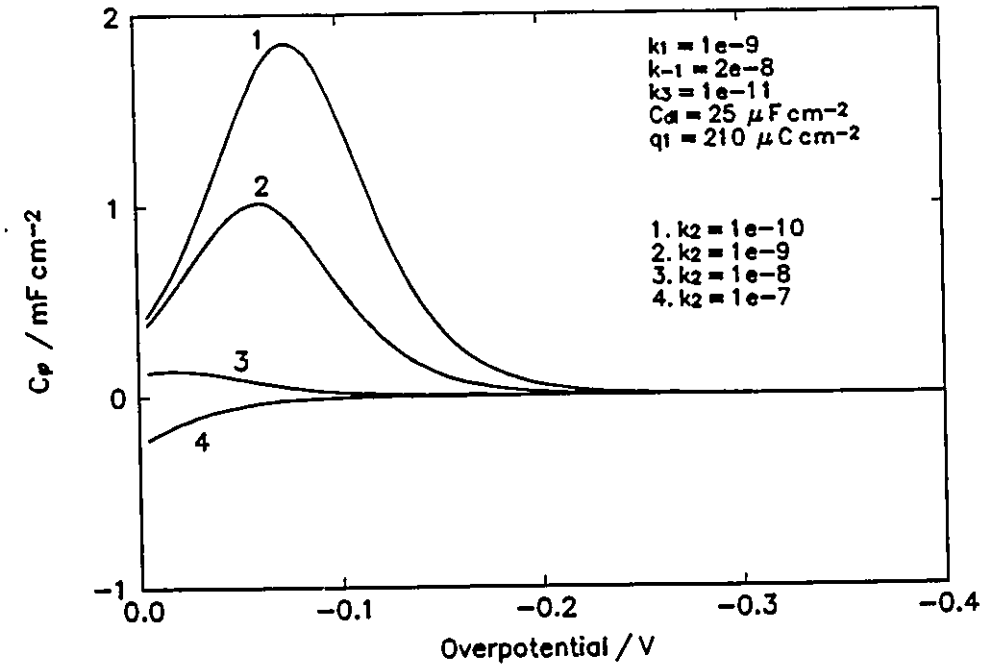

Fig.3.3 (b) The relation of θ_H vs η calculated from the parameters shown in the Fig.3.3a.

(c) The relation of C_ϕ vs η calculated from the parameters shown in the Fig.3.3a.

It is opposite to the trend of changes exhibited in the series of curves 1, 2 and 3. A more interesting situation is that curve 4 in Fig.3.3b shows a *decreased coverage* with increasing overpotential. Comparing the rate constants involved in the calculation, it can be seen in case 4 that $k_2 = 10^{-7}$ is *larger* than the values of k_1 and k_{-1}. This means that the second step of electrochemical desorption is no longer the rate-limiting step. Instead, the first step of electrochemical adsorption is then rate-determining. Therefore coverage can decrease with increase of overpotential, corresponding to a process in which the second step tends to be so quick that the H intermediate produced in the first step will be immediately consumed in the following electrochemical desorption reaction so that $\theta_H \ll 1$ or to 0.

The corresponding decrease of pseudocapacitance with increasing values of k_2 is shown in Fig.3.3c. The *negative* values of pseudocapacitance in curve 4 result from the definition of C_ϕ (eqn.(3.10)). Since it is obtained from the differentiation of curve 4 in Fig.3.3b, $(d\theta/d\eta)$, this behaviour is understandable mathematically, because θ decreases with η on curve 4 of Fig.3.3b, though the negative value of C_ϕ has no physical meaning nor is it experimentally realizable.

3.2.3.3 k_3

Influence of changing k_3 values on the form of potential-relaxation transients was also examined by means of the theoretical calculations. Fig.3.4a shows the transient curves which arise from varying k_3 from 10^{-11} to 10^{-7} while the other parameters are selected as $k_1 = 10^{-9}$, $k_{-1} = 2 \times 10^{-8}$, $k_2 = 10^{-10}$ mol cm^{-2} s^{-1}, with $C_{dl} = 25\ \mu$F cm^{-2} and $q_1 = 210\ \mu$C cm^{-2}, as used in Fig.3.3 except k_2 remains unchanged in this case. The arrests on the curves gradually decrease as k_3 increases, which means that an enhancement of the rate and participation by the desorption

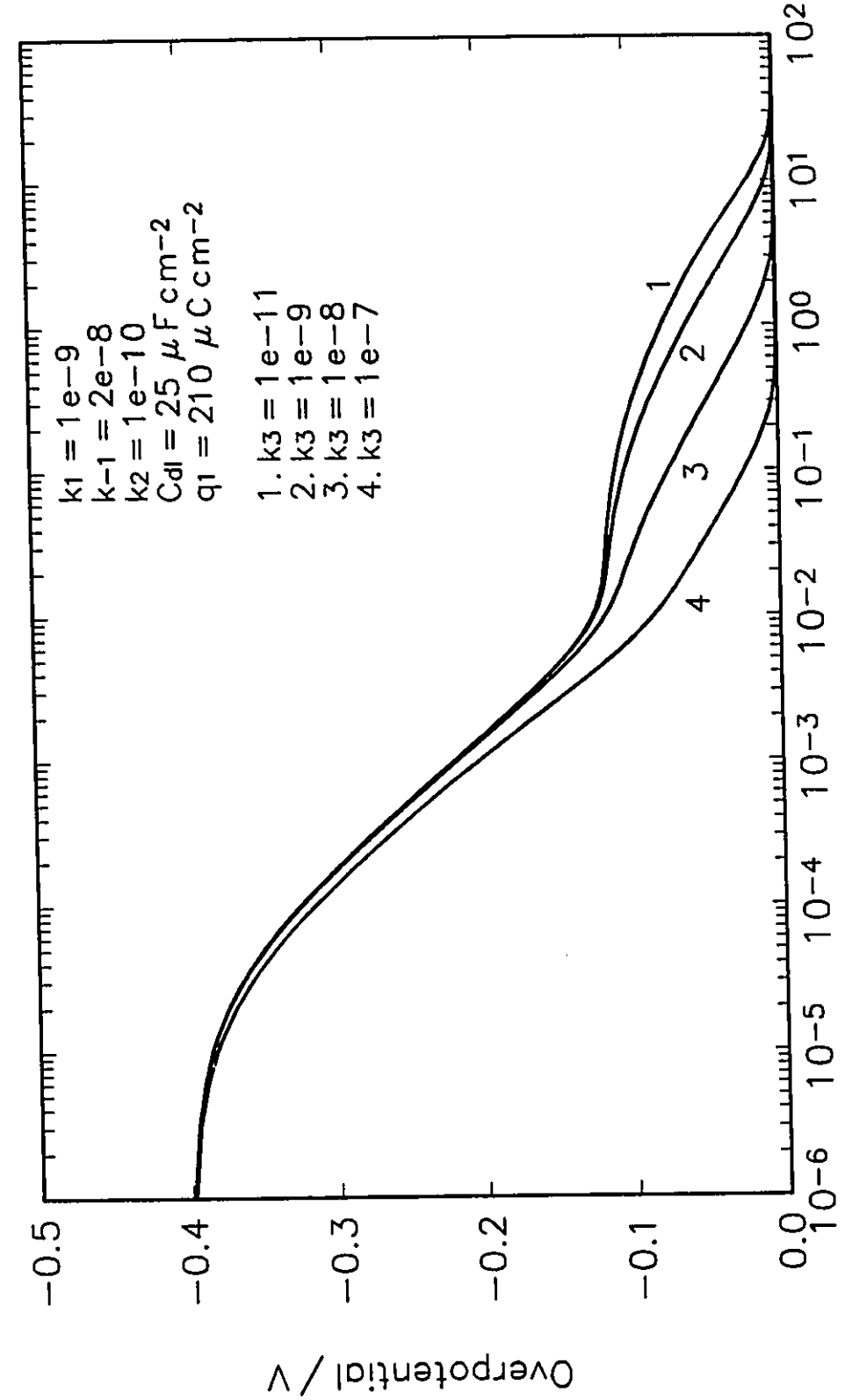

Fig.3.4 **(a) Effect of changing k_3 on calculated potential-relaxation transients. Parameters are shown in the Figure.**

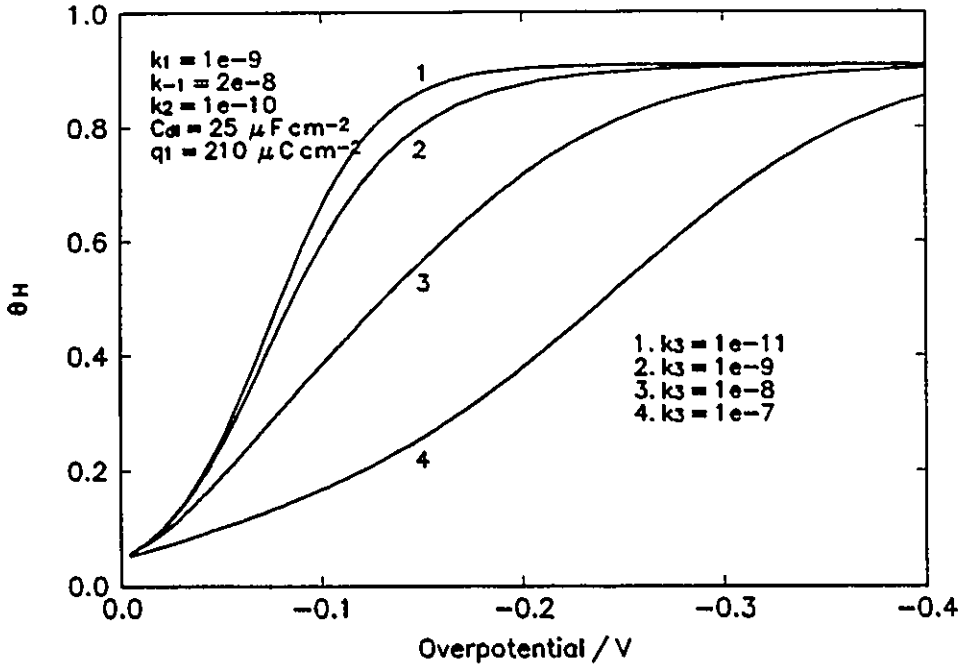

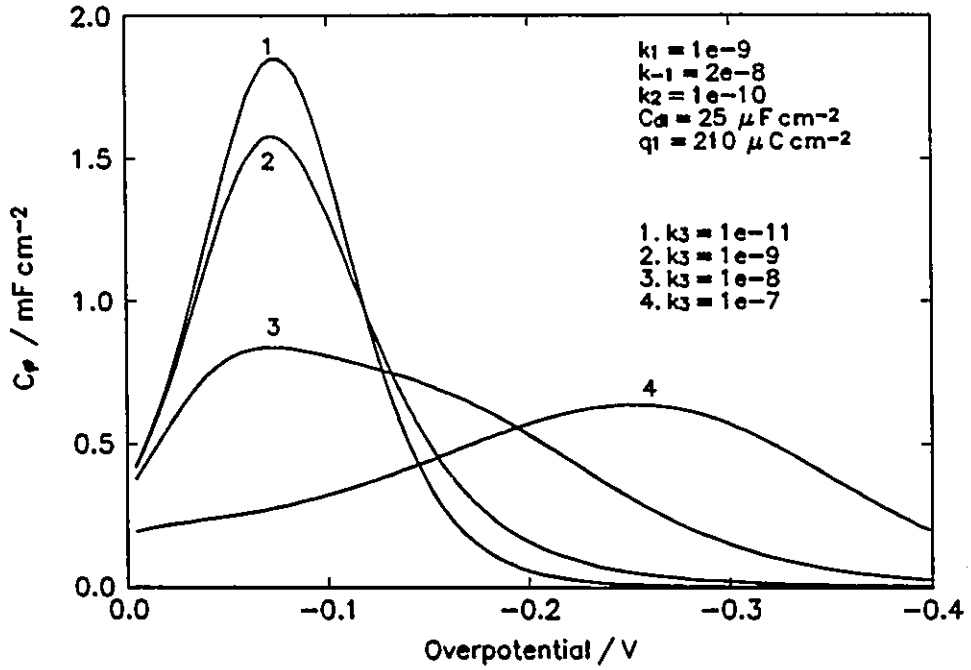

Fig.3.4 (b) The relation of θ_H vs η calculated from the parameters shown in the Fig.3.4a.

(c) The relation of C_ϕ vs η calculated from the parameters shown in the Fig.3.4a.

process of recombination is achieved. Since steps 2 and 3 are *parallel* processes for desorption of adsorbed H intermediate, following the electrochemical adsorption in step 1, the quicker of the two steps 2 or 3 will be kinetically dominant under the assumption that step 1 is much faster in both directions than either of the following two steps. This situation is indicated on curves 1, which resembles the transient for regular conditions discussed before. Curves 2 and 3 represent the cases for which all the rate constants are equivalent, indicating a mixed combination of mechanisms, i.e. a unique rate-determining step cannot be explicitly distinguished. When $k_3 = 10^{-7}$, (curve 4 in Fig.3.4a), which surpasses the values of k_1 and k_2, the rate-determining step changes to the first step.

The relations of H coverage and associated pseudocapacitance vs overpotential are shown in Figs.3.4b,c and for the same set of parameters as for Fig.3.4a. The change of coverage with overpotential in curves 3 and 4 is not as sharp as that in curves 1 and 2, and the pseudocapacitances of the former tend to become spread out over the overpotential range. This is because the reaction of recombination desorption of adsorbed H becomes dominant at higher k_3 values, so that the overpotential factor, which is the important contributor through an exponential term in the rates of electrochemical steps involving electron transfer in steps 1 and 2, is less significant in changing the H coverage and the corresponding pseudocapacitance.

3.2.3.4 C_{dl}

Fig.3.5 shows the dependence of potential-relaxation transients upon variation of C_{dl} notionally from 2.5 to 250 μF cm^{-2}. Rate constants are indicated in the inset in the Figure and were selected to be consistent with those used for the previous Figures. Increase of C_{dl} leads

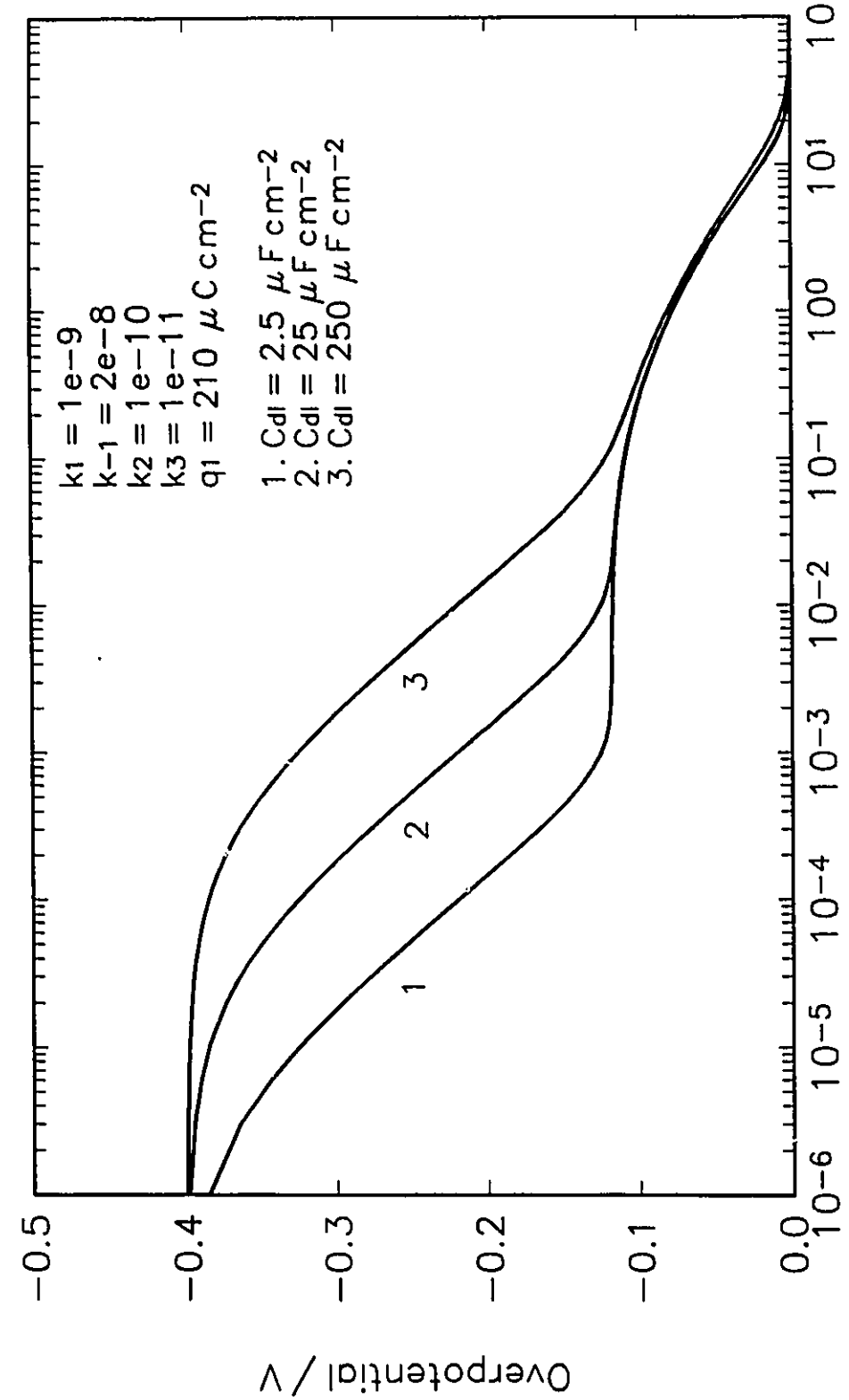

Fig.3.5 Effect of changing C_{dl} value on calculated potential-relaxation transients. Parameters are shown in the Figure.

(as expected) to a shift of the initial region of the decay transient to the longer time region; however, the slope remains unchanged. The time when the potential begins to drop is defined as the integration constant, τ, which is $\tau = bC_{dl}/2.3i_{(\eta=0)}$ (see detailed discussion in section 3.3). τ is proportional to C_{dl}, and this relation is reflected in Fig.3.5. It is significant that the arrests on the curves due to discharge of the adsorbed H are not affected in longer time region of the potential decay plots.

The θ_H vs η and C_ϕ vs η plots do not change with increase of the C_{dl} value. This can be explained from the θ_H and C_ϕ definitions (eqns.(3.9) and (3.10)) in which the C_{dl} factor is not involved.

3.2.3.5 q_1

Change of the monolayer charge q_1 leads to a shift of the H desorption arrest in the long time-scale. This is depicted in Fig.3.6 taking q_1 in the range of 210 x 10^{-4} to 210 x 10^{-8} C cm^{-2}, where q_1 = 210 x 10^{-6} C cm^{-2} could be a typical value in the experiment, e.g. in relation to monolayer u.p.d H at Pt. Increase of q_1 causes the arrest to extend over a longer time range and it takes longer time for the potential to decay towards the equilibrium value (η = 0). The decay over the short time region, due to discharge of double-layer capacitance, is virtually unchanged with variation of q_1.

A possible application of this relation can be made to the interpretation of some experimental results. When the monolayer charge is less than 210 x 10^{-6} C cm^{-2}, for example in the case where a catalyst poison covers the catalyst surface (see Section 4.III.2), the arrest on the potential-relaxation curve becomes relatively small [195]. On the other hand, when the q_1 > 210 x 10^{-6} C cm^{-2}, as corresponds to the simulation of some of the experimental relaxation

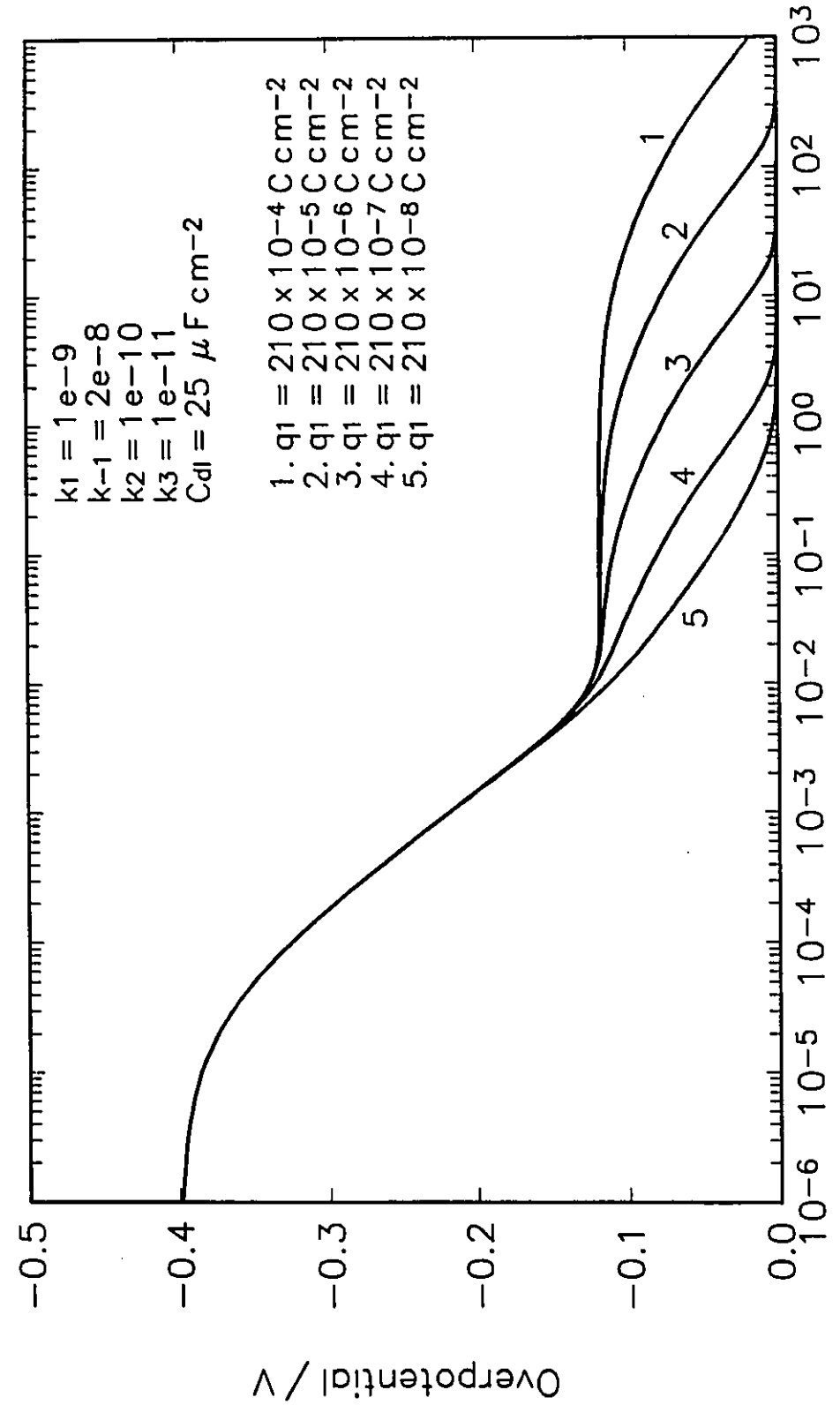

Fig.3.6 **Effect of changing q_1 value on calculated potential-relaxation transients. Parameters are shown in the Figure.**

transients, it can be attributed to the formation of metal hydride at the interphase [196] or a near-surface region of sorbed H in addition to an adsorbed H film *at* the surface.

3.3 Method of C_{dl} Measurement from Initial Potential Decay Rates in Transients

3.3.1 Basic Equations and Numerical Procedures

The *in situ* measurement of C_{dl} under the condition of immediate interruption of a significant Faradaic current passing through the interface is based on the recording and analysis of the potential-relaxation transient over *short time periods* after current interruption.

For an electrode process, the dependence of current-density, i, on overpotential, η, is represented in the usual way as (see also eqn.(1.8))

$$i(\eta) = i_0 \exp(\alpha\eta F/RT) \tag{3.12}$$

which is the Tafel equation in exponential form and where i_0 is the exchange current-density and α the transfer coefficient.

The potential-relaxation relation, $\eta(t)$, after interruption of current, $i_{t=0}$, is determined by

$$-C(d\eta/dt) = i(\eta) = i_0 \exp(\alpha\eta F/RT) \tag{3.13}$$

where C is the interfacial capacitance ($C=C_{dl}$, if C_ϕ is negligible or not involved). This equation originates from the early treatment of Armstrong and Butler [192] for the case $C = C_{dl}$, e.g. for the HER at Hg; when C includes an adsorption pseudocapacitance arising from potential dependence of coverage, θ, of an intermediate, and θ is appreciable (e.g. $0.1<\theta<1$), the interpretation of potential-relaxation transients becomes more complex than that treated in ref.[192], as examined in the paper of Harrington and Conway [15]. However, the presence of pseudocapacitance will not have influence on the C_{dl} determination in the present treatment, since the fitting of initial potential-relaxation involves only the potential response from the discharge

of the *double-layer capacitance* over the short time domain, e.g. 1 μs - 1 ms [90], as discussed in Section 3.2.1.

Integration of eqn.(3.13) (for the assumption of C being constant[3]) gives:

$$\eta(t) = a - b \log (t+\tau) \tag{3.14}$$

where

$$a = - b \log(2.3\, i_0/bC) \tag{3.15}$$

$$b = 2.3RT/\alpha F \tag{3.16}$$

and the integration constant, τ, is

$$\tau = bC/2.3\, i_{t=0} \tag{3.17}$$

From eqn.(3.13),

$$C_{dl} = i_{t=0}/(-d\eta/dt)_{t=0} \tag{3.18}$$

$i_{t=0}$ is measured experimentally at each potential for which current interruption is made. C_{dl}, corresponding to the interfacial capacitance at the overpotential, $\eta(t=0)$, at which the initial current is passing, can be calculated from eqn.(3.18) if the initial potential-relaxation slope $(-d\eta/dt)_{t=0}$ could be accurately evaluated; in the author's experience, this slope cannot be at all reliably obtained just by simply drawing a tangent to the η vs t curve "at" t=0.

It is possible, however, to proceed as follows by means of an extrapolation and curve-fitting procedure: differentiating eqn.(3.14) with respect to t, gives:

$$(-d\eta/dt)_{t=0} = -b/2.3\, \tau \; (\equiv -i_{t=0} / C) \tag{3.19}$$

Therefore, from the fitting of the initial region of a potential-relaxation curve, employing eqn.(3.14), the parameters a, b and τ can be reliably obtained, and $(-d\eta/dt)_{t=0}$ then calculated from eqn.(3.19).

This curve-fitting procedure has a number of advantages over other methods for

---

[3] It was found [85,101] that C_{dl} is, relatively speaking, a potential-independent quantity for the HER at Pt or Ni, although it is well known that C_{dl} may vary significantly with potential, especially around the potential of zero charge in dilute solutions, e.g. as at Hg.

evaluation of the apparent interfacial capacitance of the electrode, as follows:

(a) no assumptions need be made about reaction mechanisms;

(b) only the steady-state current-density before the opening of the circuit, together with the initial region of the potential-relaxation curve in digitized form, are required as the basic experimental data;

(c) the capacitance values that are obtained from eqn.(3.18) are those corresponding to the overpotentials arising at appreciable current-densities prior to interruption, i.e. C_{dl} can be measured *in situ* during passage of significant or appreciable electrolysis current;

(d) all the fitting parameters are obtained automatically by the computational procedure, i.e. no arbitrary estimations are needed; and

(e) the "IR" drop, when significant, is also automatically evaluated in a reliable way (see Section 2.2).

Thus, what we have dubbed as the "initial potential-relaxation" method involves the following steps: (a) digital recording of the potential-relaxation transient (η as a function of t data) after interruption of the polarization current, $i_{t=0}$; (b) fitting the η vs t data to eqn.(3.14) by means of a nonlinear, least squares fitting procedure (using "STATGRAPH" software) which gives the best values for the fitted constants a, b and τ for each recorded η(t) transient; (c) when the constants b and τ are thus obtained, the initial potential-relaxation slope can be calculated from eqn.(3.19) and then C_{dl} is derived using eqn.(3.18)

Fig.3.7 shows a set of η vs t relations calculated from eqn.(3.14). Parameters were taken arbitrarily as T = 300 K, C_{dl} = 25 μF cm^{-2}, exchange-current density $i_0 = 10^{-5}$ A cm^{-2} and α = 0.5. Other parameters were then calculated with a = -0.106, b = 0.119. τ varies with the

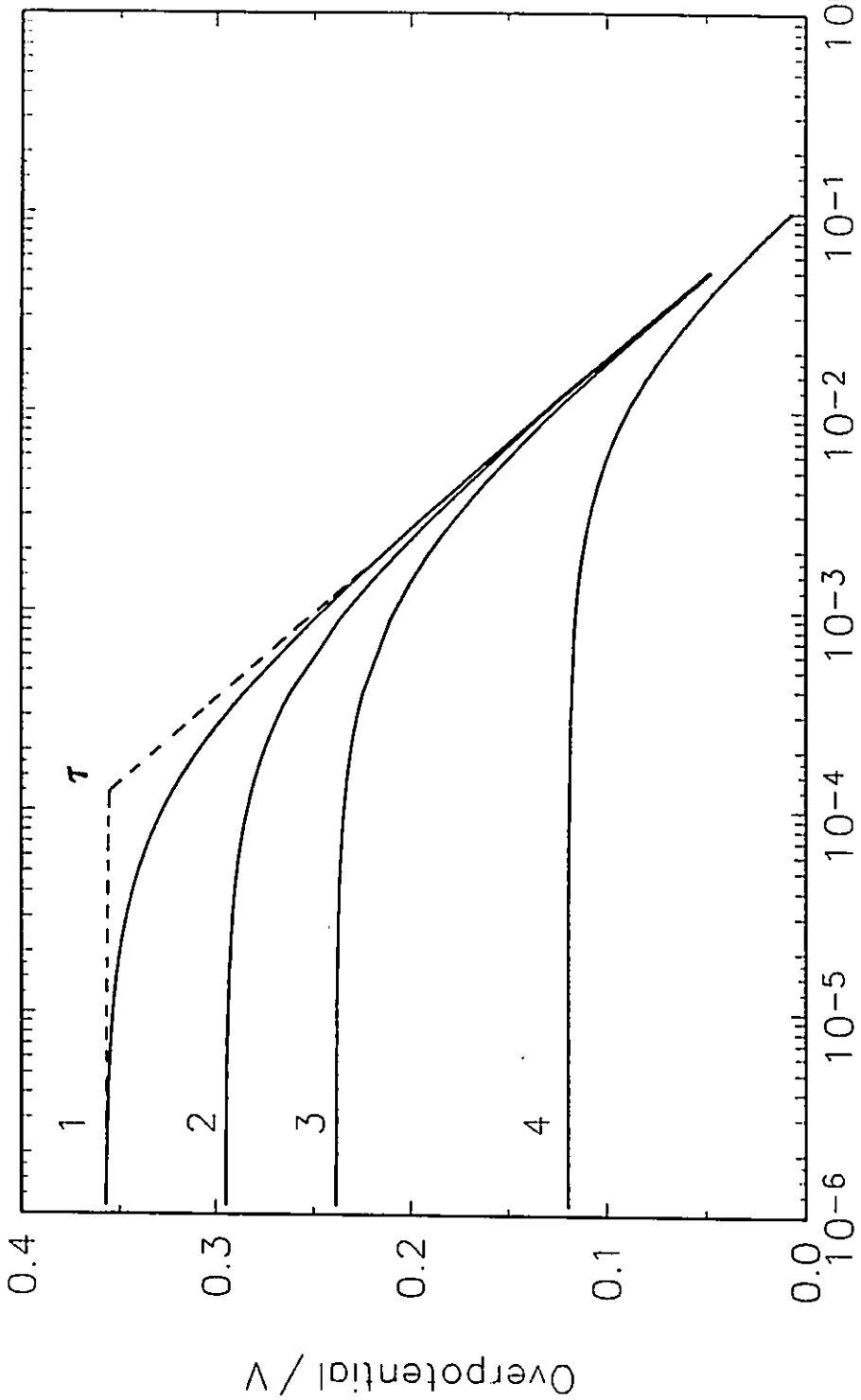

Fig.3.7 Initial potential-relaxation behaviour calculated from eqn.(3.14) $\eta(t) = a - b \log (t + \tau)$. $i_{t=0}$ are (1) 10^{-2}; (2) 3×10^{-3}; (3) 10^{-3} and (4) 10^{-4} A cm^{-2}, respectively.

initial current-density, $i_{t=0}$. In Fig.3.7, $i_{t=0}$ was selected for curves of 1) 10^{-2}; 2) 3×10^{-3}; 3) 10^{-3} and 4) 10^{-4} A cm^{-2} respectively. τ is proportional to the Tafel slope b, the double-layer capacitance C_{dl} and is inversely proportional to $i_{t=0}$. Therefore the larger the double-layer capacitance, the greater will be the value of the integration constant τ. This relation can be usefully applied also to porous electrodes for which the apparent C_{dl} values are usually very large due to high surface area; the τ value should then be expected to be large as well. τ increases also with decrease of initial current-densities, as shown in Fig.3.7.

The decay curves consist of two parts. For the range $t < \tau$, the overpotential remains almost constant, as it can be seen from eqn.(3.14) that the constant τ is then dominant in the log term and thus η is constant; when $t > \tau$, τ will become insignificant in the log term, so η will change linearly with log t having a slope of $-b$. These features can be clearly identified in Fig.3.7. Of course, the plots were obtained without consideration of the influence of pseudocapacitance in the theoretical calculation. Actually, even with the involvement of an adsorbed intermediate, the double-layer capacitance can still be distinguished easily and quantitatively (see below) from the pseudocapacitance as was shown in the theoretical treatment of potential-relaxation transients (Section 3.2.1). In the practical treatment, potential-relaxation data in the short-time range for fitting was carefully selected before the appearance of the arrest over the long time-scale, so that any influence of C_ϕ on the determination of C_{dl} was avoided.

3.3.2 Analysis Based on an Equivalent Circuit

The question arises whether the double-layer capacitance, C_{dl}, can be evaluated reliably when the pseudocapacitance, C_ϕ, associated with potential dependence of coverage by adsorbed H intermediate is significant or appreciable, i.e. when $C_\phi \gg C_{dl}$. This problem is particularly

important for the HER at Pt and Ni-Mo-Cd electrodes, since it was shown [72,101] that an appreciable potential-dependent C_ϕ for o.p.d H is involved in those cases.

While it was shown in section 3.2.1 how the kinetic analysis method can provide a quantitative basis for interpretation of relaxation transients, it is nevertheless useful also to apply the equivalent circuit concept to the analysis of experimental data since it can help in understanding the Faradaic process arising at the electrode surface. Equivalent circuits of the electrode interface are usually comprised of a double-layer capacitance, a Faradaic charge-transfer resistance, a capacitance related to the adsorption pseudocapacitance and also a Warburg impedance if diffusion is involved. Fig.3.8 shows the equivalent circuit, where C_1 represents C_{dl}, C_2 is related to, but not identical with (*cf.* refs. [15,189]), the pseudocapacitance, C_ϕ. R_1 represents the charge-transfer resistance and $R_1 + R_2$ is the overall Faradaic resistance.

In the impedance studies, the d.c. voltage is constant and the a.c. voltage modulation amplitude, E, is sufficiently small (normally $\pm$ 5 mV) so that the Faradaic resistances and pseudocapacitance can be taken as constant. Therefore, the equivalent circuit of Fig.3.8a is a valid representation of the behaviour of the HER at an assumed homogeneous surface. On the other hand, in the potential-relaxation experiments, the d.c. potential changes appreciably with time and then the Faradaic resistance and pseudocapacitance are/can be exponential functions of potential. Therefore the HER cannot then be represented by a single or unique equivalent circuit as shown in Fig.3.8a. However, in the present case, only the initial (t=0) situation is of interest. It is obvious that at $t \leq 0$, the potential is constant, since the steady-state was established before current interruption. Therefore, the equivalent circuit in Fig.3.8a can be used as a basis for evaluating the initial potential-decay slope, i.e. for $t \rightarrow 0$.

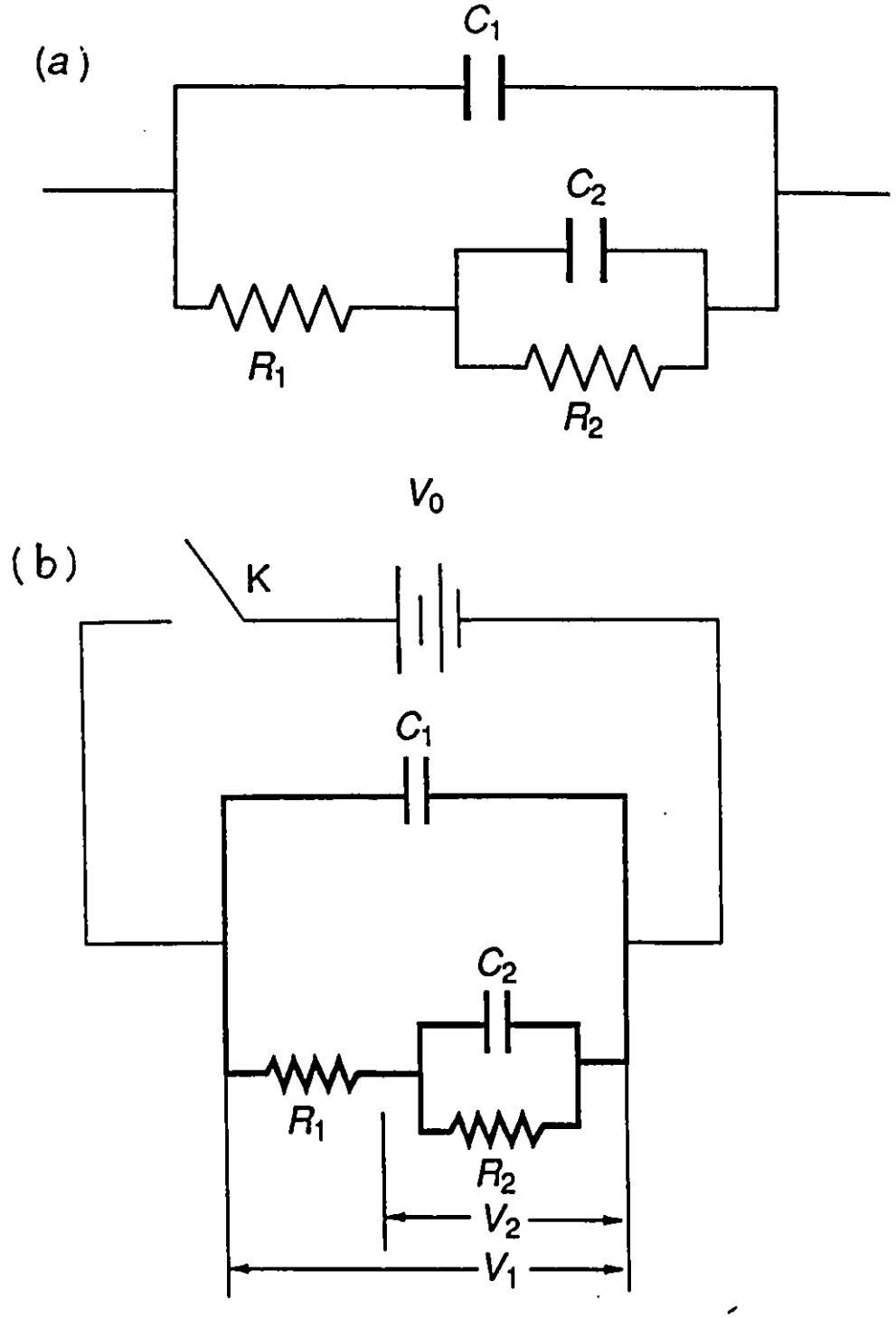

Fig.3.8 (a) Equivalent circuit representing an electrode interface, with only pure resistors (R) and capacitors (C) being involved.
(b) Equivalent circuit for open-circuit potential-relaxation analysis.

For the equivalent circuit shown in Fig.3.8b, the potential-relaxation behaviour after current interruption at switch K can be described by eqns.(3.20) and (3.21):

$$V_2/R_2 + C_2(-dV_2/dt) = (V_1 - V_2)/R_1 \tag{3.20}$$

$$- C_1(dV_1/dt) = (V_1 - V_2)/R_1 \tag{3.21}$$

where the voltages V_1 and V_2, defined in Fig.3.8b, are a function of time. The initial conditions for eqns.(3.20) and (3.21) are:

$$V_{1(t=0)} = V_0 \tag{3.22}$$

$$V_{2(t=0)} = V_0R_2/(R_1 + R_2) \tag{3.23}$$

Therefore at t = 0 (inserting eqns.(3.22) and (3.23) into (3.21)):

$$(dV_1/dt)_{t=0} = -V_0/(R_1 + R_2)C_1 \tag{3.24}$$

i.e. the initial potential-decay slope, $(dV_1/dt)_{t=0}$, is independent of C_2. In other words, the double-layer capacitance can be evaluated by means of the eqn.(3.18), separately from C_2, for a system involving significant pseudocapacitance provided that certain conditions, which will emerge later, are fulfilled.

In order to illustrate the potential-relaxation behaviour of the equivalent circuit in Fig.3.8, the following experiment was carried out: the circuit shown in Fig.3.8 was built up from hardware electronic elements and the potential-relaxation transients exhibited by the circuit were recorded by means of a digital oscilloscope. The results are shown in Fig.3.9. The values of the hardware elements which simulate the interfacial C and R functions gave the results shown in Fig.3.9 and were $R_1 = R_2 = 200\ \Omega$, $C_1 = 22\ \mu F$ ($\equiv C_{dl}$) and C_2 = (1) 2000, (2) 220, (3) 22 and (4) 0 μF respectively. V_0 was set at 0.81 V. It is clearly shown that the initial section (over 2.5 decades of time) of the four curves are coincident and thus independent on the value

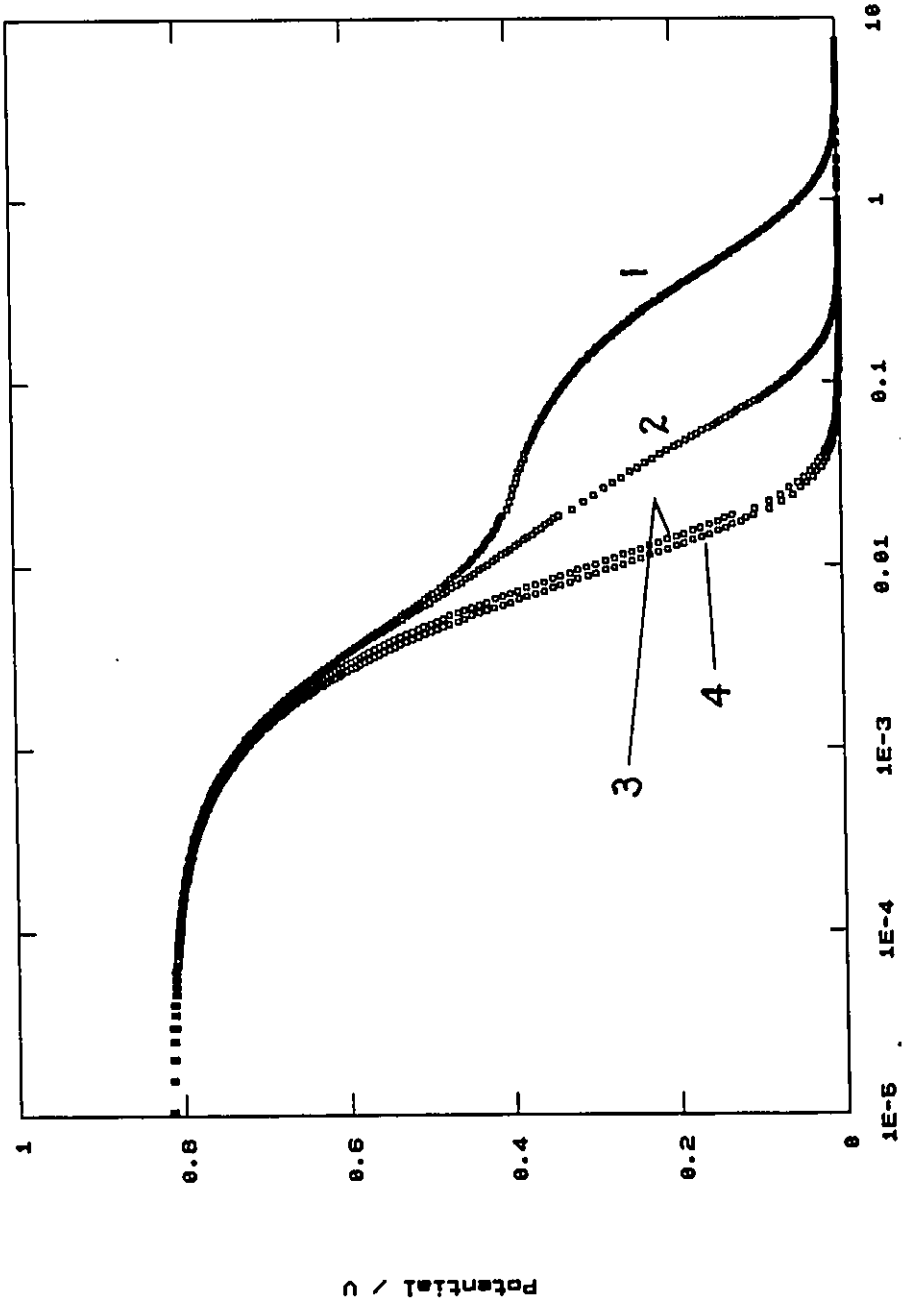

Fig.3.9 Potential-relaxation behaviour exhibited by a hardware circuit according to Fig.3.8a, taking $R_1 = R_2 = 200\ \Omega$, $C_1 = 22\ \mu F$ and $C_2 =$ (1) 2000 ; (2) 220, (3) 22 and (4) 0 μF. $V_0 = 0.81$ V.

of C_2 used. When C_2 is significantly larger than C_1 (see curve 1) a second plateau, corresponding to the discharge of C_2, appears in the longer time range ($t > 0.01$ s). The only difference of the hardware simulation experiment from reality is that both the R's and the C's can be potential dependent so the time-scales of the hardware circuit relaxation transients would be extended in reality. The main point, however, is validation of the principle that the C_{dl} ($\equiv C_1$) relaxation can be distinguished from that for C_ϕ ($\equiv C_2$) in the transients as it can in a.c. complex-plane plots over a frequency range.

3.3.3 Evaluation of C_{dl} from the Calculated Potential-Relaxation Transients

Some questions arise concerning the simulation of double-layer capacitance from initial potential-relaxation behaviour when the pseudocapacitance is significant. The accuracy in the determination of C_{dl} turns out to be dependent on the choice of time-scale in the transient curves. The selection of initial overpotential is also important, since it was found difficult to distinguish the C_{dl} and C_ϕ at *low* overpotentials [82].

Fig.3.10 shows "model" potential-relaxation curves calculated for five initial overpotentials: (1) 0.5; (2) 0.4; (3) 0.3; (4) 0.2 and (5) 0.05 V, taking $k_1 = 1 \times 10^{-9}$, $k_{-1} = 1 \times 10^{-8}$, $k_2 = 1 \times 10^{-10}$, $k_3 = 0$ (mol cm^{-2} s^{-1}), with $C_{dl} = 25\ \mu$F cm^{-2} and $q_1 = 210\ \mu$C cm^{-2}, $T = 298$ K and α being taken as 0.5, illustratively.

It is clear from Fig.3.10, that, in the short time domain, 10^{-8} to 10^{-2} s, it is only the double-layer capacitance that is discharged through the charge-transfer resistance while, over the longer time range, from 10^{-2} to 10^{1} s, discharge of the pseudocapacitance (corresponding to desorption of the ad-species) becomes dominant in the potential-relaxation transient. Since the value of C_ϕ is normally much larger than that of C_{dl} over a certain range of potential, it relaxes

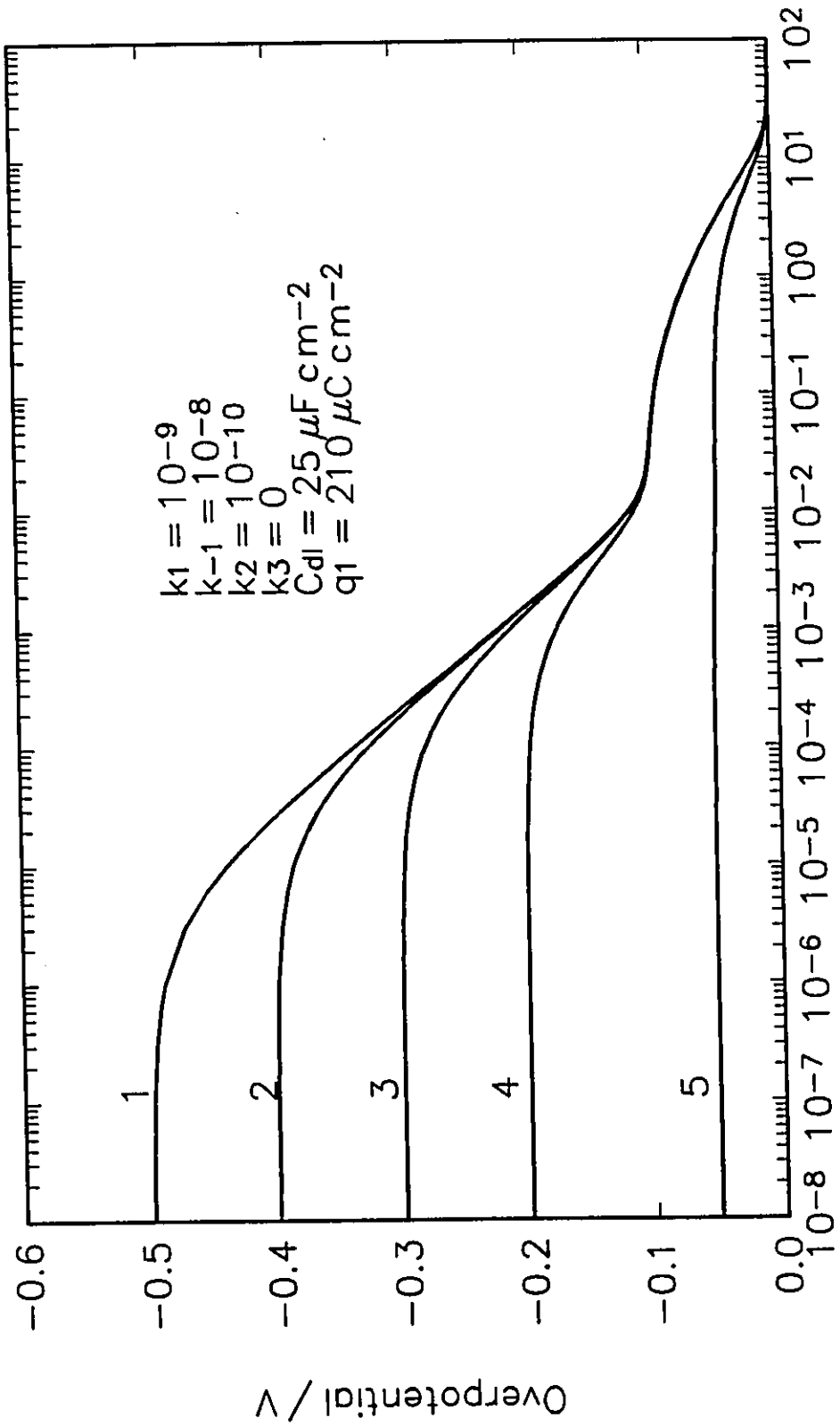

Fig.3.10 **Potential-relaxation behaviour calculated for five initial overpotentials. Parameters are shown in the Figure.**

over a much longer time-scale. Therefore, analysis of potential-relaxation curves over sufficiently short time ranges, where the influence of any pseudocapacitance is insignificant, will give only the double-layer capacitance, as concluded qualitatively in Section 3.3.1

Next, the curve-fitting procedure was applied to analyse, in the way described in Section 3.3.1, the theoretically calculated potential-relaxation curves shown in Fig.3.10, as a test of reliability of the proposed method for calculation of C_{dl}. The results are shown in Table 3.1. The initial currents, $i_{t=0}$, taken as the steady-state Faradaic currents, $i_f = v_1 + v_2$, were calculated by means of eqn.(3.2). The initial potential-relaxation slopes, $(d\eta/dt)_{t=0}$ and interfacial capacitance, $C_{t=0}$, were fitted using the procedure described in Section 3.3.1 to derive C_{dl} from the curves of Fig.3.10; the values of C_{dl} thus obtained are very close to the chosen C_{dl} = 25.0 μF cm^{-2} value which was the input reference datum for eqn.(3.6) used to generate the curves in Fig.3.10. Therefore, it is confirmed that the procedure described in Section 3.3.1 is quantitatively applicable and can provide accurate double-layer capacitance values *independent of any appreciable adsorption pseudocapacitance* associated with the electrode process.

Table 3.1 Test of procedures for treatment of initial potential-relaxation transients

η/V	$i_{t=0}$/A cm^{-2}	$-(d\eta/dt)_{t=0}$ / V s^{-1}	C_{dl}/μF cm^{-2}
0.5	2.980×10^{-1}	1.181×10^{4}	25.2
0.4	3.225×10^{-2}	1.686×10^{3}	25.2
0.3	6.063×10^{-3}	2.408×10^{2}	25.2
0.2	8.608×10^{-4}	3.427×10^{1}	25.1
0.05	2.024×10^{-5}	0.8121	23.9

Input values: C_{dl} = 25 μF cm^{-2}, q_1 = 210 μC cm^{-2}

Notice that at least eight parameters and two simultaneous differential equations were used to calculate the theoretical potential-relaxation curves in Fig.3.10, but only three parameters and the simple eqn.(3.14) were used to fit the initial curves. Note that the fitting of the potential relaxation curves at short times has no fundamental significance and the procedure is used only to provide an accurate evaluation of $(d\eta/dt)_{t=0}$ and the IR-free potential, $\eta_{t=0}$.

However, the accuracy of the fitted results depends on two factors: (a) how well eqn.(3.14) represents the initial potential-relaxation behaviour and (b) the choice of suitable ranges of the time-scale of the initial potential-relaxation data. With regard to (a), if the reaction has a linear Tafel relation, eqn.(3.14) should be valid for fitting the initial potential-relaxation data [see eqns.(3.12)-(3.14)]. For demonstrating the role of the second factor, selected ranges of the timescale for the potential-relaxation curves shown in Fig.3.10 and the corresponding fitted initial decay slopes, are listed in Table 3.2.

The "theoretical" initial decay slopes for the chosen input values are -1.818×10^4 and -0.8121 V s^{-1}, at $\eta = 0.5$ and 0.05 V, respectively. By inspecting the results from curve fitting on the potential-relaxation curves in Fig.3.10, it is obvious that the time on a log scale should be wide enough to give accurate fitting, but it should also cover short enough times that the later influence of the pseudocapacitance is avoided. For example, in Fig.3.10, it can be seen that the discharge of the pseudocapacitance begins to become significant only beyond 10^{-2} s. Hence, only when the potential-relaxation data are taken to the time 10^{-2} s or beyond for the initial decay slope analysis (10^{-7} - 10^{-2} s for 0.5 V and 10^{-6} - 7×10^{-3} s for 0.05 V), do significant errors arise (see Table 3.2). If low overpotentials are involved, e.g. 0.05 V in Fig.3.10, the pseudocapacitance starts to become discharged, so that the initial potential-relaxation region,

corresponding to discharge of C_{dl} through the Faradaic resistance, becomes too short for accurate curve fitting to be made (see Table 3.2). Therefore, potential-relaxation results for low initial overpotentials, where C_ϕ becomes significant [72,101], have to be treated more critically.

Table 3.2 Examples of evaluation of $(d\eta/dt)_{t=0}$ from quantitatively calculated model $\eta(t)$ transients

η/V	Time range / s	$-(d\eta/dt)_{t=0}$ / V s^{-1}	Relative error (%)
0.5	10^{-7} - 10^{-2}	1.2543×10^4	6.2
	10^{-7} - 10^{-3}	1.181×10^4	0 (± 0.1)
	10^{-7} - 10^{-4}	1.181×10^4	0 (± 0.1)
	10^{-7} - 10^{-5}	1.179×10^4	-0.17
	10^{-5} - 10^{-3}	1.188×10^4	0.59
	10^{-4} - 10^{-3}	1.301×10^4	10
0.05	10^{-6} - 7 x 10^{-3}	0.9343	18
	10^{-6} -1.6 x 10^{-3}	0.8121	2.6

CHAPTER IV

RESULTS AND DISCUSSION

Introduction

In this chapter, attention will be given to the analysis of experimental results derived from measurements mainly on the kinetic and o.p.d. H behaviour in the HER (and also u.p.d. H behaviour in several cases) at some electrocatalytic materials in melts and alkaline solutions. There were three types of experimental research carried out in the present work:

1) The electrocatalytic performance of the composite Ni-Mo-Cd material was studied as the cathode for the HER comparatively in $KF \cdot 2HF$ and $KOH \cdot 2H_2O$ melts. The catalytic behaviours of the electrode were characterized by Tafel measurements from which the exchange current-densities and Tafel slopes could be obtained. Complementary electrochemical methods, i.e. potential-relaxation transient and a.c. impedance measurements, as described previously, were applied to the Ni-Mo-Cd cathode material for the purpose of obtaining necessary information about the kinetics and adsorption behaviour of the o.p.d. H intermediate at this electrode, a practical high-performance cathode for H_2 evolution. A smooth Ni-Mo bulk composite alloy was also investigated for comparison with the performance of the porous Ni-Mo-Cd material. These materials comprise the work of Part I.

2) In Part II, a new method was developed for the *in situ* determination of real surface areas by the method of analysis of initial potential-relaxation transients giving C_{dl} values. It is often of practical importance to determine the real, effective area of porous catalysts, especially for the situation when there is substantial Faradaic current passing across the interface, and with

the presence of pseudocapacitance associated with the adsorbed intermediates involved at gas-evolving electrodes, e.g. the HER in this case. Several electrodes in various solution or melt media were examined. The cyclic voltammetry (CV) technique was also used in the measurement of real surface area based on the evaluation of monolayer u.p.d. H charge at Pt electrodes. With regard to its electrochemical accessibility, it was shown that a rough or shallow-pore electrode surface can be 'unfolded' experimentally by increasing the electrolyte conductivity, i.e. simplifying the transmission-line model by diminishing the distributed electrolyte resistance, as is demonstrated from a.c. impedance and potential-relaxation data in the present work.

3) The content of Part III includes discussion of poison effects on the adsorption behaviour and the electrode kinetics of the HER. Theoretical calculation was developed based on modified rate equations involving poison coverage, θ_P, and a lateral interaction factor, g. Potential-relaxation results were analysed by means of numerical simulation, and the state of the coverage by both poisons and the H intermediate was revealed from the rate constant values required for simulation of the transients. Two kinds of poison species, thiourea and arsenic oxide, were employed in the experimental kinetic and poisoning studies.

Part I. Electrocatalytic Performance of Ni-Mo Based Cathode Materials in the Melts

4.I.1 Origin of The "Hyperpolarization Effect" in the HER at Mild-Steel Cathodes in KF·2HF Melts

The operation of electrolytic F_2 production is accompanied not only by a remarkably large overvoltage at the anode [1] (a well known effect) but also, as we have found here, by appreciable analogous overvoltage effects at the cathode. This large cathodic overvoltage can

rise to 6 V or even higher (depending on the potentiostat or power supply) under certain operating conditions and lead to the failure of the cell operation. The development of anomalous high cathodic overvoltage is referred to here as the "hyperpolarization effect" but is quite different in origin from a corresponding behaviour at carbon anodes which has been referred to as the "anode effect". The latter has been the subject of considerable previous research [198-200] including earlier contributions [1-3] from this laboratory.

Many studies have been carried out on the F_2 evolution reaction at carbon anodes, especially on the so-called "anode effect" [198-200], referred to above, but relatively little work, if any, has been done previously on the cathodic effect; only a brief mention of such effects is to be found in ref.[176]

Determination of the origin of the hyperpolarization effect at mild-steel cathodes in F_2-production cells is practically important with regard to electric energy consumption and optimization of cell operation, and is also of substantial fundamental and theoretical interest, as will be apparent from the results described below.

The origin of the unusual cathode hyperpolarization has been studied in this lab [4] in some detail and some new understanding of the phenomenon has been gained. Experimental studies showed that the hyperpolarization sets in at high overpotentials; however, it could be substantially modified by electrode rotation. The hyperpolarization effect was decreased with increase of electrode rotation rate and the effect was partly "reversible", i.e. hyperpolarization increased again upon decrease or diminution of rotation rate. The test of the effect of HF content in the melt and the melt temperature on the hyperpolarization further proved that the mass-transport limitation was due to HF reactant starvation at the electrode surface on the inner

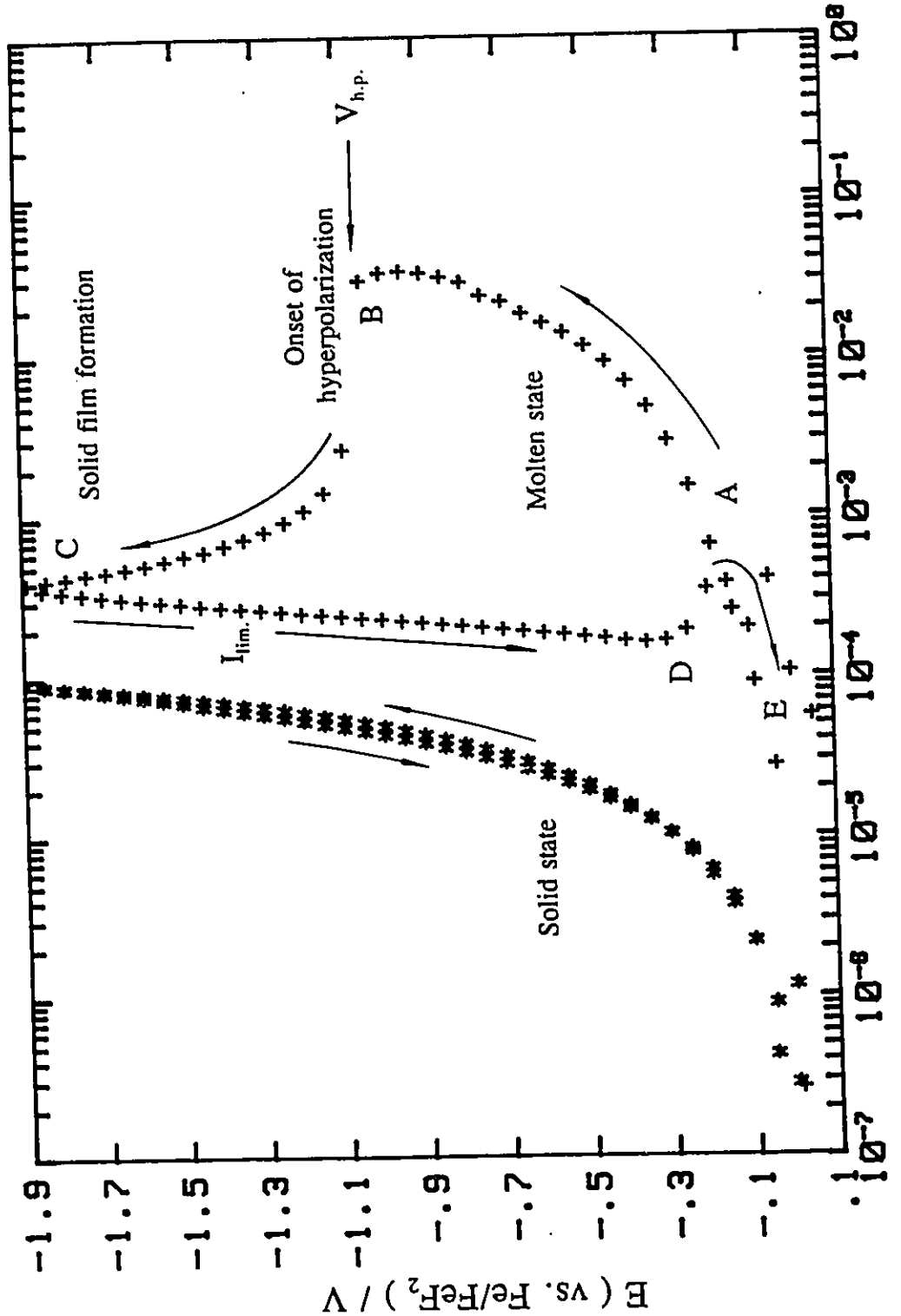

Fig.4.I.1 The hyperpolarization behaviour at a mild-steel electrode in molten (+) and solid (*) $KF \cdot 2HF$ melt near its melting point.

side of the diffusion-layer. A computer-simulation made theoretically on the basis of the Fick's diffusion laws by Qian in this lab gave excellent agreement with the experimental polarization curve for the "hyperpolarized" electrode.

The overall polarization behaviour is shown in Fig.4.I.1; the processes which are believed to be involved are listed in a summary way as follows:

a) at low current-densities, the HF content has no appreciable effect on the polarization behaviour; HF can be sufficiently rapidly transported by diffusion to the electrode interphase to meet the consumption rate corresponding to low current-density electrolysis;

b) at a critical current-density (the critical value for onset of hyperpolarization), no further increase of i with V arises;

c) beyond this point (b), i *decreases* with time and potential towards a limiting current-density, substantially less than the earlier i for the onset of hyperpolarization;

d) upon a following decrease of potential, a more or less constant limiting i is maintained until, at low enough V ;

e) some reactivation of the H_2 evolution process takes place due, it is supposed, to the re-melting of a solid KF·HF film with return to normal HF supply conditions. Then, at further, lower V's and correspondingly diminished i's ;

f) normal Tafel log i vs V behaviour is again observed and the behaviour returns to that in (a).

In conclusion, the hyperpolarization behaviour observed in cathodic H_2 evolution from KF·2HF melts arises on account of mass-transport limitation associated with HF consumption. The suddenness and "irreversibility" of the onset of the hyperpolarization effect is directly

related to HF starvation in the diffusion-layer at high current-densities which, in turn, leads to a more significant effect, the local solidification of the electrolyte in a thin film at the electrode interface with consequent development locally of an high ohmic resistance at the mild-steel cathode surface.

With increase of ten perature, both the onset currents and the subsequent limiting currents are found to increase appreciably. The temperature effect can be clearly related to the phase diagram (Fig.2.6) for the solidus/liquidus boundary in the KF·2HF or KF·xHF system, which determines the melting points of various compositions of the melt around the "KF·2HF" composition.

The results suggest that regular addition of KF·2HF or, better, HF itself, to compensate the consumption of HF, or some forced circulation of the melt in industrial cells, in addition to that caused by adventitious bubble stirring and magneto-hydrodynamic effects, may be advantageous in preventing periodic onset of hyperpolarization in operating F_2-production cells.

4.I.2 The HER Behaviour of Ni-Mo-Cd Materials in the KF·2HF and KOH·2H$_2$O melts

4.I.2.1 Tafel Relation Measurements

The choice of composite materials directed towards improvement of catalytic cathode behaviour is determined by their electronic and surface structures. The properties of single-element metals have been well systematized and studied in various previous works [27,36], as discussed in Chapter I. It was proposed that a combination of two metals from the two branches of the volcano curve (see Fig.1.2) could result in enhanced activity [50]. Jaksic reported [51,52] that a combination of Ni from the left branch with Mo from right-hand branch of the volcano curve (Fig.1.2) can result in a substantial enhancement of activity for the HER. The addition

of a small atomic fraction of Cd in the electrodeposited composite of Ni and Mo has also been found to give improved electrocatalytic performance for the HER, as was reported in ref.[168]

Alternative materials, especially porous ones, with high real/apparent surface area ratios much larger (ca. ~2 orders of magnitude) than that at mild-steel were selected as new electrocatalytic cathodes for F_2-production cells on a laboratory scale. Electrodeposited Ni-Mo-Cd electrocatalysts show favourable features as cathodes for the HER in alkaline solution [5]. The polarization performance of such electrodes is usually characterized by the exchange current-densities, i_0, and Tafel slope, b, parameters. The Tafel plot for the Ni-Mo-Cd H_2 cathode from ref.[5] gives a Tafel slope of 30 mV at low overpotentials at 368 K. This polarization behaviour is apparently much superior to that of other materials such as smooth Ni and Ni-based alloy electrodes. It was believed that the presence of cathodically-formed hydride phases could be an important, if not essential, condition for low overpotential behaviour of Ni-Mo-Cd cathodes.

In relation to the origin of this project, i.e. evaluation of electrolytic processes in the KF·2HF melt, it was of interest to investigate the electrocatalytic properties of the Ni-Mo-Cd electrode (of composition given in Section 2.1.1.1) as an H_2 cathode in the melt at 85°C. The procedure for electrode plating was based on a U.S. patent [168] as already described in Section 2.1.1 where the resulting porous, "cauliflower-like" surface appearance of the deposit can be seen in the SEM pictures. The electrode was prepared by plating the composite on the conical mild-steel substrate, so that it could be used as a rotating electrode assisting the detachment of H_2 bubbles generated during polarization.

Tafel measurements were conducted on the Ni-Mo-Cd electrode in the KF·2HF melt at

85°C. The results were compared with those at the mild-steel electrode and plotted on the same graph (Fig.4.I.2). The computer-controlled procedures for the Tafel measurements have already been described in Section 2.4.1. The plus (+) points data are for the Ni-Mo-Cd and circle (o) points for the smooth mild-steel electrode. The electrodes were rotated at 2000 rpm to assist the detachment of H_2 bubbles. The "IR" drops between the working and reference electrodes were measured by recording the initial potential-relaxation following current interruption (Section 2.2), and correction has already been made in the Tafel plots shown in Fig.4.I.2.

First, it can be seen that the current-density at a given potential on the porous Ni-Mo-Cd electrode is about two magnitudes larger than that at the smooth mild-steel electrode. This is a desired and major improvement in cathodic polarization in the HER. One of the principal contributions to the enhanced catalytic performance could arise from the large real surface area per projected cm^2 of the porous composite Ni-Mo-Cd electrode. Factors of electronic and surface structure, related to the exchange current-density, might also be reasons when the influence of the surface area factor is taken into account.

Secondly, at the Ni-Mo-Cd electrode, a small Tafel slope arises over the low overpotential region (η within 50 mV of the reversible potential) with b = 37 mV/decade which is in good agreement with the result in ref.[5]. However, an higher slope, b = 148 mV/decade, is also displayed over the higher overpotential range. This value is, however, not the one that was usually observed in Tafel plots, e.g. 120 mV or 180 mV. However, if the temperature effect is considered, here T = 358 K, the Tafel slope does not necessarily have the "typical" values, since b is also the function of temperature. Thus, it is easily calculated from the relation of $b = 2.3RT/\beta F$ that b should be equal to 142 mV at T = 358 K rather than the corresponding

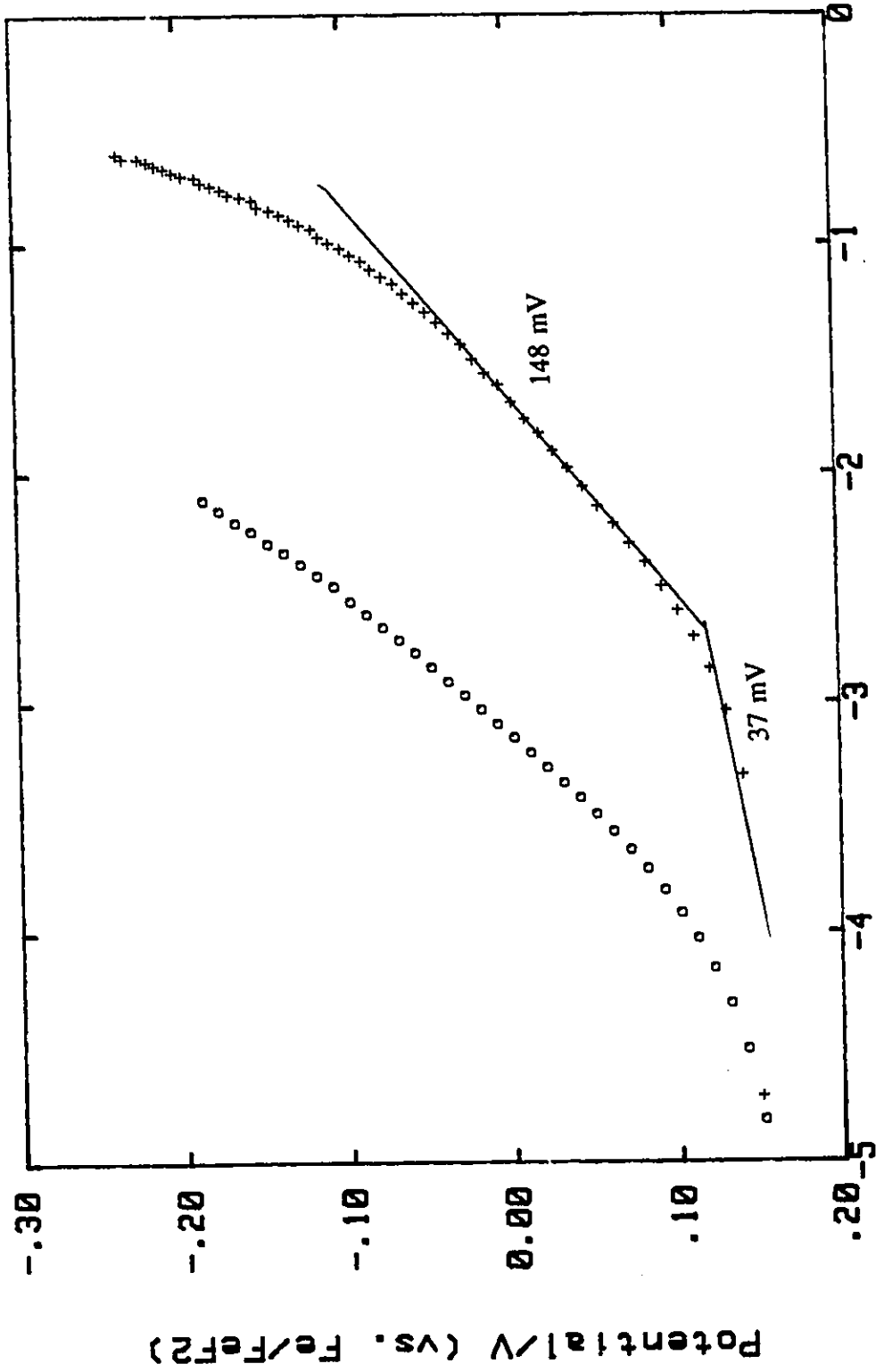

Fig.4.I.2 Tafel plots for the HER at the mild-steel electrode (o) and porous Ni-Mo-Cd electrode (+) in the KF·2HF melt at 85°C.

120 mV value at 300 K if β is taken as 0.5. In this sense, the experimentally observed Tafel slope is consistent with the conventionally expected result for a discharge-controlled step. Much higher Tafel slope values above a potential of -0.1 V were observed, as in Fig.4.I.2.

The Tafel behaviour over the high overpotential range could be due to complications arising in this special system involving a porous electrode surface coupled with the high surface tension of the KF·2HF melt [176]. Also H_2 bubbles generated in the cathodic polarization are not easily removed and the pores of the electrode could become filled with H_2 gas. Therefore, distribution of the current-density at the surface within pores would not be able to be controlled or governed in the expected way by the Tafel law. During the process of growth of the bubbles, the current would tend to become decreased by the impedance of the increasing gas space at the porous electrode surface. Values of "IR" drop in this situation would then be different from those existing at lower potentials, and these varied (probably increased) values of "IR" drop would probably be the major cause of the above behaviour observed at high overpotentials.

Note that a current-density of ca. 200 mA cm^{-2} can be reached at Ni-Mo-Cd electrode at -0.2 V (or η = -0.37 V, taking the equilibrium potential, V_0 as 0.17 V vs Fe/FeF_2), while for the smooth mild-steel electrode only 10 mA cm^{-2} can be achieved at the same potential. The Ni-Mo-Cd cathode thus provides promising performance for energy saving in practical applications of electrolysis, based on its electrocatalytic behaviour shown in Fig.4.I.2. If its corrosion behaviour in this melt could be examined with favourable results, the application of this material to the industrial operating cell would be attractive. Such corrosion behaviour, in fact, has been studied as part of the present project and is described in Section 4.I.3.

The Tafel behaviour of the Ni-Mo-Cd electrode was also examined (Fig.4.I.3) under

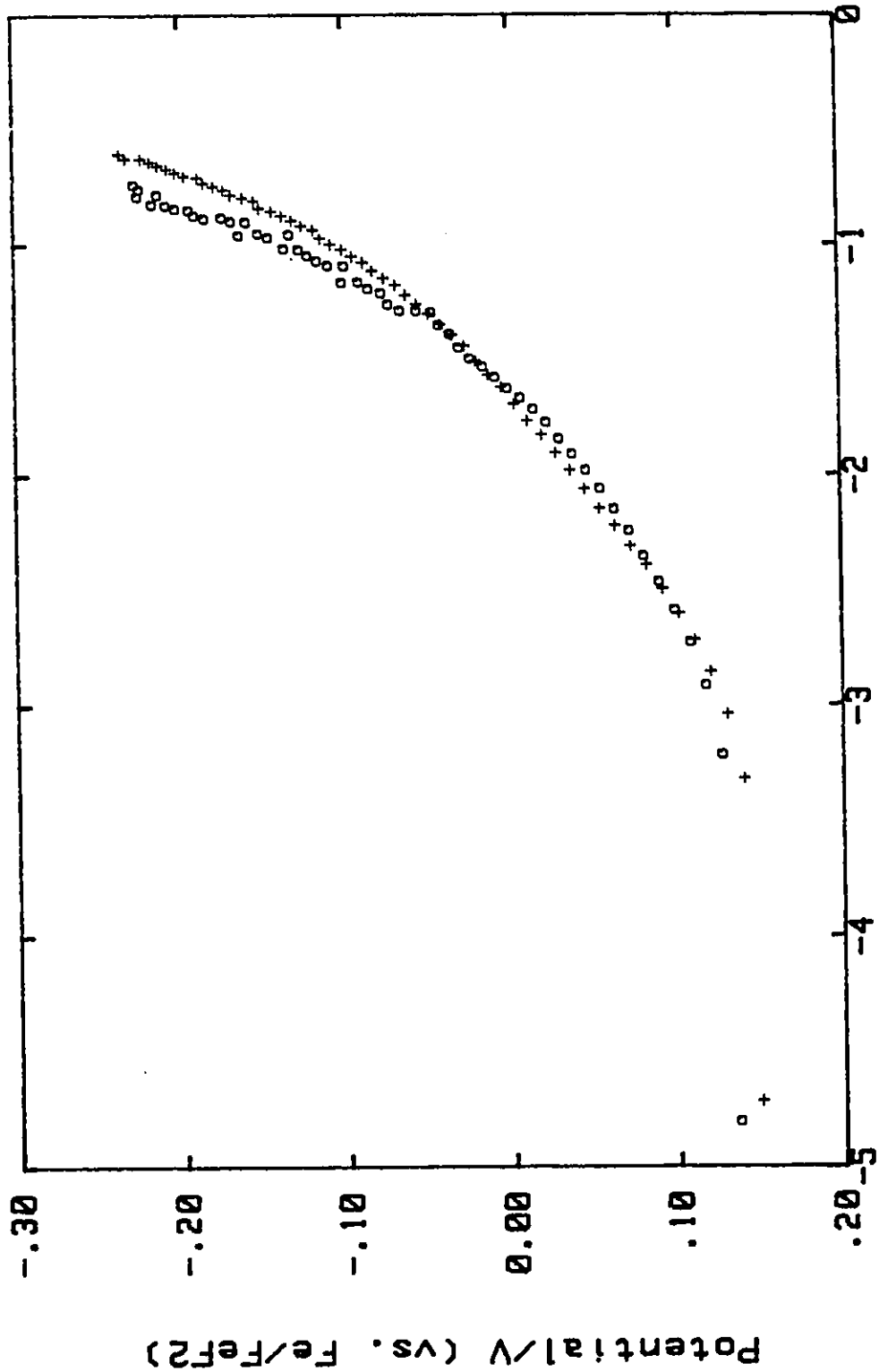

Fig.4.1.3 Rotation effect of the Ni-Mo-Cd electrode on the Tafel behaviour of the HER in the KF·2HF melt. (o) points are for stationary and (+) points for 2000 r.p.m. rotation rate.

stationary conditions, i.e. without rotation (o points), and compared with that with rotation (+ points) of the electrode. It can be seen that rotation *did* slightly improve the polarization, giving some increase of current-density at given potentials. The data points for the stationary electrode were a little scattered due to the irregular H_2 bubble growth and detachment, while for the rotating electrode, the "points" curve was rather smooth.

Study of the chemically analogous hydrate melt[1], $KOH \cdot 2H_2O$, was carried out for the first time in the present work. The objective was to make comparison of the electrochemical behaviour of these two melts in which the melt anion F^- is substituted by its analogue, OH^- ion in the "H_2O" system, while the $KOH \cdot 2H_2O$ melt could also be considered as a concentrated aqueous alkaline solution (ca. 28 M, without taking account of the activities of H_2O and OH^-). Thus, $KOH \cdot 2H_2O$ can be treated as an intermediate system between the $KF \cdot 2HF$ melt and a dilute aqueous KOH solution so that the catalytic behaviours of the Ni-Mo-Cd material for the HER could be comparatively evaluated in the above media. Note that the primary discharge step in the HER from HF will be $M + 2HF + e \rightarrow MH + FHF^-$, corresponding to the reaction $M + 2H_2O + e \rightarrow MH + OH^-(H_2O)$ in the aquo melt.

Fig.4.I.4 shows comparatively the Tafel plots for the Ni-Mo-Cd electrode in the $KF \cdot 2HF$ melt (+ points) and the $KOH \cdot 2H_2O$ hydrate melt (* points) at 85°C. It is interesting to note that the cathodic current-densities in the $KOH \cdot 2H_2O$ melt are ca. 1 or 2 magnitudes *larger* than those in the $KF \cdot 2HF$ melt at corresponding operating overpotentials. The two curves are plotted on the same y-axis scale of overpotential using calibrated equilibrium potentials calculated from

---

[1] In the aquo-system, the chemical analogue of $KF \cdot 2HF$, in the HF-system, is $KOH \cdot 2H_2O$. Each is a di-solvate of the respective salt of the solvent anion, F^- or OH^-, and both can be regarded as low temperature "melts".

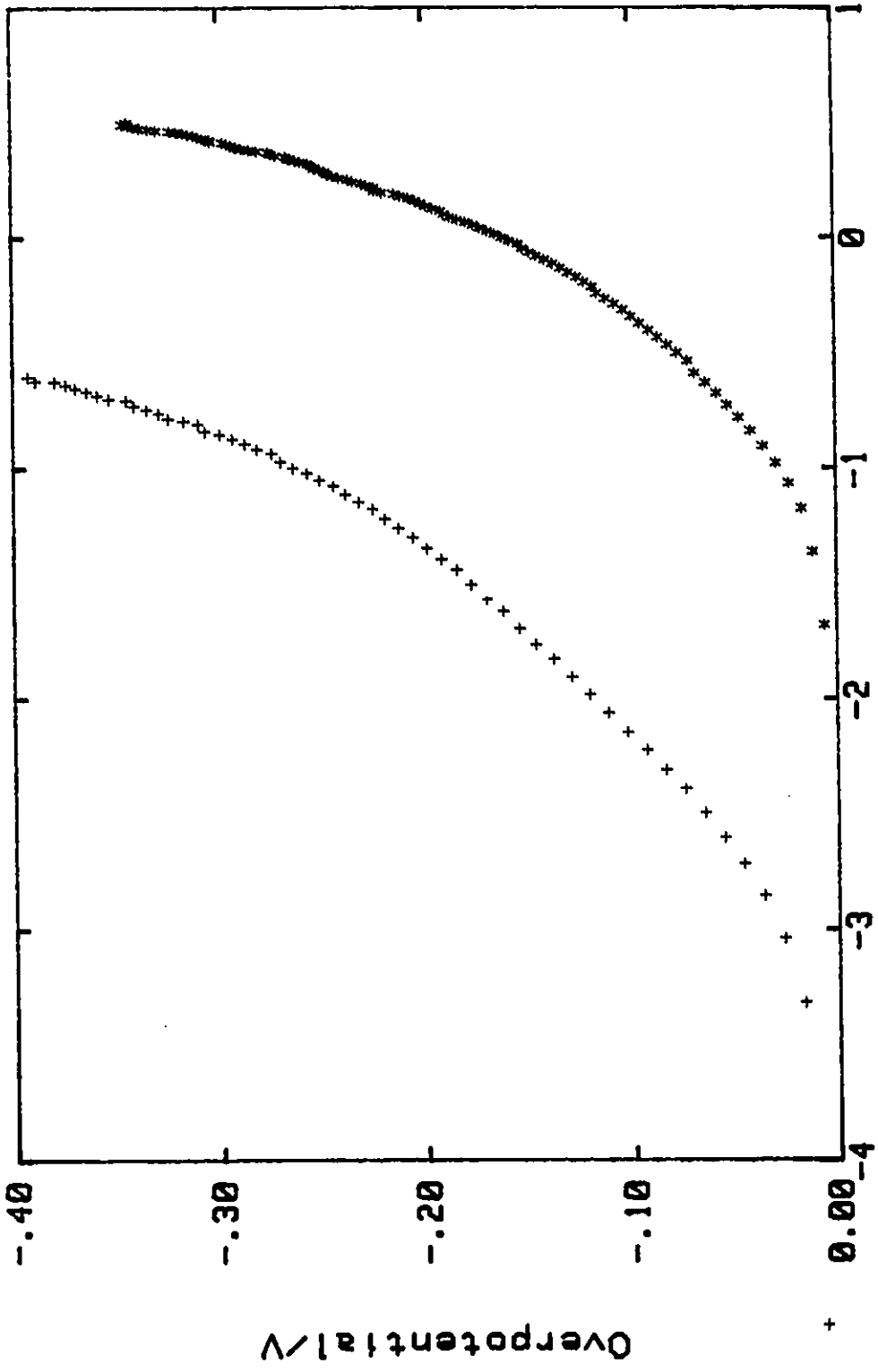

Fig.4.I.4 Tafel plots for the HER at the Ni-Mo-Cd electrode in the KF·2HF (+++ points) and KOH·2H_2O (*** points) melts.

potentials referred to different reference electrodes (see Section 2.1.1.5; reference Fe/FeF_2 for the $KF \cdot 2HF$ melt and reference Hg/HgO for the $KOH \cdot 2H_2O$ melt). In the polarization of Ni-Mo-Cd in the $KOH \cdot 2H_2O$ hydrate melt in Fig.4.I.4, the maximum current-density that could be reached was ca. 3 A cm^{-2} which was much larger than what could be obtained (200 mA cm^{-2}) in the $KF \cdot 2HF$ melt, independent of differences of IR corrections for the two systems.

In the electrochemical HER, the reactant, as HF, solvates the K^+ and F^- ions (the latter as FHF^-) in $KF \cdot 2HF$ and H_2O solvates the K^+ and OH^- ions in the $KOH \cdot 2H_2O$ melt, respectively. From well known general chemistry, it should be more difficult to discharge H from HF than H_2O (other things being equal) due to the greater electronegativity of F than O. Also the inter-molecular H-bonds in H-F$\cdot\cdot$H are very strong. Therefore more driving force, or overpotential would be expected to be required to overcome the activation energy in the process of proton discharge from HF than from H_2O.

Another important factor should also be considered, that is the accessibility of the electrode by the two electrolytes due to different wettabilities of, or contact angles of, the melts to the electrodes. Since the Ni-Mo-Cd electrode has a rough, porous surface, the inside pores are hard to be accessed by the electrolyte or melt having high surface tension [176]. The less accessible real surface area of the Ni-Mo-Cd material in the $KF \cdot 2HF$ melt was examined by the determination of C_{dl} from the initial potential-relaxation experiments. The resulting data will be described in Section 4.II.2, but it can be stated here that the real surface of the Ni-Mo-Cd electrode, determined *in situ*, evaluated in the $KOH \cdot 2H_2O$ melt for H_2 evolution was about two magnitudes larger than the value measured in the $KF \cdot 2HF$ melt. This result is in good consistency with the differing Tafel plot results shown in Fig.4.I.4.

These results indicate that the inside pores of the porous Ni-Mo-Cd electrode cannot be fully wetted by the KF·2HF melt which has high surface tension and high contact angle with gas bubbles (see Section 4.I.2.3). Therefore, the important conclusion can be reached that the porosity of an electrode material is not an intrinsic property of a given electrode for an electrochemical reaction, but strongly depends on the accessibility and conductivity (see Section 4.II.3) of the electrolyte solution in the pores.

The Tafel behaviour of a smooth, bulk, single-phase, Ni-Mo alloy electrode (o points) was also examined and compared with the corresponding behaviour at the electrodeposited Ni-Mo-Cd electrode (+ points) in the KF·2HF melt, as shown in Fig.4.I.5. The Ni-Mo electrode exhibits a small Tafel slope (46 mV) at low overpotentials but a very large (> 500 mV) slope over the high overpotential range in this melt. The large difference of current-densities at corresponding potentials, between the two electrodes, was similar to the conclusion made from the comparative plots at smooth mild-steel and porous Ni-Mo-Cd electrodes in Fig.4.I.2. The main contribution to that difference was the large real surface area of the porous Ni-Mo-Cd electrode, which enabled larger current-densities (current/apparent area) to be realized than those at the smooth Ni-Mo electrode at the same polarization potential.

4.I.2.2 Corrosion Behaviour of the Ni-Mo-Cd Material in the KF·2HF Melt

The Ni-Mo-Cd material has been examined for its favourable catalytic properties as an H_2 cathode, as described above. In order to be applied in the industrial F_2 production cells, it has to be examined for its corrosion resistivity or durability in the KF·2HF melt at 85°C. The corrosion current-density, i_{corr}, which determines the practical behaviour or stability of the Ni-Mo-Cd electrode under open-circuit conditions, in the KF·2HF melt in this case, is of interest

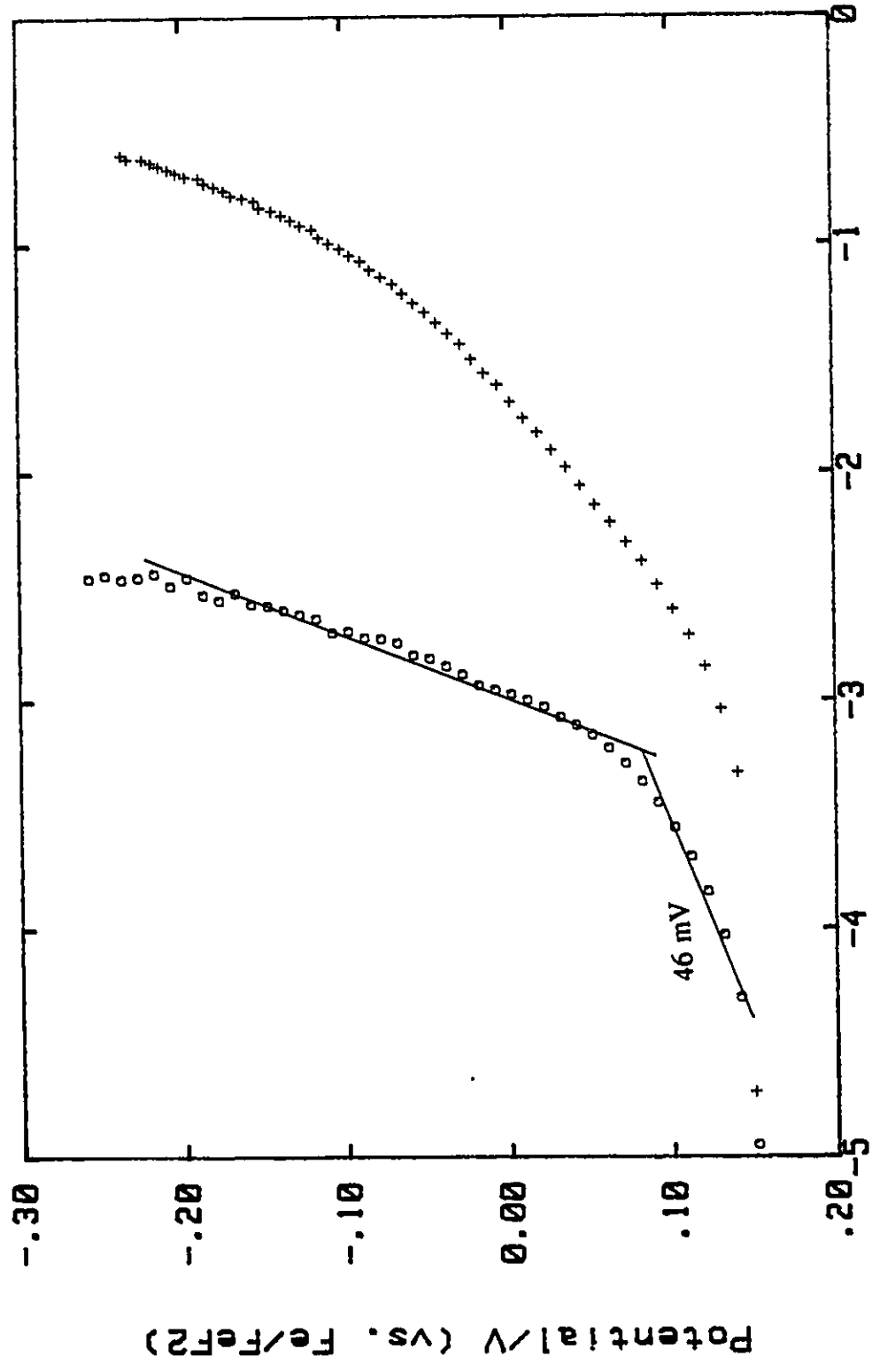

Fig.4.1.5 Comparison of Tafel behaviours for the HER at the smooth Ni-Mo ((o) points) and the porous Ni-Mo-Cd ((+) points) electrodes in the KF·2HF melt.

and practical importance.

Generally, when a metal is immersed in a melt or electrolyte solution, two processes occur simultaneously at the metal/electrolyte interface. One is anodic metal dissolution, or oxide or salt film formation:

$$M \rightharpoonup M^{n+} + ne \qquad (4.I.1)$$

the other is cathodic discharge of H_2O or HF:

$$2HF + 2e \rightharpoonup H_2 + 2F^- \text{ (as 2 } FHF^- \text{ ion)} \qquad (4.I.2)$$

The cathodic reaction could also be the reduction of any dissolved oxygen, but in this melt environment, process (4.I.2) is more probable, as virtually no O_2 is present. Under equilibrium conditions, where the corrosion potential lies between the equilibrium potentials of the anodic and cathodic processes, respectively, there will be zero *net* current at the corroding metal electrode [201], i.e.

$$\Sigma I_a = - \Sigma I_c \qquad (4.I.3)$$

where I_a and I_c are total anodic and cathodic currents respectively. For an heterogeneous surface of a metal, for example, the alloy electrode, the overall corrosion is comprised of superimposed corrosion processes on each of the homogenous elements of the polycrystalline metal surface, leading to the overall average corrosion rate of the entire surface. The anodic dissolution or film formation may involve parallel processes involving one or other, or several of the metal components of the alloy. Their corrosion behaviour depends not only on the thermodynamic tendency for reaction but also importantly the kinetics of the mixed process reactions. The contributions of these processes may be different; however, one of them could be the dominant process. In the present experiments, however, the entire current was recorded and divided by

the apparent surface area in order to obtain the overall average corrosion parameters.

At the corrosion potential V^*

$$i_a = -i_c = i_{corr} \tag{4.I.4}$$

Then, substituting the Butler-Volmer equation for each reaction,

$$i_{0a}\exp[\frac{\beta_{aa}F}{RT}(V^* - V_a^0)] - i_{0a}\exp[\frac{-\beta_{ac}F}{RT}(V^* - V_a^0)]$$

$$= i_{0c}\exp[\frac{\beta_{ca}F}{RT}(V^* - V_c^0)] - i_{0c}\exp[\frac{-\beta_{cc}F}{RT}(V^* - V_c^0)] \tag{4.I.5}$$

The potential, V^*, is the ("mixed") corrosion potential, and it lies between V_a^0 and V_c^0. When the equilibrium potentials for the two reactions are widely separated, the back reaction for either or both reactions may be negligible; then

$$i_{corr} = i_{0a}\exp[\frac{\beta_{aa}F}{RT}(V^* - V_a^0)] = i_{0c}\exp[\frac{-\beta_{cc}F}{RT}(V^* - V_c^0)] \tag{4.I.6}$$

The net current-density for change of potential above or below the corrosion potential is

$$i_T = i_a + i_c = i_{corr}\exp[\frac{\beta_{aa}F}{RT}(V - V^*)] - i_{corr}\exp[\frac{-\beta_{cc}F}{RT}(V - V^*)] \tag{4.I.7}$$

This equation resembles the Butler-Volmer equation for a single reaction, but the corrosion potential and corrosion current-density have replaced the equilibrium potential and the exchange current-density, respectively. The primary justification for writing the equation in this form is to describe the corrosion kinetics concisely. It is not meant to suggest that the corrosion potential is characteristic of a thermodynamic or reference state; the mixed corrosion condition may, in fact, be unstable if the rates of the participating reactions vary with time as often occurs especially when film formation arises.

The corrosion current-density can be determined by two methods: extrapolation of Tafel

or linear polarization measurements. From eqn.(4.I.7), the value of the cathodic Tafel slope is given by

$$d(V - V^*) / d \log i = 2.303\ RT/\beta_{cc}F \qquad (4.I.8)$$

and that of the anodic slope by

$$d(V - V^*) / d \log i = 2.303\ RT/\beta_{aa}F \qquad (4.I.9)$$

From the drawn Tafel plots, β_{cc}, and β_{aa} can then be obtained.

The exponentials in eqn.(4.I.7) may be expanded and terms higher than the linear are neglected for the condition $|i| \ll i_{corr}$, so that we obtain

$$i = i_{corr}(\beta_{aa} + \beta_{cc})\frac{F}{RT}(V - V^*) \qquad (4.I.10)$$

The linear behaviour corresponding to eqn.(4.I.10) is restricted to about $\pm$ 15 mV around the corrosion potential for $|i| \ll i_{corr}$. From the above treatment, with β_{cc} and β_{aa} derived from Tafel slopes, the corrosion current-density can be determined.

Fig.4.I.6 shows the Tafel plot for a Ni-Mo-Cd plated electrode in a KF·2HF melt at 85°C. The potential was applied in an ascending and then descending direction to within 0.30 V and 0 V. "IR" drop corrections were made during evaluation of the Tafel line with the solution resistance being taken as $R_s = 5.1\ \Omega$, the latter having been measured by means of the initial potential-relaxation procedure after current interruption.

The difference of this plot from the previous Tafel plot (Fig.4.I.2) in the same system is that a second mixed potential can be identified when potentials were scanned backward from high values of cathodic polarization. At the two mixed potentials, the net total currents were equal to zero. Around a potential of $V_1^* = 0.173$ V, the anodic reaction could be the dissolution

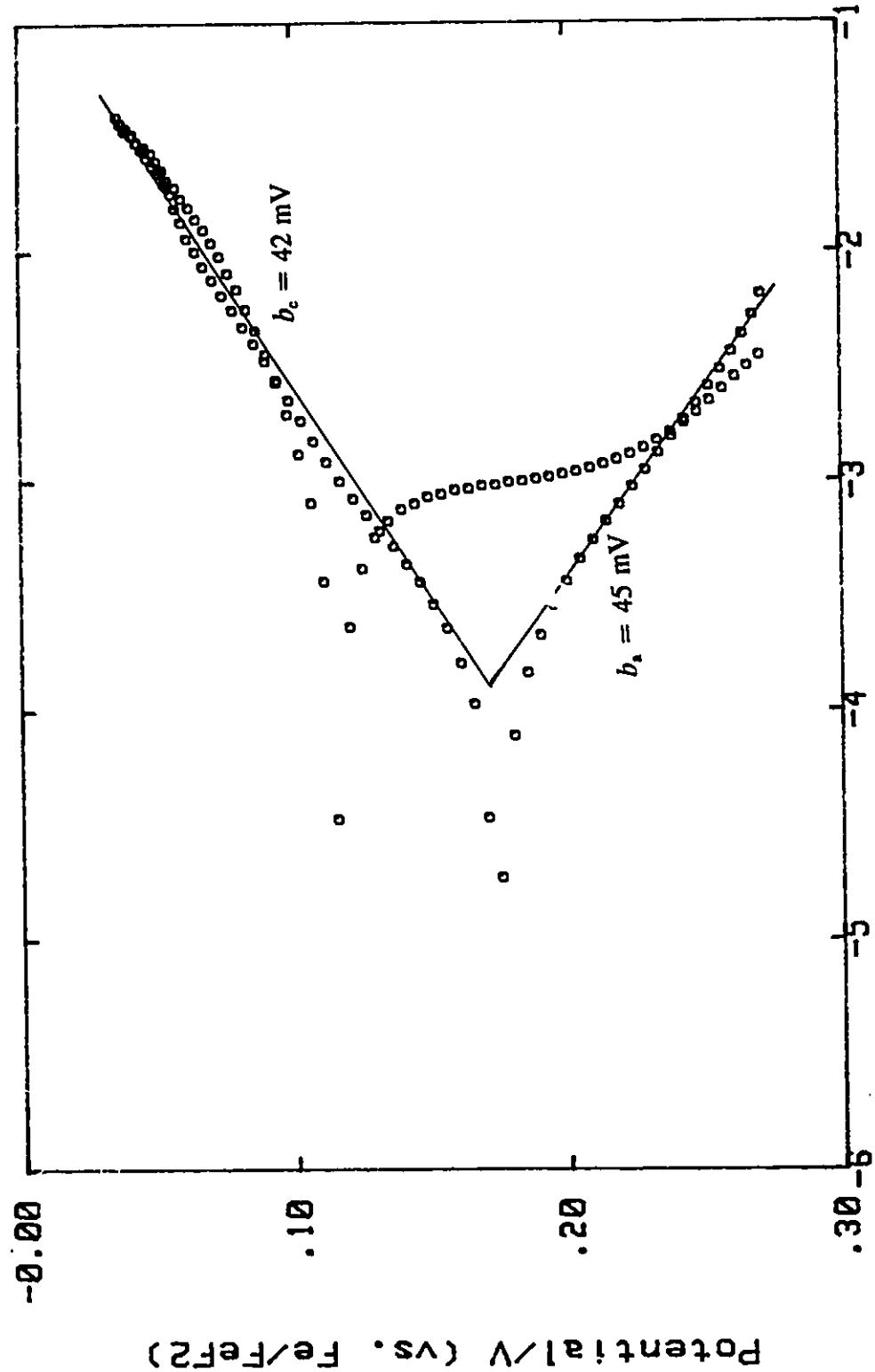

Fig.4.1.6 Tafel behaviour for the Ni-Mo-Cd electrode in the KF·2HF melt measured over the low anodic and cathodic overpotential regions.

of metal or fluoride film formation, and the cathodic reaction, could be the formation of hydride in parallel with cathodic H_2 evolution. When, however, the potential was decreased in backward scanning, another mixed process was established at $V_2^* = 0.120$ V with cathodic H_2 evolution and anodic oxidation of the hydride, which appeared to be a diffusion-controlled process. The processes of the reaction suggest that the H_2 was generated on the alloy hydride phase. The role of the hydride formed during H_2 evolution on the catalytic behaviour will be discussed in the following section.

Tafel slopes were drawn for the anodic metal dissolution with $b_a = 45$ mV, and cathodic hydride formation and H_2 evolution with $b_c = 42$ mV. According to eqns.(4.I.8) and (4.I.9) at T = 358 K, β_{cc} and β_{aa} can be calculated as 0.59 and 0.62 respectively. The extrapolation of the two linear Tafel regions to their intersection at the corrosion potential, $V_1^* = 0.173$ V, then gave a corrosion current-density, $i_{corr} = 1.4 \times 10^{-4}$ A cm^{-2}.

The measurement of corrosion current-density was also carried out by another technique, that of linear polarization with potential excursions restricted to ± 15 mV around the corrosion potential. Fig.4.I.7 shows the I vs V curve for potentials around ± 10 mV of the corrosion potential $V_1^* = 0.169$ V, where the total current was zero. As we see, V_1^* was unstable (V_1^* in Fig.4.I.6 is 0.173 V). The corrosion potential lies, of course, between the equilibrium potentials of the anodic and cathodic processes, respectively, but is not defined by the state of the system in a thermodynamic sense; it may vary if the rates of the participating reactions change with time, as noted earlier. The I vs V data plotted in Fig.4.I.7 were brought into eqn.(4.I.10), taking $\beta_{cc} = 0.59$ and $\beta_{aa} = 0.62$, then the i_{corr} could be calculated from the slope of the I vs V curve, giving, for this case, $i_{corr} = 1.8 \times 10^{-4}$ A cm^{-2}.

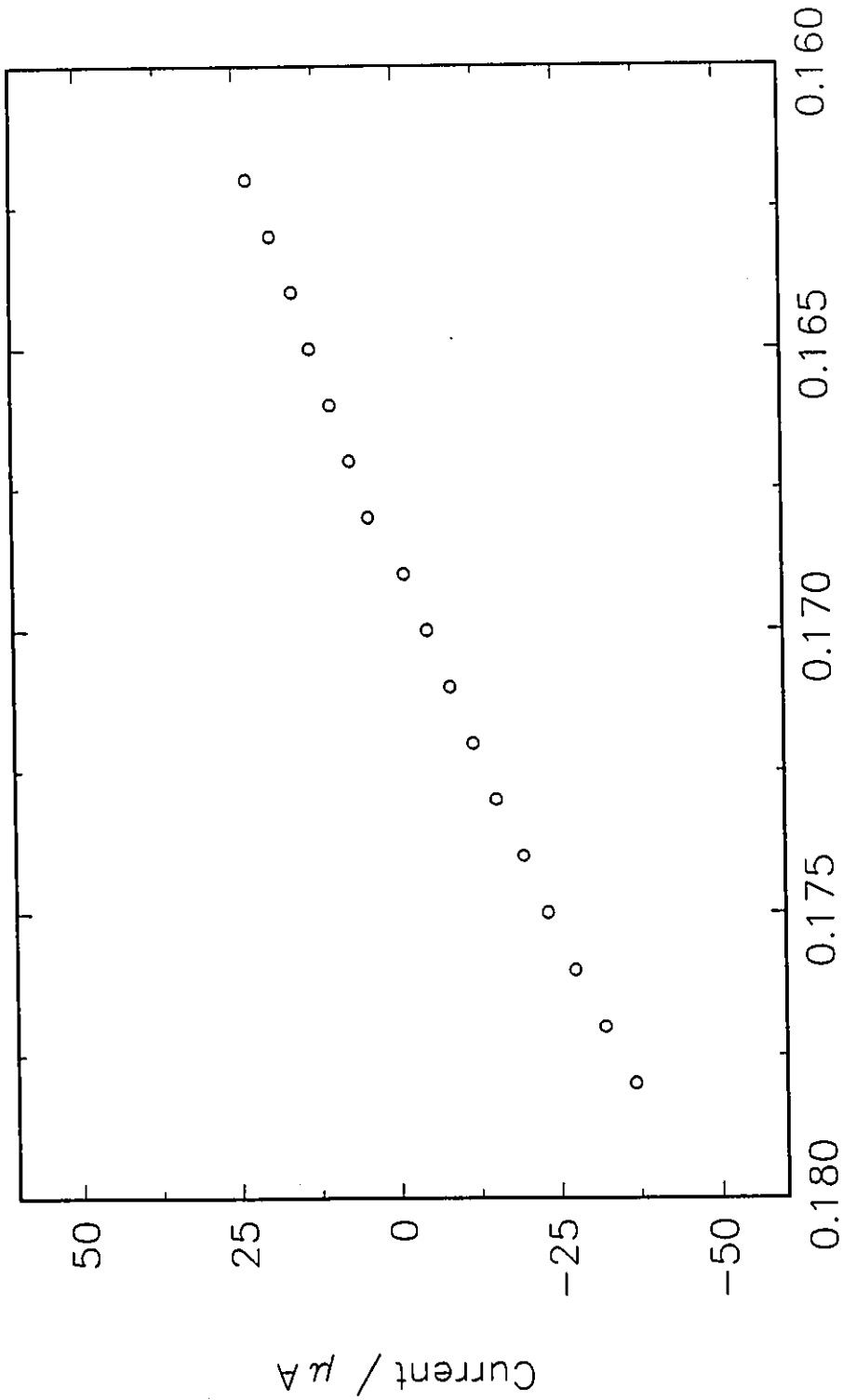

Fig.4.I.7 **Relation of current vs potential for the Ni-Mo-Cd electrode in the KF•2HF melt in the region near the equilibrium potential.**

Comparing the two values of i_{corr}, derived by the two different methods, it can be seen that they are in reasonable agreement with each other. Taking account of the roughness factor of the porous Ni-Mo-Cd plated electrode, which is about 140 determined from the comparison of the C_{dl} values of the rough, porous Ni-Mo-Cd and the smooth Ni-Mo bulk electrodes (see Section 4.II.2), we can calculate that the *real* i_{corr} is about 1.2×10^{-6} A cm^{-2}. This is a small value in comparison with $i_0 = 2.1 \times 10^{-5}$ A cm^{-2} for the mild-steel electrode in the same system (see our quarterly report to Cameco Corporation, January 1989).

From the determination of corrosion current-density, i_{corr}, at the Ni-Mo-Cd material in the KF·2HF melt, we conclude that the electrodeposited Ni-Mo-Cd composite is quite corrosion resistive. The "alkaline" nature of KF·2HF, or the small extent of H^+ ion dissociation in the melt would probably be the major reason, because HF with KF does not dissociate to "free" protons in the melt, but reacts rather as an H-bonded solvating agent for the F^- ion ($HF + F^- \rightarrow F\text{-}H\text{-}F^-$); a similar conclusion applies about the "acid" strength of HF in the melt. In fact, as we have mentioned earlier, the KF·2HF system should be regarded as a solvate of KF, like $KOH \cdot 2H_2O$ in the aquo-system. Therefore displacement reactions indicated in eqns.(4.I.1) and (4.I.2) would be less likely to occur. From these points of view, the Ni-Mo-Cd material *can* be suggested as an H_2 cathode for practical application in industrial F_2-production cells.

The corrosion behaviour of the Ni-Mo-Cd under *open-circuit condition* was also examined in KF·2HF at 85°C. A SEM picture of the electrode surface (see Fig.4.I.8a) was taken after one hour exposure of the electrode to the KF·2HF melt. The appearance of the surface was not much different from that of the fresh surface without immersion in the melt (Fig.2.2). Comparing the two cases, there is no evidence of any obvious corrosion reaction

(a)

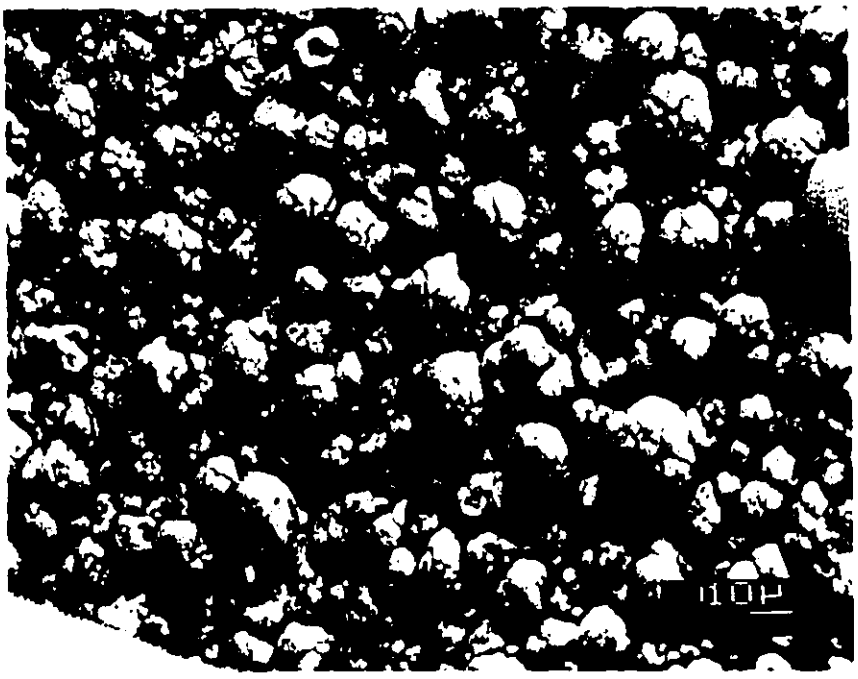

(b)

Fig.4.I.8 SEM pictures of the Ni-Mo-Cd electrode exposed in the KF·2HF melt under open-circuit conditions (a) for one hour; and (b) for one week.

occurring at the electrode, provided that the time of exposure to the melt was short.

For longer term testing of the durability or stability in the $KF \cdot 2HF$ melt, the electrode was set up in the melt on open-circuit for one week. The surface then looked dark when it was removed from the melt but under the SEM, as shown in Fig.4.I.8b, it still retained the "cauliflower-like" appearance, though a small extent of etching could be observed.

Following the above tests, further experiments were made on the corrosion of this type of electrode under open-circuit conditions for a period of one month. A SEM picture (Fig.4.I.9a) shows the appearance of this electrode surface. Pitting holes can apparently now be observed on the "cauliflower-like" deposits. This indicates corrosion would eventually occur on this alloy after a moderate period of time (a couple of weeks) on open-circuit, though kinetically this process is slow, as was found in the shorter-term experimental tests. However, this effect may not be entirely negative on the catalytic behaviour, since the pitting holes could actually increase the active surface roughness while the deposit could still function well as an electrocatalyst because its thickness was substantial (ca. 20 μm, as in Fig.2.2). It would still perform properly unless the deposit layer was completely lost. (This, we believe, would take at least several months under open-circuit conditions). If the electrode was, however, operated under working conditions, i.e. biased cathodically for H_2-evolution, the observed corrosion phenomena would neither occur at all or be negligible due to cathodic protection. The results in Fig.4.I.9b justify this conclusion.

A series of experiments were carried out simultaneously by putting another electrode in the melt for a period of one month, but this electrode was polarized at a small constant cathodic current of 10 μA or, as we say, under *cathodic protection*. Fig.4.I.9b shows the surface of the

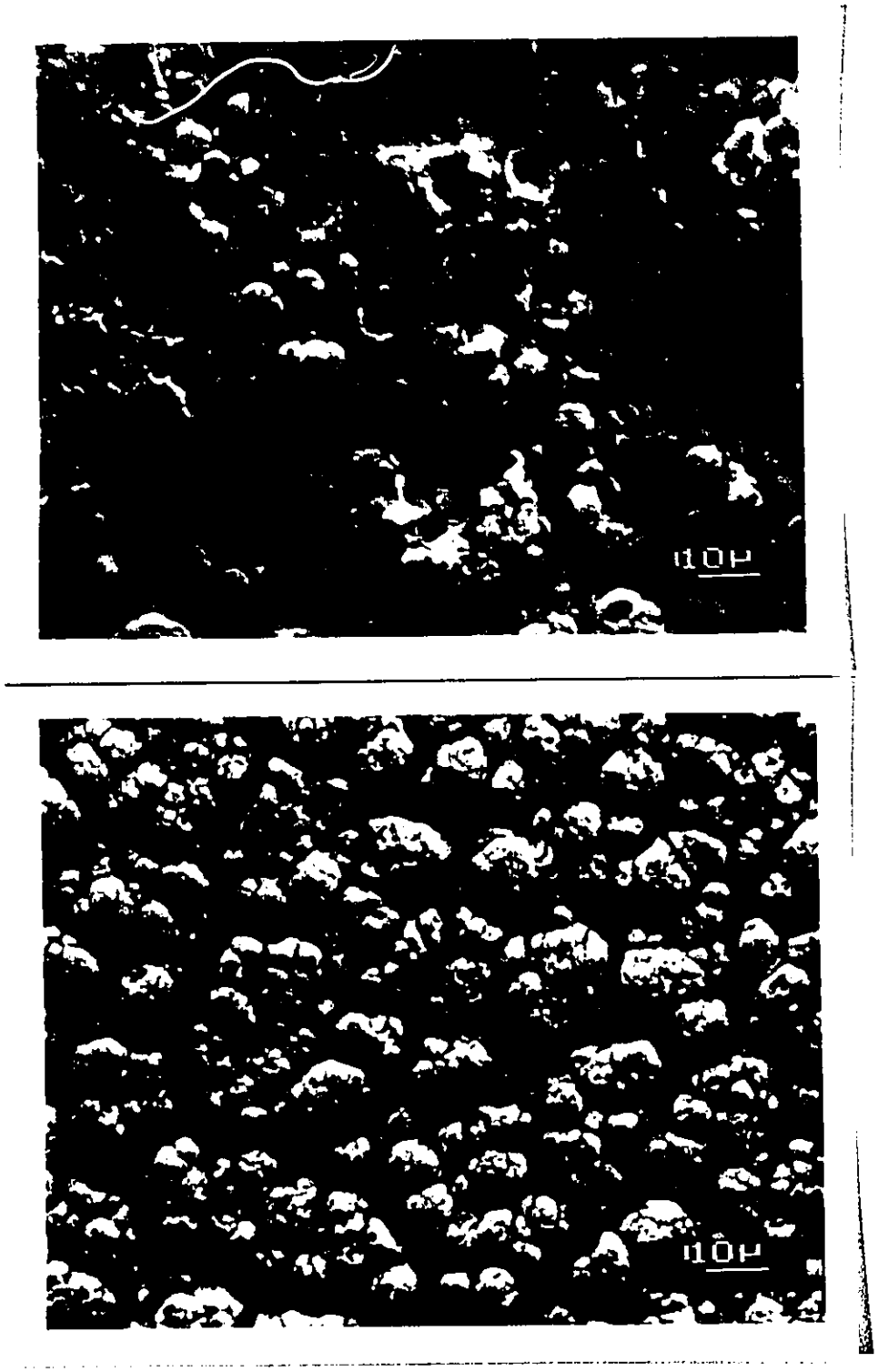

Fig.4.I.9 SEM pictures of the Ni-Mo-Cd electrode exposed in the KF·2HF melt (a) for one month under open-circuit condition; and (b) for one month, but with cathodic protection at i = -10 μA.

electrode after it had been taken out from the melt. Its appearance was virtually as it was before the polarization and admission to the melt. No pitting is observable except for appearance of some small cracks on the surface. Therefore, after this investigation, this electrodeposited material still appears quite satisfactory as a catalyst for cathodic H_2 evolution in the KF·2HF melt at elevated temperature.

While the present corrosion experiments were conducted over a nominally "long period" of time of 30 days, it was still short compared with practically expected lifetimes of cell cathodes where at least a year would be an anticipated operating period. Probably an experiment extended to a 3-month period would be more realistic. As noted above, the cathodes are automatically "cathodically protected" under continuous cell operation, so corrosion rates will be much attenuated; then only corrosion during cell "down times" needs to be worried about (a maximum of 1-month down-time for one year's operation can be assumed).

The Ni-Mo-Cd material was further examined for 80 days by immersion in the melt under open-circuit conditions at 85°C. A SEM picture (Fig.4.I.10) was taken to inspect the change of surface structure due to corrosion. It can be seen this time that the fine structure of the surface, having the "cauliflower" appearance, has gone, though the general "up-and-down" morphology still remains. It is possible that the original surface layers of the deposits have been etched after this long-term corrosion. However, the deposited layer, which was about 20 μm thick, has not been completely removed and, in fact, was largely intact, so the mild-steel substrate was not exposed. The electrode at this stage still functioned, however, quite well as an electrocatalyst material for cathodic H_2 evolution, although it would not have such good performance as the original one.

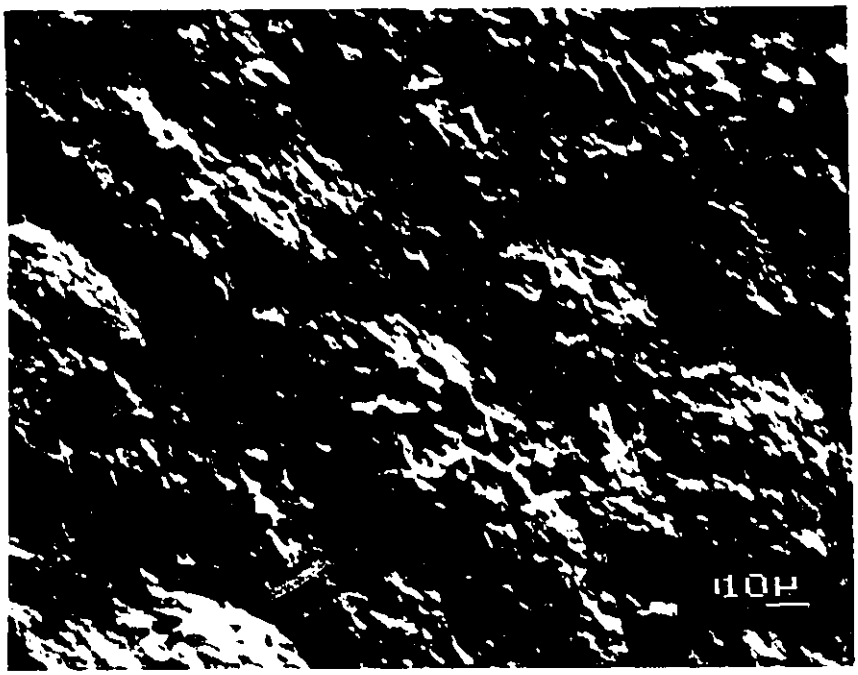

Fig.4.I.10 SEM pictures of the Ni-Mo-Cd electrode exposed in the KF·2HF melt under open-circuit conditions for 80 days.

4.I.2.3 Contact Angle Measurements at Ni-Mo-Cd Material in $KF \cdot 2HF$, $KOH \cdot 2H_2O$ Melts and 1 M KOH Solution

It had been observed (Section 4.I.2.1) that the electrodeposited Ni-Mo-Cd material performed differently in its Tafel behaviours in the $KF \cdot 2HF$ and $KOH \cdot 2H_2O$ melts. C_{dl} values determined from the initial potential-relaxation experiments (Section 4.II.2) in these two melts also indicated a great difference of surface accessibilities. One major possibility of this behaviour should be attributed to the different surface tensions and contact angles at the two solid/melt/gas interphases. Experiments on direct contact-angle measurement were therefore conducted in the present work, employing a contact-angle goniometer (Section 2.3).

Fig.4.I.11 illustrates the factors defining the contact angle. There must be a balance of forces acting on the line of contact between phases through point A, and which are associated with the surface tension of the solid/gas interface; viz: $\gamma_{s/g}$, and solid/liquid, $\gamma_{s/l}$, as well as the surface tension of the liquid/gas interface, $\gamma_{l/g}$. A $\gamma_{l/g}$ line is drawn from the tangent of the curve at the gas/liquid interface. Without making any assumptions about the mechanisms by which these forces act, we can write, for the equilibrium position of the line of contact between phases:

$$\gamma_{l/g} \cos \psi = \gamma_{s/g} - \gamma_{s/l} \qquad (4.I.11)$$

where ψ is the contact angle. It is convenient, in practical applications, to consider the ratio:

$$w = \cos \psi = (\gamma_{s/g} - \gamma_{s/l}) / \gamma_{l/g} \qquad (4.I.12)$$

which has also been called the "wetting coefficient". If $w = 1$ ($\psi = 0$, the gas phase forms a sphere), the solid is completely wetted by the liquid, while if $w = -1$ ($\psi = 180°$) the solid is not wetted. When w lies between ± 1, the solid is incompletely wetted.

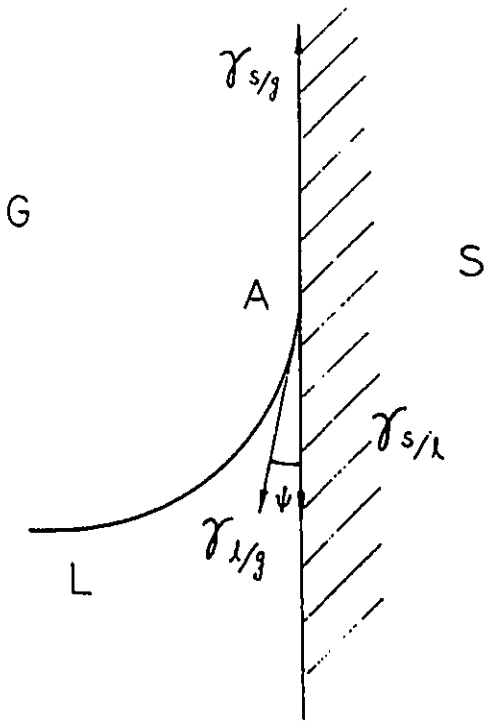

Fig.4.I.11 A schematic diagram representing a gas/liquid/solid interphase. ψ is the contact angle, and γ the surface tension.

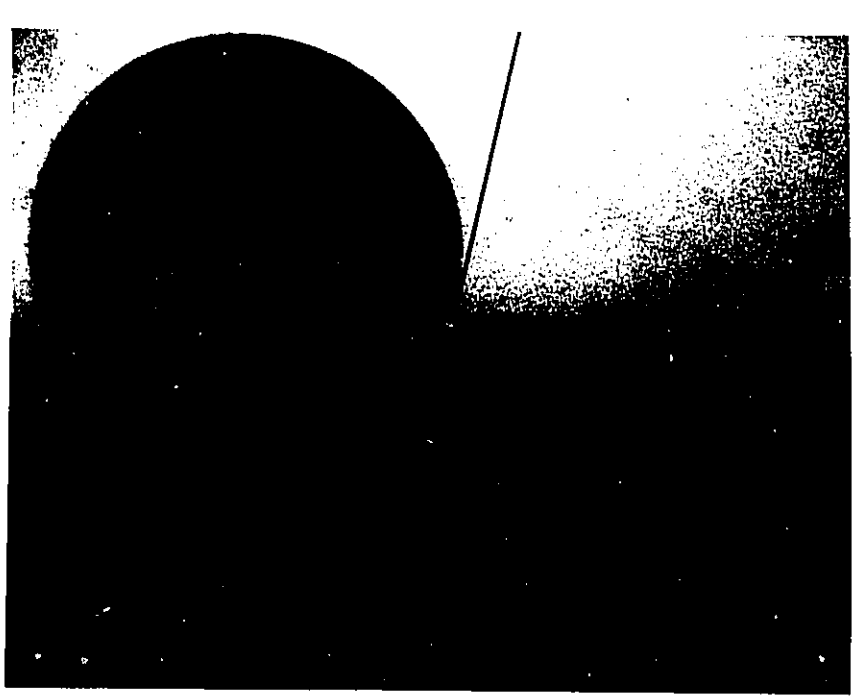

(a)

Fig.4.I.12 (a) The contact angle, 78°, of an H_2 bubble at the Ni-Mo-Cd electrode measured in the KF·2HF melt at 80°C.

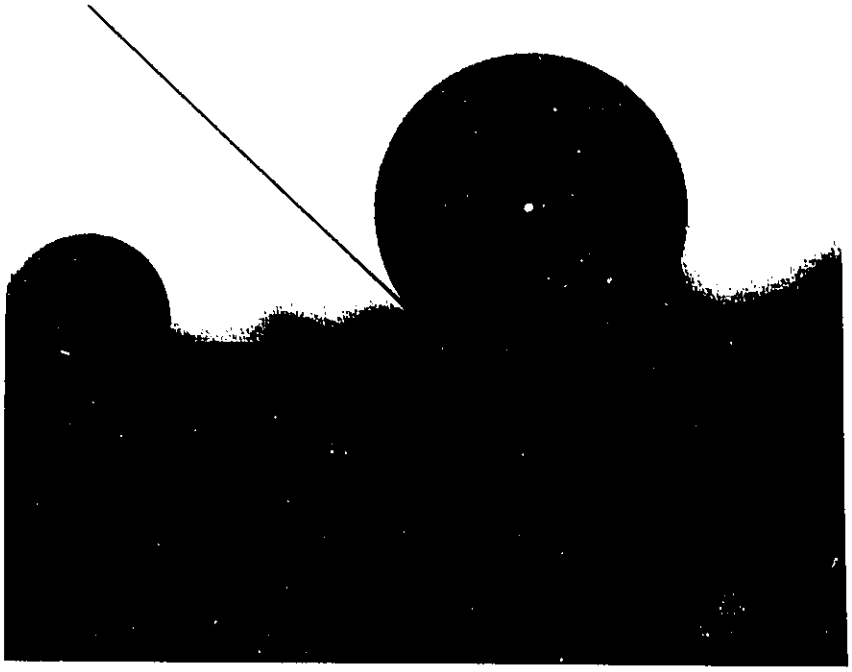

(b)

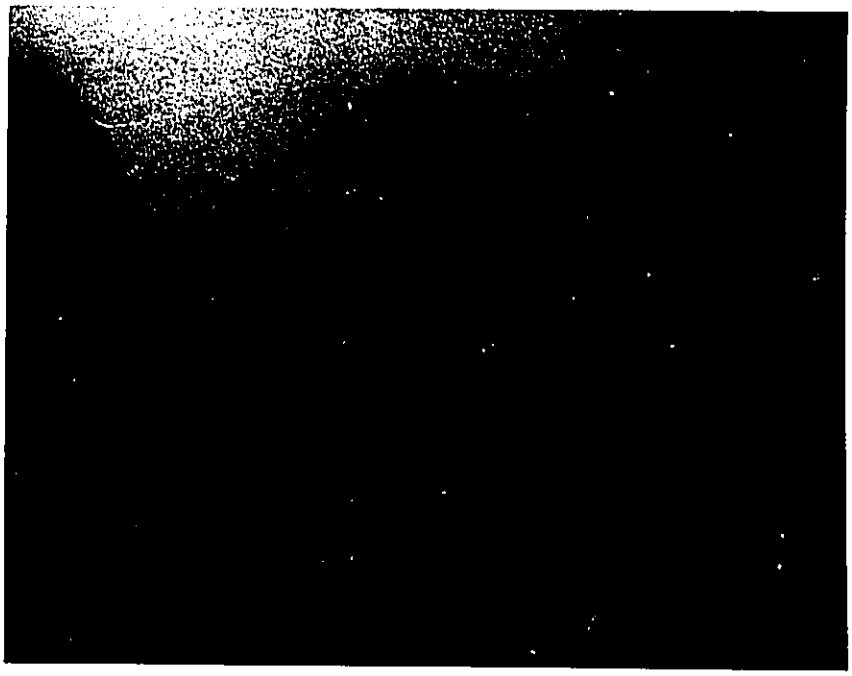

(c)

Fig.4.I.12 (b) The contact angle, 44°, of an H_2 bubble at the Ni-Mo-Cd electrode measured in the $KOH \cdot 2H_2O$ aquo-melt at 80°C.

(c) The contact angle, 22°, of an H_2 bubble at the Ni-Mo-Cd electrode measured in 1 M KOH solution at room temperature.

The Ni-Mo-Cd composite was deposited on a flat mild-steel plate. Apparent contact angles[2] were measured in three electrolyte media: KF·2HF at 80°C, KOH·$2H_2O$ at 80°C and 1 M aqueous KOH solution at room temperature. A specially designed cell for this aspect of the work was made from acrylic plastic and was conveniently transparent. The H_2 bubbles, which could be individually observed under magnification, were generated directly on the deposited surface of the plate polarized as an electrochemical cathode, corresponding to initiation of H_2 evolution.

Fig.4.I.12a, b, c show, respectively, the contact angle pictures obtained photographically at the Ni-Mo-Cd plate/H_2 bubble interphases, within the KF·2HF melt, the KOH·$2H_2O$ hydrate melt and the 1 M KOH solution. The spherical forms are H_2 gas bubbles while the flat bottom parts are the surfaces of solid Ni-Mo-Cd plates; both of them are in contact with the electrolyte (the bright areas). From the "shape" of the bubbles in contact on the plate (i.e. the extent to which they are spherical), it could be seen how it was possible for the bubbles to become much more easily detached from the electrode surface when the latter was in the hydrate media, than in the KF·2HF melt, where they tend to grow larger rather than become detached and displaced from the surface.

The measured contact angles, 22° in the 1M KOH solution, 44° in the KOH·$2H_2O$ hydrate melt and 78° in the KF·2HF melt, may indicate that the surface tension of the KF·2HF melt was higher than that of the aquo-systems. The recorded photos here are stationary images

---

[2] Since the Ni-Mo-Cd deposits are not microscopically smooth in comparison with a machined, polished metal surface, the reclination of bubbles at the former type of surface is microscopically different from that at smooth surfaces and the contact situation is therefore not exactly the same.

of H_2 bubbles during the polarization process; their shapes may change with time as more H_2 is generated in them. A motion picture or video would be relatively more vivid in revealing the practical situation, which was, unfortunately, not available for presentation with this thesis. However, these pictures give a good general visual impression about the momentary situation in the H_2-evolution process occurring at the electrode interface. The average residence time of bubble coverage will certainly influence the relative electrochemical behaviour of electrodes in these different electrolytes as reflected from the apparent C_{dl} values measured by the initial potential-relaxation method (Section 4.II.2). The origin of the effect is evidently well supported by the present results of contact-angle measurement experiments.

4.I.3 A.C. Impedance Behaviour of Ni-Mo-Cd in KF·2HF and KOH·2H$_2$O Melts

4.I.3.1 Impedance Method

Impedance spectroscopy [188] is a useful procedure for determination of C_{dl} and the adsorption pseudocapacitance, C_ϕ, for certain electrode reactions [101,118]. However, the difficulty involved in applying impedance studies to a porous electrode is to develop a theoretically based model to explain the constant phase-angle element (CPE) required to represent the experimentally observed behaviour of many real solid-electrode systems, including the impedance behaviour reported in the present work. As mentioned earlier, the equivalent circuit of Fig.4.I.13a is valid for representing an electrode interface. Since the time constants for C_{dl} (with a given R_P) are usually much smaller than those for C_ϕ, two separated semi-circles or peaks are expected in the complex-plane plots or the Bode phase spectra; the C_{dl} response appears in the high-frequency range while C_ϕ corresponds to the low-frequency range. These

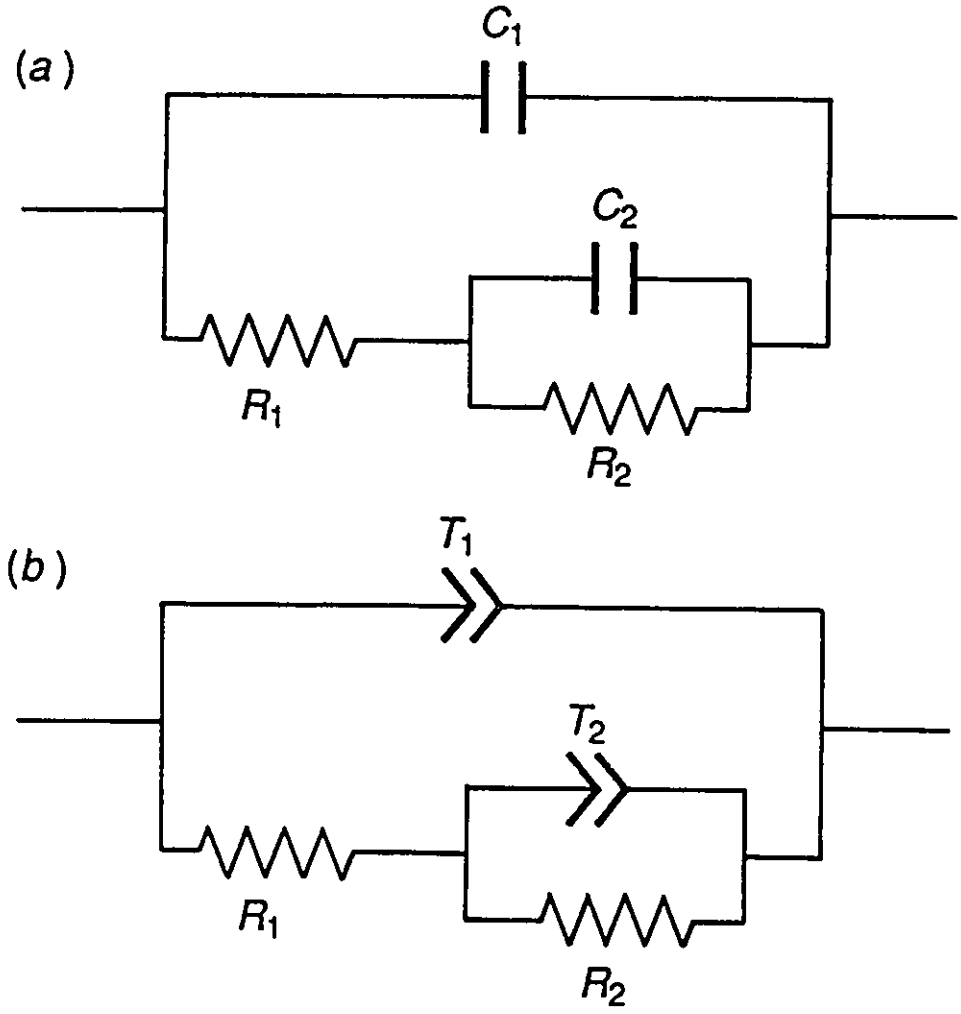

Fig.4.I.13 Equivalent circuits representing an electrode interface. (a) Only pure resistors (R) and capacitors (C) are involved; (b) two CPEs are involved, T_1 and T_2 are the time constants.

two frequency ranges correspond, respectively, to the short and longer time domains in the relaxation transients.

It is found that in most cases for solid electrodes, the semicircles in the complex-plane plots are "depressed" below the Z' axis. The depressed impedance curves can be best fitted by the so-called CPE model [188], although the microscopic link between the surface structure and the equivalent-circuit elements corresponding to the CPE is still not well understood; however, the requirement for a CPE to represent the frequency-response is believed to be connected with surface roughness and inhomogeneity [188,202], and the related matter of microscopic current distribution.

The equivalent circuit involving a CPE, used in the present work, is shown in Fig.4.I.13b. In this case, the impedance of pure capacitances in Fig.4.I.13a are replaced by the CPE defined as:

$$Z_{CPE} = 1 / T(j\omega)^{\alpha} \qquad (4.I.13)$$

where T is a time constant and α is here the exponent parameter ($0.5 \leq \alpha \leq 1$). On smooth, homogeneous electrodes, T becomes identical with C as $\alpha = 1$. Experimentally, the exponent α represents a clockwise rotation, by a constant angle, $90°(1-\alpha)$, of the straight line corresponding to the behaviour of the complex-plane plot for a simple RC circuit.

4.I.3.2 Analysis of Impedance Results for the HER at Ni-Mo-Cd in KF·2HF and KOH·2H$_2$O Melts

The A.C. impedance response of the porous Ni-Mo-Cd electrode is rather complex due to its surface inhomogeneity and roughness. The frequency response of the impedance, as represented in the complex-plane plot, exhibited two semi-circles which were associated

respectively with the modulation of charges held in C_{dl}, and C_ϕ, the latter due to adsorption of the H intermediate in the HER at the Ni-Mo-Cd electrode. Correspondingly, two peaks could always be identified in the phase-angle Bode-plot. Impedance behaviours of the Ni-Mo-Cd electrode were measured comparatively in the $KF \cdot 2HF$ and $KOH \cdot 2H_2O$ melts, separately. Results were then analysed by means of CNLS fitting from the model equivalent circuit shown in Fig. 4.I.13b, and thus the parameters representing the catalytic and adsorption behaviours of the H_2 reaction, e.g. C_{dl}, C_ϕ and α, could be satisfactorily obtained and compared.

Fig.4.I.14 shows the experimental data (circle points) : (a) the impedance complex-plane Z′ (real) vs Z″ (imaginary) plots; (b) the Bode phase vs log ω plots for the HER at the porous Ni-Mo-Cd electrode in the $KF \cdot 2HF$ melt. The three steady-state *over*potentials were -50, -80 and -100 mV for curves (1), (2) and (3) respectively. The corresponding solid lines represent the best-fit results computer-simulated in terms of the equivalent circuit in Fig.4.I.13b.

Two semi-circles, which are highly depressed, can be identified in the above complex-plane Z′ vs Z″ plot. Meanwhile, two corresponding maxima in the phase-angle plots are also clearly resolved. The responses in the high frequency range correspond to modulation of the charge on C_{dl}, represented in Fig.4.I.13b as T_1 (the CPE component; when $\alpha = 1$, $T_1 \equiv C_{dl}$). The response in the low frequency region is attributed to C_ϕ ($T_2 \equiv C_\phi$, when $\alpha = 1$) which is potential-dependent. Therefore the state of H adsorption at the Ni-Mo-Cd electrode in $KF \cdot 2HF$ melt can be characterized from this impedance result. This H pseudocapacitance response, arising on account of appreciable coverage of o.p.d. H at the Ni-Mo-Cd electrode, resembles the result at the Pt electrode which was previously studied [72] in this lab. The impedance response data for further low frequencies ($\omega < 0.01$ Hz) were too scattered to be reliably

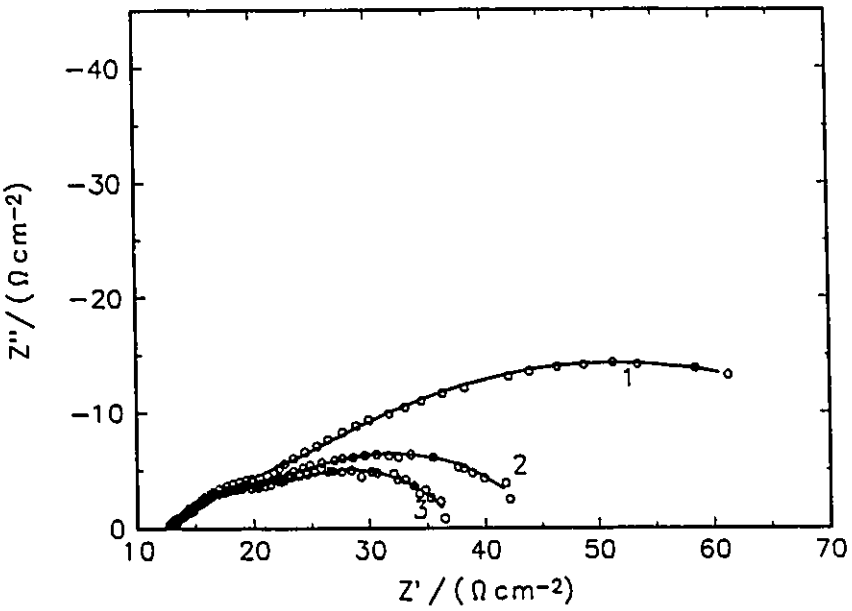

Fig.4.I.14 (a) The impedance complex-plane plots for the HER at the Ni-Mo-Cd electrode in the KF•2HF melt at (1) -50; (2) -80 and (3) -100 mV, respectively. Points are experimental results and solid lines the best-fit results using the equivalent circuit in Fig.4.I.13b.

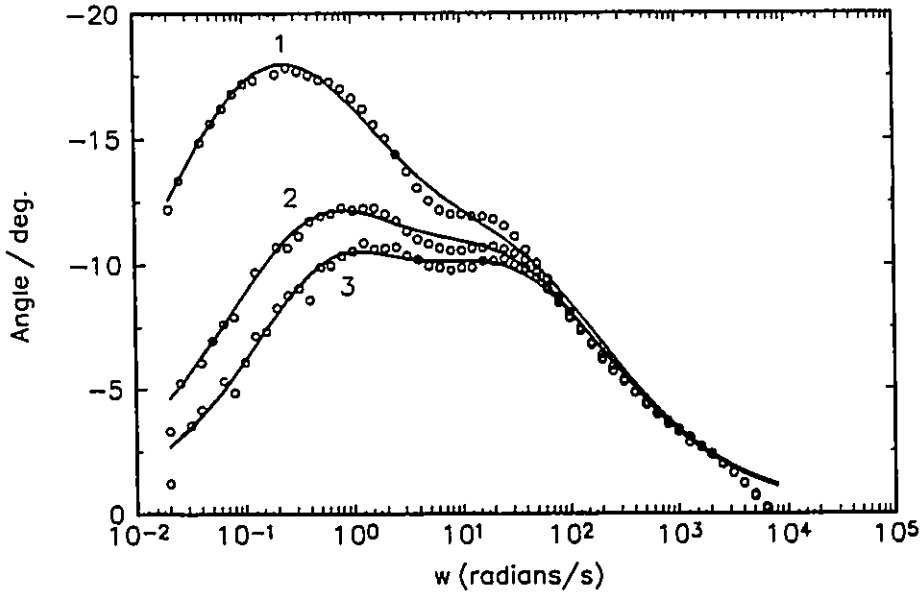

Fig.4.I.14 (b) Bode phase plots for the HER at the Ni-Mo-Cd electrode in the KF•2HF melt, corresponding to Fig.4.I.14a.

measured and interpreted, so are not shown here.

The extent of depression of the semi-circle is quite large, corresponding to the fractional exponent, α, being rather small as found from the fitting result (see Table 4.I.1). This may arise on account of the porosity of the Ni-Mo-Cd electrode as well as the low wettability due to the high surface tension [176] and large contact angle of the melt (Section 4.I.2.3). When the inside pores of the porous surface are incompletely accessible to the melt, a situation arises that the electronic signal does not penetrate deep into the porous structure. The observed impedance spectra for such systems are generally in the form of depressed semi-circles in the complex-plane plot and small values of phase angle in the Bode-phase plot, as has been discussed in the literature [188,202-206].

Table 4.I.1 Best-fit values of impedance parameters of the equivalent circuit elements of Fig.4.I.13b for the Ni-Mo-Cd electrode in the KF·2HF melt at 85°C

Overpotential / mV	$T_1(C_{dl})$ /(mF cm^{-2})$^{\alpha 1}$	α_1	$T_2(C_\phi)$ /(mF cm^{-2})$^{\alpha 2}$	α_2
- 50 (curve 1)	0.97 ± 0.51	0.59 ± 0.03	11.7	0.60 ± 0.03
- 80 (curve 2)	0.91 ± 0.39	0.57 ± 0.03	12.8	0.69 ± 0.04
-100 (curve 3)	0.87 ± 0.31	0.60 ± 0.04	9.6	0.52 ± 0.05

The above impedance results were determined in the low overpotential region (< -100 mV), where the adsorption of H was significant and changing appreciably with potential. At higher overpotentials, the second semi-circle in the complex-plane plot and the second maximum in the Bode-phase angle plot at low frequency range become diminished which indicates less or no response from the pseudocapacitance due to little or no change of the coverage by adsorbed H over that region. The fitting results (solid lines) are quite satisfactory and closely represent

the experimental data (o points). It can be seen that the average C_{dl} value is ca. 0.92 mF cm^{-2}, which is quite close to the result (average 0.81 mF cm^{-2}) determined from the initial potential-relaxation method (see Section 4.II.2) for the same system. The pseudocapacitances due to o.p.d H adsorption in the HER are in the range of 9.6 - 12.8 mF cm^{-2} varying with applied overpotential in the range η = -50 to -100 mV (Table 4.I.1).

Comparative experiments were carried out at the Ni-Mo-Cd material in the analogue $KOH \cdot 2H_2O$ hydrate melt. Fig.4.I.15 shows the similar impedance results (circle points) obtained: (a) the complex-plane Z′ (real) vs Z″ (imaginary) plots; (b) the Bode phase vs log ω plots. Again, the three steady-state *over*potentials were -50, -80 and -100 mV for curves (1), (2) and (3) respectively. The corresponding solid lines represent the best-fit curves which were obtained from simulation in terms of the equivalent circuit of Fig.4.I.13b.

Though the first semi-circle in the high frequency range is hardly distinguishable from the second one at low frequencies in the complex-plane plot, the existence of two maxima in the phase-angle plots proves the significance of o.p.d. H adsorption in the HER for this case, in addition to the response of C_{dl} which can always be identified in an electrochemical system. The "semi-circles" still appear in an arc form, but they seem less "depressed" compared with the behaviour of the electrode in the $KF \cdot 2HF$ melt. The experimental data (circle points) look smoother, probably because of the easier detachment of H_2 bubbles in the $KOH \cdot 2H_2O$ medium than in the fluoride melt.

Table 4.I.2 shows the best-fit results of the impedance parameters for the Ni-Mo-Cd material in the $KOH \cdot 2H_2O$ hydrate melt. It is seen that the values of C_{dl} are quite large, having an average value of 83 mF cm^{-2}, indicating a high effective surface area of the porous Ni-Mo-Cd

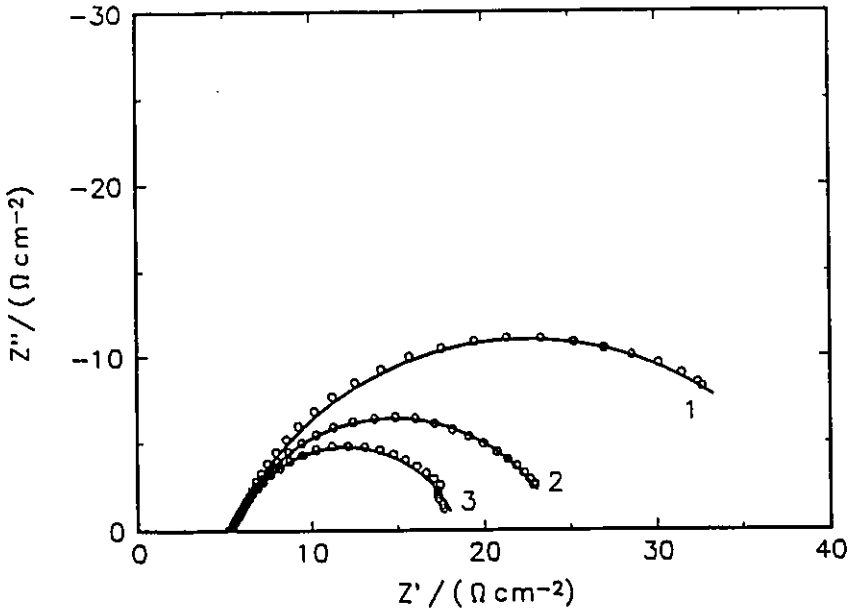

Fig.4.I.15 (a) The impedance complex-plane plots for the HER at the Ni-Mo-Cd electrode in the $KOH \cdot 2H_2O$ melt at (1) -50; (2) -80 and (3) -100 mV, respectively. Points are experimental results and solid lines the best-fit results using the equivalent circuit in Fig.4.I.13b.

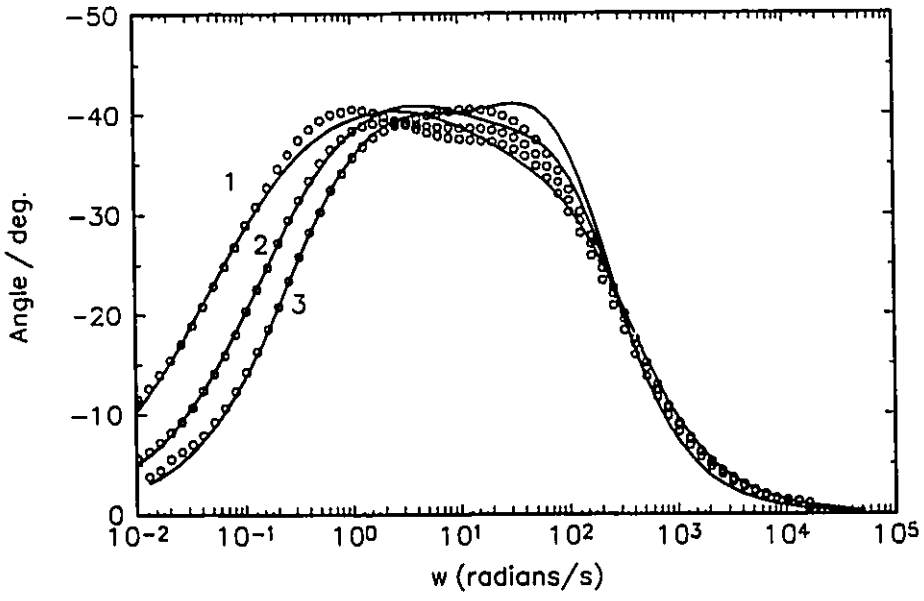

Fig.4.I.15 (b) Bode phase plots for the Ni-Mo-Cd in $KOH \cdot 2H_2O$ melt, corresponding to Fig.4.I.15a.

electrode in this aqueous melt. The values of α vary from 0.7 - 0.85, which means the electrode still functions as a porous material. Since the CPE exponent, α, is not only an intrinsic property of a given porous electrode, but also depends strongly on the conductivity of electrolyte solution in the pores [83] (see Section 4.II.3), the observed values of α (< 1.0) may also be partly determined by the conductivity of the $KOH \cdot 2H_2O$ solution whose concentration is ca. 28 M.

Fig.4.I.16 shows the conductivity of KOH solutions at various concentrations [207] at 298K. A maximum can be identified at a concentration of ca. 6 M, and further increase of concentration of KOH only reduces the conductivity of the electrolyte appreciably.

Table 4.I.2 Best-fit values of impedance parameters of the equivalent circuit elements of Fig.4.I.13b for the Ni-Mo-Cd electrode in $KOH \cdot 2H_2O$ melt at 85°C

Overpotential / mV	$T_1(C_{dl})$ /(mF cm^{-2})$^{\alpha 1}$	α_1	$T_2(C_\phi)$ /(mF cm^{-2})$^{\alpha 2}$	α_2
- 50 (curve 1)	81.4 ± 2.5	0.79 ± 0.13	410	0.77 ± 0.09
- 80 (curve 2)	90.6 ± 3.5	0.82 ± 0.17	524	0.70 ± 0.04
-100 (curve 3)	82.2 ± 3.2	0.85 ± 0.15	426	0.75 ± 0.03

The determined average value of C_{dl} (83 mF cm^{-2}) of the Ni-Mo-Cd electrode in the $KOH \cdot 2H_2O$ hydrate melt is in reasonable agreement with the values measured from the potential-relaxation technique (Section 4.II.3) in the same system. High values of C_ϕ further prove the significance of chemisorption of the o.p.d. H intermediate at this electrode in $KOH \cdot 2H_2O$ and its role in the HER at this material.

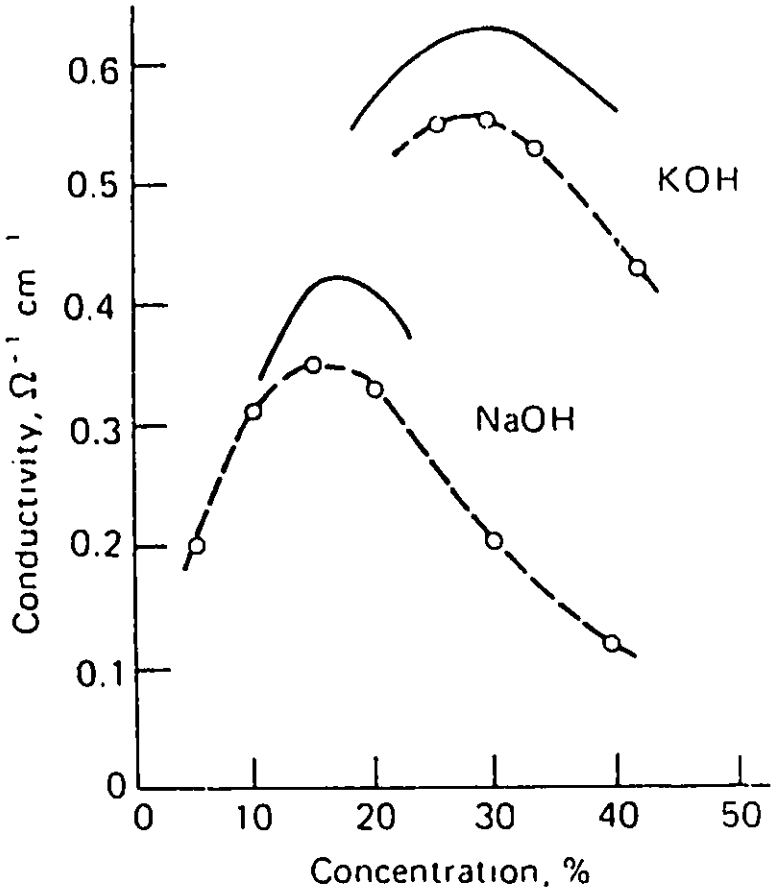

TABLE C.3 Properties of Potassium Hydroxide Solutions

Wt., %	KOH concentration		Density d_4^{20}	g/L at 20°C	Specific conductance at 20°C, $\Omega^{-1}cm^{-1}$	Freezing point, °C	Viscosity at 20°C, cP
	Molality	Molarity at 20°C					
4	0.7427	0.7372	1.034	41.36	0.15	−2	1.08
8	1.550	1.527	1.071	85.68	0.28	−6	1.18
12	2.431	2.373	1.109	133.1	0.38	−11	1.29
16	3.395	3.271	1.147	183.5	0.47	−17	1 44
20	4.456	4.229	1.186	237.2	0.54	24	1.62
24	5.629	5.246	1.226	294.2	0.60	−35	1.86
28	6.932	6.326	1.267	354.8	0.62	−49	2.17
32	8.388	7.469	1.309	418.9	0.60	−61	2.57
36	10.03	8.678	1.352	486.7	0.56	−46	3.11
40	11.88	9.911	1.396	558.4	0.52	−35	3.88
44	14.00	11 31	1.442	634.5	—	−29	5.11
48	16 45	12.73	1.488	714.2	—	−4	6.73

Fig.4.I.16 Conductivity of KOH solutions at various concentrations.

4.I.4 Potential-Relaxation Behaviours of the Ni-Mo-Cd Electrode in KF·2HF and KOH·2H$_2$O Melts

4.I.4.1 Analysis of Potential-Relaxation Transient Results

Full curves of the potential-relaxation transients were recorded following current interruption at the Ni-Mo-Cd electrode in the KF·2HF melt. Fig.4.I.17 shows four such transient curves at initial current-densities of (1) 209; (2) 148; (3) 92 and (4) 45 mA cm^{-2}, respectively. Three digital oscilloscopes were used in tandem in order to record data expanded over 9 decades of time (from 2 μs to 2000 s), and the data were computer processed so that points could be distributed evenly on a logarithmic scale of time and joined smoothly. Potentials were expressed in terms of overpotentials calibrated from the equilibrium potential.

Attempts were made to simulate the experimental behaviour employing the theoretical treatment described in Section 3.2. The solid line on curve 4 in Fig.4.I.17 was obtained through many efforts at curve-fitting from rate equations by means of the nonlinear least-squares routine operated automatically on the CMS mainframe computer. The fitting result was, however, not very satisfactory in this case in terms of consistency between the experimental data and theoretical calculation, which means the experimental potential-relaxation behaviour could not be simply described by the theoretical treatment based on the ideal Langmuir isotherm applied to the HER. It was found that difficulty in the theoretical simulation arose particularly for the cases involving the porous electrode material, probably due to the influence of porosity and uneven potential distribution inside the pores.

An empirical equivalent circuit treatment for the impedance work involving a CPE was rather successful for fitting the experimental results at the porous electrode (Section 4.I.3.2), but a rate-constants treatment was not available here to apply to the special conditions arising in

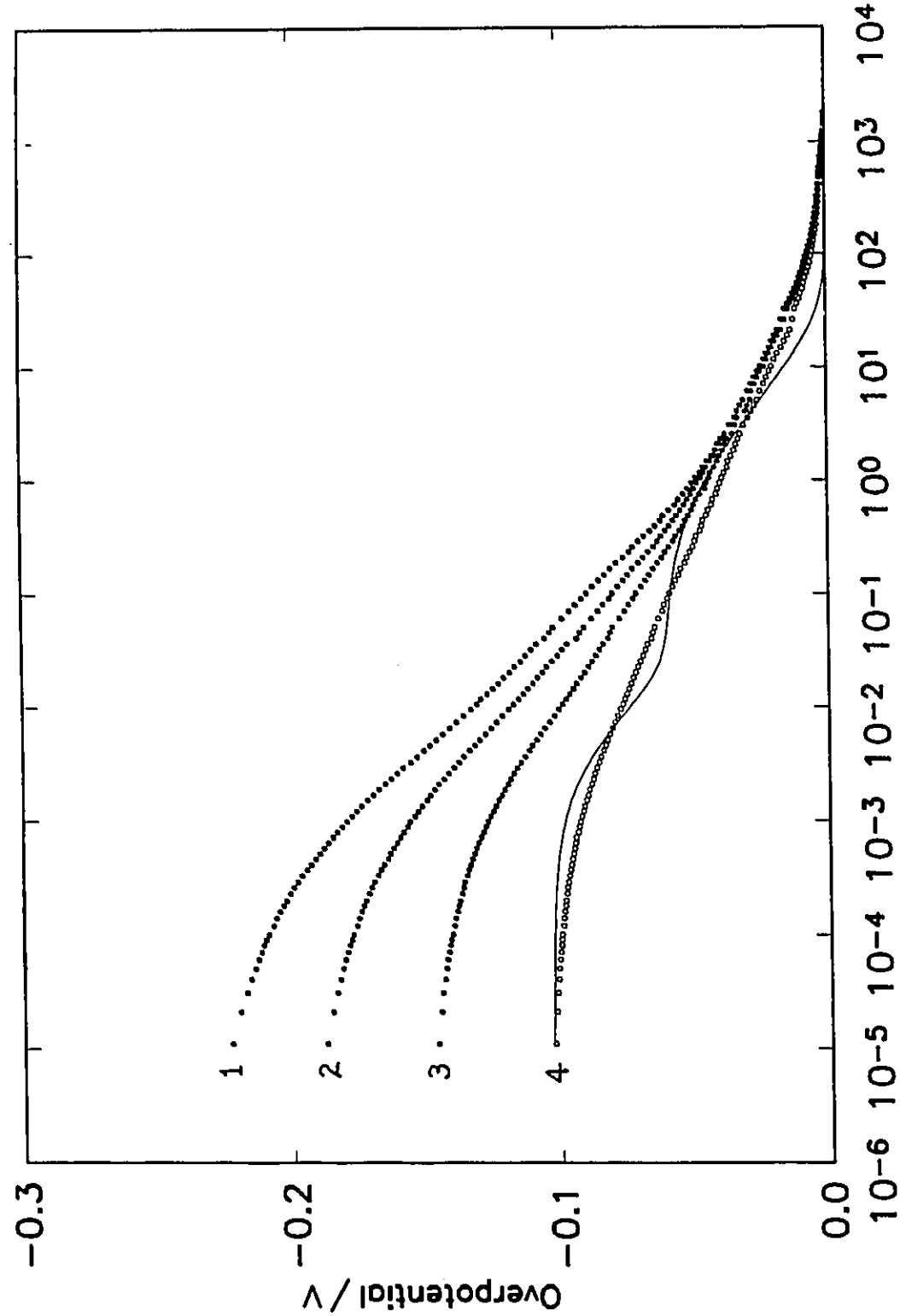

Fig.4.1.17 Full-range potential-relaxation transients for the HER at the Ni-Mo-Cd electrode in the KF·2HF melt. $i_{t=0}$ are (1) 209; (2) 148; (3) 92 and (4) 45 mA cm^{-2}, respectively. The solid line represents the simulation result.

potential-relaxation. In addition, incomplete accessibility of the electrode, related to the high interfacial tension and large contact angle in the KF·2HF melt could also lead to complications in the potential-relaxation behaviour.

Though whole curve fitting by means of the theoretical kinetic approach was found to be not possible, determination of C_{dl} from the fitting of the initial regions of potential-relaxation transients had been very successful (see Section 4.II.2), since the initial range of the transients is determined mainly by discharge of C_{dl}. In fact, the surface area of the Ni-Mo-Cd electrode in KF·2HF melt in the HER was satisfactorily determined *in situ* using that technique.

It has been reported that an hydride phase is formed during electrodeposition in the electrode preparation process [5]. Hydride can also be formed in the cathodic H_2 evolution process as it was shown (see Fig.4.I.6) that a quasi-equilibrium potential, corresponding to an hydride phase, could be identified which was more negative than the reversible H^+/H_2 potential. In such a case, the potential-relaxation process involves discharge of C_{dl}, *as well as* a C_ϕ associated with the self-decomposition of any 3-dimensional hydride phase (Section 4.I.4.2), in addition to the known desorption process of 2-dimensional adsorbed H. The hydride decomposition process is experimentally indicated by observation that H_2 evolution continues to take place on open-circuit, through a "corrosion type" mixed reaction. More detailed discussion will follow in the next section.

Fig.4.I.18 shows the potential-relaxation transients of the Ni-Mo-Cd electrode in the $KOH \cdot 2H_2O$ solution. A reversible H_2 reference electrode (RHE) was used in this hydrate melt. The form of the potential decay transient in the range 2 μs to 2 s appears normal, similar to that

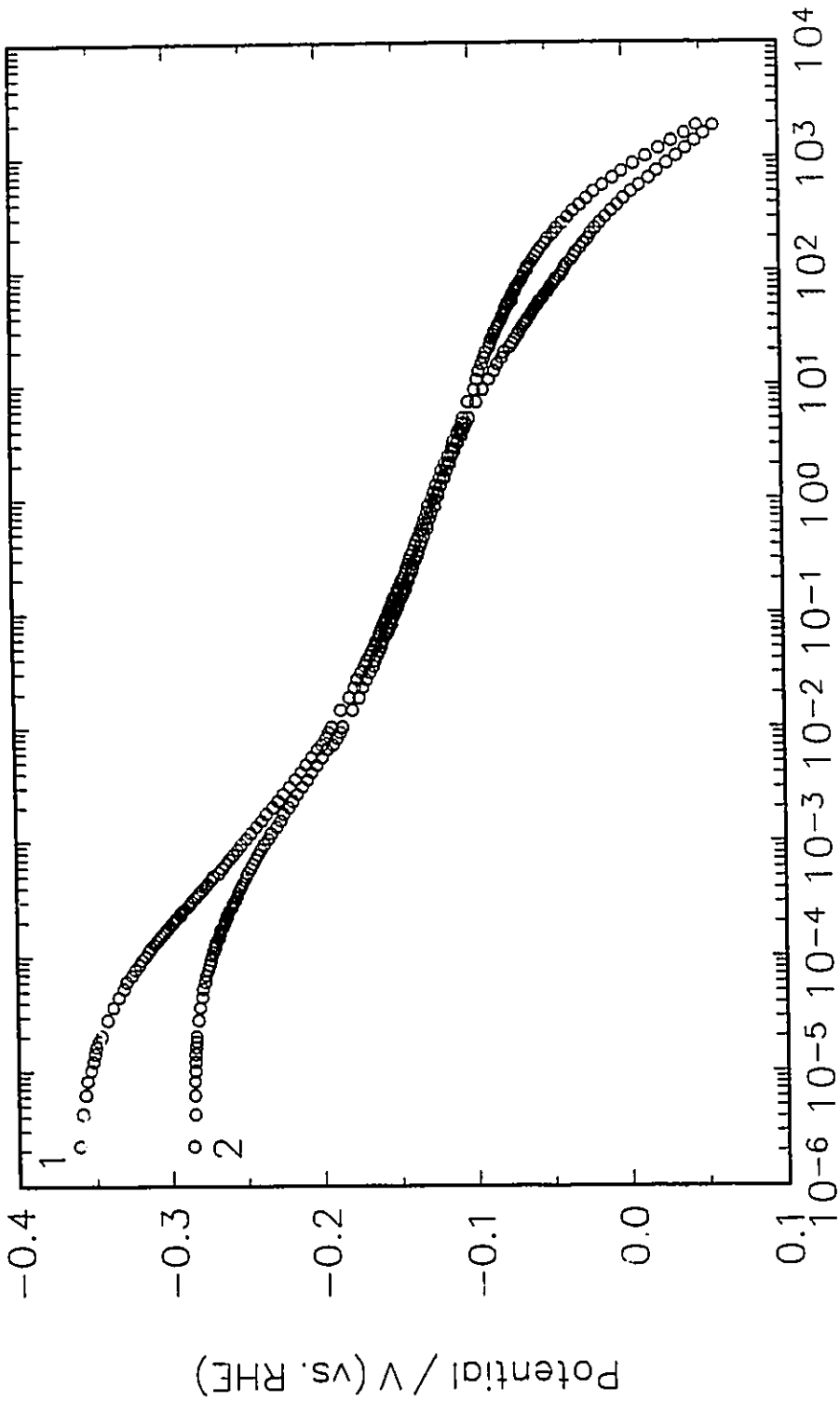

Fig.4.1.18 Full-range potential-relaxation transients for the HER at the Ni-Mo-Cd electrode in the $KOH \cdot 2H_2O$ melt.

for other electrodes, e.g. Pt [82], with the potential remaining initially level (on the log t scale) followed by a linear drop. However, abnormal behaviour arises in the longer time region (> 10 s) insofar as potential-relaxation transients do not gradually approach 0 V, but drop to a more positive potential region below the RHE equilibrium potential. Theoretical simulation was not attempted for this case.

4.I.4.2 Hydride Effect

When a hydride phase, e.g. Ni_xH, (here "Ni" represents the Ni-Mo-Cd composite) is present, which can establish a range of quasi-reversible potentials more negative than the hydrogen reversible potential, depending on X [5,127], self-discharge can take place on open-circuit at a mixed potential by means of an anodic and cathodic process coupled as parallel reactions, viz. through the formal scheme:

$$Ni_xH + OH^- \rightleftharpoons xNi + H_2O + e \text{ (anodic)} \qquad (4.I.14)$$

$$H_2O + e \rightarrow OH^- + \tfrac{1}{2}H_2 \text{ (cathodic)} \qquad (4.I.15)$$

The H_2 evolution in eqn.(4.I.15) proceeds by one of the usual two-step reactions involving adsorbed H as the intermediate either on Ni-Mo-Cd metal or Ni_xH sites. The above anodic type process is coupled, as in a corrosion-type process, with the H_2 evolution taking place at some mixed potential.

The above type of self-discharge is to be contrasted with that involved in desorption of adsorbed H in the HER itself on various other metals, e.g. Pt, where processes $MH_{ads} + OH^- \rightleftharpoons M + H_2O + e$ and $MH_{ads} + H_2O + e \rightarrow M + H_2 + OH^-$ occur on open-circuit (see processes I and II in Section 3.2). The latter two processes involve the discharge of 2-dimensionally *ad*sorbed H. For Ni-based composite materials, such as the Ni-Mo-Cd electrode in this case,

both types of reactions involving discharge of 3-dimensional *ab*sorbed H and 2-dimensional *ad*sorbed H would occur spontaneously in open-circuit potential-relaxation transients. When this situation arises, potential-relaxation behaviour cannot be described simply by the kinetic rate equations which consider only the *ad*sorbed H species in the HER processes; therefore simulation, which is based on the kinetic theory described in Section 3.2, of the experimental behaviour cannot be applied in this case, at least not without substantial modification.

The potential of the electrode will fall with time on open-circuit in the usual way on account of continuing discharge of C_{dl} in the short-time range. Discharge of the pseudocapacitance, C_{ϕ}, which would now include both *ad*sorbed and *ab*sorbed H, will also arise on account of the potential dependence of the coverage, θ_H, of the adsorbed H, and of the lattice fraction, X_H, of the sorbed H species over the longer time scale. The question is what is the time sequence for the two processes. Is there one step that relaxes faster than the other, or do both states of H become discharged together within the same time domain?

It is clear that the discharge of the *ab*sorbed H from the Ni_xH interfacial region (order of several nm near the surface) will be a diffusion-controlled step in the lattice, treated in terms of change of the lattice fraction, X_H, with time; while, the state of chemisorbed H must be treated in the usual way in terms of the 2-dimensional surface site fraction, θ_H, that is for H *ad*sorbed at the surface of the Ni-Mo-Cd and Ni_xH phases. Experimentally, it is not possible to distinguish the 2-dimensional *ad*sorbed H from the 3-dimensional hydride H by the electrochemical procedures used in the present work, though the role of a diffusion process involving the latter could probably be identified.

In Fig.4.I.18, the observed abnormal potential-relaxation behaviour over the long time

region near the RHE potential could be attributed to the mixed contribution from discharges of both *ad*sorbed and *ab*sorbed H intermediates.

Continuing relaxation of potential at open-circuit to potentials more positive to the RHE could arise on account of several possibilities. Since the electrochemical cell was sealed, purged and saturated with H_2, influence of O_2 dissolved in the solution was unlikely. Cyclic voltamnietry experiments were conducted at the Ni-Mo-Cd electrode with the aim of attempting to elucidate the electrochemical behaviour of hydrogen at the electrode surface in relation to hydride formation, and to determine the role of possible spontaneous oxidation (corrosion) that could occur over potential ranges around or near the H_2 reversible potential.

Fig.4.I.19 shows cyclic voltammetry curves obtained for the Ni-Mo-Cd electrode in the $KOH \cdot 2H_2O$ melt at a potential sweep-rate of 50 mV s^{-1}. As can be seen, some anodic process arises in the potential range ca. +0.2 V to +0.4 V vs RHE. A corresponding cathodic process can also be identified in the cathodic direction of the sweep, and it appears just positive to the potential at which the HER commences. It was observed that the surface reaction was not reversible over the i vs V profile.

There are several possibilities for the above results: (a) overlap between the potential ranges for hydrogen desorption and surface oxide formation; (b) the decomposition of significant *ab*sorbed H from the Ni_xH lattice and (c) co-evolution of H_2 or its re-oxidation on a following sweep going in the positive potential direction.

It has been reported [5] that the process occurring positive to the RHE is mainly due to the formation of surface oxide, $Ni(OH)_2$. However, other works [127] have demonstrated that the CV behaviour, such as in Fig.4.I.19, arises from a process involving *ab*sorbed H diffusing

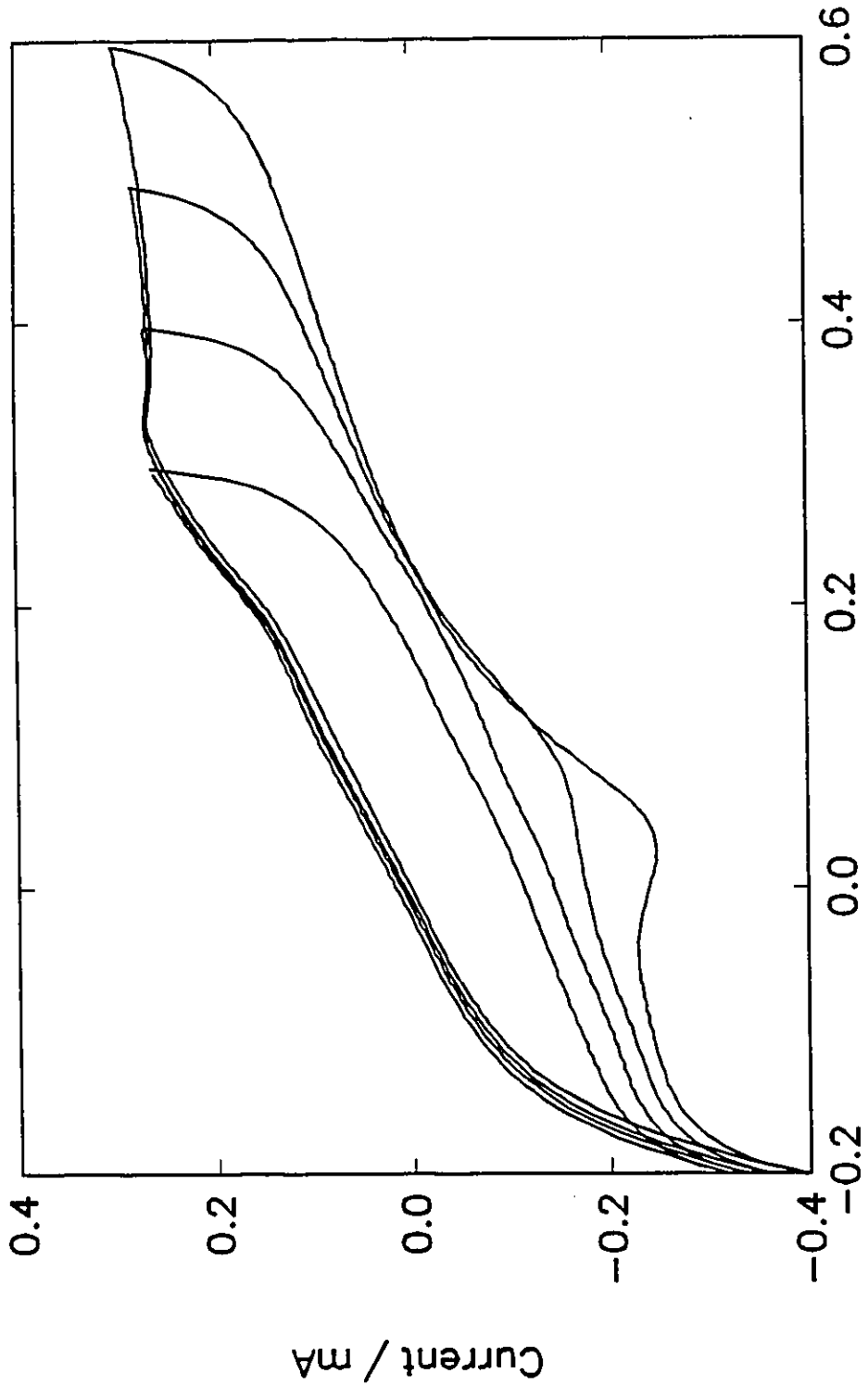

Fig.4.I.19 Cyclic voltammetry plots for the Ni-Mo-Cd electrode in the $KOH \cdot 2H_2O$ melt. Sweep-rate is 50 mV/s.

from the hydride phase as it was shown that linearity existed between anodic peak current, $i_{p,a}$, in the CV plots and square-root of sweep-rate. The influence of re-oxidation of H_2 was excluded by employing a rotating electrode.

It seems to the present author that surface oxidation reactions are more probable over the region positive to the RHE potential. This is based on the fact that (1) thermodynamically, surface oxidation of Ni-based composites will occur spontaneously when the electrode is introduced into the aqueous electrolyte, as was found for pure Ni (in the HER study) which had to be sealed in an H_2 atmosphere prior to the experiment and had to be polarized immediately after immersion in solution; (2) the equilibrium potential of the hydride phase for the reaction in eqn.(4.I.14) is presumed to arise *above*, or more *negative*, to the reversible H_2 potential; (3) in the potential-relaxation experiment, shown in Fig.4.I.17 for Ni-Mo-Cd in the $KF \cdot 2HF$ melt, the potential did not fall to a value below the H_2 equilibrium potential because no surface oxide could be formed in such a melt. Therefore the continuing drop of potential at Ni-Mo-Cd below the RHE potential, observed in $KOH \cdot 2H_2O$ shown in Fig.4.I.18 is most probably due to surface oxide formation.

The reversible potential for reaction in eqn.(4.I.14), almost equal to the mixed potential, will depend on the lattice site fraction, X_H, in a form similar to the Nernst equation:

$$E_{rev} = E^0 - (RT/F) \ln [X_H / (1 - X_H)] \qquad (4.I.16)$$

where E^0 is the reversible potential when $X_H = 0.5$, and the real value of E^0 relevant to the standard RHE will depend on the thermodynamic properties of the hydride phase. A plot based on this equation for the E_{rev} vs X_H relation is shown in Fig.4.I.20. Here E^0 was arbitrarily taken as 0 V. It can be seen that decrease of lattice fraction X_H will result in a decrease of cathodic

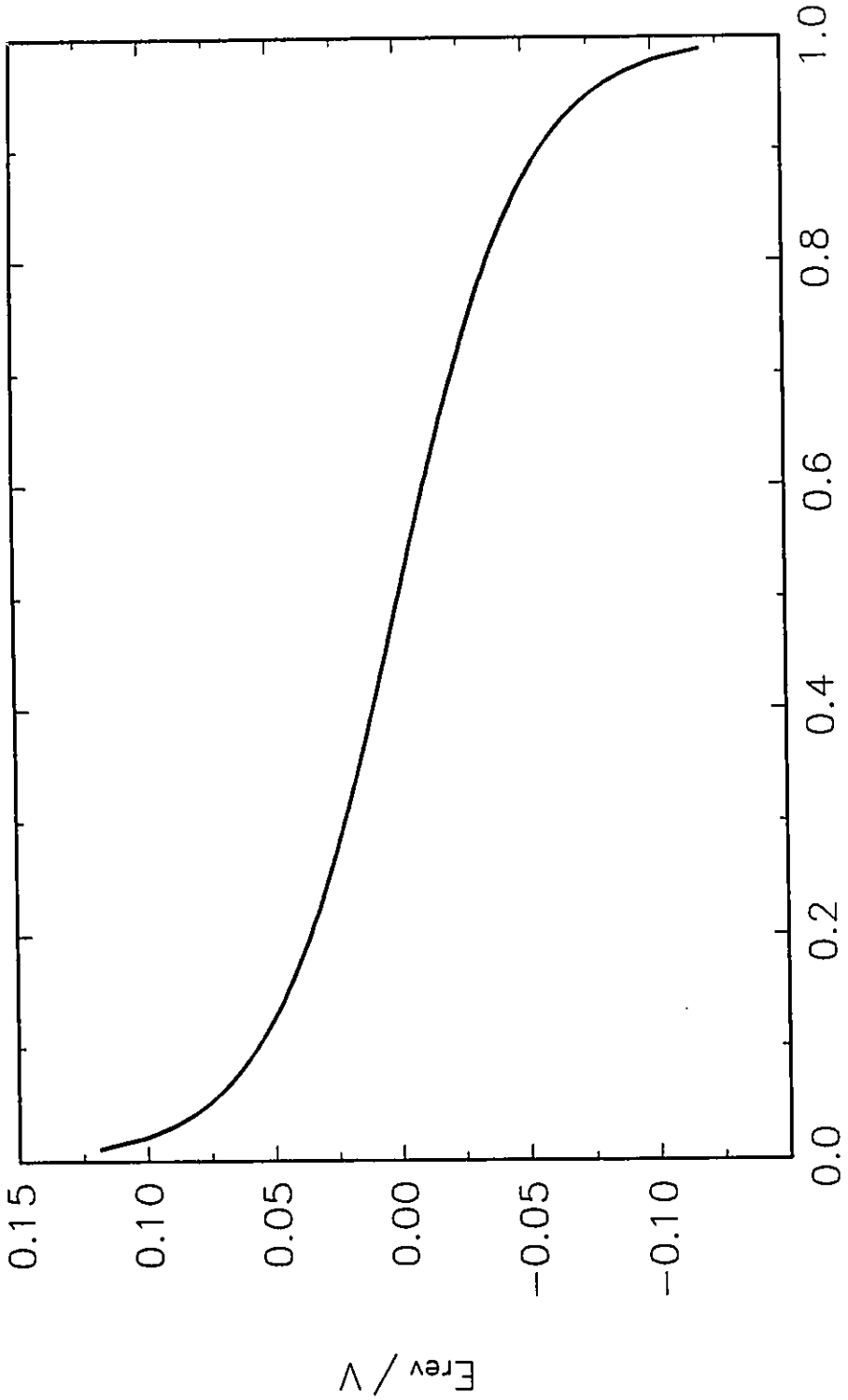

Fig.4.1.20 Calculated E_{rev} vs X relation according to eqn.(4.1.16).

potential. The extent of open-circuit evolution of H_2 on the porous Ni-Mo-Cd electrode will be determined by the amount of the Ni_xH hydride species in the electrode material, near its surface. When $X_H \rightarrow 1$, the open-circuit potential-relaxation is determined initially mainly by the double-layer capacitance; when $X_H < 1$, the continuing fall of potential follows the E vs. X_H curve in a descending direction with discharge of the much larger capacitance, C_ϕ, associated with the sorbed H and also the change of adsorbed H coverage, θ_H.

In terms of the proposed equilibrium state of Ni_xH, and its formation and removal rates, $i_1 = i_{-1}$, a quasi-equilibrium condition can be written as:

$$k_1 (1 - X_H) \exp [F\eta/2RT] = k_{-1} X_H \exp [-F\eta/2RT] \qquad (4.I.17)$$

(with β taken as 0.5); hence

$$X_H = (K_1 \exp [F\eta/2RT]) / (1 + K_1 \exp [F\eta/2RT]) \qquad (4.I.18)$$

where $K_1 = k_1/k_{-1}$. This type of relation is the isotherm for "intercalation" of H, e.g. similar to that known for Li^+ into TiS_2 [208].

Part II. *In situ* Determination of Real-area of Porous, Gas-evolving Electrocatalysts

4.II.1 Determination of Surface Area Based on a Prototype System at Pt

4.II.1.1 Introduction

As has been emphasised in Chapter I, the determination of the electrochemically accessible, real surface area of a rough or porous electrode has long remained a substantial problem in electrode-kinetic studies, especially of porous or high-area electrocatalyst materials that are commonly employed in various practical applications to minimize polarization power losses. The values of the determined real surface area are usually found to be dependent on the nature of the method applied. Basically, the techniques used for measurements of real surface area can be divided into two categories [79]: *ex situ* and *in situ* methods.

The *ex situ* methods, typically BET and mercury porosimetry, measure the geometric area or pore volume fraction that is accessible to either an inert gas or mercury under pressure. However, the measured geometric area may not, by any means, be necessarily that which is wettable by electrolytes or that which is electrochemically active or accessible for electrode reactions.

The existing, commonly used *in situ* methods may be divided into three groups [79]: (i) methods based on measurements of the double-layer capacitance, C_{dl}, in potential ranges where double-layer charging and discharging are the only processes [209-212] ("ideal polarizability" region); (ii) methods based on the Gouy-Chapman-Stern theory to determine the diffuse-layer capacitance, C_d, e.g. as proposed by Parsons and Zobel [81]; and (iii) methods for measurement of the monolayer extent of adsorption of an indicator species, e.g. underpotential-deposited H

[89,112,115], metals [213] or suitable organic probe molecules [214,215], or the charge for oxide monolayer formation [216-218], depending on the electrode metal.

In the case of Hg electrodes in electrolytes where the interface is ideally polarizable over an appreciable range of potentials, the determination of C_{dl} by means of a.c. impedance or charging transient methods is well known and unambiguous. Also, the method of potential-relaxation, following current interruption (which is part of the subject matter of this section), can also be applied, giving C_{dl} for the case of Hg [192]. The method (i) depends on assumption or knowledge of some absolute value for C_{dl} at the same smooth reference surface.

The *in situ* methods of groups (i) and (iii), as mentioned above, are not normally applicable in the *overpotential* region where the simultaneous Faradaic current is usually very much greater than either the double-layer charging current or the current corresponding to the formation or desorption of a monolayer of ad-species; in any case, the latter two currents are transient. The methods of group (ii) also may not be good candidates, since they all require a sufficiently dilute solution that the diffuse-layer capacitance is small, which cannot be satisfied for the conditions under which most practical electrochemical processes are operated.

In the present work, a method based on analysis of the open-circuit potential-relaxation behaviour at an electrode, following interruption of a polarizing current, as described in Section 3.3, was developed for the measurement of C_{dl} within the overpotential region [82,83,90,219]. The a.c. impedance method has also been used as a complementary comparative procedure.

The real, electrochemically active, area of a rough or porous electrode can be calculated from the experimentally determined value of C_{dl} in the overpotential region if the C_{dl} for the corresponding smooth, flat electrode is known or measurable under the same conditions. For

practical purposes, in comparing the performance of one porous electrocatalyst with another, it is usually the relative values of the real/apparent area ratio, R, of the preparations that are required rather than their exact values; hence, the value of the C_{dl} per real cm^2 for the corresponding smooth electrode material may not be required exactly; a tolerance of $\pm$ 15-20% may be acceptable since R values for practical porous electrocatalyst materials are often 100 to 500 x [72].

The HER from KOH solution on a bright, smooth Pt electrode and a porous, plated Pt one (platinized Pt) was examined comparatively as a prototype system. It is believed that this system provides the best example for C_{dl} measurements in the overpotential region, since the kinetics of the HER and its associated H-adsorption pseudocapacitance at a Pt electrode have been well investigated previously [72,101]. Moreover, the Pt electrode has the unique characteristic that its real, electrochemically accessible, surface area can be directly measured *in situ* reliably and accurately by means of slow cyclic voltammetry using the well established monolayer u.p.d. H charge, and its value checked for constancy over a range of sweep-rates in linear sweep voltammetry. This then provides a reliable standard for the R value of the porous Pt electrode against which values determined by other method as described below, can be compared and the methods thus validated, or otherwise.

Experimental conditions of the electrochemical experiments and the theoretical bases of the methods have been described in the previous sections. The following will describe experimental measurements on real surface areas of some porous electrodes in comparison with those of smooth ones by several experimental techniques. The validity of the initial potential-relaxation technique for *in situ* determination of C_{dl} will then be verified.

4.II.1.2 Evaluation of Real-Area by the Cyclic Voltammetry Method

Fig.4.II.1a shows the CV profile for a bright Pt electrode used in 0.5 M H_2SO_4 solution. The significance of the u.p.d. H peaks has been investigated fully elsewhere [89]. The charge under the CV peaks, corrected for double-layer charging, corresponds to adsorption of a monolayer of H adatoms with one H per Pt metal atom in the surface. For smooth polycrystalline Pt, the commonly accepted value of this charge, q_1, is 210 ± 3 μC cm^{-2} [220]. The real surface area of the Pt electrode used, calculated from the H desorption peaks in Fig.4.II.1, taking $q_1 = 210$ μC cm^{-2}, is 0.537 ± 0.005 cm^2. Therefore, the roughness factor (real/geometric area) of the smooth Pt electrode used was 1.68 (geometric area = 0.32 cm^2). All experimental current-densities and C_{dl} values per cm^2 reported here are based on this real surface area of 0.537 cm^2.

The SEM picture of the platinized Pt electrode used in this experiment was already illustrated in Fig.2.3. Fig.2.3b shows one of the spherical regions seen on the surface displayed in Fig.2.3a. Fig.2.3c shows an enlargement of the edge area between the spherical structure and the flat surface. It is seen that, microscopically, the surface of the plated Pt electrode is piled up uniformly with small particles having dimensions of length $l \approx 0.2$ and width $d \approx 0.02$ μm. The thickness of the plated Pt layer is ca. 2-3 μm and from the SE micrographs it is evident that the plated Pt electrode contains shallow pores at the surface. The real/apparent surface area ratio for the plated Pt electrode should evidently be quite large.

Fig.4.II.1b shows the CV profile for the plated porous Pt in 1.0 M H_2SO_4 at a potential sweep rate of 0.01 V s^{-1}, noting that the y-axis is for apparent current-density. The CV profile in Fig.4.II.1b is very similar to that for the bright Pt electrode under the same conditions. This

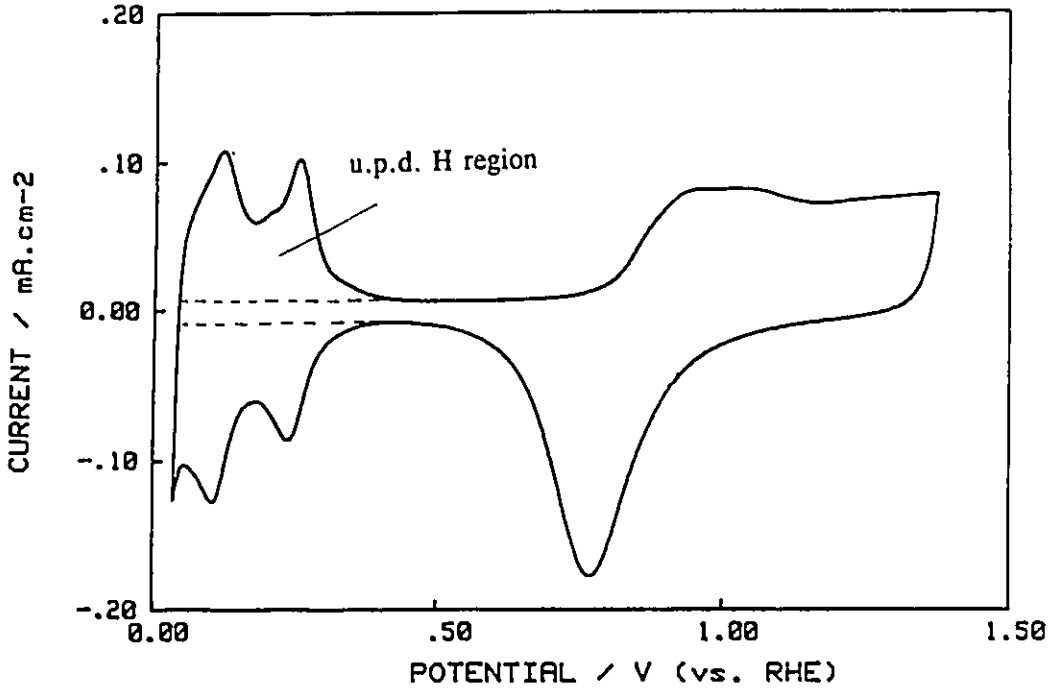

Fig.4.II.1 (a) Cyclic voltammetry plot for a bright Pt electrode in 0.5 M H_2SO_4 solution. Sweep-rate is 20 mV/s.

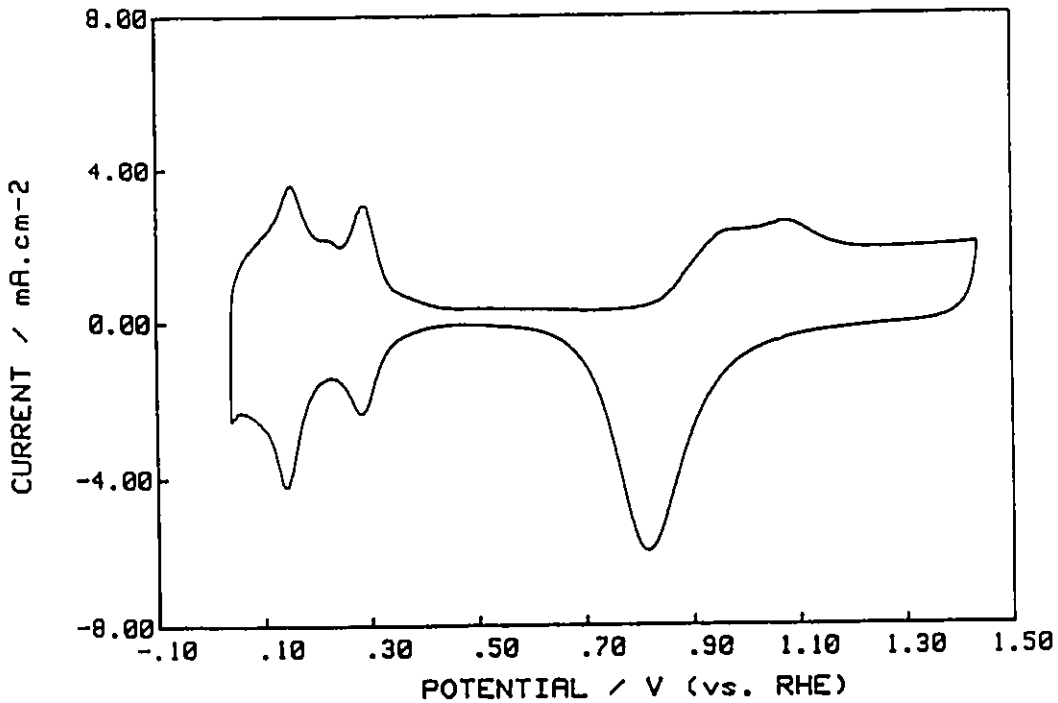

Fig.4.II.1 (b) Cyclic voltammetry plot for the plated Pt electrode in 1 M H_2SO_4 solution. Sweep-rate is 10 mV/s.

implies that diffusion processes and the electrolyte resistance effect inside the pores are insignificant at such a low sweep-rate and high concentration of acid. It was observed, however, that the CV profile started to become distorted at sweep-rates greater than 0.04 V s^{-1}. This is, of course, due to kinetic and IR effects [222,225] on the form of the CV profile. However, provided the voltage excursion is maintained sufficiently large in the (anodic) sweep, the same charge will be evaluated from the integral of the I vs V profile independent of the involvement of kinetic irreversibility and IR-drop effects on the CV profile.

The roughness factor of the plated Pt electrode is found to be 25 based on comparison with that for the bright, smooth Pt electrode, calculated by comparing the total charge under the u.p.d H peaks with a correction for the double-layer charging contribution.

It should be emphasized that the completion of the u.p.d. monolayer of H just prior to onset of a measurable rate of H_2 evolution takes place only with Pt, Ir and Rh electrodes [220]. Pt, Ir or Rh are thus the only electrode materials whose real surface areas per apparent cm^2 can be measured *in situ* reliably and accurately by the CV method under conventional conditions. Therefore, the present experimental investigations are on a firm and absolute basis, i.e. the real surface area of the electrode (as a reference value) was known exactly by a reliable method. This is especially important in the case of comparing the real area of the porous plated Pt electrode with that of the bright Pt one by means of other (non CV) methods, as will be described below.

4.II.1.3 Evaluation of C_{dl} from Initial Potential-Relaxation Transients

In Section 3.3, the method of *in situ* C_{dl} determination from the initial regions of potential-relaxation transients was thoroughly and critically described, and tested in various

ways. Based on procedures described in Section 3.3, C_{dl} can be satisfactorily distinguished from the influence of C_ϕ due to an adsorbed intermediate. In this part of work, bright and platinized Pt electrodes were used comparatively as a test model for determination of C_{dl} and hence the ratio of real/apparent surface area of the porous, plated Pt electrode was obtained. The resulting values could then be compared with the "exact" value based on u.p.d. H accommodation, and the method thus validated, or otherwise, as explained in Section 4.II.1.1.

Fig.4.II.2a shows experimental open-circuit potential-relaxation curves, over a full range of time, for the HER at the bright Pt electrode in 2 M KOH solution with the following initial current-densities: (1) 2.47 x 10^{-2}; (2) 1.60 x 10^{-2}; (3) 1.07 x 10^{-2} and (4) 6.50 x 10^{-3} A cm^{-2}. Fig.4.II.2b shows both experimental (square points) potential-relaxation curves in the initial time range (5 x 10^{-6} - 2 x 10^{-3} s) corresponding to the curves in Fig.4.II.2a, and the fitted curves (solid lines), using eqn.(3.14) for the procedure as described in Section 3.3. The experimental conditions and results from the fitting procedure for each curve in Fig.4.II.2b are listed in Table 4.II.1.

Table 4.II.1 C_{dl} values for the bright Pt electrode (s = 0.537 cm^2) in 2 M KOH, derived by the initial potential-relaxation rate method (from Fig.4.II.2b)

curve	$-\eta$/V	$i_{t=0}$/A cm^{-2}	$-(d\eta/dt)_{t=0}$ / V s^{-1}	C_{dl}/μF cm^{-2}
4	0.248	6.50×10^{-3}	225	28.8±0.5
3	0.283	1.07×10^{-2}	380	28.1±0.5
2	0.314	1.60×10^{-2}	600	26.7±0.5
1	0.348	2.47×10^{-2}	934	26.4±0.5

The full-range potential-decay curves in Fig.4.II.2a are quite similar to the theoretically simulated curves shown in Fig.3.1a. They are characterized by two distinguishable regions: in

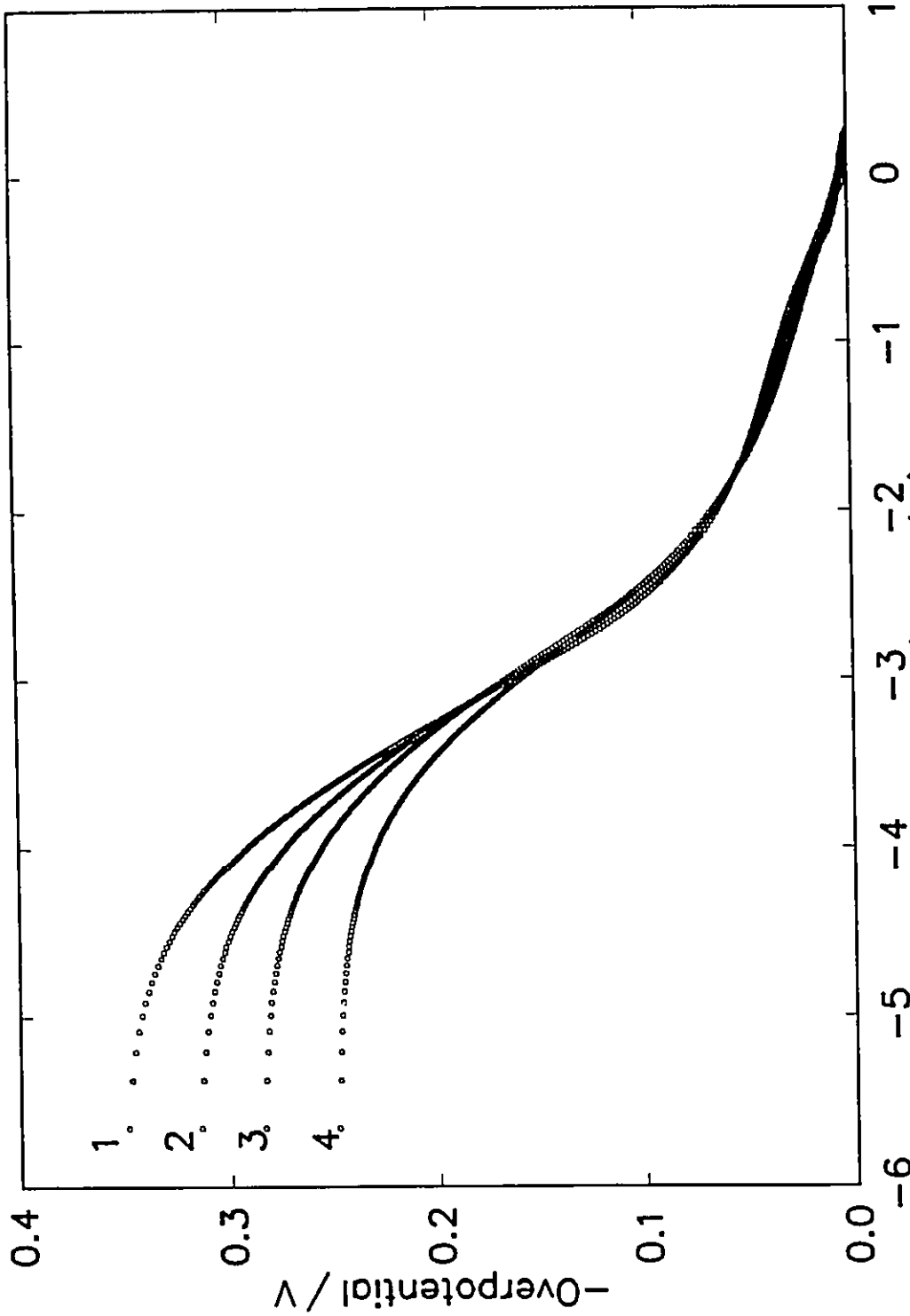

Fig.4.II.2a Full-range potential-relaxation transients for the HER at the bright Pt in 2 M KOH solution. $i_{t=0}$ are (1) 24.7; (2) 16.0; (3) 10.7 and (4) 6.5 mA cm^{-2}, respectively.

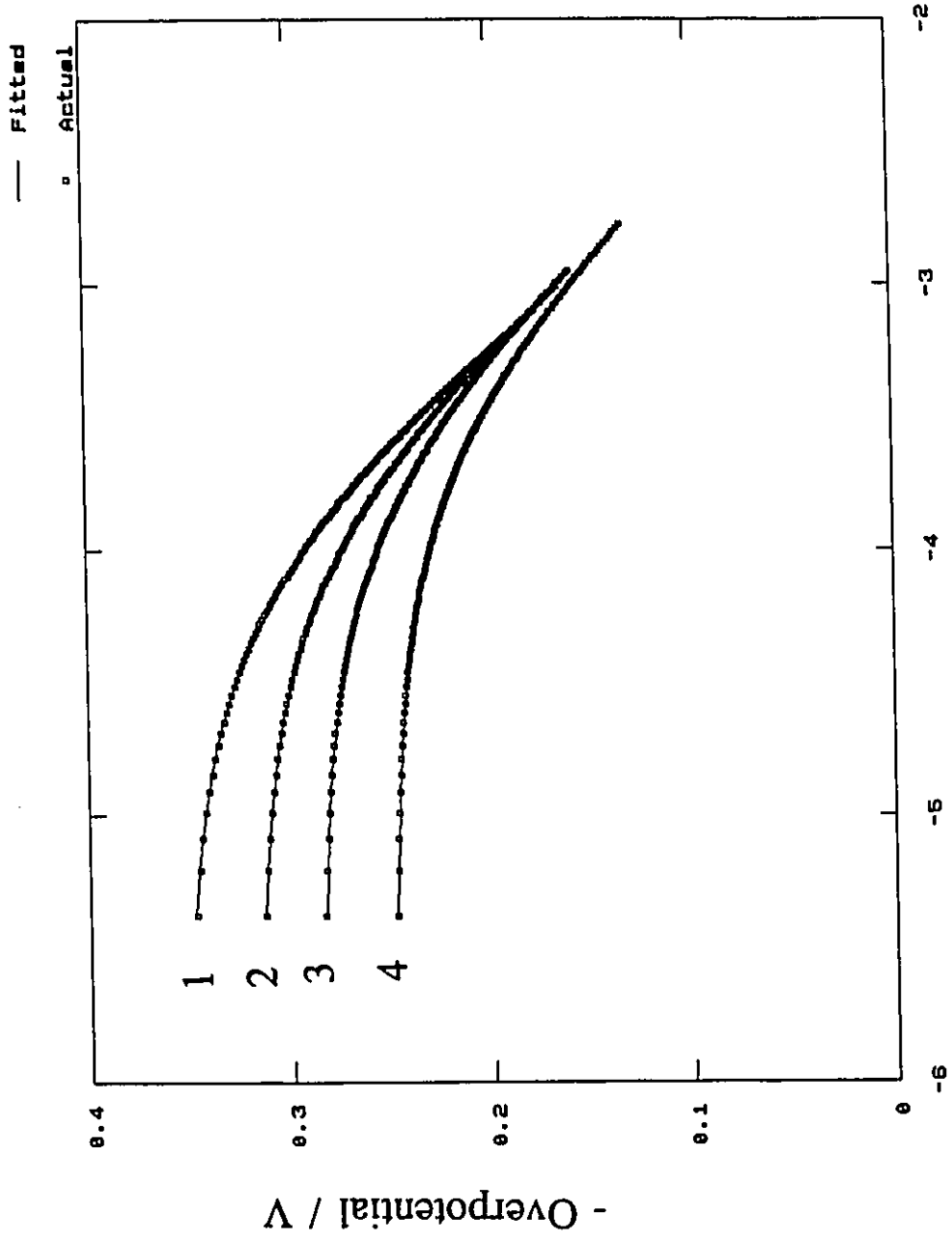

Fig.4.II.2b Initial potential-relaxation transients corresponding to the curves in Fig.4.II.2a. Solid lines are best-fitted results to the experimental data (points).

the short time range, 10^{-6} - 10^{-3} s, it is only C_{dl} that is discharged through the charge-transfer resistance while, over the longer time range, 5 x 10^{-3} - 1 s, discharge of the C_{ϕ} becomes dominant in the transient behaviour. A *constant (average) value* of C_{dl}, 27.6 $\pm$ 1.0 μF cm^{-2}, was determined by applying the initial potential-decay rate curve-fitting procedure (Section 3.3) to the curves over the restricted time range of 10^{-6} - 10^{-3} s.

Fig.4.II.3 shows experimental (points) and fitted (solid lines) potential-relaxation curves over an initial short range of time (5 x 10^{-6} to 10^{-3} s), for the HER at the plated Pt electrode in 4 M KOH solution, taken from four initial current-densities (Table 4.II.2). A similar fitting procedure was used as for the bright Pt electrode. The results from the fitting are listed in Table 4.II.2. It is seen the potential transients begin to fall linearly with log t over longer time domain, since the τ value is bigger for this porous electrode (see discussion in Section 3.3).

The full range potential-relaxation curves are again characterized by two distinguishable regions (not shown here), similar to the case of the bright Pt electrode. A constant value of C_{dl}, 8.3 $\pm$ 0.2 mF cm^{-2} for the porous Pt electrode, was obtained from the fitting procedure to the curves over the time range of 5 x 10^{-6} to 10^{-3} s. The roughness factor of the plated Pt compared with bright Pt is then obtained as 301$\pm$5.

Table 4.II.2 C_{dl} values for the plated Pt electrode (s = 0.197 cm^2) in 4 M KOH, derived by the initial potential-relaxation rate method (from Fig.4.II.3)

curve	$-\eta$/V	$i_{t=0}$/A cm^{-2}	$-(d\eta/dt)_{t=0}$ / V s^{-1}	C_{dl}/mF cm^{-2}
1	0.164	0.866	103.6	8.36
2	0.146	0.632	75.3	8.39
3	0.133	0.499	59.2	8.43
4	0.121	0.380	45.9	8.28

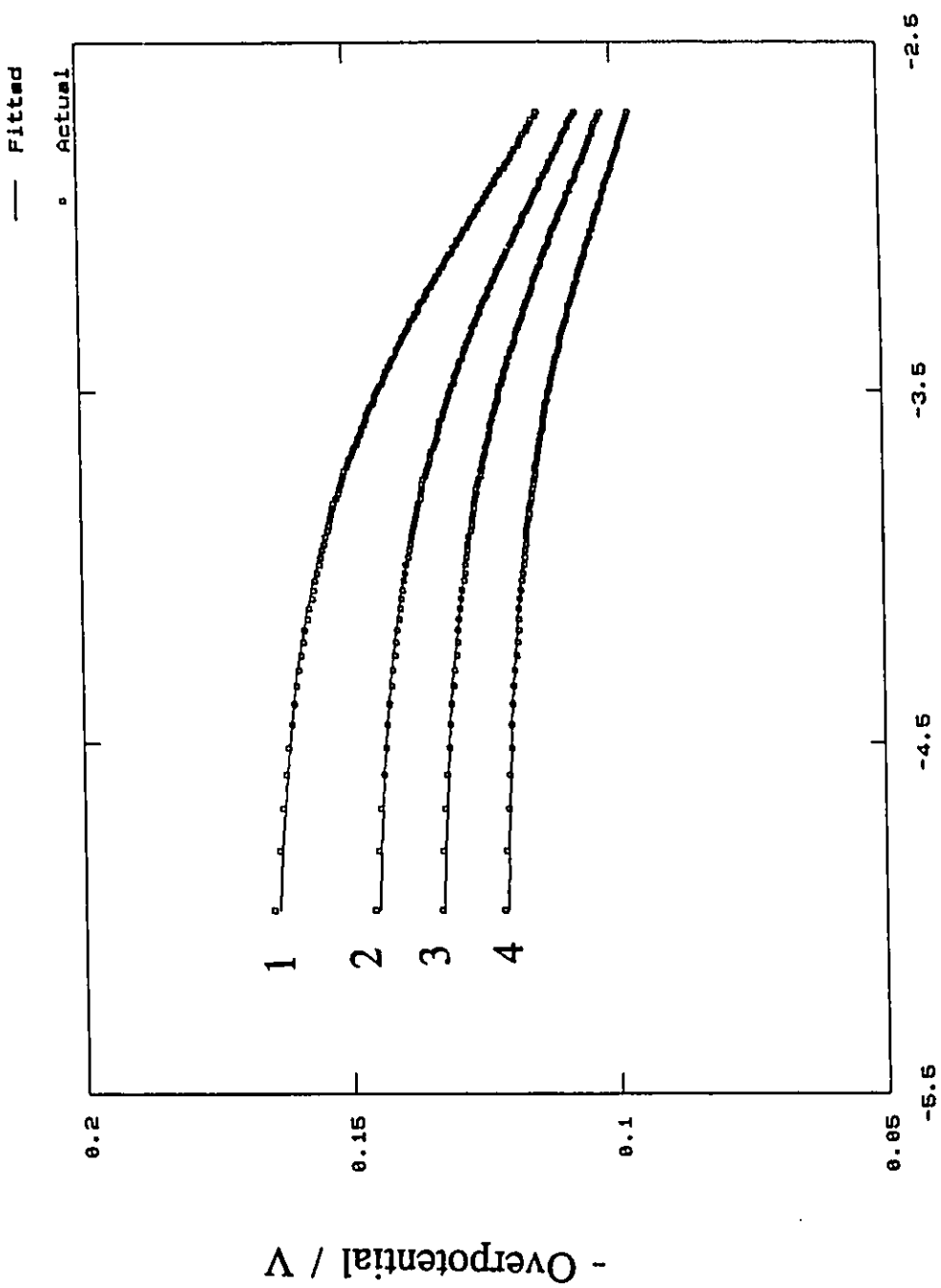

Fig.4.II.3 Initial potential-relaxation transients for the HER at the plated Pt in 4 M KOH solution. $i_{t=0}$ are (1) 0.87; (2) 0.63; (3) 0.50 and (4) 0.38 A cm^{-2} respectively. Solid lines are best-fitted results to the experimental data (points).

4.II.1.4. A.C. Impedance Results at Pt Electrodes

In this Part, the *in situ* method of frequency response impedance procedures will be described and applied to the porous plated Pt electrode. Especially, the dependence of the experimentally measured apparent porosities of the plated Pt electrode upon the conductivity of the electrolyte will be examined.

4.II.1.4.1 Transmission-Line Model

Discussions related to the CPE model were reviewed in a recent publication [188], and referred to Section 4.I.3.1. Scheider [203], for example, suggested a branched transmission line to model the experimental CPE behaviour.

Various attempts have, however, been made to account for the effect of surface roughness of a self-symmetric kind on impedance behaviour in terms of fractal surfaces [204-206] since the fractional exponent, α, in the empirical representation of CPE behaviour can be directly related to the fractal dimension, D, $\alpha = (D - 1)^{-1}$. However, interfaces having a fractal character do not always exhibit CPE behaviour [202,205]. Related problems of current distribution have been dealt with in sophisticated ways [87,223] but have led to controversial conclusions [204-206].

The transmission line model [87] for a single pore is illustrated in Fig.4.II.4a in which R_l and R_s are the ohmic resistances of the electrolyte and the solid electrode material, respectively, Z_f is the electrode-reaction Faradaic impedance and C_{dl} is the double-layer capacitance. Essentially, the inhomogeneity of the distribution of current and potential in a pore is caused mainly by IR_l-drop across elements of the ohmic solution resistance under a constant electrode potential. (For most metal electrodes, R_s can be considered as effectively negligible).

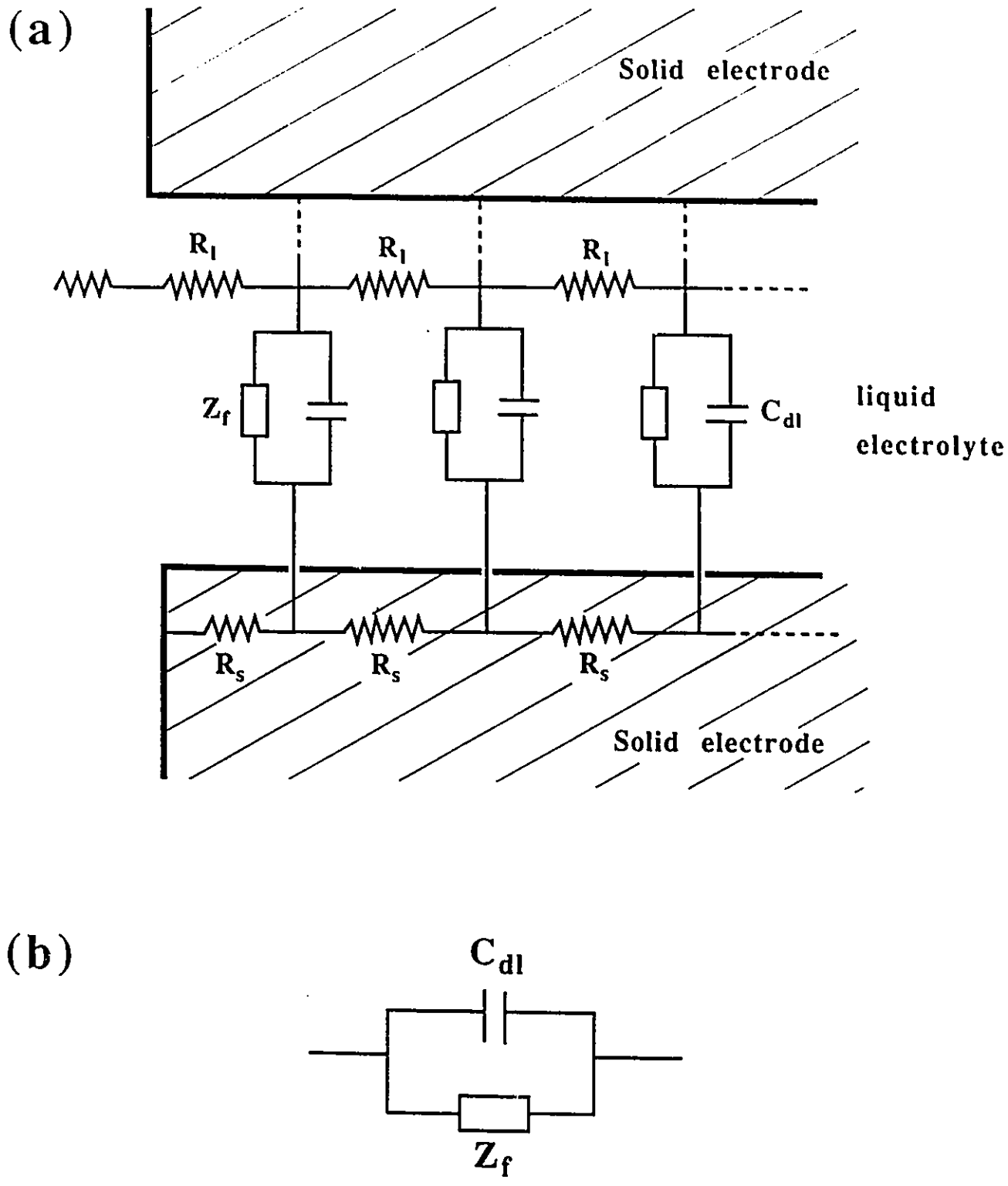

Fig.4.II.4 (a) Transmission-line model for a single pore. R_l and R_s are the ohmic resistance of the electrolyte and the solid electrode material, respectively, Z_f is the electrode faradaic impedance and C_{dl} is the double-layer capacitance. (b) When $R_l=R_s=0$, the equivalent circuit in (a) becomes that shown as (b).

In terms of transmission-line theory, the effective signal penetration depth is proportional to $(Z_f/R_l)^{1/2}$. The transmission-line model predicts that for a semi-infinite pore (i.e. the pores behave as though they are infinitely deep), the phase angle of the pore impedance is half that of the interfacial impedance which would be measured if the electrodes were flat.

The transmission-line model has proven to be highly successful; however, calculations and experimental results [87] have shown that transmission-line models become unreliable for shallow pores, i.e. when the pore diameter becomes comparable with or larger than the effective signal penetration depth, $(Z_f/R_l)^{1/2}$. That is, in the cases of geometrically shallow pores and/or significantly small solution resistances, the transmission-line model needs to be modified. For example in Fig.4.II.4a, if $R_l = R_s = 0$, i.e. the conductivity of both electrode and electrolyte are sufficiently high, then the equivalent circuit in Fig.4.II.4a can be simplified to the one shown in Fig.4.II.4b which, in fact, represents a flat electrode. In terms of transmission-line theory, the effective signal penetration depth can become semi-infinite if the solution resistance, R_l is sufficiently small.

Therefore, the key factor is to eliminate or minimize the solution's ohmic resistance inside pores (R_s can be neglected for most practical porous metal electrodes). If the electrolyte resistance could be reduced to negligible values, then the potential-relaxation and the impedance behaviour of the porous electrode having sufficiently shallow pores could experimentally be 'unfolded' completely with respect to electrochemical kinetic accessibility of the total surface.

4.II.1.4.2 A.C. Impedance Experimental Results and Analysis for Pt Electrodes

The experimental impedance data (+ points) for the HER at the bright Pt electrode in 2 M KOH are shown in Fig.4.II.5 in which (a) are Z' vs Z" complex-plane plots, (b) and (c)

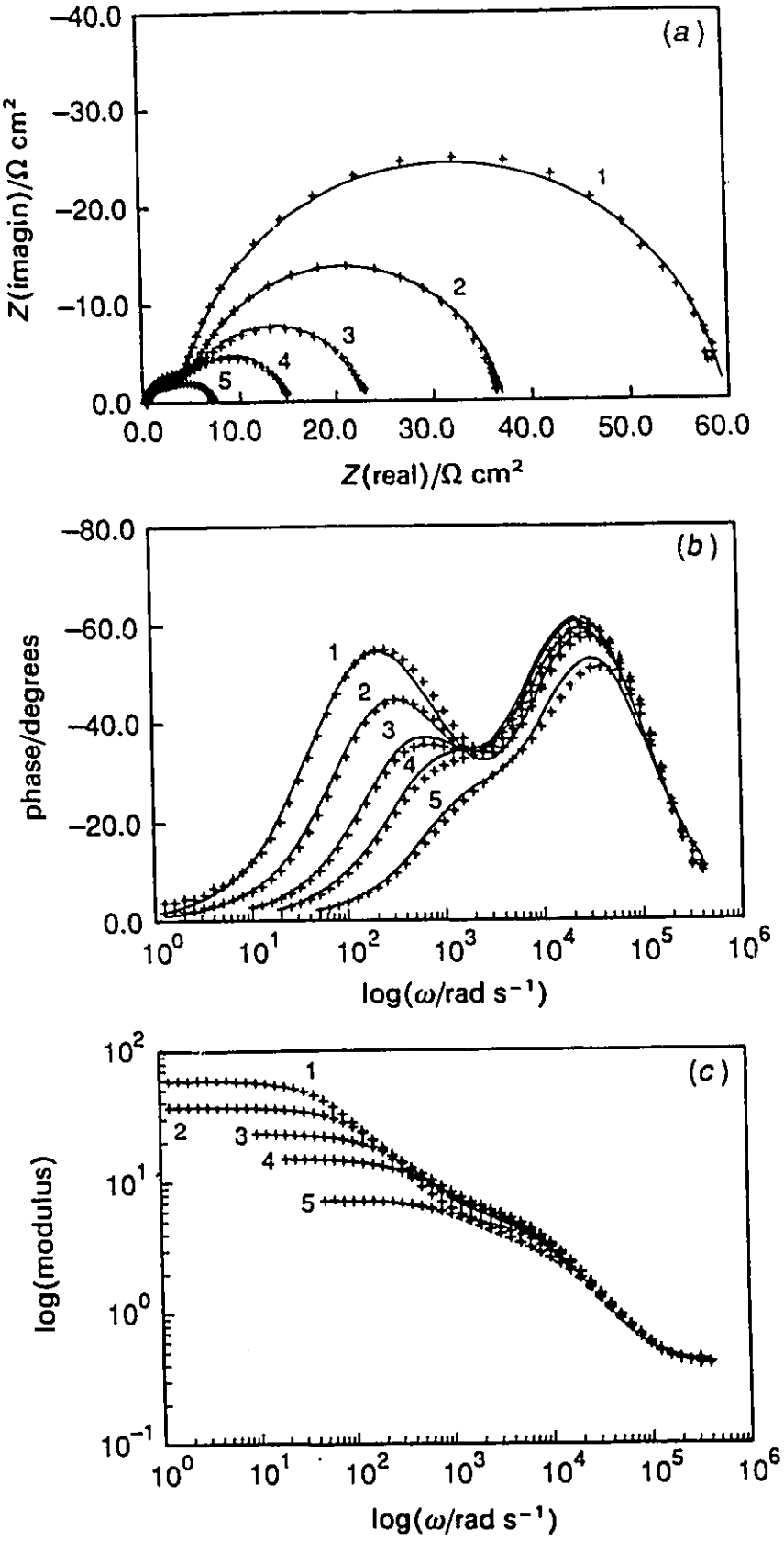

Fig.4.II.5 Impedance results (+) fitted by means of the equivalent circuit in Fig.4.I.13b (solid lines) for the HER at bright Pt in 2 M KOH solution. (a) complex-plane plots; (b) Bode phase plots and (c) log|Z| vs log ω plots.

are Bode plots in phase and log (modulus) vs log (angular frequency), respectively. The d.c. overpotentials are (1) -0.03, (2) -0.05, (3) -0.075, (4) -0.10 and (5) -0.15 V, respectively. Note that, in Fig.4.II.5a, two semi-circles are well resolved in the complex-plane plots, and two corresponding maxima in the phase-angle plots (Fig.4.II.5b). The responses in the low-frequency region correspond to C_ϕ associated with potential dependence of chemisorption of the o.p.d. H, and those in the high-frequency region to C_{dl}. This C_ϕ response, arising on account of appreciable coverage at Pt by the o.p.d. H intermediate, corresponds to the arrest in the potential-relaxation plots in Fig.4.II.2a in the time domain ca. $10^{-2.3}$ to $10^{-0.5}$ s. The significant coverage of Pt by o.p.d. H is clearly brought out by these results, confirming the conclusions of some previous work done in this lab [72,101].

In Fig.4.II.5, the corresponding solid lines represent the best-fit curves in terms of the equivalent circuit of Fig.4.I.13b, while the best-fit values of the equivalent circuit elements are listed in Table 4.II.3.

Table 4.II.3 The best-fit values of the equivalent circuit elements of Fig.4.I.13b for the data shown in Fig.4.II.5

curve	η/mV	$R_1/\Omega cm^{-2}$	$T_1(C_{dl})/\mu Fcm^{-2}$	α_1	$R_2/\Omega cm^{-2}$	$T_2/(\mu Fcm^{-2})^{\alpha 2}$	α_2
1	30	4.45	27.9	1.0	54.8	505	0.91
2	50	5.51	28.1	1.0	31.1	492	0.90
3	75	5.96	27.7	1.0	16.2	410	0.91
4	100	4.96	27.9	1.0	9.40	430	0.89
5	150	3.24	28.1	1.0	3.36	520	0.90

It can be seen from Fig.4.II.5 that the fitting was excellent. Since $\alpha_1 = 1.0$ (see Table 4.II.3), the parameter corresponds, in fact, to the behaviour of a pure capacitor which can hence

be identified with the double-layer capacitance, C_{dl}. In other words, the double-layer capacitance is homogeneously distributed over the bright Pt electrode surface as might be expected for the HER in 2 M KOH solution. The best-fit value for C_{dl} is found to be constant, 27.9 $\pm$ 0.2 μF cm^{-2}, almost independent of potential.

However, the parameter α_2 in Table 4.II.3 differs from 1.0 (α_2 = 0.90 $\pm$ 0.01), which indicates that T_2 does not represent a pure capacitance. This implies, interestingly, that the bright Pt electrode surface, although homogeneous with respect to its double-layer capacitance, is not homogeneous for the o.p.d. H adsorption reaction, that is, the distributions of C_{dl} and C_ϕ on the Pt electrode surface are significantly different. This is consistent with the conclusions from our previous studies, in which it was deduced that the adsorption of o.p.d. H arose only on some active site fraction of the Pt electrode surface, and with the conclusions of Frumkin et al. [221] on this point, for the kinetic and adsorption behaviour of the HER at Pt.

Figs.4.II.6 and 7 show the experimental data (cross points): (a) the impedance complex plane Z' vs Z" plots and (b) the Bode phases vs log ω plots, for the HER at the porous plated Pt electrode in 2.0 and 0.5 M KOH solutions, respectively. A similar experiment was also carried out at the same porous Pt electrode in 1 M KOH solution for the purpose of comparison. The best-fit values of the equivalent-circuit elements for each curve in various concentration of KOH solutions are listed in Table 4.II.4.

It can be seen that the fittings of the experimental curves in Fig.4.II.6 are mostly excellent. The poorer fitting in Fig.4.II.7 is due to lower conductivity of the electrolyte (0.5M), while the seriously depressed 'semi-circles' cannot be fully described by the equivalent circuit in Fig.4.I.13b.

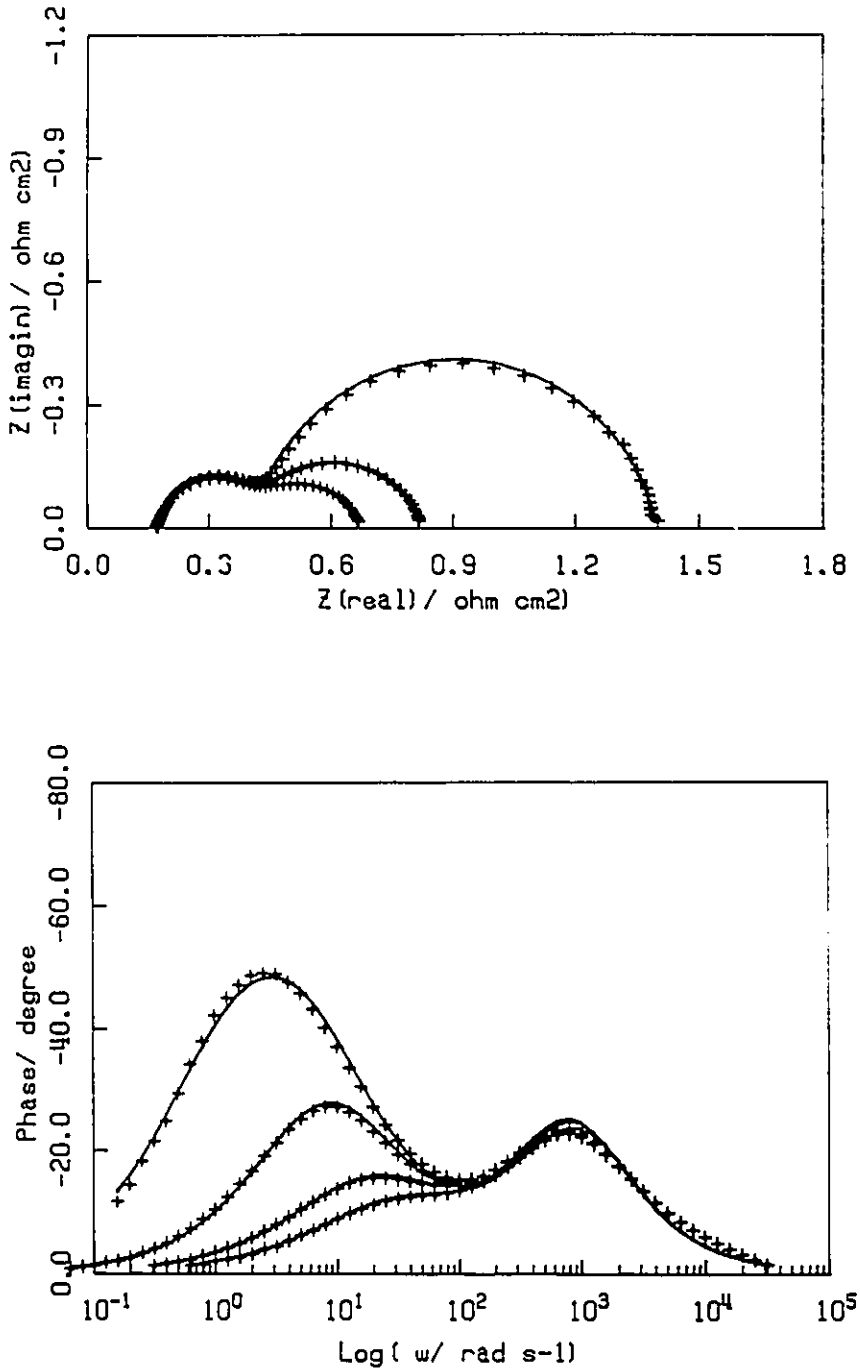

Fig.4.II.6 Impedance results (+) fitted by means of the equivalent circuit in Fig.4.I.13b (solid lines) for the HER at plated Pt in 2 M KOH. (a) complex-plane plots; (b) Bode phase plots.

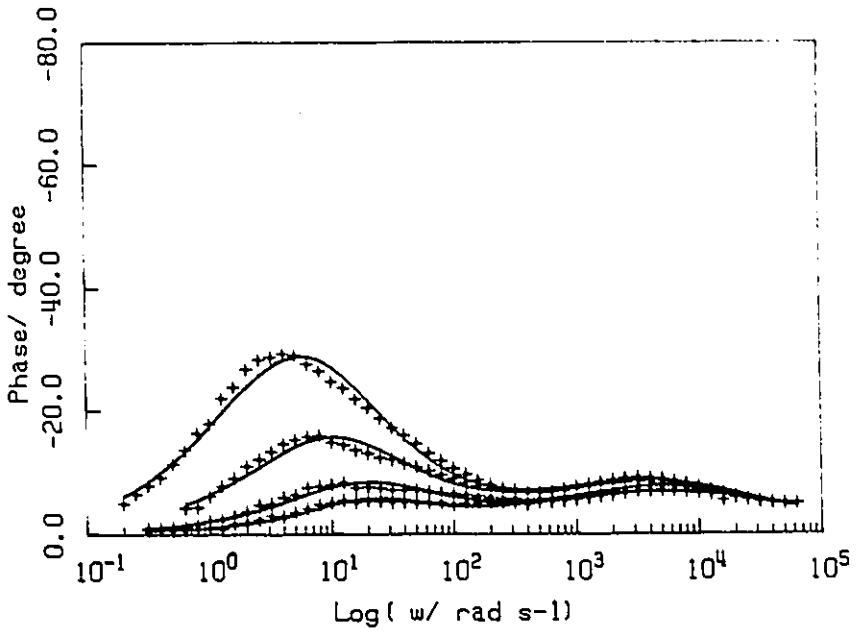

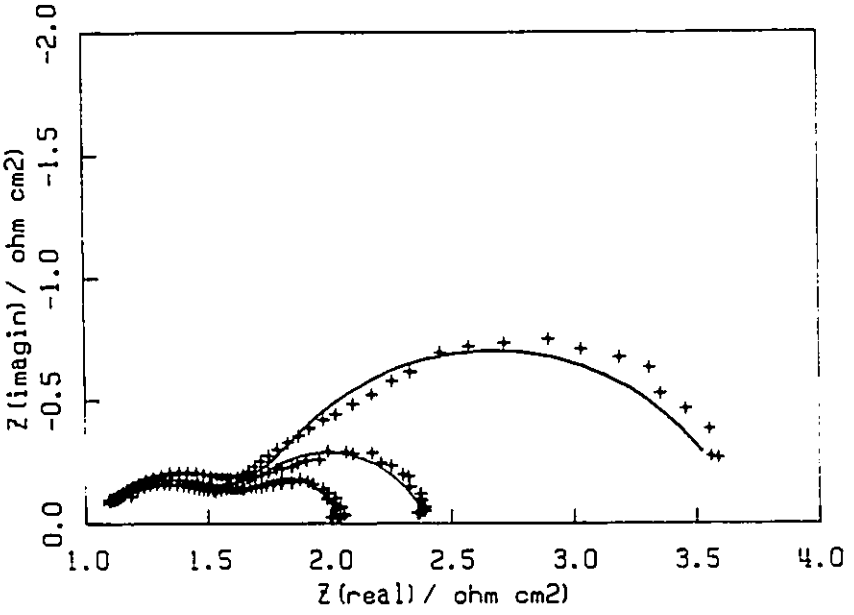

Fig.4.II.7 As for Fig.4.II.6, except that the concentration of KOH solution is 0.5 M.

Table 4.II.4 Summary of best-fit values of the equivalent circuit elements of Fig.4.I.13b for the data shown in Fig.4.II.6 and 7 in 2 and 0.5 M KOH respectively, in comparison with results in 1 M KOH at plated Pt electrode

Concentration of KOH / M	$T_1(C_{dl})$ /(mF cm^{-2})$^{\alpha 1}$	α_1	$T_2(C_\phi)$ /(mF cm^{-2})$^{\alpha 2}$	α_2
0.5	29.5 - 51.3	0.55 ± 0.03	218 - 483	0.85 ± 0.05
1.0	23.7 - 26.3	0.72	202 - 513	0.82 ± 0.03
2.0	7.3 ± 0.3	1.0	281 - 372	0.82 ± 0.05

From the impedance results and fitted data shown above, the following conclusion can be drawn. First, the observation of two semi-circles in the complex-plane plots (Fig.4.II.6-7a) and the two peaks in the Bode phase plots (Fig.4.II.6-7b) indicate that mainly the time-constants associated with two capacitances determine the modulation and resulting frequency response behaviour of the system.

It was found that the impedance behaviour of the HER at the porous plated Pt electrode is actually quite similar to that at the bright Pt (see Fig.4.II.5). This suggests, incidentally, that there is no difference in reaction mechanism and H adsorption behaviour between the plated and bright Pt electrodes.

Secondly, as the concentration of KOH is changed from 0.5 to 1.0 and on to 2.0 M, which corresponds to the conductivity being increased [207] (see Fig.4.I.16), the values of α_1 become changed from 0.55 to 0.72 to 1.0, respectively. As predicted by the transmission-line model, $\alpha_1 = 0.5$ suggests that the electrode consists of semi-infinite pores (the pores behaving as though they are infinitely deep). In other words, in 0.5 M KOH, the plated Pt electrode behaves like a standard porous electrode but in 2.0 M KOH its porosity becomes 'unfolded', approaching the behaviour, in impedance, of a flat electrode. The key factor here is that the

penetration depth becomes larger as the conductivity of the electrolyte is increased. When the conductivity of the electrolyte has become sufficiently high, the ohmic resistances R_l, in Fig.4.II.4a, all become, of course, substantially diminished.

It is interesting to point out that, for the *same* plated Pt electrode, α_1 varies from 0.55 to 1.0 (see Table 4.II.4). This implies that α is not an intrinsic factor for a given porous electrode but is strongly dependent on the conductivity of the electrolyte solution. This result suggests that it is unjustified to calculate the geometrical properties or fractal structures of porous electrodes based on experimentally determined α values without considering the conductivity of the electrolyte used and other experimental conditions, as practised often in some of the studies in the recent literature [202,205].

The present results suggest how important it is in practical industrial applications to increase the conductivity of electrolytes for effective and maximized utilization of the total surface area of porous electrodes.

Thirdly, comparing the best-fit C_{dl} value for the plated Pt electrode in 2.0 M solution, 7.3 ± 0.3 mF cm^{-2} ($\alpha_1 = 1.0$, see Table 4.II.4) with that, 27.9 ± 0.2 μF cm^{-2}, measured for the bright Pt electrode ($\alpha_1 = 1.0$, Table 4.II.3), a roughness factor of 262 ± 10 would be obtained. This value is quite close to the "calibrated" result, 290, determined by the slow CV (u.p.d. H) method (see Section 4.II.1.2), and 301 ± 5, obtained from initial potential-relaxation (see section 4.II.1.3). In other words, in sufficiently concentrated KOH solution, the real electrochemical surface area of the plated Pt electrode can evidently be determined by using the impedance method for evaluation of C_{dl} values.

Finally, it can be seen from Table 4.II.4 that a much larger time constant T_2 value is also

obtained, as observed for a bright Pt electrode, which corresponds to the pseudocapacitance, C_ϕ, contributed by adsorption of the H intermediate in the HER. C_ϕ is potential dependent, as may be expected. The α_2 values for both bright and porous Pt electrodes are in the range 0.8 - 0.9, smaller than unity, suggesting inhomogeneous adsorption of the MH_{ad} intermediate.

4.II.2 Real-Areas of Porous Ni-Mo-Cd Electrodes in KF·2HF and KOH·2H$_2$O Melts

From Section 4.II.1 above, it is seen that the method of initial potential-relaxation in determination of C_{dl} was proved to be reliable both on the basis of theoretical treatment and from the experimental results employing the prototype system at Pt electrodes by comparison of CV and a.c. impedance measurements; very good agreement was obtained from the results of various techniques. The method was then applied to some systems of practical interest. The electrocatalytic behaviour of the electrodeposited, porous Ni-Mo-Cd electrode was already described in Section 4.I.2 from Tafel and impedance measurements.

In this work, the real-areas of the composite Ni-Mo-Cd electrodes in the HER were examined by means of the initial potential-relaxation method in three media: the KF·2HF melt, the analogous KOH·2H$_2$O hydrate melt and comparatively in 0.5 M aq. KOH solution.

Fig.4.II.8 shows the initial potential-relaxation results (points) and the best fitted curves (solid lines) for initial current-densities of (1) 214; (2) 143; (3) 107; and (4) 71.5 mA cm^{-2}, respectively, at Ni-Mo-Cd in the KF·2HF melt. It was found that it was very difficult for the H_2 bubbles generated at the cathode in this melt to become detached due to an unfavourable contact angle; hence a cone-shaped electrode was made as a rotating electrode (200 rpm) from which H_2 bubble detachment could be facilitated. For comparison, a smooth, bulk, Ni-Mo alloy electrode was used in the melt assuming a similar mechanism at these two electrodes.

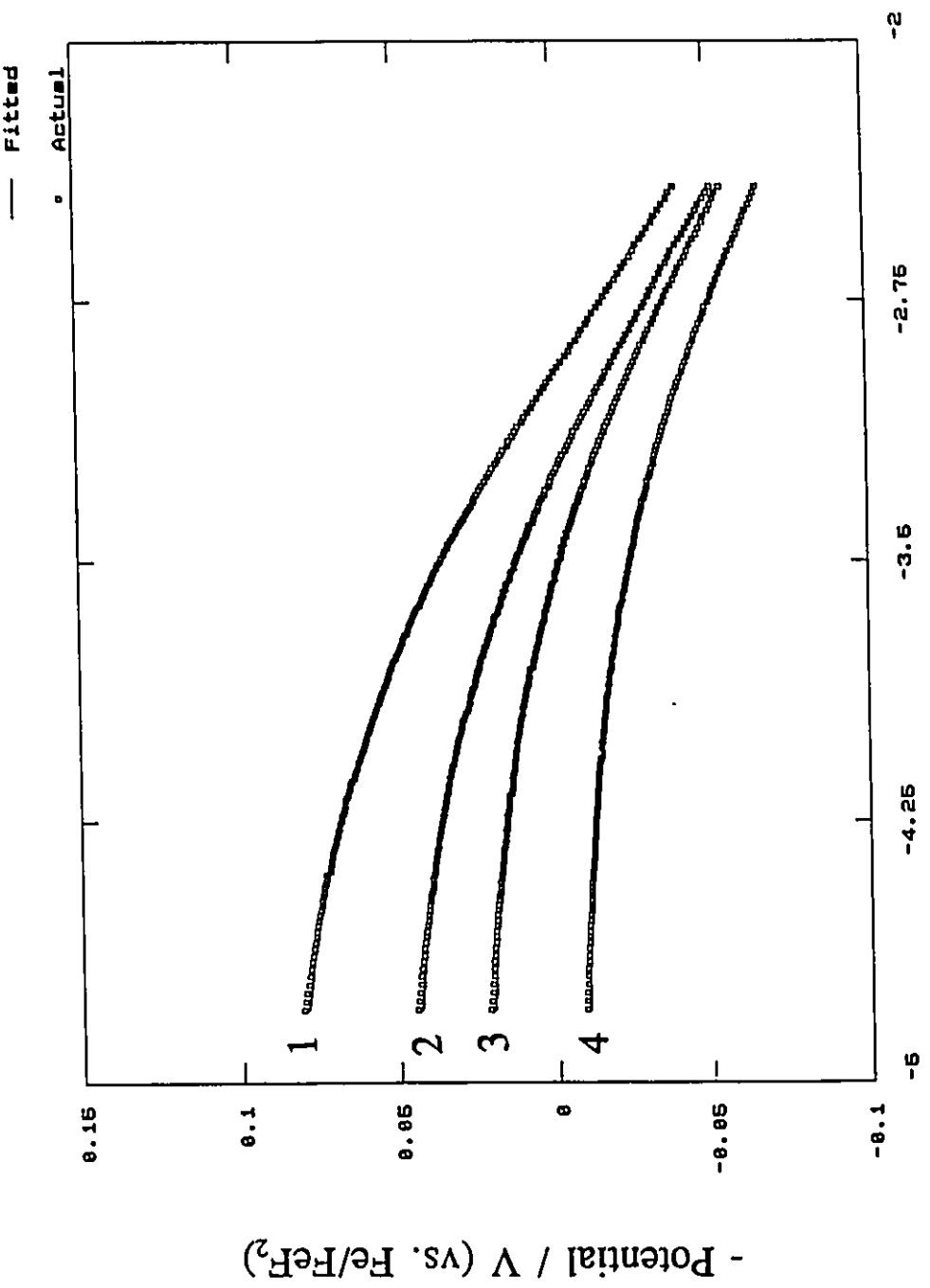

Fig.4.II.8 Initial potential-relaxation transients for the HER at the Ni-Mo-Cd in the KF·2HF melt. $i_{t=0}$ values are (1) 214; (2) 143; (3) 107 and (4) 71.5 mA cm^{-2}, respectively. Solid lines are best-fitted results to the experimental data (points).

The values of the measured C_{dl} of the porous Ni-Mo-Cd and the smooth Ni-Mo electrodes in the KF·2HF melt are shown in Fig.4.II.9a. The C_{dl} of the porous Ni-Mo-Cd electrode (solid circles) was found to have an average value of 810 ± 10 μF cm^{-2}, while the C_{dl} of the smooth Ni-Mo electrode (solid box) had an average value of 5.9 ± 2.0 μF cm^{-2}. The data for the smooth electrode were obtained at high cathodic potentials. This is because high overpotentials are more easily attained at smooth electrodes than at porous electrodes under the same currents, so that high η values are required on the smooth electrodes for C_{dl} determination by the potential-relaxation method. In this sense, high currents can be obtained at low overpotentials at the porous electrodes, which favourably minimizes the power consumption when such materials are employed as electrolysers. It is seen that the measured C_{dl} of the porous Ni-Mo-Cd electrode is two-magnitudes larger than that of the smooth Ni-Mo electrode and the roughness factor is calculated to be 140.

In fact, it was found that the behavior of the porous Ni-Mo-Cd electrode in the KF·2HF melt did not perform at all similarly to that in the aqueous media where C_{dl} [5] was found to be much larger than the value obtained here (see Section 4.I.2). A parallel experiment was carried out at this electrode in the analogue KOH·2H_2O hydrate melt. The experimental conditions were the same as before. The values of C_{dl} were obtained from initial potential-relaxation measurements as shown in Fig.4.II.9b. The gradual decrease of the measured C_{dl} with increasing cathodic potential is believed to be due to the effects of more filled pores by H_2 bubbles. The initial potential-relaxation method measures the real-area *in situ* just at the moment when the current is interrupted. Thus, it reflects the *in situ* surface condition when the gas was evolving.

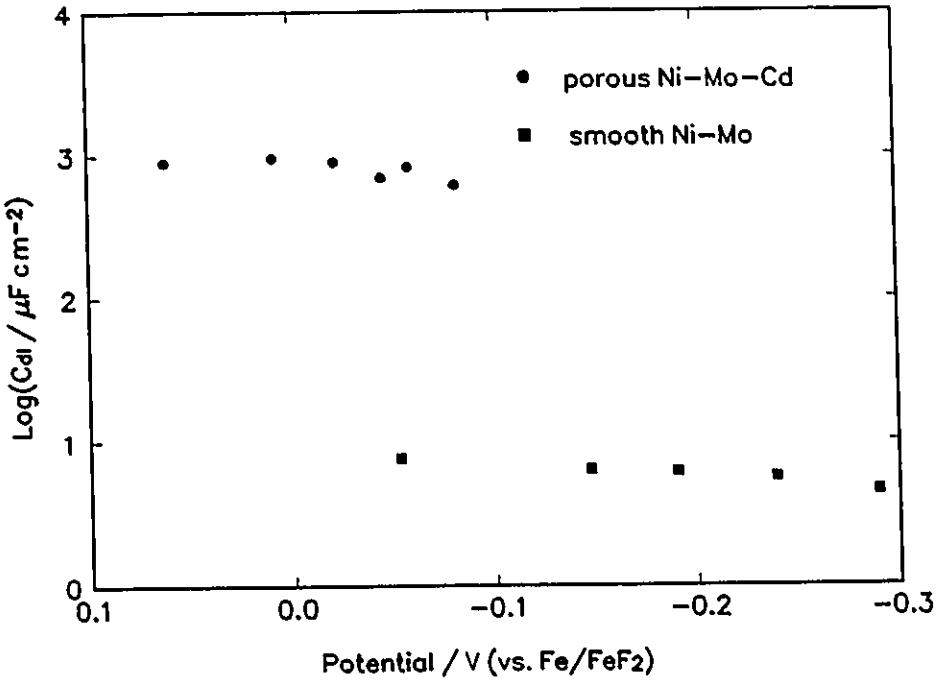

Fig.4.II.9a Log(C_{dl}) vs potential plots for the HER at the porous Ni-Mo-Cd (circle points) and smooth Ni-Mo (square points) electrodes in the KF·2HF melt derived by means of the initial potential decay rate method.

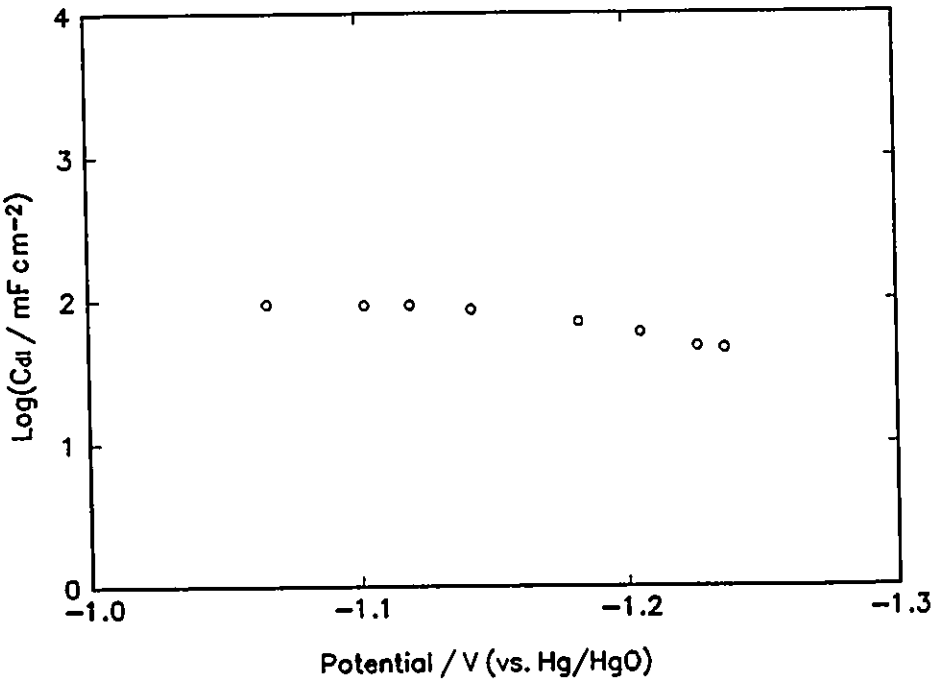

Fig.4.II.9b Log(C_{dl}) vs potential plots for the HER at the porous Ni-Mo-Cd electrode in the KOH·2H_2O melt derived by means of the initial potential decay rate method.

The average C_{dl} value over the potential region is calculated to be 73 $\pm$ 12 mF cm^{-2}. This is about two-magnitudes larger than the value in the KF·2HF melt at the same electrode. This interesting result indicates that, in addition to the electrode materials, the electrolytes involved in the study are also important factors in evaluating the performance in terms of apparent catalytic behavior in electrolysis processes. The total real-area of the Ni-Mo-Cd porous electrode may not be fully wetted because of the relatively high surface tension of the KF·2HF melt [176] and high contact angle at its interface with gases (see Section 4.I.2.3).

Fig.4.II.10a shows the curve fitting of initial potential-relaxation transients, plotted on a log time scale, for electrodeposited Ni-Mo-Cd in 0.5 M KOH at 298 K for the HER. The circles represent the experimental points and the solid lines the computer-fitted results obtained from eqn.(3.14). The goodness of fit of the experimental data is evidently excellent, so that from the fitted curve, the fitting constants can be reliably obtained and C_{dl} determined.

Fig.4.II.10b shows the plot of C_{dl} vs potential for the Ni-Mo-Cd electrode in 0.5 M KOH solution. An average value of about 90 $\pm$ 10 mF cm^{-2} was measured for Ni-Mo-Cd in the overpotential range 50 - 200 mV.

The capacitance value of 90 mF cm^{-2} is also larger than that obtained in the much more concentrated $KOH \cdot 2H_2O$ hydrate melt, for the same electrode material. One reason may be the different wettabilities of the electrode surface by the two electrolytes. It was found that the electrode had a smaller contact angle in 0.5 M KOH solution than the $KOH \cdot 2H_2O$ melt (see Section 4.I.2.3), so more inside pores of the porous Ni-Mo-Cd electrode are expected to be accessed by the former solution, thus the C_{dl} value is expected to be larger. It is known the conductivities of the solutions are widely different. High conductivity of solution leads to better

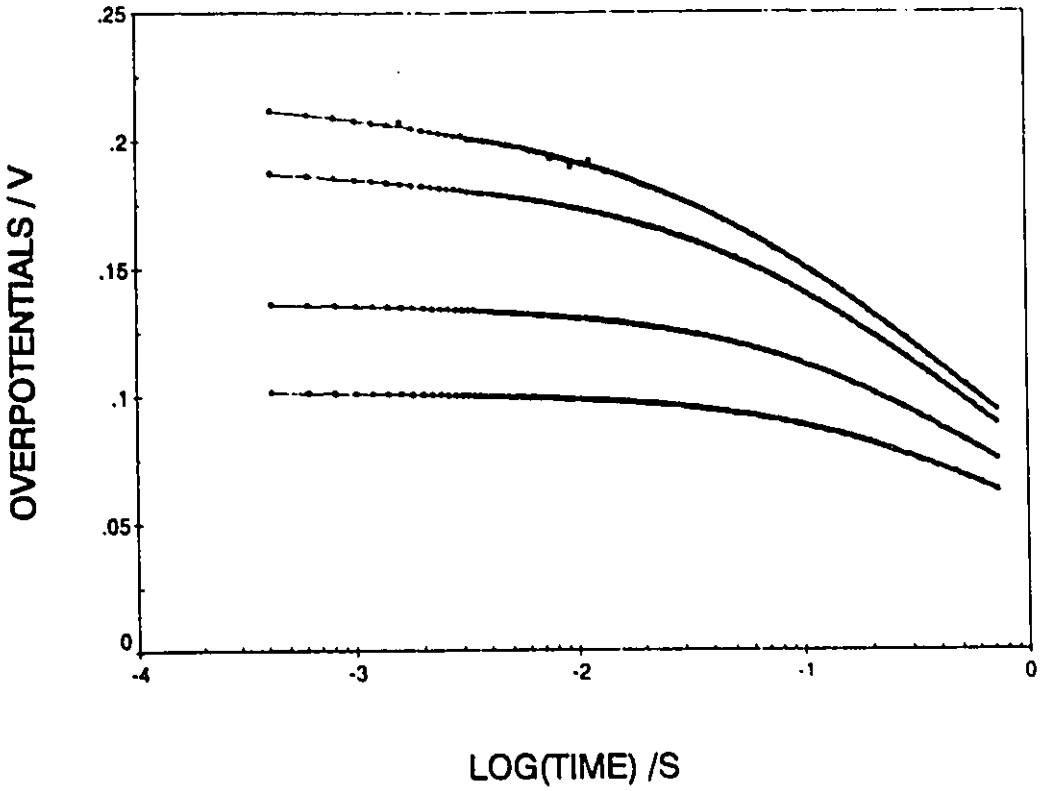

Fig.4.II.10a Initial potential-relaxation transients for the HER at the Ni-Mo-Cd in 0.5 M KOH solution. Solid lines are best-fitted results to the experimental data (points).

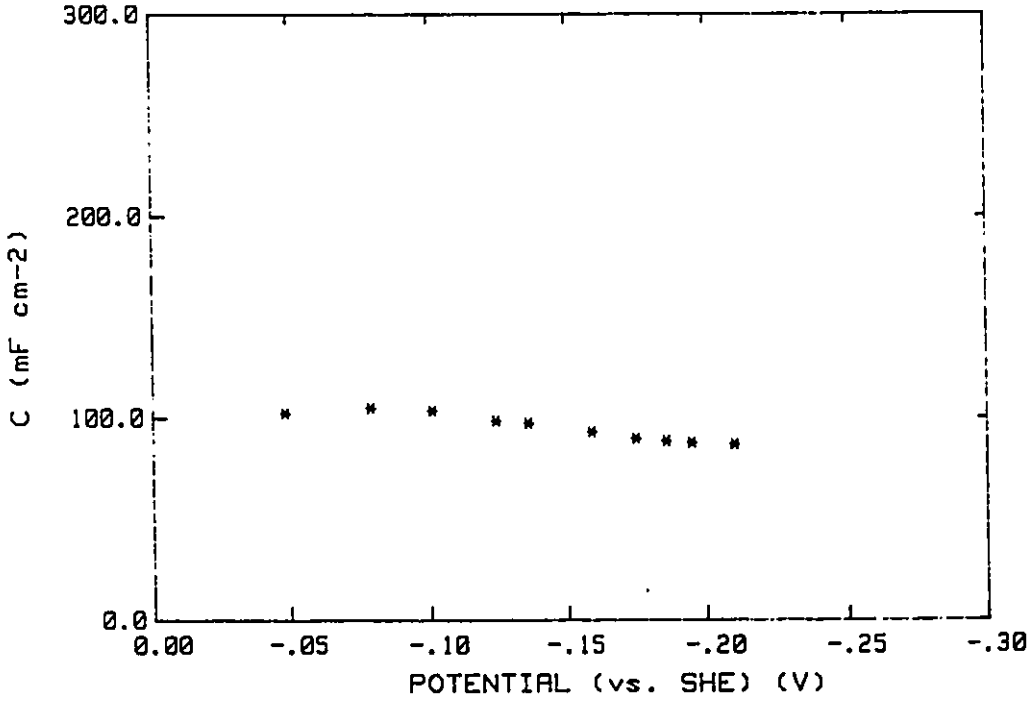

Fig.4.II.10b Log(C_d) vs potential plots for the HER at the porous Ni-Mo-Cd electrode in 0.5 KOH solution derived by means of the initial potential decay rate method.

electrical accessibility of internal surface area by diminishing the distributed internal electrolyte resistance, so that the internal surface becomes 'unfolded' with regard to its potentiality for electrochemical response, as demonstrated in Section 4.II.3 below, where the detailed study of this factor is discussed.

4.II.3 Unfolding of the Electrochemically Accessible Surface of Porous Electrodes

It is well known that porous electrode structures exhibit polarization and impedance behaviour that depends on distributed internal resistance and interfacial capacitance in a complicated way associated with microscopic inhomogeneity of current-density distribution. In Section 4.II.1, C_{dl} was quantitatively examined for a well defined electrode system, platinized Pt, the real area of which, per apparent cm^2, was unambiguously determined from its u.p.d. H accommodation. Also under cathodic polarization, C_{dl} behaviour was evaluated by potential-relaxation and a.c. modulation under conditions of varied internal electrolyte resistivity.

Fig.4.II.11 shows log C_{dl} vs overpotential plots for the HER at the plated Pt electrode in (1) 0.1, (2) 0.2 (3) 1.0 (4) 2.0 and (5) 4.0 M KOH solutions, respectively, determined by the initial potential-relaxation rate curve-fitting procedure described in Section 4.II.1.3. Note that the y-axis data, C_{dl} per cm^2, were calculated on the basis of the apparent geometric electrode surface area ($s = 0.195\ cm^2$).

Based on the value of C_{dl} for smooth Pt, which is $27.6 \pm 1.0\ \mu F\ cm^{-2}$, the apparent roughness factor values (= ratio of C_{dl} values for the plated and bright Pt electrodes) can be calculated (Table 4.II.5).

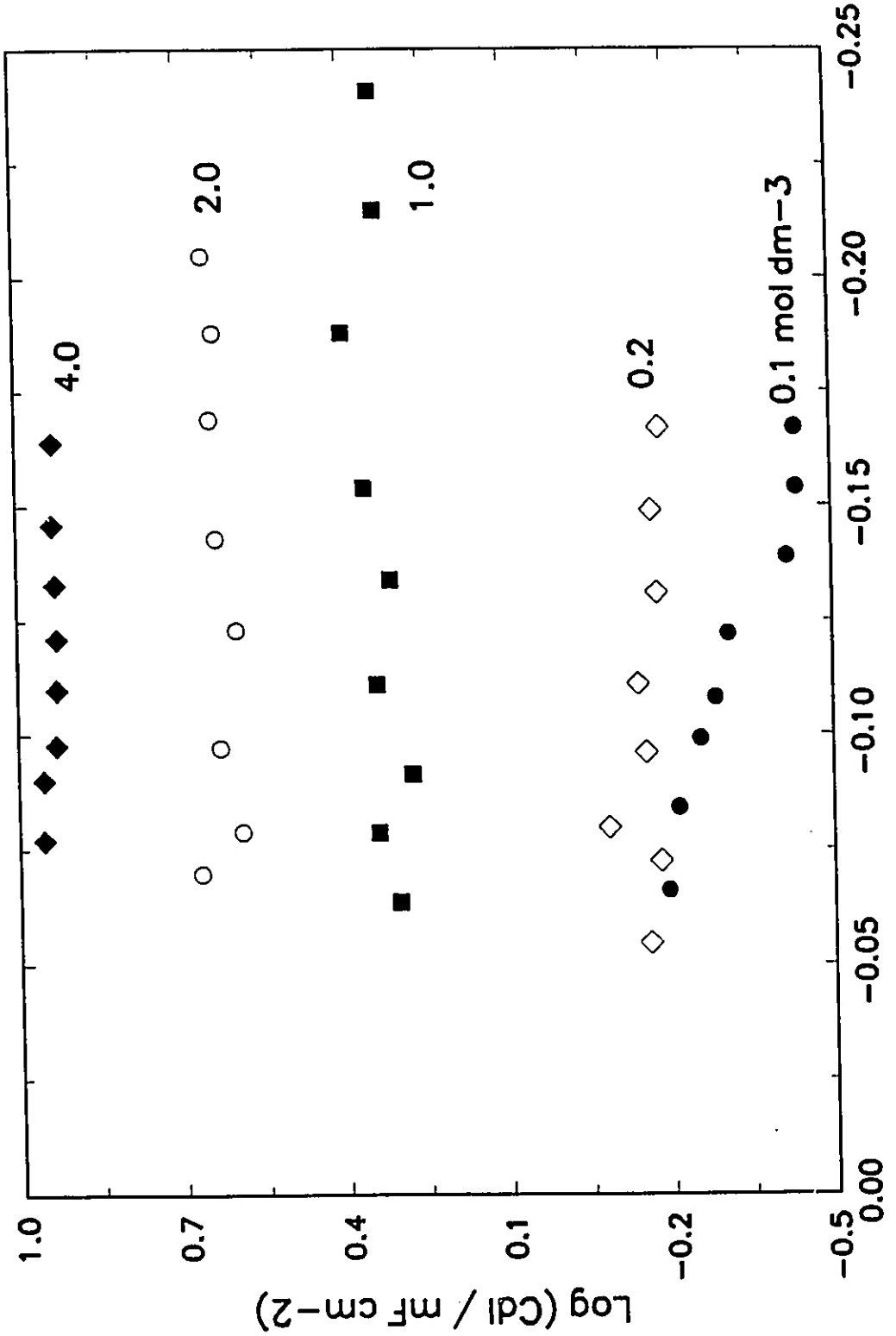

Fig.4.II.11 $Log(C_{dl})$ vs overpotential plots for the HER at the plated Pt in KOH solutions of various concentrations. C_{dl} values are determined by means of the initial potential decay rate method.

Table 4.II.5 Summary of determined C_{dl} and apparent roughness factor values of the plated Pt electrode by means of the initial potential-relaxation rate method for five concentrations of KOH

concentration of KOH / M	C_{dl}/mF cm^{-2}	roughness factor
0.1	*ca.* 0.37 - 0.61	*ca.* 13.4 - 22.1
0.2	*ca.* 0.65 - 0.85	*ca.* 23.6 - 30.8
1.0	*ca.* 2.01 - 2.50	*ca.* 72.8 - 90.6
2.0	*ca.* 3.92 - 4.66	*ca.* 142 - 169
4.0	*ca.* 8.18 - 8.43	*ca.* 296 - 305

It is important and interesting to see in Fig.4.II.11 and Table 4.II.5 that the experimentally determined C_{dl} value *increases* as the concentration of KOH solution is raised and the apparent roughness factor is ca. 20 times larger in the 4.0 than in the 0.1 M KOH solution. Since the electrolyte ohmic resistance inside pores is relatively large in dilute KOH solution, the resulting IR-drop is serious inside the pores and renders only a rather small fraction (ca. 5% in 0.1 M) of the pore surface available for the HER. In other words, the penetration depth of the electrochemical reaction is only about 5% in 0.1 M of that in 4.0 M KOH solutions.

In 4.0 M KOH solutions, the determined roughness factor, 300 $\pm$ 5 (see Table 4.II.5), is in reasonable agreement with the values 290 and 262 $\pm$ 10, determined by the CV and impedance methods, respectively. These results indicate, for 4.0 M KOH solution, that the relaxation response of the porous plated Pt electrode is almost completely 'unfolded' for C_{dl} measurements, as was concluded from the impedance results discussed earlier in this section.

The initial potential-relaxation rate method utilized here was also applied to the HER at the bright Pt electrode in 0.1, 0.2, 1.0, 2.0 and 4.0 M solutions, respectively (see Table 4.II.6). The determined C_{dl} had a constant value, independent of the concentration of KOH used. This

result confirmed that the concentration dependence of the measured C_{dl} values, listed in Table 4.II.5, is due just to the porosity of the plated Pt electrode and the consequent distributed internal resistance.

Table 4.II.6 Summary of C_{dl} values of bright Pt determined by the initial potential-relaxation rate method for several concentrations of KOH solution

concentration of KOH / M	C_{dl} / μF cm^{-2}
0.1	25.7 ± 1.2
0.2	28.7 ± 1.7
1.0	29.5 ± 1.5
2.0	27.6 ± 1.0

The C_{dl} values determined by the initial potential-relaxation method are effectively the steady-state quantities, since they are evaluated for an initial (previous) steady-state situation, from the corresponding initial potential-relaxation rate, $(d\eta/dt)_{t=0}$.

Fig.4.II.12 shows IR-corrected Tafel plots for the HER on the plated Pt electrode in (1) 0.1, (2) 0.2, (3) 1.0, (4) 2.0 and (5) 4.0 M KOH solutions, respectively. Curve 6, in this Figure is for the HER on the bright Pt electrode as described in section 4.II.1 for 2.0 M KOH solutions. Note that the point-by-point anodic activation procedure was applied to all results in Fig.4.II.12, as described in Section 2.1.4.

Tafel polarization experiments on the HER at the activated, smooth, bright Pt electrode were also conducted in 0.1 - 4.0 M KOH solutions (results not shown here). It was found they are independent of the concentration of the KOH solutions used. This is not surprising since the rates of electrochemical steps of the HER are independent of OH^- concentration for alkaline

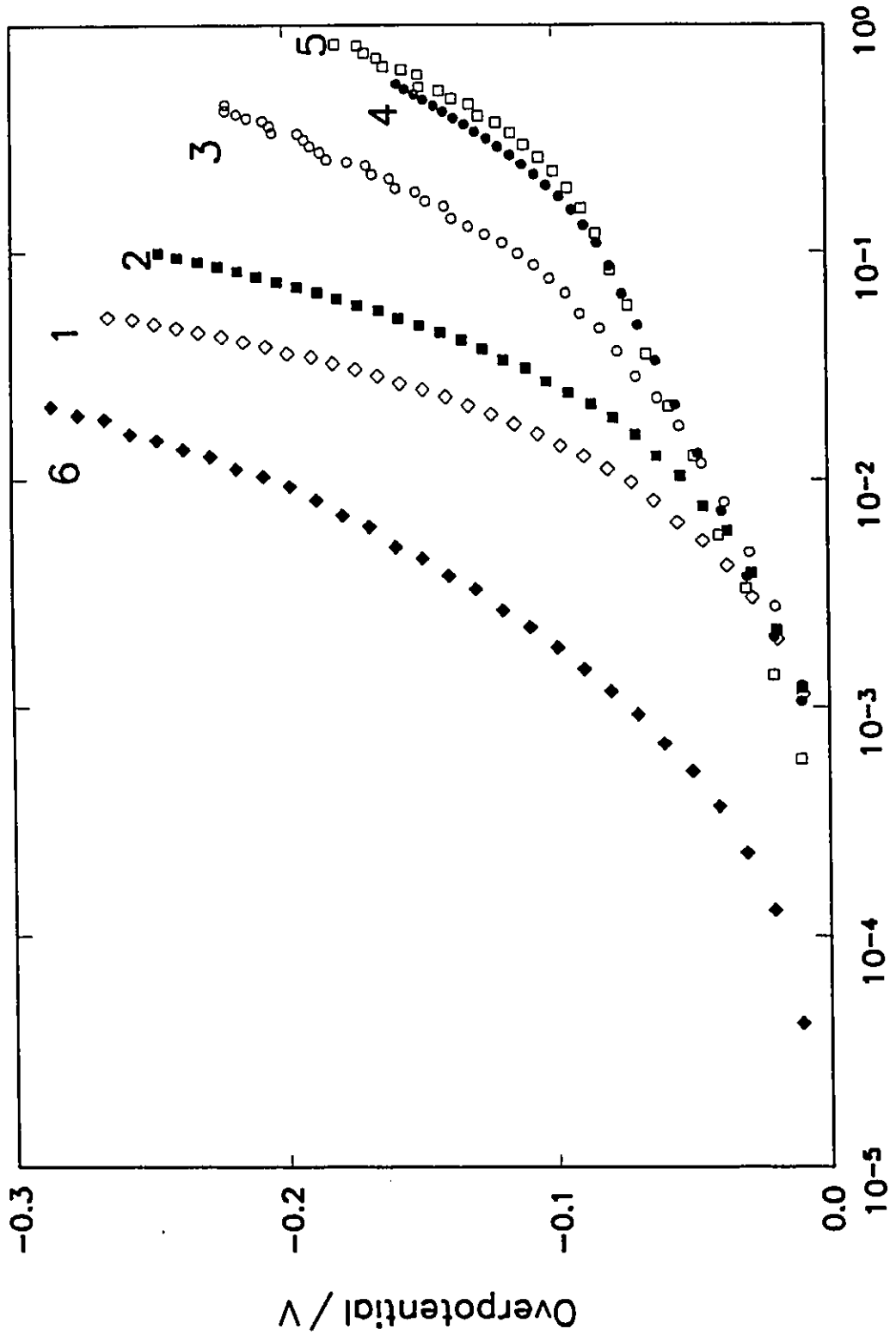

Fig.4.II.12 Tafel plots for the HER at the plated Pt electrode in (1) 0.1; (2) 0.2; (3) 1.0; (4) 2.0 and (5) 4.0 M KOH solutions, respectively. Curve 6 is for the bright Pt in 2 M KOH solution.

solutions at high pH (although water activity can become decreased), and also do not normally involve any diffusion process involving electrolyte ions. Therefore, the apparent concentration dependence of the Tafel behaviour of the HER on the porous plated Pt electrode, as illustrated in Fig.4.II.12, must be due to the porosity effect associated with the geometrical micro-structure of the plated Pt electrode.

As shown in Fig.4.II.12, the steady-state current-densities increase as the concentration of KOH increases at the same overpotential value. That is because the accessibility of the pores of the plated Pt electrode increases as the concentration of KOH is made larger.

It is interesting and important to point out the increase of the steady-state current, i, at a constant overpotential of say -0.15 V, is found to be proportional to the increase of the determined C_{dl} as the concentration of KOH is increased from 0.1 to 4.0 M (see Table 4.II.7).

Table 4.II.7 Summary of the ratios of the determined C_{dl} values (see Table 4.II.5) and the steady-state currents at an overpotential, η, of -0.15 V (see Fig.4.II.12) in a 4 M KOH solution to the respective values found for the other four KOH concentrations

concentration of KOH, x / M	C_{dl} (4 M)/ C_{dl} (x M)	η = - 0.15 V i (4 M)/ i (x M)
0.1	23	25
0.2	13	13
1.0	3.4	3.3
2.0	1.9	1.3
4.0	1	1

The results in Table 4.II.7 thus demonstrate that, as the concentration of KOH is increased from 0.1 to 4.0 M, the extent to which the currents is increased are equal to the extent

to which the electrochemically accessible surface areas are 'unfolded', since the C_{dl} values are proportional the real electrode areas, as emphasized earlier. In fact, these results provide further confirmation of the earlier conclusion that C_{dl} values determined by the present methods can be reliably associated with the real surface areas of porous electrodes that are accessible for the HER, or other continuous Faradaic reactions.

PART III Poison Effects on H Adsorption Behaviour and Kinetics of the HER at Pt

4.III.1 Introduction

The presence of catalyst poisons usually greatly modifies the electrocatalytic behaviour of electrodes. For example, the kinetics of the HER are sensitively influenced by adsorption of catalyst poisons such as arsenic, thiourea, etc. which decrease the coverage of the o.p.d. H intermediate, as found in the present work. Usually, poisons also raise the overpotential at a given current-density or correspondingly diminish currents at given overpotentials. Adsorbed poisons will not only competitively occupy available adsorption sites but can also interact with the H atoms already covering the surface [147]. In the present project, interest in the effects of poisons on the HER has arisen both for fundamental reasons related to other aspects of the work and, not least, on account of the involvement of As impurities (arising from the HF) in the practical operation of F_2-production cells.

From a general heterogenous catalysis point of view, it is usually considered that poisons, e.g. sulphur, arsenic, deactivate catalysed reactions [153,154] through irreversible adsorption of the poison compounds on the metal. Taking the example of sulphur, its adsorption to the metal surface can be characterized by determining the chemisorption energy or the strength of its bonding to surface atoms. The electronic structure of the valence-electron shell of sulphur is $3s^2 3p^4$; therefore bonding involves s and p orbitals. Bond formation with transition elements involves mainly their d-orbitals. Adsorption of poison species to the metal surface then takes place through bonding by donation of lone-pair (s, p) electrons to empty d-orbitals.

Catalyst poisoning by sulphur is a severe problem commonly encountered in the

application of many supported metal catalysts. The lifetime of metal catalysts may be greatly shortened and the catalytic performance altered by the presence of trace amounts of sulphur contaminants in the feed resulting in irreversible adsorption of sulphur compounds on metals [226,227]. Because of the practical importance of sulphur poisoning, a considerable body of information has been accumulated concerning the interaction of sulphur with metal surfaces [153,154,228]. Much of the attention has been focused on the nature of metal-sulphur bonding and the mechanism of sulphur adsorption on metal surfaces. The influence of sulphur adsorption on hydrogen-to-metal bonding has also been reported in a number of studies [229-231].

In gas-solid catalysis, sulphur has been studied extensively and it has been found that it modifies the selectivity of metallic catalysts; thus, in the case of competitive hydrogenations this effect is due to electronic modifications, induced by the adsorbed sulphur [142].

In the present work, poison effects of thiourea, $(NH_3)_2C{=}S$, and arsenic oxide, As_2O_3, on the adsorption behavior of H in the HER at Pt were quantitatively studied. Similar to sulphur compounds such as thiourea, elemental As, or compounds such as AsH_3, have lone-pair electrons which are easily combined with empty d-orbitals of transition metals. It is this feature that leads to a strong adsorption of S and As compounds at electrode surfaces and such processes are usually irreversible. The occupancy by the poison species on the surface generally diminishes the coverage of the o.p.d. H and decreases currents at given potentials in the HER.

Although arsenic was introduced into the melt or solutions as As_2O_3, it is probable that the effective poisoning species are As(0) and As(-III), as AsH_3, which arise owing to electrochemical reduction of the As(III). In fact, AsH_3 was detectable in the evolved H_2 gas in appropriate experiments and elemental As can be deposited electrolytically as a semi-metal [147].

It is known that poisoning elements are more strongly chemisorbed when they are in low oxidation states, corresponding to greater donicities.

Open-circuit potential-relaxation experiments were carried out and the transients were recorded and analysed by means of kinetic simulation, considering poison coverage and lateral interaction effects of the adsorbed species at the surface. Information about coverages, θ_H and θ_P, and pseudocapacitance, C_ϕ, associated with the H in the presence of poison (P) adsorption was successfully obtained.

When trace amount of poison species, e.g. thiourea, As_2O_3, are added into the solution, significant changes arise in the kinetic behaviour of the HER manifested in the potential-relaxation and steady-state kinetics of the process. Theoretical rate equations for the HER should then be modified involving θ_P and g factors in the form of the Frumkin-type isotherm, which enable the behaviour of potential-relaxation transients for such conditions to be interpreted.

4.III.2 Kinetic Aspects of Poisoning Effects on the Potential-Relaxation Behaviour

4.III.2.1 Theoretical Treatments

The involvement of poisons in the kinetics and mechanisms of the HER is investigated here first by making theoretical calculations of the rates of the electrochemical processes involved, considering both the coverage of poison, θ_P, and the lateral interaction factor, g. Other complementary experiments have also been made (see Section 4.III.4)

According to the steps of HER in eqn.(3.1), the separate rates for each of the individual forward and backward steps of the reaction are presented in eqn.(4.III.1a-f):

$$v_{1,f} = k_1 (1-\theta_H-\theta_P) \exp [F\eta/2RT] \exp [-\beta g(\theta_H+\theta_P)]$$

$$= k'_1 (1-\theta_H-\theta_P) \exp [F\eta/2RT] \quad (4.III.1a)$$

$$v_{1,b} = k_{-1} \theta_H \exp [-F\eta/2RT] \exp [(1-\beta)g(\theta_H+\theta_P)]$$

$$= k'_{-1} \theta_H \exp [-F\eta/2RT] \quad (4.III.1b)$$

$$v_{2,f} = k_2 \theta_H \exp [F\eta/2RT] \exp [\beta g(\theta_H+\theta_P)]$$

$$= k'_2 \theta_H \exp [F\eta/2RT] \quad (4.III.1c)$$

$$v_{2,b} = k_{-2}(1-\theta_H-\theta_P)\exp[-F\eta/2RT] \exp[-(1-\beta)g(\theta_H+\theta_P)]$$

$$= k'_{-2}(1-\theta_H-\theta_P)\exp[-F\eta/2RT] \quad (4.III.1d)$$

$$v_{3,f} = k_3 \theta_H^2 \exp [2\beta g(\theta_H+\theta_P)]$$

$$= k'_3 \theta_H^2 \quad (4.III.1e)$$

$$v_{3,b} = k_{-3} (1-\theta_H-\theta_P)^2 \exp [-2(1-\beta)g(\theta_H+\theta_P)]$$

$$= k'_{-3} (1-\theta_H-\theta_P)^2 \quad (4.III.1f)$$

For convenience, the exp terms of eqn.(4.III.1a-d) include η defined for a cathodic process as positive, so the arguments of exps for "forward" steps are positive. Correspondingly, for eqn.(4.III.1a) the argument of exps in $\beta g(\theta_H+\theta_P)$ is negative, based on g values being positive for repulsive interactions.

In eqn.(4.III.1a-f), the surface concentrations of the reagent (H_2O or H_3O^+) are included with the rate constants, as before. θ_H is the coverage by H and θ_P the coverage by poison; g is a 2-dimensional lateral interaction factor. The exponential term involving the $\beta g\theta$ factor in the rate equations corresponds to a change of activation energy with coverage communally by H and P due to interactions. When $g > 0$ the interaction is repulsive amongst the adsorbed atoms while $g < 0$ corresponds to attractive forces.

In eqn.(4.III.1), v_f and v_b represent forward and backward rates of each reaction step, with the previously defined net rate $v = v_f - v_b$, applied to each step. We see that k's are quantities involving an exponential term in which β, g, θ_H and θ_P factors are included. This modification originates from the Frumkin isotherm [8] as was also similarly treated in Gileadi's work earlier in this lab [119], but on a different problem.

In terms of a Langmuir adsorption isotherm representing an idealized case, the relation of fractional coverage to the overpotential was already described by eqn.(3.11). In many systems of practical interest, surface heterogeneity and lateral-interaction effects should be considered, as in the case of poison adsorption on an electrode surface. It is assumed (*cf.* ref [119]) that the equilibrium constant K′ decreases exponentially with increasing coverage :

$$K'_1 = K_1 \exp [-g\theta] \qquad (4.III.2)$$

where g is the interaction factor expressing the interaction energy as a multiple of RT. The coverage θ should include the coverages by both the adsorbed species communally, i.e. $\theta = \theta_H + \theta_P$. Therefore the eqns.(4.III.3) and (4.III.4)

$$k'_1 = k_1 \exp [-\beta g(\theta_H+\theta_P)] \qquad (4.III.3)$$

and

$$k'_{-1} = k_{-1} \exp [(1-\beta)g(\theta_H+\theta_P)] \qquad (4.III.4)$$

can be obtained by bringing $K_1 = k_1/k_{-1}$ and $K'_1 = k'_1/k'_{-1}$ into eqn.(4.III.2) and taking β=0.5.

When the complicated situation of the poison effect is considered, eqn.(4.III.1), which includes interaction and poison coverage factors, should be inserted into eqns.(3.6) and (3.7) for theoretical description of the potential-relaxation and adsorption behaviour. Thus, the two differential equations can be solved numerically by making suitable modifications of the computer programme used for simpler cases.

Three model potential-relaxation transients at initial overpotentials of -0.4, -0.3 and -0.2 V were obtained from these theoretical calculations as shown in Fig.4.III.1a. Kinetic parameters were selected empirically but according to some actual experimental results on poison effects [195]. Here, in Fig.4.III.1a, $k_1 = 10^{-9}$, $k_{-1} = 2 \times 10^{-9}$, $k_2 = 10^{-11}$, $k_3 = 10^{-12}$ mol cm^{-2} s^{-1}, $C_{dl} = 25$ μF cm^{-2}, $q_1 = 21$ μC cm^{-2}, $g = 5$ and $\theta_P = 0.9$ are taken. Based on experiments to be described later, it was found reasonable to take the θ_P value as 0.9 because the bonding of poisons to transition metal surfaces is appreciably strong, an effect which originates from the donation of lone-pair electrons of the poison species to the empty d-orbitals of the metal. A value of the monolayer charge $q_1 = 21$ μC cm^{-2} was used here, because only 10% ($1 - \theta_P = 0.1$) of the surface is available for the H adsorption. $g = 5$ is a reasonable value representing the coverage-dependent lateral interaction energy between the adsorbed species on the surface.

There is one significant and important difference of these relaxation curves from those which arise without the influence of poisons, as shown in Fig.3.1a. The arrests which clearly arise in the latter case become almost absent in the long time region (0.1 s - 100 s) in Fig.4.III.1a. This is because the coverage by H is strongly reduced by the competitively adsorbed poison (90% poison coverage on the surface), so the surface charge for H deposition is substantially diminished, and correspondingly the discharge pseudocapacitance becomes insignificant over the long time region. In this way the potential-relaxation transient can be used as a sensitive and quantitative indication of the presence of surface impurities at electrodes that are electroactive for H chemisorption.

Fig.4.III.1b shows the corresponding coverage, θ_H, and the pseudocapacitance, C_ϕ, calculated from the definitions in eqn.(3.9) and (3.10), using the same set of kinetic parameters

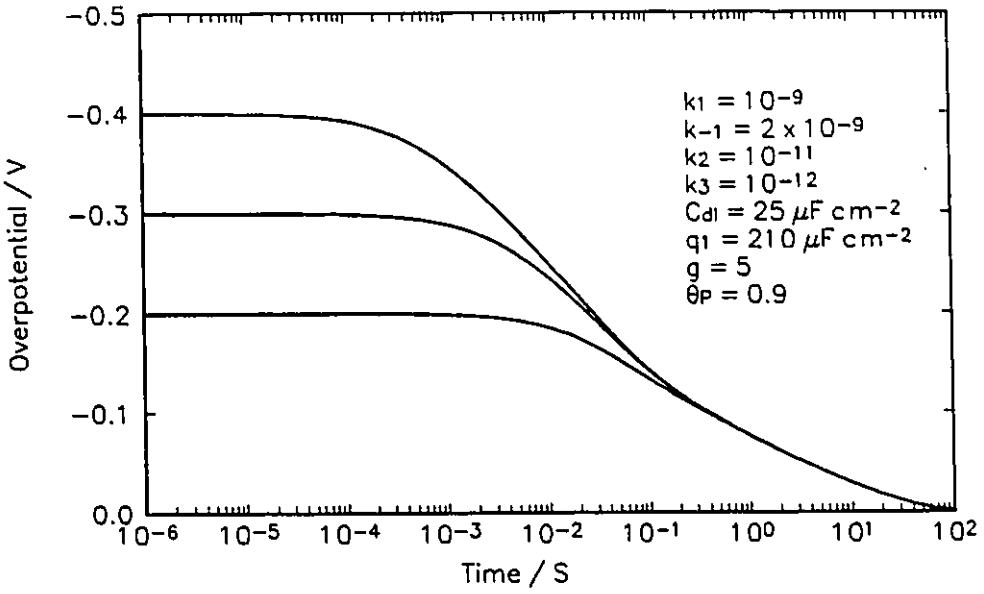

Fig.4.III.1a Calculation of potential-relaxation transients as a model in the presence of poison.

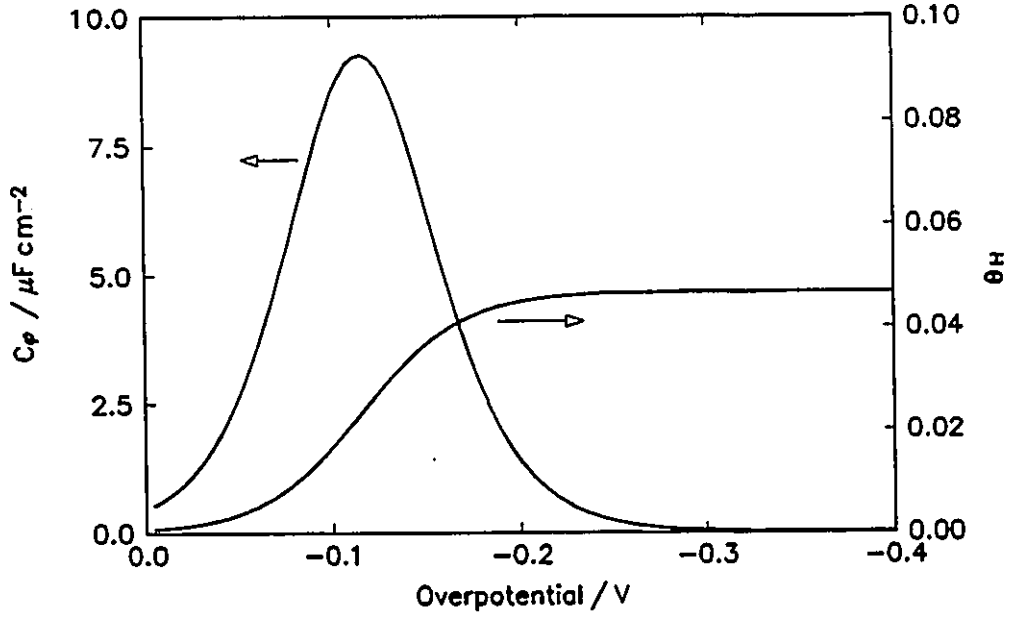

Fig.4.III.1b Relations of θ_H vs η and C_ϕ vs η, calculated from the parameters in Fig.4.III.1a.

as for Fig.4.III.1a. The forms of these curves resemble that of Fig.3.1b in which a poison effect was not considered. The coverage, θ_H, remains unchanged over the high overpotential region and the maximum in the pseudocapacitance is present in the low overpotential region.

However, the θ_H values in Fig.4.III.1b are much smaller and the maximum θ_H reaches only 48% of the *available* free surface sites for H adsorption which is 10% of the actual total surface (recall θ_P=0.9). This interesting result can be attributed to the interaction effect between the adsorbed surface poison and the electrosorbed H intermediate, that is the repulsive forces tend to expel the H intermediate from adsorption on the available free surface sites. This is a situation which leads to "unsaturated" H adsorption. However, when a poison is not present, it is known [89] that the cathodic H_2 evolution at Pt, Rh or Ir usually proceeds via an o.p.d H intermediate which must be additional to the H of the u.p.d monolayer already existing at the equilibrium potential.

It can be seen from the scale of pseudocapacitance in Fig.4.III.1b that the values of C_ϕ are also substantially reduced (C_ϕ in Fig.3.1b is on a mF cm^{-2} scale). This is understandable from its definition since the monolayer charge, q_1, (here 21 μC cm^{-2}) is much less than that for full monolayer coverage which is normally ca. 210 μC cm^{-2} in the absence of coverage by a poison, at polycrystalline Pt.

4.III.2.2 Effect of Kinetic Parameters Involving Poisons

It is useful to show the results of some theoretical calculations on the kinetics of, and H adsorption behaviour in, the HER, using some empirically chosen rate constants shown in Fig.4.III.1a, which are, however, physically reasonable. The effects of variation of the lateral interaction parameter, g, and of θ_P on the kinetic and H coverage behaviour in the HER were

evaluated, as is shown below.

4.III.2.2.1 θ_P

First, in Fig.4.III.2a, is shown the effect of θ_P on the Tafel relation for g taken as 1 as an example. Kinetic and other parameters were taken as $k_1 = 1 \times 10^{-3}$, $k_{-1} = 1.5 \times 10^{-8}$, $k_2 = 1 \times 10^{-9}$, $k_3 = 1 \times 10^{-10}$ (mol cm^{-2} s^{-1}), with $C_{dl} = 25$ μF cm^{-2} and $q_1 = 210$ μC cm^{-2}. The Tafel relation was calculated from the Faradaic current which is proportional to the rate of electron production at a given overpotential, η, so $i_f = F(v_1 + v_2)$. In Fig.4.III.2a, the currents at given overpotentials decrease as θ_P increases from 0.1 to 0.9 as might be intuitively expected. This calculated behaviour is consistent with that of experimentally observed Tafel relations in that the currents are usually diminished with introduction of poisons. The irreversible adsorption of the poison on the surface blocks the sites active for H adsorption and thus for H_2 evolution, leading to reduced Faradaic currents.

Fig.4.III.2b shows the corresponding effect of θ_P on the electrosorption isotherm for θ_H as $f(\eta)$ with $g = 1$. The kinetic parameters are the same as for Fig.4.III.2a. It is easy to understand that θ_H will be reduced when more poison covers the metal surface, as is clearly shown in Fig.4.III.2b.

4.III.2.2.2 g

In Fig.4.III.3a is shown how the $\theta_H(\eta)$ isotherm depends on g for $g = 0$ to 10 over an overpotential range of 0.4 V. The kinetic parameters are taken as $k_1 = 1 \times 10^{-8}$, $k_{-1} = 1.5 \times 10^{-8}$, $k_2 = 1 \times 10^{-9}$, $k_3 = 1 \times 10^{-10}$ (mol cm^{-2} s^{-1}), with $C_{dl} = 25$ μF cm^{-2} and $q_1 = 210$ μC cm^{-2}. $\theta_P = 0.1$ is unchanged for this set of calculations, i.e. P, at a given coverage, is irreversibly

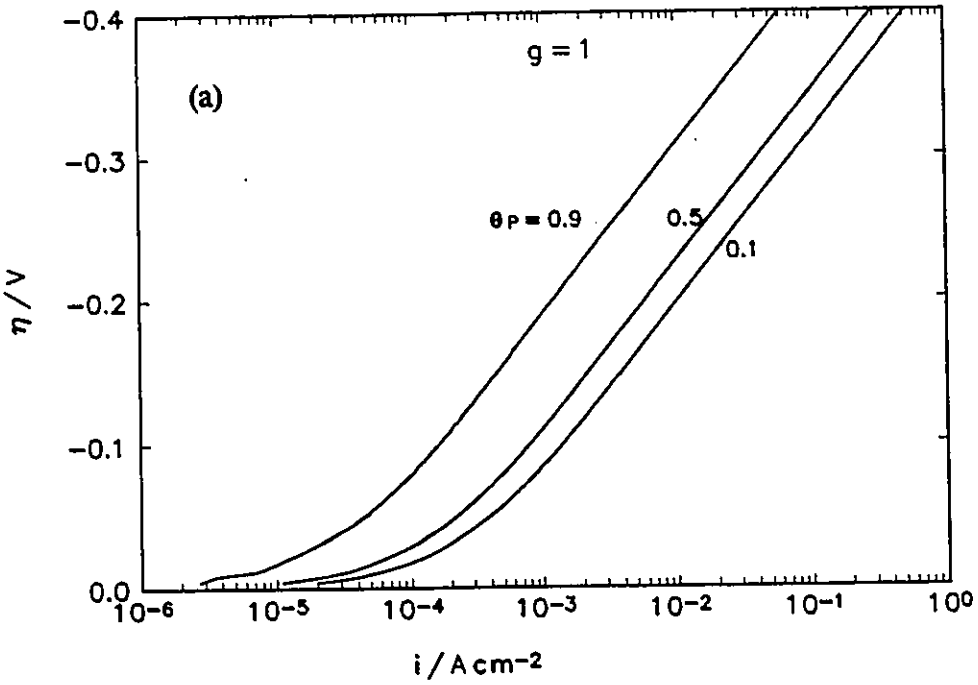

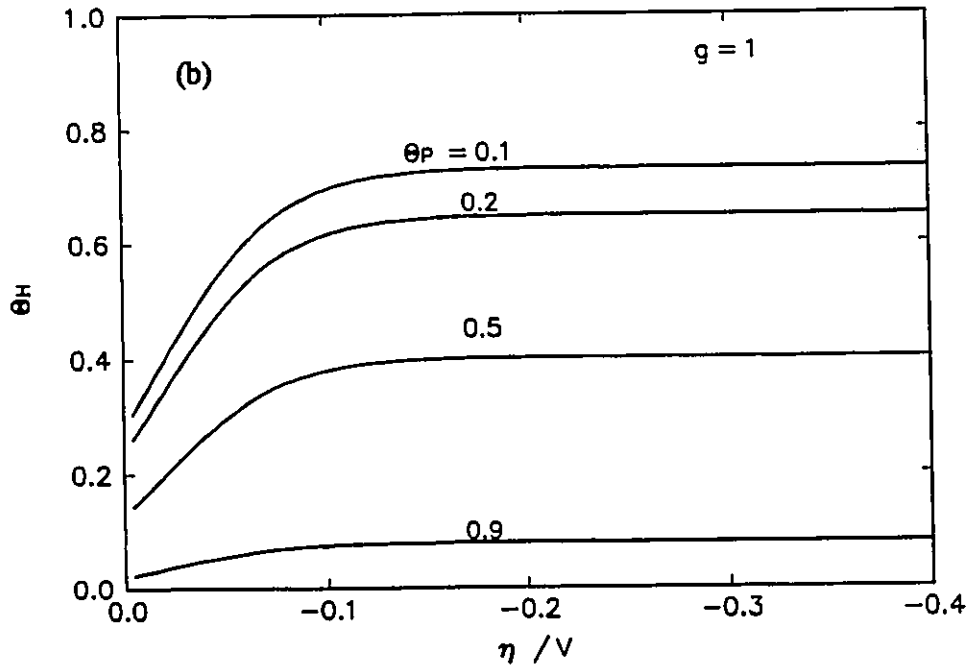

Fig.4.III.2 (a) The effect of θ_P on Tafel relations for the HER, taking g = 1, as an example.
(b) The θ_H vs η relations correspond to (a).

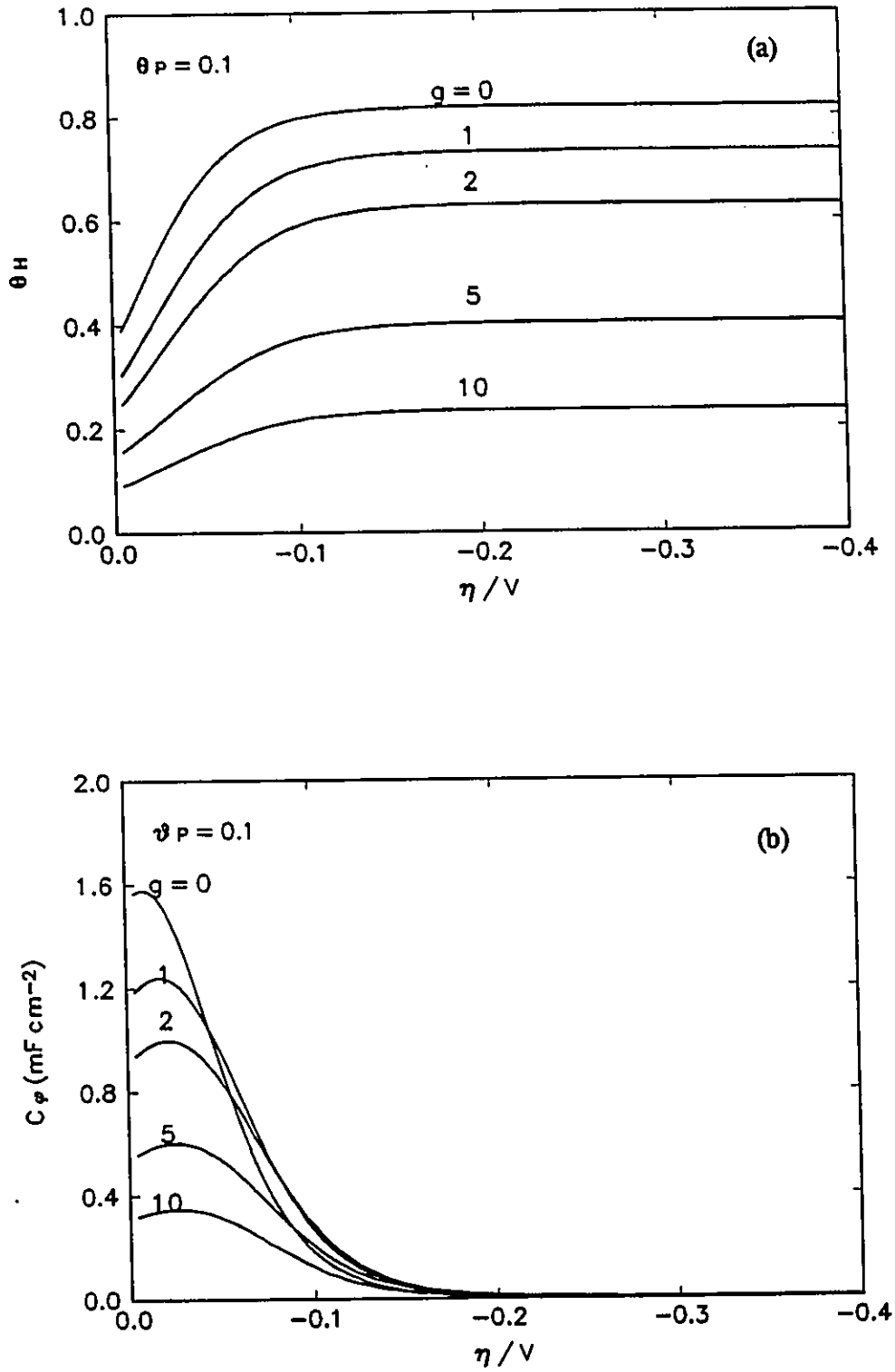

Fig.4.III.3 (a) The effect of g values on the θ_H vs η relations for the HER, taking $\theta_P = 0.1$.
(b) The C_ϕ vs η relations correspond to (a).

bound. The corresponding $C_\phi(\eta)$ relations are shown in Fig.4.III.3b from which it is seen that increase of g, for a given $\theta_P = 0.1$, causes substantial decreases of the C_ϕ values, corresponding to diminution of the θ_H values shown in Fig.4.III.3a. A positive g value corresponds to repulsive lateral interactions as defined in eqn.(4.III.1). The change of value of g from 0 to 10 means an increase of pairwise repulsive energy between the adsorbed species at the surface; thus θ_H becomes reduced due to diminution of adsorbed H by the competitively adsorbed poison.

Note that for the steady-state conditions considered here for o.p.d. H behaviour in mechanism 1,2 ($k_2 < k_1$; $k_2 > k_3$), increase of the g value lowers the C_ϕ profile without broadening it, as would be the case for the equilibrium C_ϕ behaviour treated in earlier papers [88,197]. This is because k_2 is being changed with θ_H in comparison with k_1 which is changed in the opposite direction with increasing θ_H.

Changes of positive g values affect the Tafel relationship (for $\theta_P = 0.1$) in an interesting way as illustrated in Fig.4.III.4a from which it can be shown (Fig.4.III.4b) that a maximum in current, at e.g. a nominal η value of -0.3 V, arises when $g \approx 5$. These calculations were performed with g values taken up to 75 (corresponding to a change of apparent Gibbs energy of adsorption of H by 75RT J mol^{-1}) but it is unlikely that such large values would arise in reality. The large range of g was taken simply to define the trend of the results and identify the maximum which arises actually at some relatively small value of g.

4.III.2.2.3 k's

In the presence of poisons, rate constants should be expressed in terms of k's modified by the "Frumkin isotherm" factor in eqns.(4.III.3) and (4.III.4) which include an extra

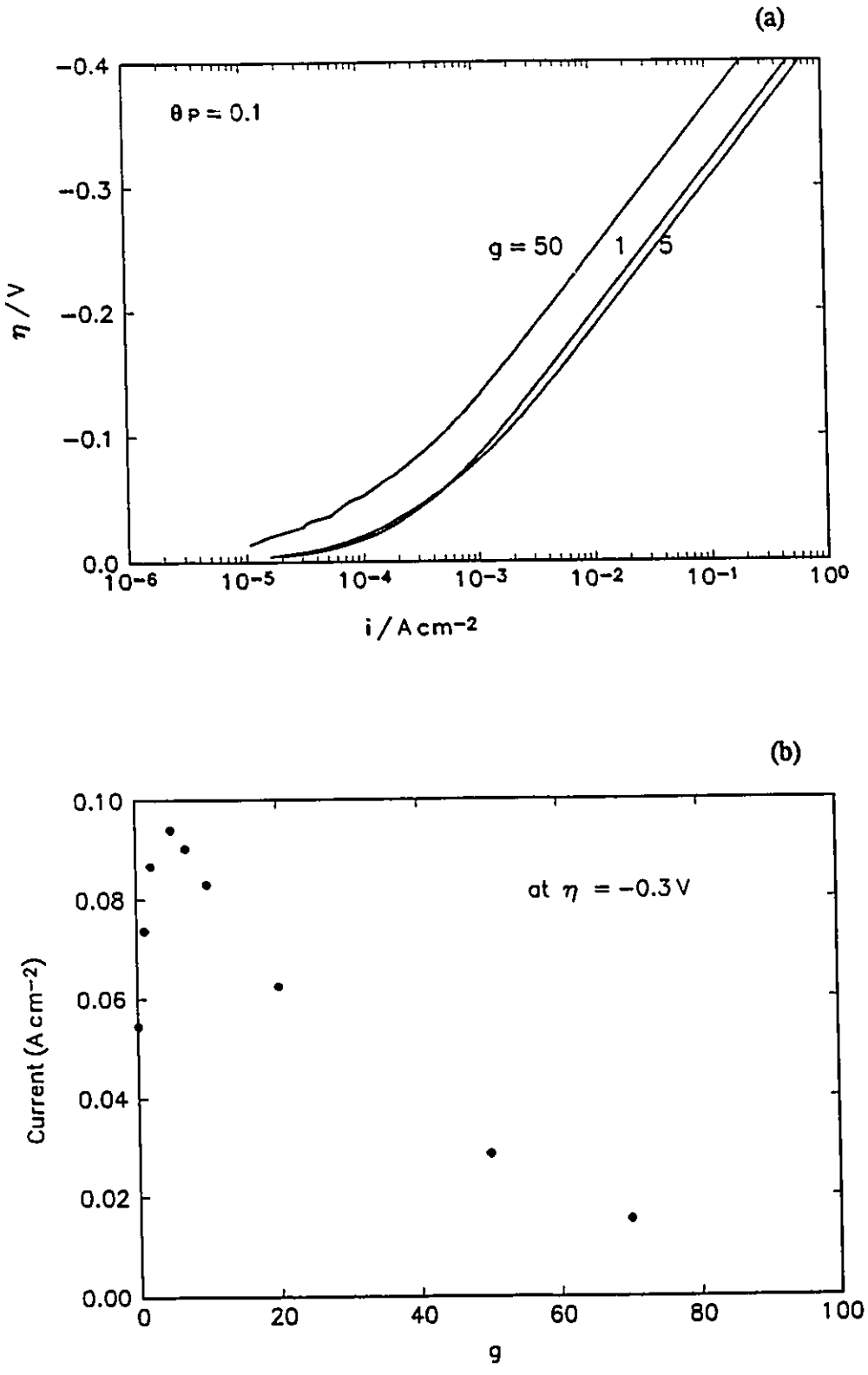

Fig.4.III.4 (a) The effect of g values on Tafel plots for the HER, taking $\theta_P = 0.1$.
(b) Dependence of currents calculated from Tafel plots at η = -0.3 V on the g values.

exponential term differing from the ideal Langmuir isotherm representation due to the change of activation energy by lateral interaction. The modified rate constants are then represented in the form of $k' = k \exp[-\beta g(\theta_H + \theta_P)]$. The sign in the exponential term varies for different rate constants; usually negative signs apply to the steps involving formation of adsorbed H, as used in eqn.(4.III.1). The signs also comply with the physical meaning of the interaction factor g: positive g values are defined for repulsive and negative g for attractive interactions.

The influence of poisons due to changes of θ_P and g values on the rate constants, k', was also investigated. The rate constant k' data can be employed to construct Tafel type relations for k' values of the component steps as a function of overpotential in a way similar to that shown by Parsons [25] in another context. Fig.4.III.5 gives two cases for g values varying from 1 to 10 with θ_P being kept unchanged at 0.1. For the purpose of convenient comparison, the k's are combined with the overpotential in the exponential term, with the exception of k'_3, since step 3 is the recombination desorption reaction without the direct involvement of overpotential. The relations of η vs k'exp[Fη/2RT] were then calculated and are plotted in Fig.4.III.5.

For Fig.4.III.5a, $\theta_P = 0.1$, $g = 1$, the Langmuir rate constants are taken as $k_1 = 1 \times 10^{-8}$, $k_{-1} = 1.5 \times 10^{-8}$, $k_2 = 1 \times 10^{-9}$, $k_3 = 1 \times 10^{-10}$ (mol cm^{-2} s^{-1}), (C_{dl} and q_1 are actually not involved in the calculation of the rates, see eqn.(4.III.1)). It can be seen that k'_1 is larger than k'_2 over the entire overpotential region. This is the case for which the electrochemical desorption (step 2) determines the rate of the HER. When the g value is increased in Fig.4.III.5b for which $g = 10$, k'_2 surpasses k'_1 in the high overpotential range, leading to a transition of rate-controlling step from the electrochemical desorption step 2 to the electrochemical sorption step 1 ("discharge control") for the HER.

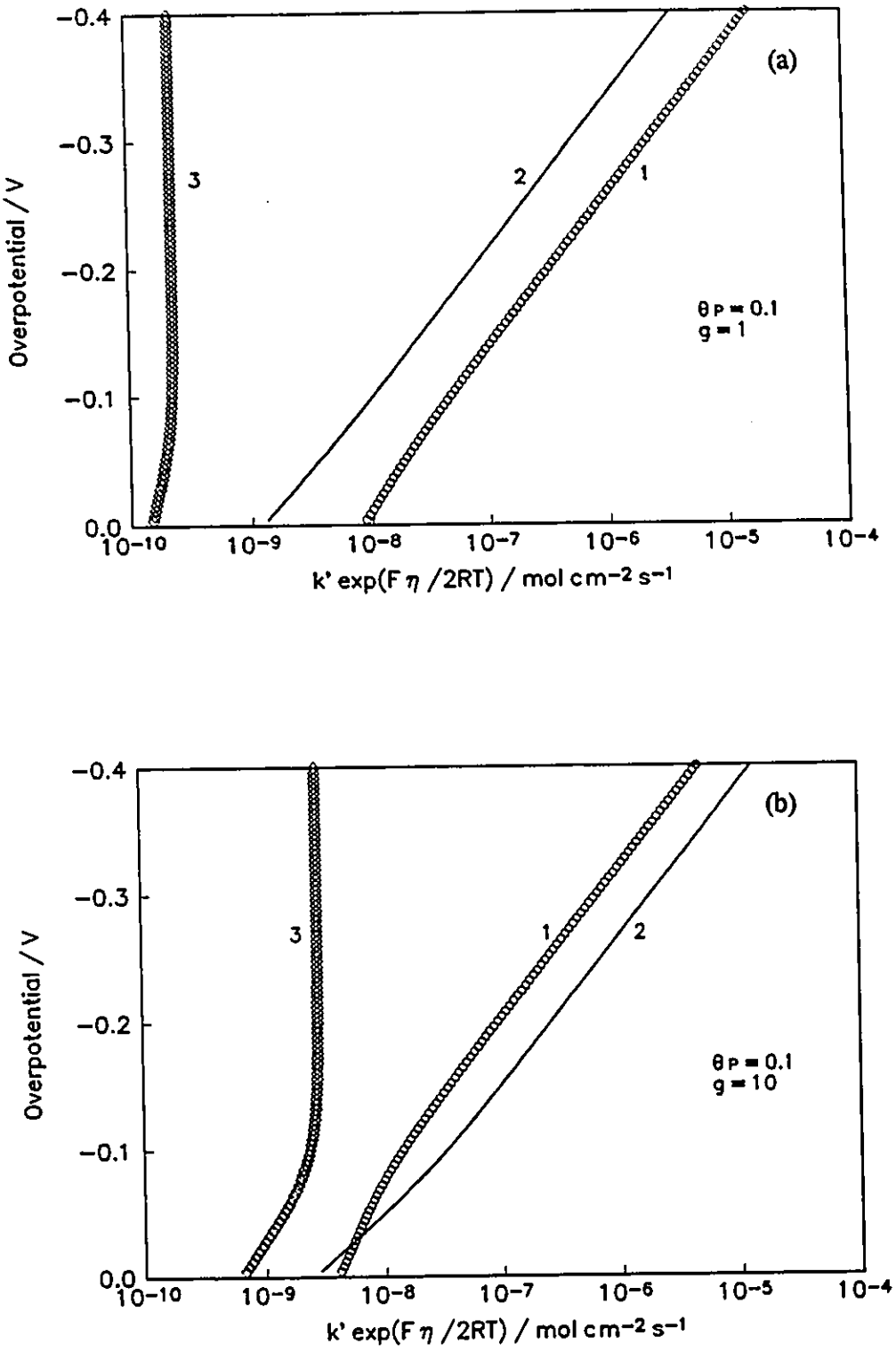

Fig.4.III.5 (a) Relations of rate constants, k', in combination with the exp(Fη/2RT) term (except k_3') to overpotential. (a) $\theta_P = 0.1$, g = 1. (b) $\theta_P = 0.1$, g = 10.

Strong repulsive interaction (g = 10) induced by the adsorbed poison inhibits the first step reaction but tends to accelerate the second step of the HER. Meanwhile, the rate constant k'_3 for step 3 (H+H recombination) becomes enhanced with increasing value of g probably because of weakening of the bond of the adsorbed H to the cathode metal.

Fig.4.III.6 shows the η vs $k'\exp[F\eta/2RT]$ relation with $\theta_P = 0.5$, g = 5. Compared with the behaviour in Fig.4.III.5b, it can be seen that increase of θ_P can also cause a transition of reaction mechanism similar to the effect of increasing the value of g. This correlates with the intuition that greater coverage by a poison on the surface would bring about stronger mutual interaction between the adsorbed species. Therefore increase of poison coverage has the same effect on the rate constants and reaction mechanisms as larger positive g values.

4.III.2.3 Reaction Mechanisms and Rates of Component Steps

Since the terms "rate-controlling" or "rate-determining" step have very frequently been used in discussions of reaction mechanisms and kinetics at electrodes, it is necessary here to clarify the concept of rate-determining step in the HER. The relations of the three reaction steps of the HER can be illustratively described in the way as following :

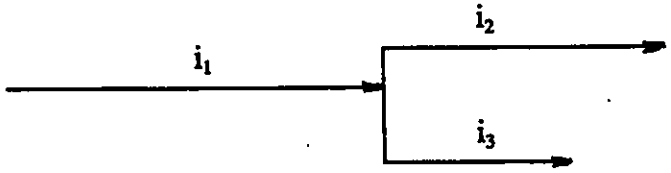

The current of the first step, i_1, is in a consecutive relation to i_2 or i_3 while i_2 and i_3 are in parallel. This relation is similar to that used in an electronic component circuit which comprises R_1 constructed in series with two other resistances, R_2 and R_3, in parallel. The total current i_1 passing R_1 is equal to the sum of i_2 and i_3, which pass through R_2 and R_3 respectively.

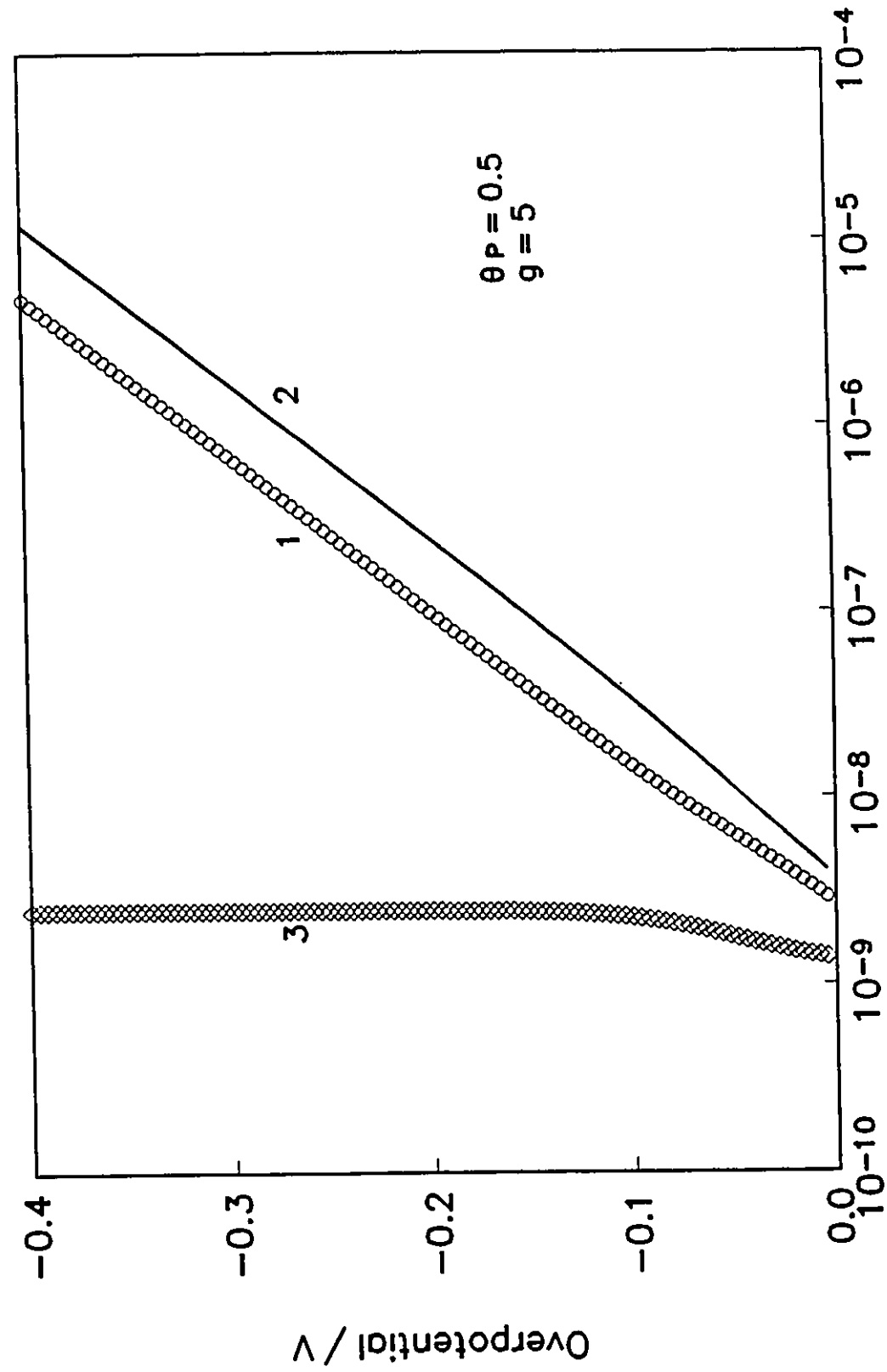

Fig.4.III.6 Relations of rate constants, k', in combination with the exp(Fη/2RT) term (except k_3') to overpotential. $\theta_P = 0.5$, g = 5.

Accordingly, the rate of step 1 is equal to the sum of rates of steps 2 and 3 in the HER, i.e. $i = i_1 = i_2 + i_3$.

When only step 1 and step 2 are considered, it is apparently the step having the smaller electrochemical rate constant, (often erroneously referred to as the "slow step"), that limits the total rate. However, between step 2 and step 3, it is the *faster* step that determines the overall rate. For example, if step 1 and its reverse are faster than step 2 and step 3, the rate-limiting step will be determined by the quicker one between step 2 and 3. However, if step 1 has a rate constant smaller than that of either step 2 or 3, step 1 is definitely the limiting one.

The rates discussed above are referred as the "net rate" in each step of the HER. Since the reaction mechanism includes forward and backward steps, the contribution of each individual step to the mechanism is thus complex. However, for $-\eta >$ ca. 0.1 V, the back reaction rates are usually insignificant compared with the forward ones, because the former decrease exponentially with overpotential.

Fig.4.III.7a shows the relations of the rates of each individual step to overpotential as calculated by means of eqn.(4.III.1). The parameters used are $k_1 = 1 \times 10^{-8}$, $k_{-1} = 1.5 \times 10^{-8}$, $k_2 = 1 \times 10^{-9}$, $k_3 = 1 \times 10^{-10}$ (mol cm^{-2} s^{-1}), $C_{dl} = 25\ \mu$F cm^{-2} and $q_1 = 210\ \mu$C cm^{-2}, $\theta_P = 0.1$ and $g = 1$. It can be seen that $v_{1,f}$ is equal to $v_{2,f}$ at overpotentials above -0.15 V, as is well known. $v_{1,b}$ is still quite significant compared to the other rates. v_3 is independent of overpotential in the high-η range, and the change of v_3 at low η is due to the change of coverage with η over this overpotential region (see previous Figures of θ_H vs η).

The net rates of each step ($v = v_f - v_b$, $r = Fv$) in Fig.4.III.7a are plotted in Fig.4.III.7b. Curves 1, 2 and 3 represent r_1, r_2, and r_3, respectively; curve 4 shows the total

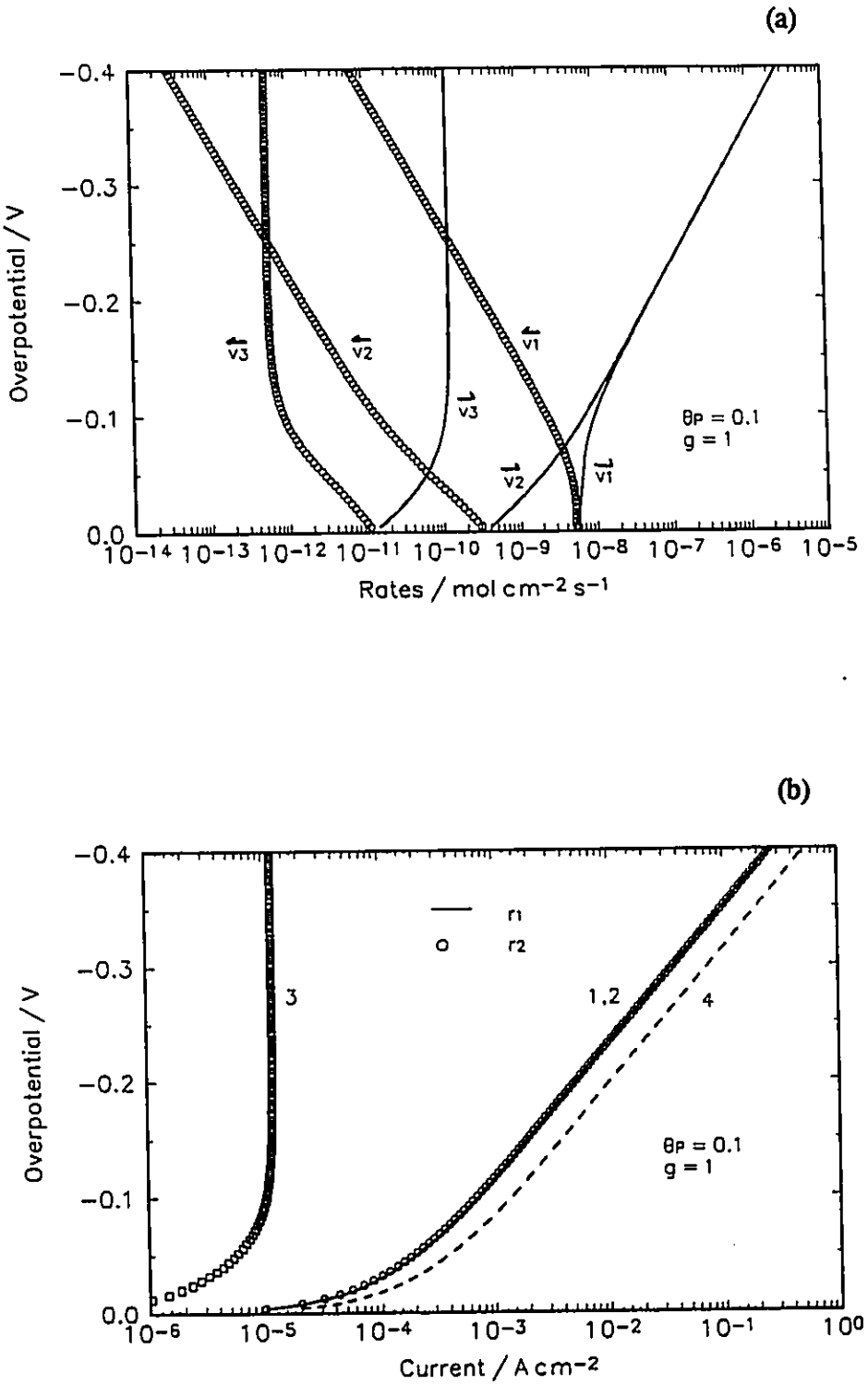

Fig.4.III.7 (a) Relations of individual rates of the HER steps (eqn.(4.III.1)) to overpotential. $\theta_P = 0.1$, g = 1. (b) The relation of net rates of each step to the overpotential. Curves 1, 2 and 3 are for v_1, v_2 and v_3, respectively. Curve 4 is for the total Faradaic current.

current-density which is equal to $r_1 + r_2$, or twice r_1 or r_2, since Faradaic electron transfer is only involved in the first two steps. In this plot, the relation of $r_1 = r_2$ is explicitly revealed.

4.III.3 Treatment of Full-Range Potential-relaxation Transients in Unpoisoned Solution

Before further study on poisoning effects on the kinetic behaviour of the HER was made, adsorption and kinetic behaviour of the Pt electrode in "clean", unpoisoned solutions was investigated. The *full-range* potential-relaxation transients at Pt electrodes were treated by the methods described in Section 3.2., which showed how potential-relaxation behaviour can be described theoretically in terms of reaction rates in the HER (see eqns.(3.6) and (3.7)) and simulation procedures.

Fig.4.III.8 shows the fitted results for the *full-range* open-circuit potential-relaxation behaviour, based on the same set of experimental data shown Fig.4.II.2a. The potential-relaxation transients for the HER were recorded at a bright, activated Pt electrode in 2M KOH solution (298 K). The electrode was anodically activated at +1.1 V (vs RHE) before each potential transient was recorded on the digital oscilloscope. The open circles represent experimental data and the solid lines are the best-fit results from the theoretical calculations (simulation behaviour). The fitting results yield the following rate-constants and other parameters: $k_1 = 3.1 \pm 2 \times 10^{-8}$, $k_{-1} = 6.0 \pm 1 \times 10^{-9}$, $k_2 = 2.9 \pm 1 \times 10^{-10}$, $k_3 = 8.0 \pm 1 \times 10^{-14}$ mol $cm^{-2}s^{-1}$, $C_{dl} = 27.8\ \mu F\ cm^{-2}$ and $q_1 = 89\ \mu C\ cm^{-2}$. The transients starting at different initial potentials should give one set of kinetic parameters since they are independent of initial overpotentials at open-circuit.

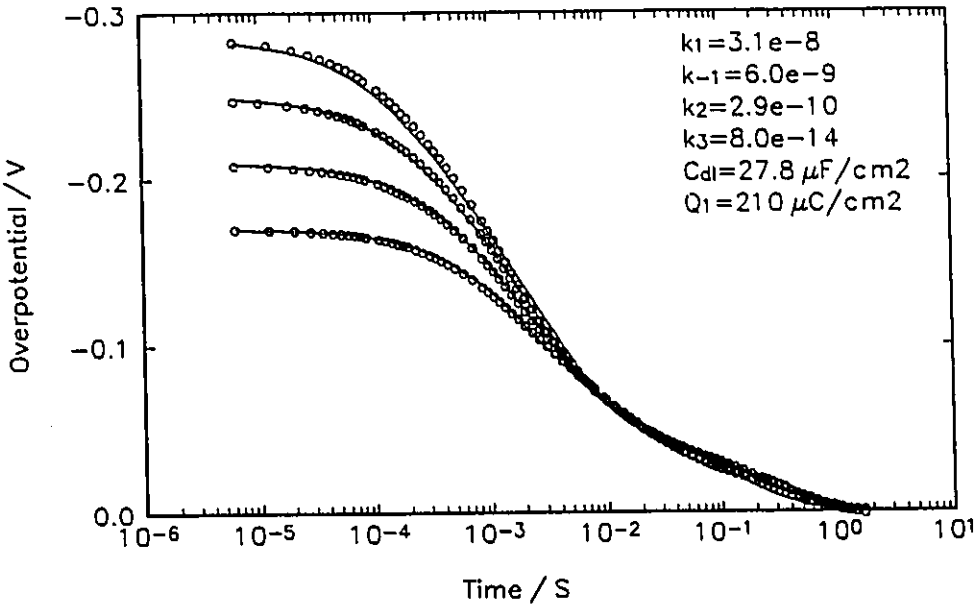

Fig.4.III.8a Simulation of full-range potential-relaxation behaviour for the HER at the bright Pt in 2 M KOH solution, (data based on Fig.4.II.2a). The evaluated kinetic parameters are shown in the Figure.

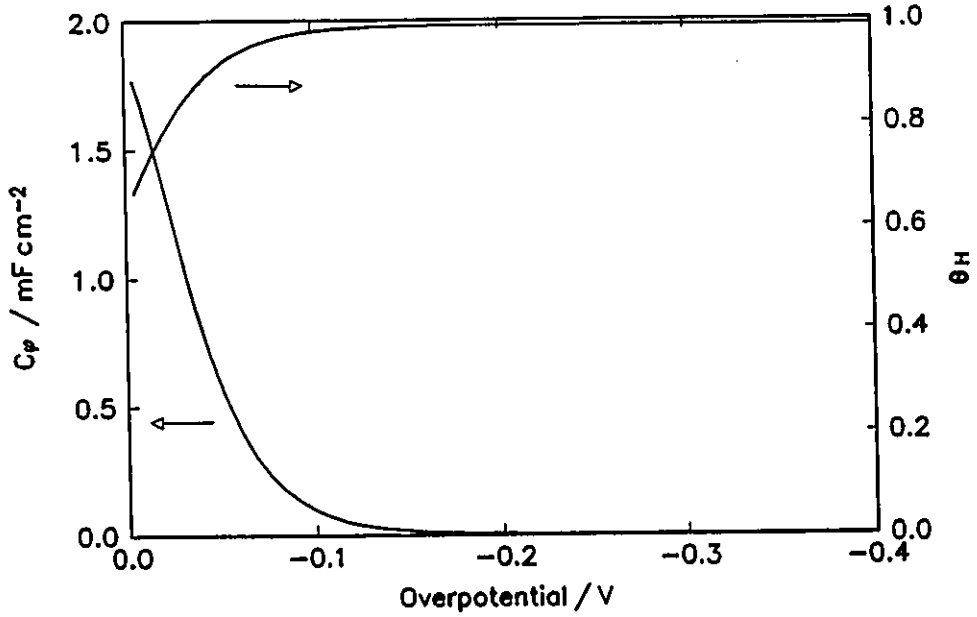

Fig.4.III.8b Corresponding relations of θ_H vs η and C_ϕ vs η, obtained from the parameters shown in Fig.4.III.8a.

It is evident that the fitting result is very satisfactory. From the simulation kinetic parameters, the coverage of adsorbed H, θ_H, and the associated pseudocapacitance, C_ϕ, were calculated. The plots of θ_H vs η and C_ϕ vs η relations are shown in Fig.4.III.8b. The H coverage changes from 0.7 to ca. 1 in the low overpotential region and approaches to 1 at high overpotentials. Correspondingly, C_ϕ decreases dramatically from 2.0 mF cm^{-2} (much larger than C_{dl}) to small values in this overpotential region. Note that the peak of C_ϕ (usually observed in many electrochemical systems) cannot be identified in this case. Since $k_1 > k_{-1}$ here, the C_ϕ maximum (not available here) shifts to a potential more positive than the reversible H_2 potential. (see theoretical calculation result in Fig.3.2c showing how the C_ϕ peak shifts to smaller cathodic overpotentials as k_{-1} decreases.)

The double-layer capacitance at bright Pt in 2 M KOH solution was determined as C_{dl} = 27.8 μF cm^{-2}, in excellent agreement with the results on the same system obtained by the initial potential-relaxation method (see Section 4.II.1.3). The monolayer charge q_1 was measured to be 89 μC cm^{-2} which is smaller than the "full monolayer coverage" value of 210 μC cm^{-2} in the ideal situation. This means that ca. 58% of the Pt surface is inactive in the H_2 evolution reaction. Similar conclusions can be found in other literature [8,196].

4.III.4 Poisoning Effect of Thiourea on Adsorption and Kinetic Behaviour of Pt in Alkaline Solution

Thiourea, $(NH_2)_2C{=}S$, is known to be a strong adsorbate with the S atom bonding to the surface of metals. The poisoning effect of thiourea in an electrochemical system was first studied at Hg by Schapink [232] and Parsons [233]. Thiourea is believed to become decomposed

and reduced under cathodic polarization to partially charged S^{2-} ions which are strongly adsorbed on the electrode surface in the course of H_2 evolution. Here, its influence on the o.p.d. H adsorption behaviour and the related catalytic performance of the poisoned Pt electrode was examined in some detail.

Experimentally, open-circuit potential-relaxation experiments were carried out at bright Pt electrodes in 0.5 M NaOH solution. 1 ppm of thiourea as a poison in catalysis studies, was introduced into the solution.

Fig.4.III.9a shows the potential-relaxation transients with (curve a) and without (curve b) the presence of thiourea poison in the solution. Curve a was measured in the poisoned solution ($i_{t=0}$ = 0.81 mA cm^{-2}). Curve b was obtained in the clean solution ($I_{t=0}$ = 38.6 mA cm^{-2}). In Fig.4.III.9a, the points indicate experimental data and the solid lines the numerical simulation using eqn.(4.III.1). A major difference of the relaxation in the poisoned solution from that in the clean solution is that the arrest over the milli-second region *disappears* in the former case. Correspondingly, the time scale for decline of overpotential at Pt (in this example) between say -0.27 and -0.05 V is substantially extended by nearly two decades.

A set of rate constants and parameters were obtained from the simulation of the "poison" potential-relaxation (curve a), as k_1 = 2.7 x 10^{-9}, k_{-1} = 1.8 x 10^{-8}, k_2 = 7.8 x 10^{-10}, k_3 = 1.5 x 10^{-11} (mol cm^{-2} s^{-1}), C_{dl} = 32.7 μF cm^{-2}, q_1 = 5.1 μC cm^{-2}, g = 3.8 and θ_P = 0.93. It is interesting to find that ca. 93% of the surface is covered by the poison, which competitively occupies the active sites which would otherwise be occupied by the adsorbed H.

The coverage by H, θ_H, and C_ϕ, were also calculated from the above equations. As shown in Fig.4.III.9b, the H occupies about 0.6% of the total surface, ten-times less than the

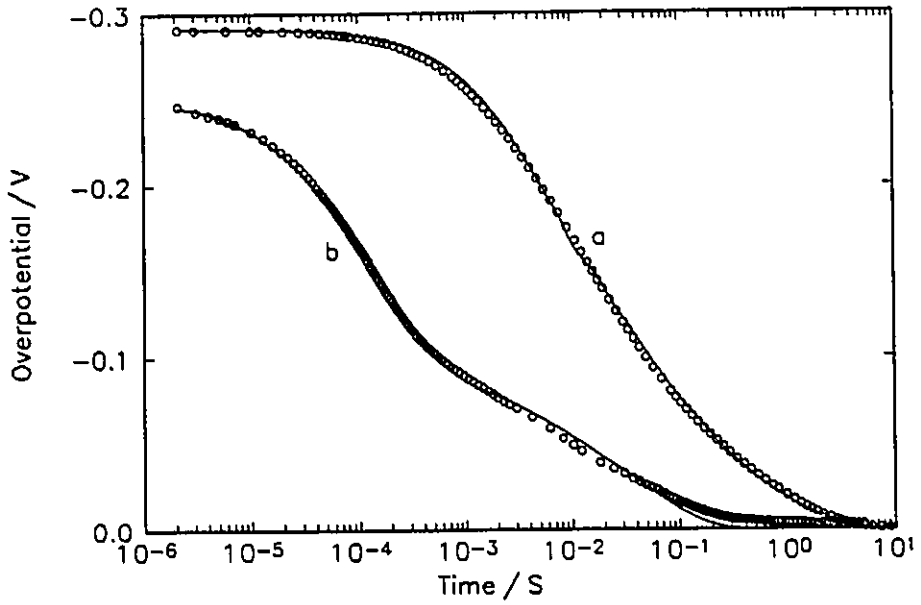

Fig.4.III.9a Potential-relaxation transients for the HER at Pt in 0.5 M NaOH. Curve a is for the presence of 1 ppm thiourea poison. The simulation parameters are $k_1 = 2.7 \times 10^{-9}$, $k_{-1} = 1.8 \times 10^{-8}$, $k_2 = 7.8 \times 10^{-10}$, $k_3 = 1.5 \times 10^{-11}$ mol cm^{-2}s^{-1}, $C_{dl} = 32.7\ \mu$F cm^{-2}, $q_1 = 5.1\ \mu$C cm^{-2}, g = 3.8 and $\theta_P = 0.93$. Curve b is obtained for clean solution.

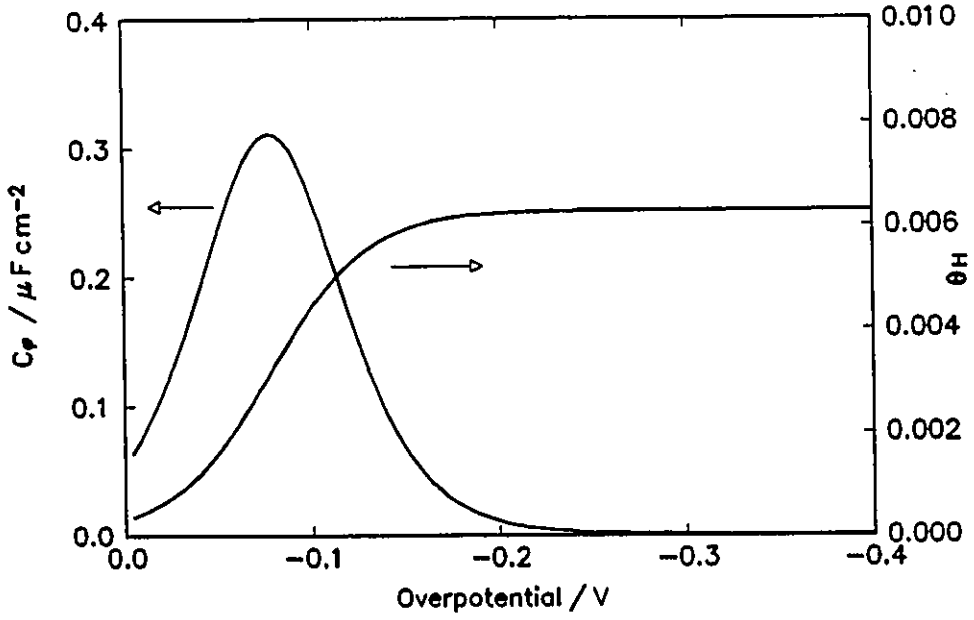

Fig.4.III.9b Corresponding relations of θ_H vs η and C_ϕ vs η, obtained from the parameters shown in Fig.4.III.9a.

available sites (7%, since $\theta_P \approx 0.93$). This, it is supposed, must be mainly because of the mutual interactions among the surface adsorbates caused by the presence of the poison. The small value of pseudocapacitance, C_ϕ ($< C_{dl}$) evidently indicates that the H is prevented from further adsorption due to competition by co-adsorbed poison on the surface.

The effect of adsorbed thiourea as poison was also examined by means of impedance measurements for comparison. Fig.4.III.10 shows the complex plane Z' vs Z'' plots, Bode phase plots and log |Z| vs log ω plots for a bright Pt electrode in a clean (curve b, dotted lines) and 0.1 ppm thiourea-poisoned (curve a, solid lines) 0.5 M NaOH solution at η=-50 mV. In the clean solution, the second semi-circle is clearly developed (curve b) in the complex plane plot at low frequencies with a complementary second peak on the Bode phase plot, which are associated with the adsorption of the o.p.d. H intermediate [189].

In the poison case, however, the second semi-circle in the complex plane plot and second peak in the phase plot almost disappear (curves a). This must be due to the competitive adsorption of the poison which leads to substantial decrease of H coverage and corresponding reactive pseudocapacitance. This result supplementarily supports the conclusion deduced from the potential-relaxation results and analysis shown in Fig.4.III.9.

Tafel relations for the Pt electrode were measured in the KOH solution with and without the presence of thiourea, as shown in Fig.4.III.11. Curve a is for 1 ppm thiourea poisoned solution, and curve b for the clean solution. It can be seen clearly that introduction of poison in the solution substantially reduces the current-densities at corresponding overpotentials compared to those for unpoisoned Pt. Current-densities on curve a are nearly one decade smaller than on curve b, indicating that the adsorption of poison significantly impedes the

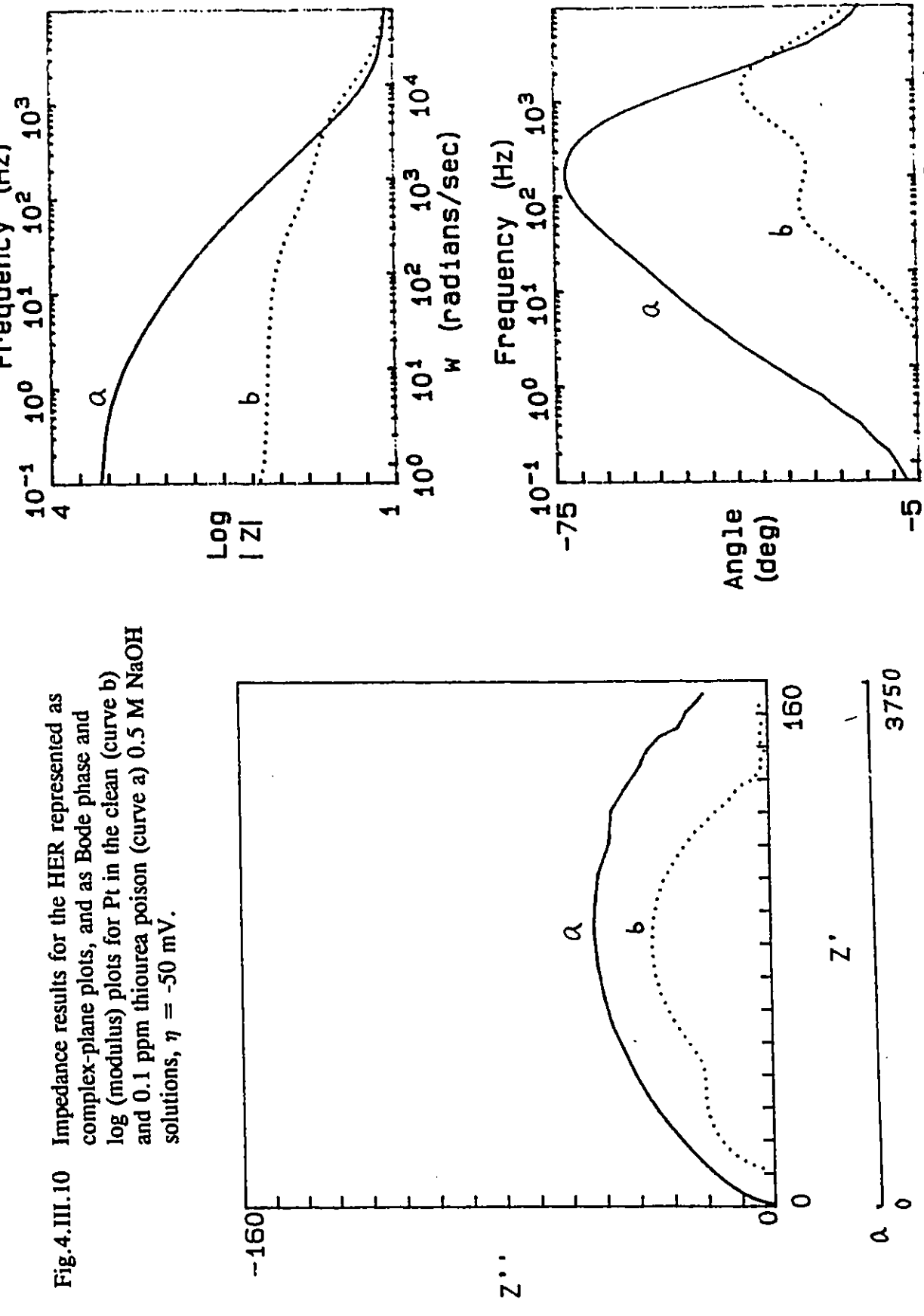

Fig.4.III.10 Impedance results for the HER represented as complex-plane plots, and as Bode phase and log (modulus) plots for Pt in the clean (curve b) and 0.1 ppm thiourea poison (curve a) 0.5 M NaOH solutions, η = -50 mV.

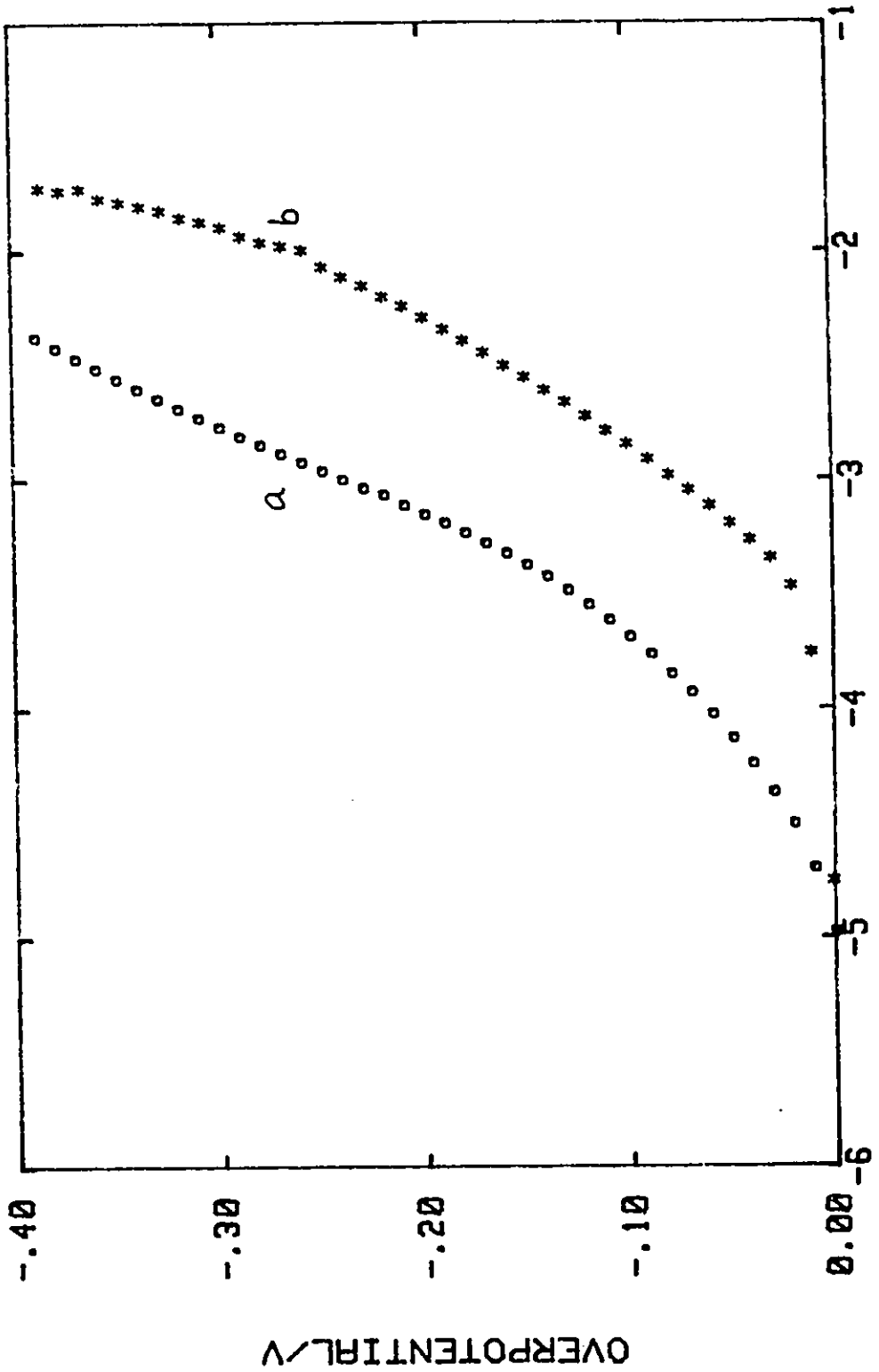

Fig.4.III.11 Tafel plots for the HER at Pt in the clean (curve b) and thiourea poisoned (curve a) 0.5 M NaOH solutions.

electrode activity, and leads to the loss of electrocatalytic activity of Pt electrode for the HER. The electronic structure of the metal surface may also be altered due to the poison adsorption, with electron-pair donation, as is also indicated by the change of evaluated rate constants from the potential-relaxation results for the poisoned solution.

The rate constant (k') data required for simulation of the potential-relaxation curves can also be employed to construct Tafel type relations for k' values of the component steps as a function of overpotential. For the purpose of convenient comparison, the k's are combined with the overpotentials in the form of exponential terms, with the exception of k'_3. The relation of η to $k'\exp[F\eta/2RT]$ is then calculated from the rate constants derived in the simulation calculations and plotted as follows.

Results are shown in Fig.4.III.12a and 12b for the non-poisoned and the thiourea-poisoned Pt electrodes, respectively. The rate constants derived from the fitting curves in Fig.4.III.9a are used. Without poison, step 2 in the HER is clearly rate-controlling with only a small parallel contribution from step 3 (through k'_3). In the presence of thiourea, the situation becomes reversed in that step 1 now clearly becomes rate-determining but the rate constant for step 3 (H+H recombination) actually becomes enhanced, probably because of weakening of the bond of adsorbed H to the cathode metal.

4.III.5 Poisoning Effect of As_2O_3 on Adsorption and Kinetic Behaviour at Pt in the KF·2HF Melt

Study of kinetic behaviour of Pt in the HER in the KF·2HF melt was conducted for the first time in the present work. In the presence of As_2O_3, kinetic behaviour of the HER as well as u.p.d. H adsorption, will be greatly influenced mainly through competitive adsorption of the

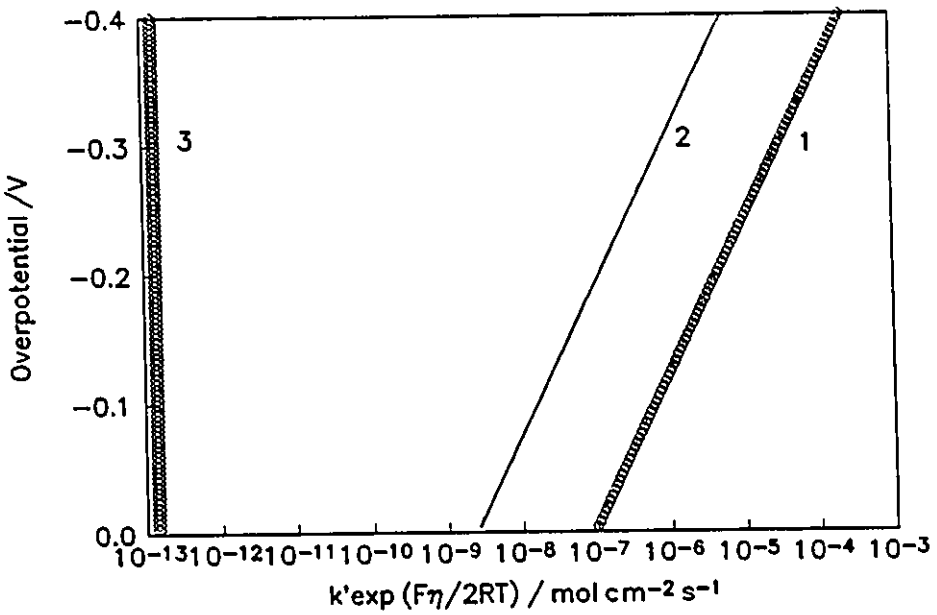

Fig.4.III.12a Relations of rate constants, k', in combination with exp (Fη/2RT) term (except k_3') to overpotential for the rate constants obtained from simulation of potential-relaxation at Pt in clean solution.

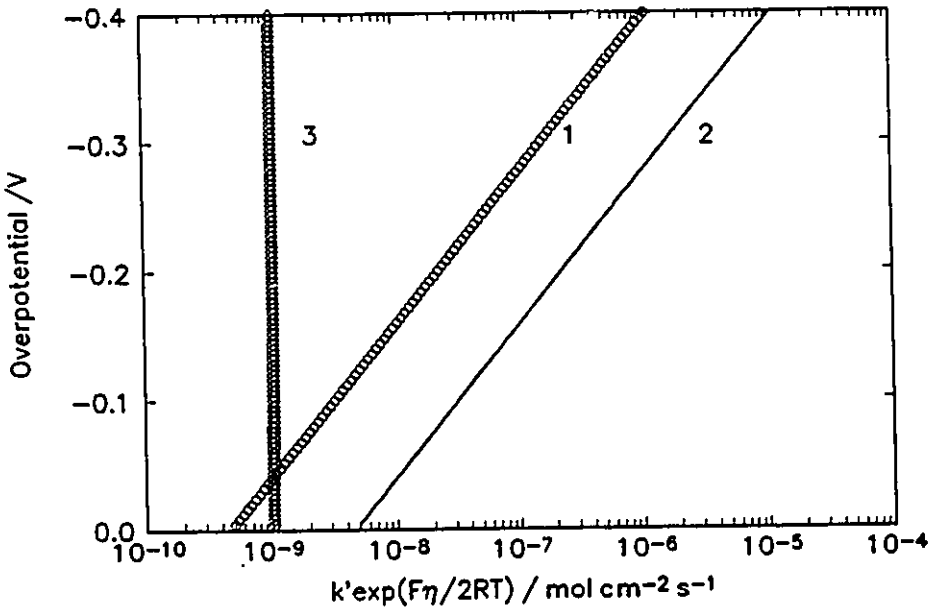

Fig.4.III.12b As for (a), but in 1 ppm thiourea poisoned 0.5 M NaOH solution.

arsenic poison at the active sites on the metal. Agair, lateral interactions amongst the adsorbed species will cause change of H coverage and surface electronic structure of the electrocatalyst, and hence modify the catalytic behaviour of the metal electrode.

4.III.5.1 Cyclic Voltammetry of Pt in As_2O_3 Poisoned KF·2HF Melt

The poison effect of As_2O_3 on the adsorption behaviour of u.p.d. H at Pt was studied here by means of cyclic voltammetry. Fig.4.III.13 shows the CV plots for bright Pt in the KF·2HF melt at 85°C with the addition of 1.4×10^{-4} M (weight percent) of As_2O_3 powder. In order to prevent possible moisture being present in the melt which would lead to complications in the CV plots, a small amount of P_2O_5 was added to absorb (react with) any water present in the melt. The rate of potential scan was 100 mV/s. It is observed that over the potential region of 0.2 - 0.5 V (vs Fe/FeF_2) where the u.p.d monolayer H is formed, the peaks and the charges of the u.p.d. H in the presence of poison are diminished in comparison with those for the clean melt (Fig.4.III.13). The adsorbed As poison, as may be expected, competitively occupies the active sites which would otherwise be taken by the u.p.d. H adsorption in this potential region.

It is interesting to see that an oxidation peak at ca. 1.0 V and a reduction peak at ca. 0.7 V can be clearly identified. These seem to be due to oxidation and reduction reactions of the arsenic species, though the process is not reversible. Further cycling to more positive potential leads to formation of fluoride at the Pt electrode, and As (V) (as AsF_6^-) may then be produced and dissolved into the electrolyte. When the upper limit of cycling is decreased to 1.1 V and 0.8 V, the u.p.d. H peaks are further suppressed. This is because arsenic poison occupies adsorption sites at Pt and causes the u.p.d. H adsorption to diminish if the arsenic species is not removed by oxidation at higher potentials.

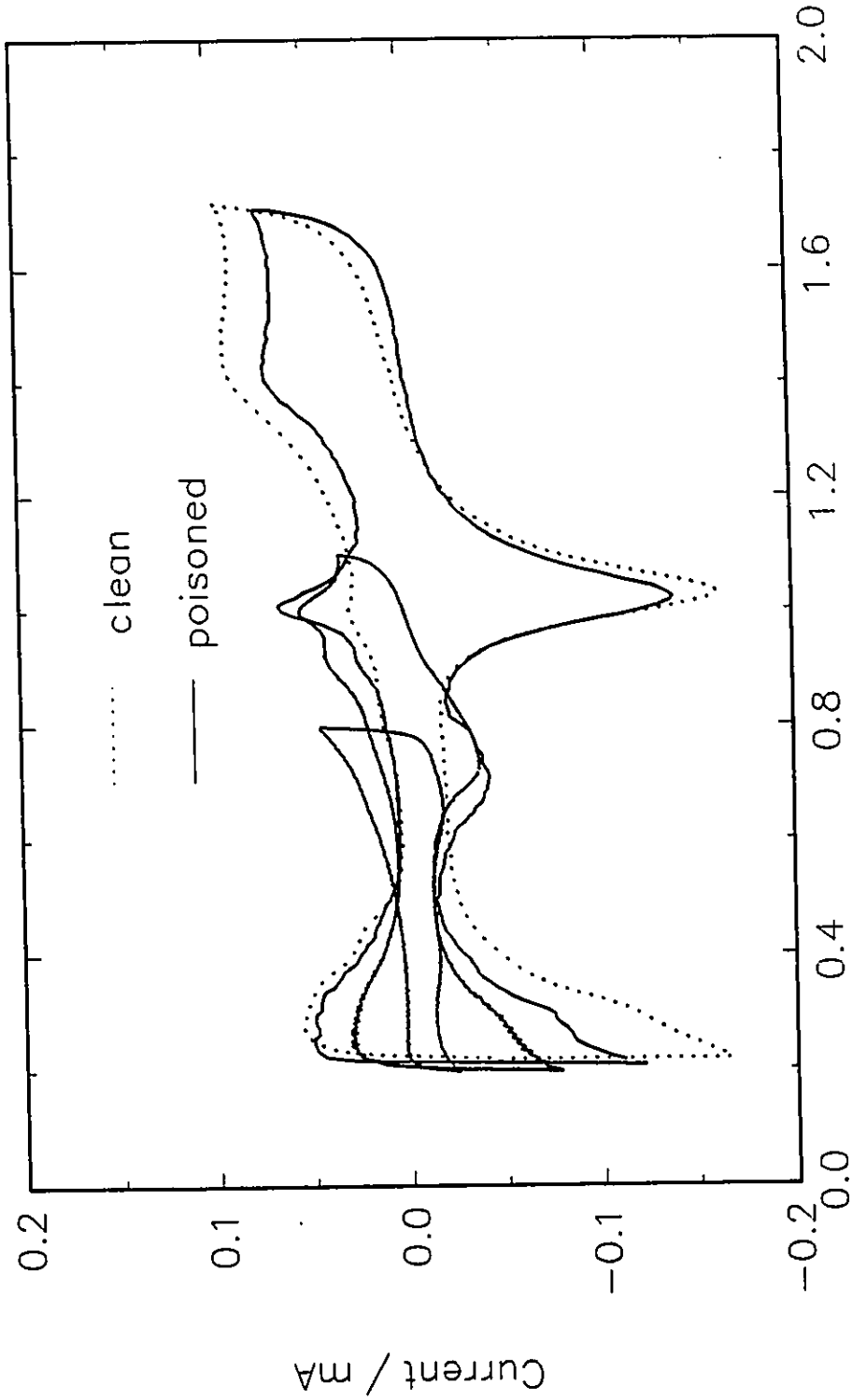

Fig.4.III.13 Cyclic voltammetry at the Pt electrode in the KF·2HF melt. Solid lines are measured in the melt in the presence of 1.4×10^{-4} M As_2O_3 poison and the dotted line is for the clean melt.

4.III.5.2 Potential-relaxation Transients at Pt in As_2O_3 Poisoned KF·2HF Melt

Fig.4.III.14a shows the potential-relaxation transients at the Pt electrode with introduction of 1.4×10^{-5} M (weight percent) of As_2O_3 (curve 2) in the KF·2HF melt in comparison with the behaviour in "clean" melt (curve 1). Again, the transient in the presence of poison shifts to longer time domain than that for the clean melt, and the arrest disappears on curve 2, due to the diminution of H adsorption through competition by arsenic species.

Quantitatively, kinetic parameters were obtained from the simulation of curves 1 and 2, as shown in Table 4.III.1.

Table 4.III.1 Comparison of simulation parameters for the HER at Pt in unpoisoned and 1.4×10^{-5} M As_2O_3 poisoned KF·2HF melt

KF·2HF melt	unpoisoned	As_2O_3 poisoned
k_1 (mol $cm^{-2}s^{-1}$)	2.0×10^{-7}	1.6×10^{-10}
k_{-1}	3.0×10^{-8}	2.1×10^{-10}
k_2	3.8×10^{-10}	1.0×10^{-15}
k_3	3.8×10^{-14}	2.1×10^{-11}
C_{dl} (μF cm^{-2})	8.94	6.49
q_1 (μC cm^{-2})	115	8.5
g		3.3
θ_P		0.53

Apparently, the k values for the poisoned melt are much smaller than those without poison, corresponding to inhibition of the HER by the poison adsorption. Other quantities are also characterized, as listed in Table 4.III.1.

The relations of θ_H and C_ϕ to η for the poison case are plotted in Fig.4.III.14b. The features of these relations are similar to those for the other poison situations. The variation of

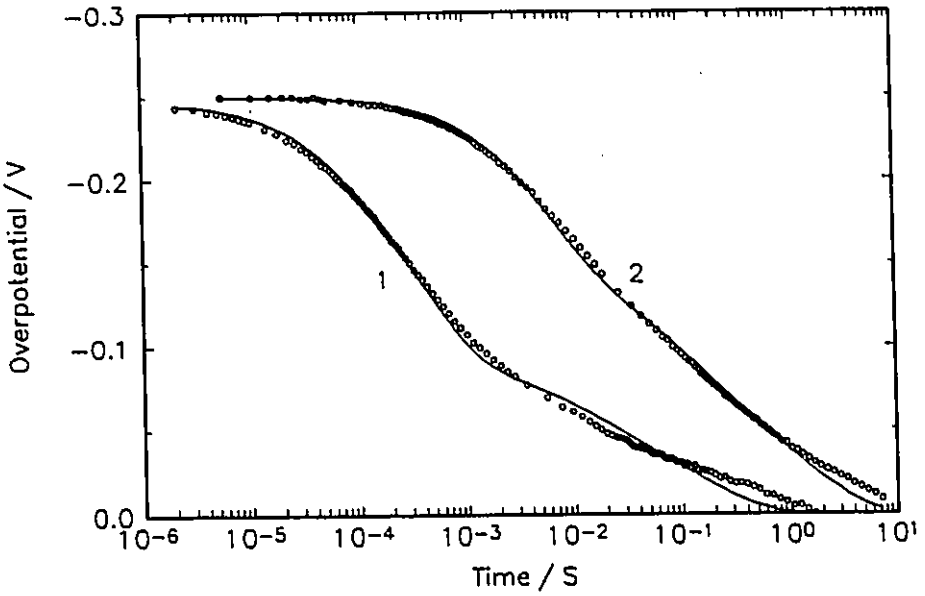

Fig.4.III.14a Potential-relaxation transients for the HER at Pt in KF·2HF melt. Curve 2 is for the presence of As_2O_3 poison, and curve 1 is for the clean melt. The simulation parameters are listed in Table 4.III.1.

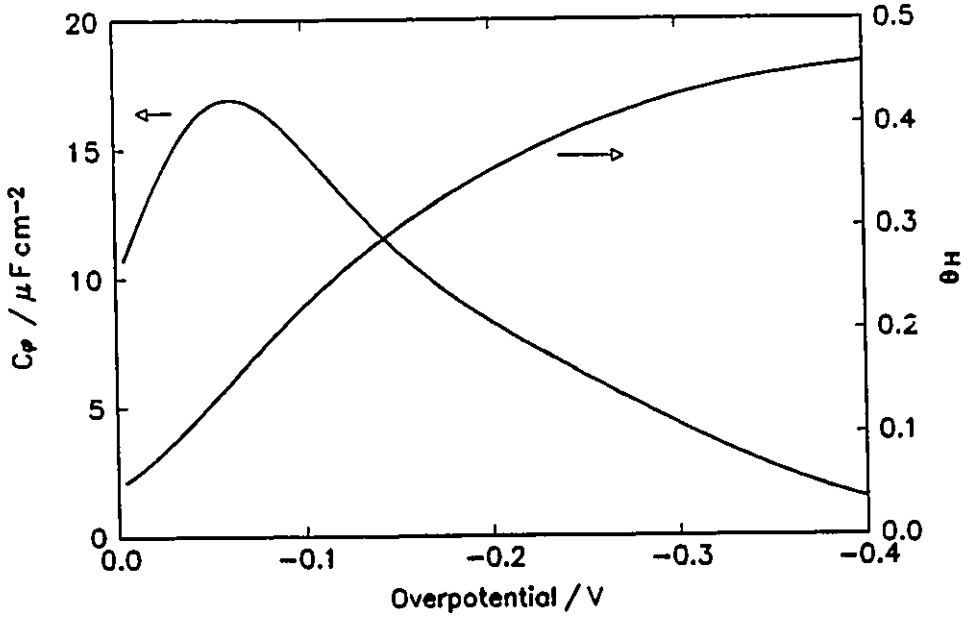

Fig.4.III.14b Corresponding relations of θ_H vs η and C_ϕ vs η, obtained from the parameters shown in Fig.4.III.14a.

θ_H with potential becomes small which is to be attributed to the role of increasing value of k_3 in the reaction. Thus, the recombination step becomes more significant in the presence of poison, since physically, poisons adsorb on the surface sites and prevent H from further adsorption; this, in fact, promotes H desorption through repulsive interaction in step 3.

4.III.6 Poisoning Effect of As_2O_3 on Adsorption and Kinetic Behaviour of the HER at Pt in KOH Solution

4.III.6.1 Cyclic Voltammetry at Pt in As_2O_3 Poisoned KOH Solution

The influence of different concentrations of poisons on CV was examined. Fig.4.III.15a shows CV plots for Pt in 2 M KOH solutions; curve 1 was measured in clean, non-poisoned solution, curve 2 was for addition of 5.0×10^{-8} M As_2O_3 and curve 3 for the presence of 5.5×10^{-7} M As_2O_3 poison. It can be seen that the presence of arsenic causes no great modification of the shapes of the u.p.d. H peaks but both the peaks for the "strongly" and "weakly" adsorbed H are decreased uniformly with increase of arsenic concentration. Processes in the high positive potential region are surface oxide formation at Pt, coupled with oxidation of adsorbed arsenic species into As(V) (as AsO_3^- dissolved into the solution).

Fig.4.III.15b shows CV plots for Pt in 5.0×10^{-8} M As_2O_3 poisoned solution. Curve 1, 2 and 3 were measured at 1.3, 1.0 and 0.7 V upper limit potentials, respectively. The u.p.d. H peaks are greatly suppressed when the potential is scanned only to lower-limit values, e.g. curve 3. This suggests that coverage by arsenic species is greater over the 0.05 - 0.5 V region if the potential has not been scanned high enough to oxidize the arsenic poison to As(V) species which are less adsorbed (smaller donicity) or dissolved as AsO_3^- ions into the solution.

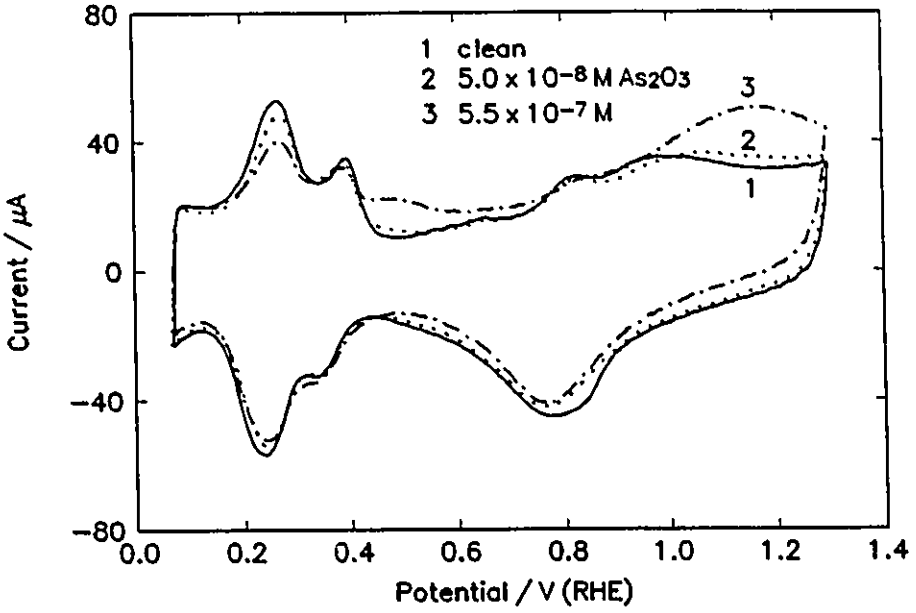

Fig.4.III.15a Cyclic voltammetry in 2 M KOH at the Pt electrode. Curve 1 is measured in the clean melt, curve 2 in the presence of 5.0 x 10^{-8} M As_2O_3 poison and curve 3 with 5.5 x 10^{-7} M As_2O_3 poison.

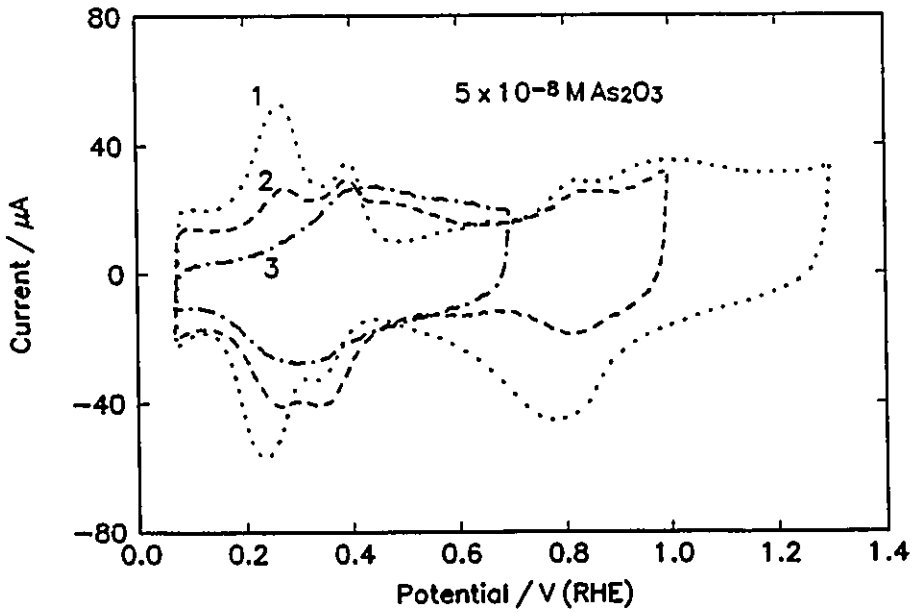

Fig.4.III.15b Cyclic voltammetry in 2 M KOH at Pt electrode measured in the in the presence of 5.0 x 10^{-8} M As_2O_3 poison.

4.III.6.2 Potential-relaxation Transients at Pt in As_2O_3 Poisoned aq. KOH Solution

Fig.4.III.16 shows potential-relaxation transients measured at the Pt electrode in 2 M aq. KOH solutions. Curve 1 is obtained in clean, unpoisoned solution, curves 2 and 3 are transients in the presence of 5.0×10^{-8} M and 5.5×10^{-7} M As_2O_3 poison in solution, respectively. The electrode was activated by anodic polarization at +1.1 V for 5 seconds to remove any adsorbed arsenic compound at the electrode through the anodic oxidation reaction. Each potential-relaxation was recorded under the same conditions, the electrode was then polarized at the initial potential for 5 seconds prior to each current interruption. It can be clearly seen that as the poison concentration is increased, the whole curves shift to longer time domains and the arrest, which is displayed on curve 1 for the clean solution, gradually diminishes (curve 2) and disappears (curve 3).

Simulation treatments were made as usual. Curves for the presence of poisons were simulated (solid lines) as described previously. The resulting kinetic parameters are listed in Table 4.III.2.

It is seen that increasing concentration of poison leads to decreased monolayer charge, q_1, and increased values of g and θ_P, as expected.

The relations of θ_H vs η and C_ϕ vs η for curves 2 and 3 are plotted in Fig.4.III.17a,b. For the case of low poison concentration, the θ_H can still reach around 0.8, since there is only ca. 8.2% ($\theta_P = 0.082$) of the surface covered by poison species. In a more concentrated poison solution, the coverage by o.p.d. H becomes very small ($\theta_H = 0.0016$ in Fig.4.III.17b), corresponding to almost the entire surface (99.8%) being occupied by the adsorbed As species. The mutual interaction is strong (g=5.1) in this case. The positions of the C_ϕ peaks differ in

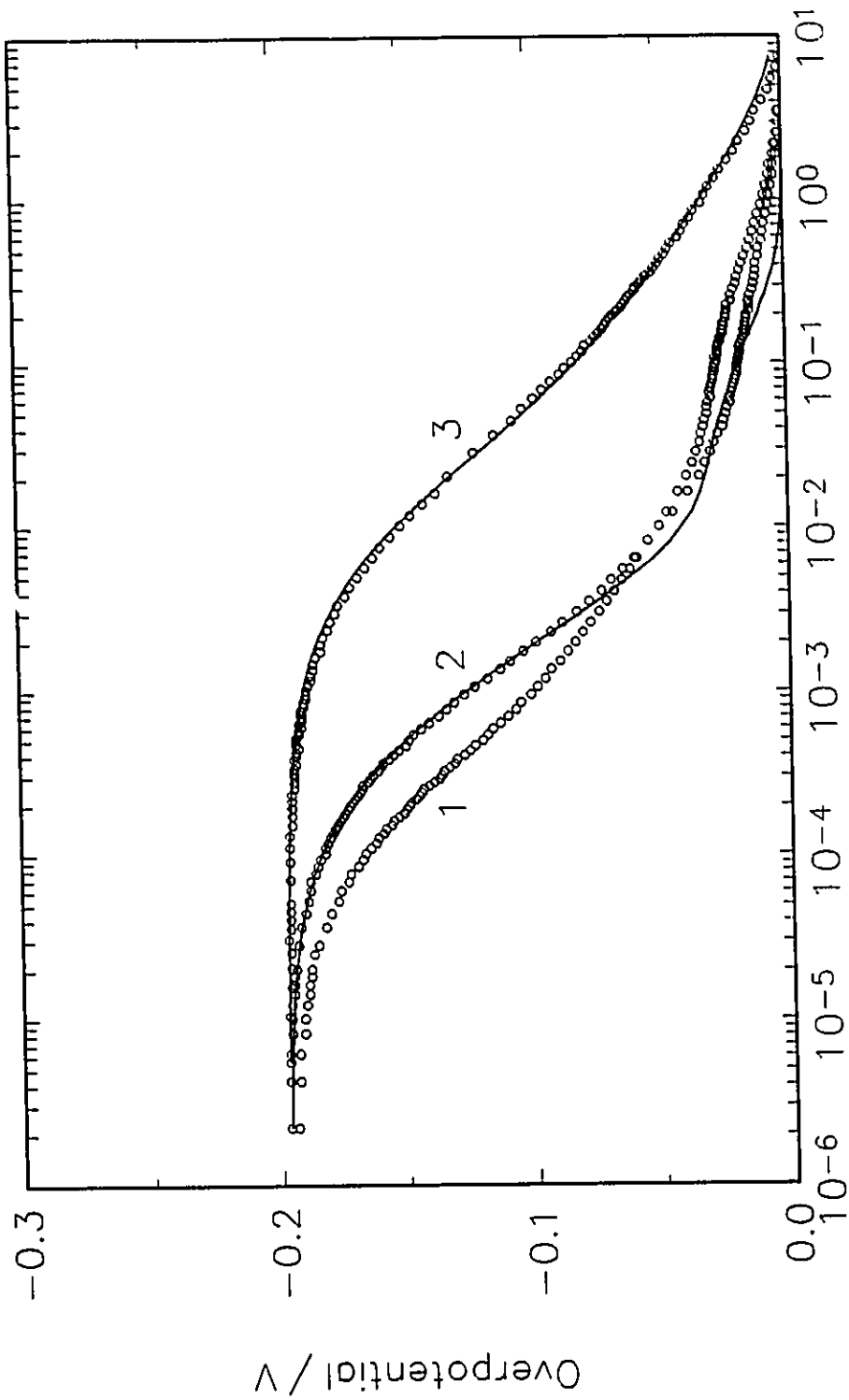

Fig.4.III.16 Potential-relaxation transients for the HER at Pt in 2 M KOH. Curve 1 is for clean solution; curves 2 and 3 are for 5.0×10^{-8} M and 5.5×10^{-7} M As_2O_3 poison solutions. The simulation parameters for curves 2 and 3 are listed in Table 4.III.2.

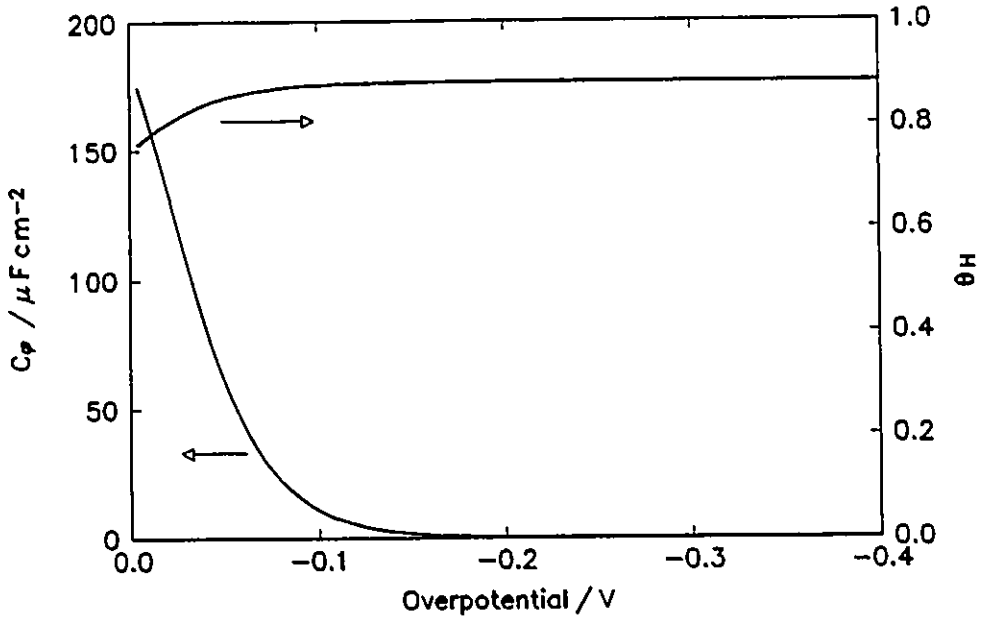

Fig.4.III.17a Corresponding relations of θ_H vs η and C_ϕ vs η, obtained from the parameters of curve 2 in Fig.4.III.16.

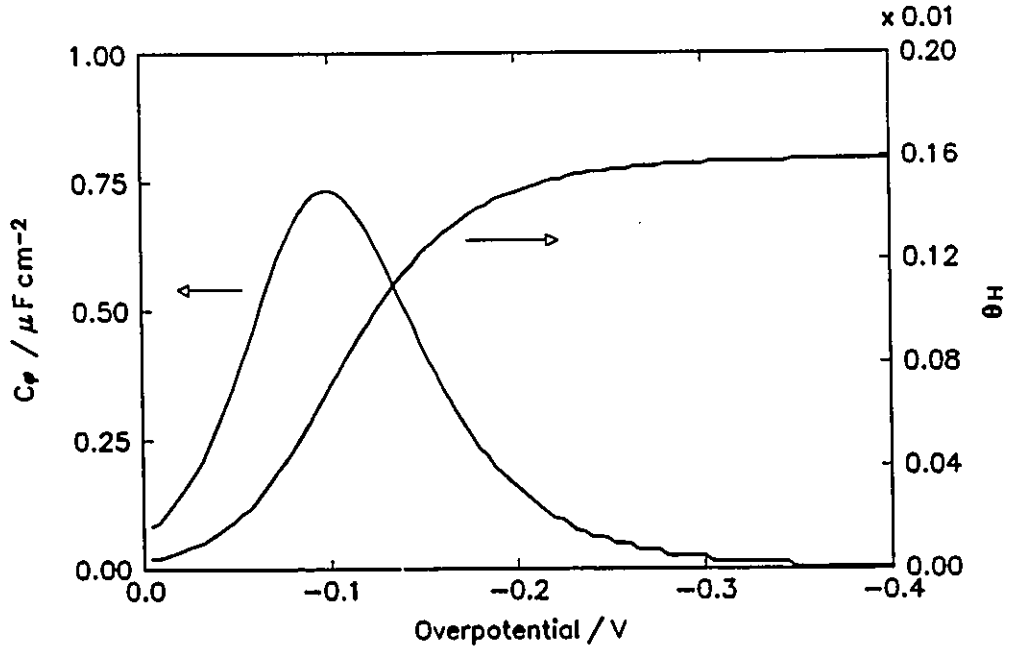

Fig.4.III.17b Corresponding relations of θ_H vs η and C_ϕ vs η, obtained from the parameters of curve 3 in Fig.4.III.16.

Table 4.III.2 Comparison of simulation parameters for the HER at Pt for two concentrations of As_2O_3 poisoned solutions

2 M KOH solutions	5.0×10^{-8} M As_2O_3	5.5×10^{-7} M As_2O_3
k_1 (mol $cm^{-2}s^{-1}$)	6.9×10^{-9}	3.6×10^{-10}
k_{-1}	2.3×10^{-10}	2.5×10^{-8}
k_2	3.1×10^{-11}	4.9×10^{-10}
k_3	1.1×10^{-12}	6.5×10^{-8}
C_{dl} (μF cm^{-2})	30.2	25.2
q_1 (μC cm^{-2})	59	5.8
g	2.3	5.1
θ_P	0.082	0.84

these two Figures, which is because of different ratios of k_1/k_{-1} (larger for the higher concentration of poison in the solution), as shown in Table 4.III.2.

It was found that currents decrease with time under steady-state polarization at constant overpotential in the poisoned solution, as shown in Fig.4.III.18 for Pt polarized at -0.2 V constantly. The I vs t relation suggests that poison adsorption increases progressively, blocking the active sites at the metal and leading to decrease of current in the HER. Therefore the initial currents for potential-relaxation transients depend on when the circuit will be interrupted in the steady-state polarization experiment. Potential-relaxation experiments were carried out by pre-polarizing the electrode at the initial potential for a longer time (60 s) before opening the circuit.

Fig.4.III.19a shows the potential-relaxation behaviours at Pt electrode in 2M KOH solutions; curve 1 was obtained for unpoisoned solution; curve 2 for the electrode pre-polarized for 5 s and curve 3 for 60 s at -0.2 V in the presence of 5.0×10^{-8} M As_2O_3.

Simulation of curve 3 gave the following parameters: $k_1 = 2.9 \times 10^{-10}$, $k_{-1} = 1.0 \times 10^{-10}$, $k_2 = 1.3 \times 10^{-11}$, $k_3 = 3.0 \times 10^{-11}$ (mol $cm^{-2}s^{-1}$), $C_{dl} = 30.2$ μF cm^{-2}, $q_1 = 41.7$ μC cm^{-2},

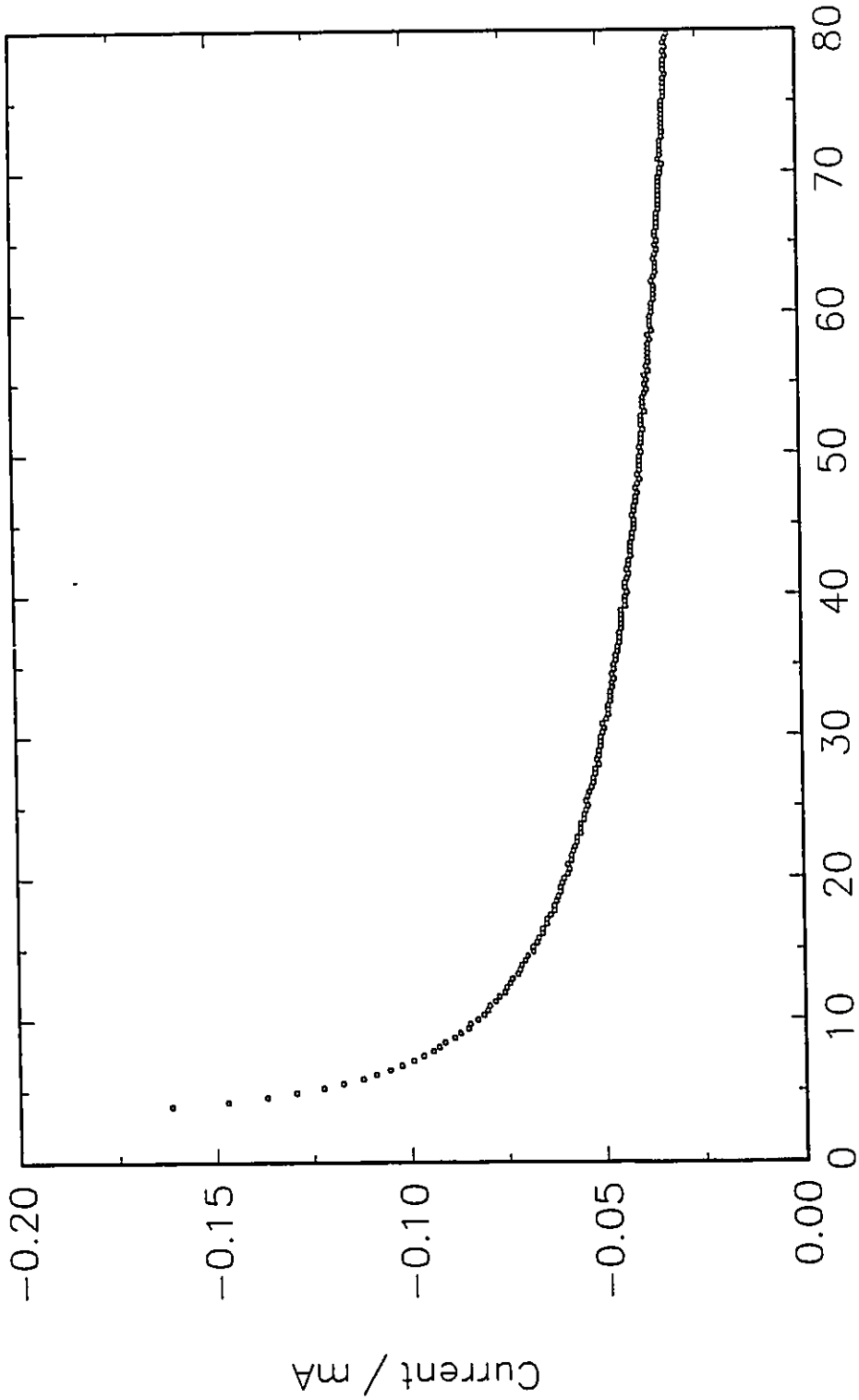

Fig.4.III.18 Current response for cathodic polarization at -0.2 V at Pt in 2 M KOH solution.

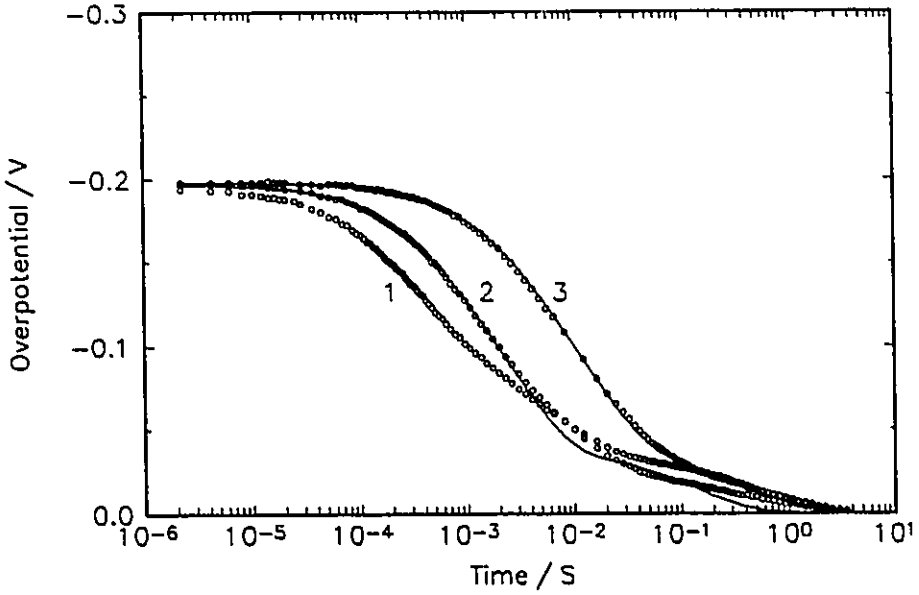

Fig.4.III.19a Potential-relaxation transients for the HER at Pt in 2 M KOH. Curve 1 is for clean solution; curves 2 and 3 are transients following pre-polarization for 5 s and 60 s, respectively, in the presence of 5.0×10^{-8} M As_2O_3 poison.

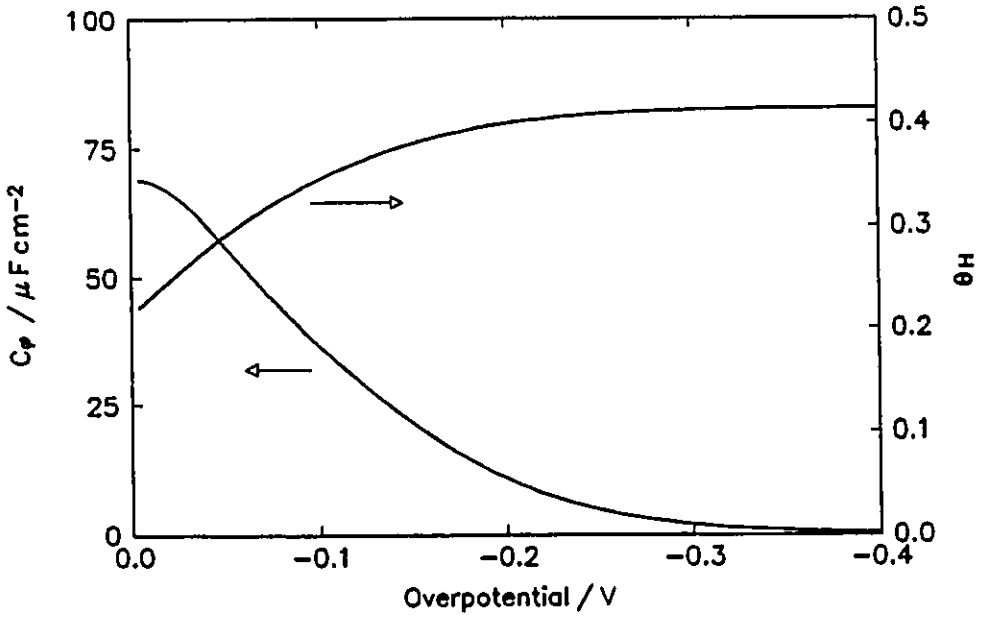

Fig.4.III.19b Corresponding relations of θ_H vs η and C_ϕ vs η, obtained from the parameters of curve 3 in Fig.4.III.19a.

g = 4.7 and θ_P = 0.22 (curves 1 and 2 are the same as shown in Fig.4.III.17). The longer times of prior polarization lead to increased coverage by poison (larger values of θ_P) and decreased values of rate constants. As for the other cases, the transient curves tend to shift to the longer time domain, decaying more slowly with increasing pre-polarization time, probably due to reduction of the poison species.

For the longer time of pre-polarization (curve 3), relations of θ_H vs η and C_ϕ vs η are plotted in Fig.4.III.19b, which shows that θ_H and C_ϕ become smaller compared to the result in the previous case of curve 2 (the same curve 2 in Fig.4.III.16). More poison is adsorbed on the surface (θ_P = 0.22) and interaction among the adsorbed species become stronger (g = 4.7). The less sensitive dependence of C_ϕ on η is due to the increasing significance of the recombination step ($k_2 < k_3$ in that case).

4.III.6.3 Tafel Behaviour of Pt in As_2O_3 Poisoned KOH Solutions

Figs.4.III.20a,b show Tafel plots for the HER at Pt under various conditions of poisoning and pre-polarization. In Fig.4.III.20a, concentrations of As_2O_3 for the curves are (1) 0; (2) 5 x 10^{-8} and (3) 5.5 x 10^{-7} M. Surface activation conditions were as for the other cases. Note, these conditions were exactly the same as for the situation prior to the potential-relaxation measurement (here, one Tafel data point corresponds to one *initial* steady-state overpotential for the potential-relaxation). In Fig.4.III.20b, the concentration of As_2O_3 for curves 2 and 3 is 5.0 x 10^{-8} M (curve 1 is for clean solution), but pre-polarization times for each potential are (2) 5 s and (3) 60 s, respectively.

It is seen from the above two Tafel-plot figures that current-densities are substantially decreased with increasing concentration of poison and with longer times of pre-polarization.

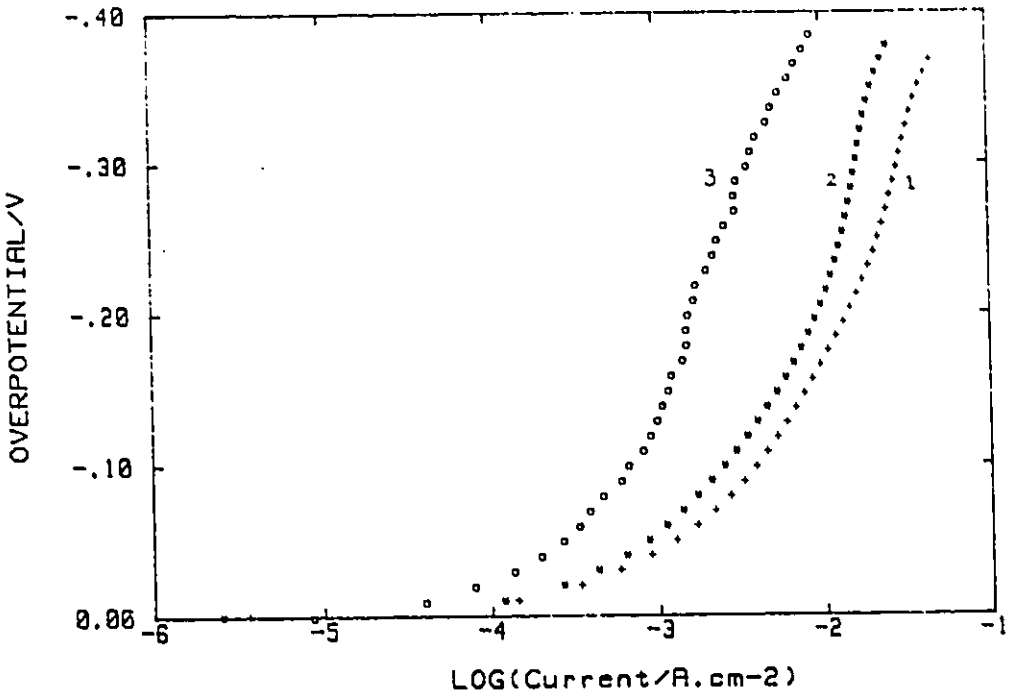

Fig.4.III.20a Tafel plots for the HER at Pt in 2 M KOH. Curve 1 is for clean solution; curves 2 and 3 are for 5.0 x 10^{-8} M and 5.5 x 10^{-7} M As_2O_3 poison solutions.

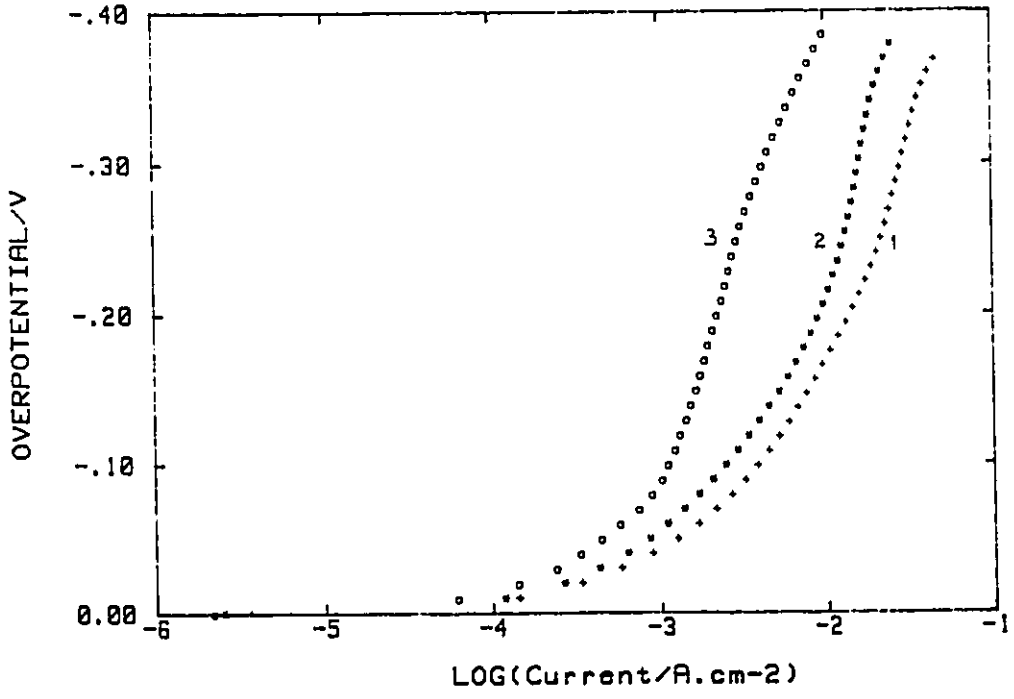

Fig.4.III.20b Tafel plots for the HER at Pt in 2 M KOH. Curve 1 is for clean solution; curves 2 and 3 are for 5 s and 60 s pre-polarization, respectively, in the presence of 5.0 x 10^{-8} M As_2O_3 poison.

This suggests that more adsorption by the poison diminishes the catalytic activity of Pt for the HER. Modification of the electronic structure at the metal surface due to poison adsorption and lateral interaction is possible, since the Tafel slopes are observed to be different depending on the conditions of poisoning.

Elemental As can even be *deposited* on the metal surface under long time cathodic polarization [147,234], as found in the present work by qualitative analysis; thus it is known that arsenic, cathodically deposited at Pt, is semi-metallic [147]. At coverages above one monolayer, electro-crystallization of arsenic probably occurs, as in metal deposition. AsH_3 may also be produced in the HER process, as was found from the analysis of the H_2 evolved in the acid media. As_2O_3 poison may be present in solution/melt in the form of anions, AsO_3^- or AsO_2^-, which diffuse to the double-layer region in a concentration gradient and further adsorb onto the metal surface where they can be reduced. In fact, poisons begin to become adsorbed on the surface at the potentials *positive* to the reversible H_2 potential as it was evident from the CV plots that the u.p.d. H peaks become suppressed by the adsorption of poison.

CHAPTER V

CONCLUSIONS AND CONTRIBUTIONS TO ORIGINAL RESEARCH

1. Catalytic behaviour of the electrodeposited Ni-Mo-Cd composite material for the HER was characterized by Tafel polarization measurements in the KF·2HF melt at 85°C. The superior catalytic behaviour of Ni-Mo-Cd over mild-steel cathodes can be attributed both to its micro-porous structure with high surface area and the electronic properties of the surface. A small Tafel slope b = 37 mV was observed at low overpotentials which is probably due to a catalytic effect of an hydride phase formed during H_2 evolution or in the preparation process of electrode deposition. The current-densities at Ni-Mo-Cd for given potentials were found to be nearly two orders of magnitude larger than those at corresponding smooth Ni-Mo bulk alloy electrodes. This is also supported by the results of C_{dl} determined from the initial potential-relaxation and a.c. impedance methods at the two electrodes.

2. For the first time, comparative Tafel polarization behaviour of Ni-Mo-Cd for the HER was examined in the analogous KOH·$2H_2O$ hydrate melt in comparison with that in the KF·2HF melt. It was observed that Tafel currents in the former melt were two magnitudes larger than those in the latter melt at given potentials, and the related results were obtained from the determination of C_{dl} by initial potential-relaxation experiments. Surface accessibilities of the porous electrode by the two melts having different surface tensions and contact angles at the interphase provided a reasonable explanation for this effect. This suggests that the inside pores of the porous Ni-Mo-Cd electrode cannot be

fully wetted by the KF·2HF melt. This means that the electrocatalytic performance depends not only on the electrode material and its morphology but also on the nature of the electrolyte.

3. The corrosion current-density of Ni-Mo-Cd in the KF·2HF melt was determined as i_{corr} = 1.2 x 10^{-6} A cm^{-2} (with allowance for the surface roughness factor having been made), which is a small value compared to that measured for the mild-steel. It is believed that KF·2HF melt is to be regarded as an alkaline media in the HF/F system in which the reaction of metal dissolution is kinetically slow. SEM pictures were obtained at various periods of exposure to the melt under open-circuit conditions. It was found the surface of the electrodeposited composite would not be severely damaged until three months or longer time of exposure in the melt.

4. Impedance results for the HER at the composite Ni-Mo-Cd electrode were obtained both in the KF·2HF and $KOH·2H_2O$ melts for comparison. Depressed semi-circles in complex plots were observed in both electrolytes and this behaviour arises due to the porosity of the electrode. Two semi-circles in the complex plots and two peaks in the phase-angle Bode plots can be identified corresponding to discharge of C_{dl} at high frequency and $C_{\phi,H}$ over the low frequency region. Fitting of experimental data in terms of an equivalent circuit and CPE model designed for porous electrodes, provided information on the surface roughness factor (from C_{dl}) and the H adsorption behaviour (from $C_{\phi,H}$).

5. A 3-dimensional hydride phase at the near surface region (several nm) can be formed on Ni-based alloy materials. It is generated during cathodic H_2 evolution as it was found

at Ni-Mo-Cd that a quasi-equilibrium potential more negative to the reversible H_2 potential was established. The decomposition of such an hydride phase under open-circuit conditions complicates potential-relaxation behaviour especially over the long time domain.

6. The validity of a newly developed initial potential-relaxation method for determination of C_{dl} was tested by means of a theoretical treatment and further proved using a real electronic hardware circuit. It is uniquely useful under conditions where a simultaneous significant Faradaic current is passing and where an appreciable adsorption pseudocapacitance arises. A prototype system consisting of a Pt electrode in KOH solution was employed to demonstrate its effectiveness. C_{dl} values were compared by means of three techniques: cyclic voltammetry, a.c. impedance and initial potential-relaxation transients, and the results were in excellent agreement with each other.

7. The *apparent* electrochemically accessible surface area for the HER at a plated, porous Pt electrode increases with increasing electrolyte conductivity. The effective roughness factor was found to be ca. 20 times larger in 4 M than in 0.1 M KOH solutions. The area of porous Pt (having relatively shallow pores) evidently becomes completely 'unfolded' in 4M KOH with respect to its potentiality for electrochemical response. The present work shows that the effective catalytic behaviour of the porous electrode is not only an intrinsic property of a given surface, but also strongly depends on the conductivity of electrolyte in the pores, related to their electrochemical accessibility.

8. A theoretical model was established for interpretation of potential-relaxation transients following current interruption, which is described by kinetic rate equations using a

Langmuir isotherm model for H adsorption in the HER. Effects of values of rate constants, C_{dl}, q_1, etc. on the reaction behaviour and mechanisms are theoretically calculated and discussed in depth. Simulation of potential-relaxation transients at bright Pt in KF·2HF melt and KOH solutions was successfully carried out by means of approximations to the theoretical model, and the fitting of the results was very satisfactory. A set of rate constants and other parameters were quantitatively obtained, enabling, then, the relation of θ_H vs η and C_ϕ vs η to be calculated.

9. Trace amounts of thiourea, $(NH_3)_2C{=}S$ (1 ppm), can be strongly and irreversibly adsorbed on the surface through bonding of sulphur to metal surface atoms by lone-pair electron donation. Quantitative examination of the potential-relaxation transients by simulation through modified Frumkin-type rate equations which take into account poison coverage, θ_P, and the interaction factor, g, gives a set of kinetic parameters. When thiourea is present in the solution, the potential decays much slower and the arrest corresponding to discharge of adsorbed H also disappears in comparison to that in a clean solution. It is found that 93% of the surface is covered by the thiourea poison at bright Pt in 2 M KOH in the case of the HER.

10. Impedance results also supplementarily support the conclusion deduced above. Only one semi-circle in the complex plot and one peak in the Bode phase plot were identified in the presence of poison, indicating diminution of adsorbed o.p.d. H at the electrode.

11. The recombination reaction step 3 (H+H recombination) becomes significant in the presence of thiourea poison. This is examined through comparison of individual step rates with and without the influence of poison. The effect is probably due to weakening

of bonding of H to the metal surface induced by the adsorbed poison. It is also found, in the thiourea poisoned solution, that the reaction mechanism for the HER changes from electrochemical desorption of H with step 2 rate-determining (in clean solution) to electrochemical formation of step 1 rate-controlling.

12. Tafel plots for the HER at Pt in the presence of thiourea show that the currents are much smaller than that in the clean melt at a given potential. It diminishes the catalytic activity of the metal catalyst for the HER. Poison blocks the active sites for the reaction; some modifications of the electronic structure of the metal surface are also possible.

13. Cyclic voltammograms for Pt in As_2O_3-poisoned KF·2HF melt and 2 M KOH solution show that u.p.d. H peaks are suppressed compared to those obtained in clean media. The u.p.d. H peaks or corresponding charges becomes decreased if the upper-limit of cycle potential is less positive. This suggests that As_2O_3 can be oxidized at higher potentials which leads to less adsorption of the arsenic poison at the surface.

14. Similar effects of As_2O_3 to those with thiourea poison are observed from the potential-relaxation technique and Tafel measurements, i.e. the coverage by adsorbed H is decreased by poison blocking and the reaction rate of H_2 evolution reduced. Again, the recombination reaction is found to be significant through evaluations of k_3. The time effect of poison was also investigated. As_2O_3 can be reduced at cathodic polarizations into elemental As, which will possibly crystallize in the form of deposited semi-metallic arsenic when it is accumulated above one monolayer.

REFERENCES

1. L. Bai and B.E. Conway, *J. Appl. Electrochem.* **18**, 839 (1988)
2. L. Bai and B.E. Conway, *J. Appl. Electrochem.* **20**, 916 (1990)
3. L. Bai and B.E. Conway, *J. Appl. Electrochem.* **20**, 925 (1990)
4. S. Qian and B.E. Conway, *J. Appl. Electrochem.* in press (1993)
5. B.E. Conway, H.A. Kozlowska, M.A. Sattar and B.V. Tilak, *J. Electrochem. Soc.* **130**, 1825 (1983)
6. J. Tafel, *Z. Phys. Chem.* **50**, 641 (1905)
7. A. Frumkin, *Z. Phys. Chem.* (Leipzig) **A164**, 121 (1933)
8. A. N. Frumkin, in *Advances in Electrochemistry and Electrochemical Engineering*, Vol.1, P. Delahay (ed.), Interscience, N.Y. (1961) p. 65
9. M. Volmer and R. Wick, *Z. Phys. Chem.* **172**, 429 (1935)
10. J.A.V. Butler, *Proc. Roy. Soc. London*, **A157**, 423 (1936)
11. J. O'M. Bockris, *J. Electrochem. Soc.* **99**, 366c (1952)
12. P. Stonehart and P.N. Ross, *Catal. Rev. - Sci. Eng.* **12**, 1 (1975)
13. B.E. Conway, *J. Electrochem. Soc.* **124**, 410C (1977)
14. B.E. Conway, L. Bai and D.F. Tessier, *J. Electroanal. Chem.* **161**, 39 (1984)
15. D.A. Harrington and B.E. Conway, *J. Electroanal. Chem.* **221**, 1 (1987)
16. S. Trasatti, in: *Electrochemical Hydrogen Technologies*: H. Wendt (ed.), Elsevier, Amsterdam (1990) p. 1
17. M. Enyo, in: *Comprehensive Treatise of Electrochemistry*, Vol.7, B.E. Conway, J.O'M.

Bockris, E.B. Yeager, S.U.M. Kahn and R.E. White (eds.), Plenum Press, N.Y. (1983) p. 173

18. B.V. Tilak, P.W.T. Lu, J.E. Colman and S. Srinivasan, in: *Comprehensive Treatise of Electrochemistry*, Vol.2, J.O'M. Bockris, B.E. Conway, E. Yeager and R.E. White (eds.), Plenum Press, N.Y. (1981) p. 1

19. R.R. Adzic, in: *Advances in Electrochemistry and Electrochemical Engineering*, Vol.13, H. Gerischer and C.W. Tobias (eds.), Wiley, N.Y. (1985) p. 159

20. K. Viswanathan, B.V. Tilak, *J. Electrochem. Soc.* **131**, 1551 (1984)

21. A.T. Kuhn and P.M. Wright, in: *Industrial Electrochemical Processes*, A.T. Kuhn (ed.), Elsevier, Amsterdam (1971) p. 560

22. M. Yasuda, K. Fukumoto, Y. Ogata and F. Hine, in: *Electrochemical Engineering in the Chlor-Alkali and Chlorate Industries*, F. Hine, R.E. White, W.B. Darlington and R.D. Varjian (eds.), The Electrochemical Society, Pennington, N.J. (1988) p. 219

23. B. Combrade, in: *Hydrogen as an Energy carrier*, G. Imarisio and A.S. Strub (eds.), Dordrecht, D. Reidel (1983) p. 183

24. H. Gerischer, *Z. Phys. Chem.* N.J. **8**, 137 (1956)

25. R. Parsons, *Trans. Faraday Soc.* **34**, 1053 (1958)

26. C. Bailleux, A. Damien and A. Montet, *Intl. J. Hydrogen Energy*, **8**, 529 (1983)

27. R. Parsons, *Surf. Sci.*, **18**, 28 (1969)

28. S. Arrhenius, *Z. Phys. Chem.* **4**, 226 (1889)

29. B.E. Conway, in: *Theory and Principles of Electrode Processes*, The Ronald Press Company, N.Y., (1965) p. 93

30. S. Glasstone, K.J. Laidler and H. Eyring, in: *Theory of Rate Processes*, McGraw-Hill Book Co. Inc., N.Y., (1940)

31. J. O'M. Bockris and A.K.N. Reddy, in: *Modern Electrochemistry*, Vol.2, Plenum Press, N.Y., (1977) p. 1231

32. P.L. Williams, in: *Faraday: A Scientific Biography*, Chapman and Hall, London, (1965)

33. J. O'M. Bockris, in: *Modern Aspects of Electrochemistry*, Vol.1, Chapter 4, J. O'M. Bockris (ed.), Butterworths, London (1954)

34. J. Horiuti and M. Polanyi, *Acta Physicochim.*, URSS, **2**, 505 (1935)

35. R.W. Gurney, *Proc. Roy. Soc.*, London, **A134**, 137 (1932); **A186**, 378 (1932)

36. B.E. Conway and J. O'M. Bockris, *J. Chem. Phys.*, **26**, 532 (1957)

37. P. Ruetschi and P. Delahay, *J. Chem. Phys.*, **23**, 195 (1955)

38. S. Trasatti, *J. Electroanal. Chem.*, **39**, 163 (1972)

39. G.C. Bond, *Catalysis by Metals*, Academic Press, N.Y. (1962)

40 G.C. Bond, *Disc. Faraday Soc.*, **41**, 200 (1966)

41. R.P. Messmer, S.K. Knudson, K.H. Johnson, J.B. Diamond and C.Y. Yang, *Phys. Rev.* B, **13**, 1396 (1976)

42. H. Wendt and V. Plzak, *Electrochim. Acta.*, **28**, 27 (1983)

43. Norsk Hydro, *Method for preparing active cathodes for electrochemical processes*, British Pat. 1,548,147 (4 July 1979)

44. M.M. Jaksic, *Journal of Molecular Catalysis*, **38**, 161 (1986)

45. M.M. Jaksic, *Electrochim. Acta*, **29**, 1539 (1984)

46. A.K. Huq and A.J. Rosenberg, *J. Electrochem. Soc.*, **111**, 260 (1964)

47. M. Jaksic, *Materials Chemistry and Physics*, **22**, 1 (1989)

48. M. Jaksic, *Intl. J. Hyarogen Energy*, **12**, 727 (1987)

49. M.H. Miles, *J. Electroanal. Chem.*, **60**, 89 (1975)

50. S. Srinivasan and F.J. Salzano, *Intl. J. Hydrogen Energy*, **2**, 53 (1977)

51. M. Jaksic, C.M. Lacnjevac, R.T. Atanasoski and R. Adzic, in: *Proceedings of the O. de Nora Symposium on Chlorine Technology*, Milan, O. de Nora (1979) p. 57

52. M. Jaksic, *Intl. J. Hydrogen Energy*, **11**, 519 (1986)

53. L. Brewer, *Science*, **161**, 115 (1968)

54. L. Brewer, in: *Electronic Structure and Alloy Chemistry of Transition Elements*, P.A. Beck (ed.), Interscience, N.Y. (1963)

55. M.H. Miles and M.A. Thomason, *J. Electrochem. Soc.*, **123**, 1459 (1976)

56. H. Kita, *J. Res. Inst. Catalysis*, Hokkaido Univ., **13**, 151 (1965)

57. B.E. Conway and B.V. Tilak, in *Advances in Catalysis*, Vol. 38, D.D. Eley, H. Pines and P.B. Weisz (eds.), Academic Press Inc., (1992) p. 1

58. J. O'M. Bockris and A.M. Azzam, *Trans. Faraday Soc.*, **48**, 145 (1952)

59. J. O'M. Bockris and E.C. Potter, *J. Chem. Phys.*, **20**, 614 (1952)

60. R. Parsons, *J. Chem. Phys.*, **49**, 82 (1952)

61. R. Parsons, *Trans. Faraday Soc.*, **47**, 1332 (1951)

62. A.R. Despic, *Bull. Soc. Chim.* (Belgrade), **30**, 293 (1955)

63. A.R. Despic and J. O'M. Bockris, *J. Chem. Phys.*, **33**, 389 (1960)

64. B.E. Conway and J. O'M. Bockris, *Naturwissenschaften*, **19**, 446 (1956)

65. B.E. Conway, D.J. Mackinnon and B.V. Tilak, *Trans. Faraday Soc.*, **66**, 1203 (1970)

66. B.E. Conway, in: *Modern Aspects of Electrochemistry*, Vol.16, J. O'M. Bockris and B.E. Conway (eds.), (1985) p. 103

67. J.O. Hirschfelder and E. Wigner, *J. Chem. Phys.*, 7, 616 (1939)

68. I. Jofa, *Acta Physico. Chim.*, **10**, 903 (1939)

69. S. Schuldiner, *J. Electrochem. Soc.*, **99**, 1 (1952)

70. E. Yeager, in: *Transactions of the Symposium on Electrode Processes*, Philadelphia, John Wiley and Sons, N.Y. (1961) p. 145

71. J. O'M. Bockris and R. Watson, *J. Chem. Phys.*, **49**, 1 (1952)

72. B.E. Conway and L. Bai, *J. Electroanal. Chem.*, **198**, 149 (1986)

73. A. Saraby-Reintjes, *J. Chem. Soc. Faraday Trans.*, **1, 82**, 3343 (1986)

74. J. Divisek, *J. Electroanal. Chem.*, **214**, 615 (1986)

75. G.J. Brug, M. Sluyters-Rehbach, J.H. Sluyters and A. Hamelin, *J. Electroanal. Chem.*, **181**, 245 (1984)

76. R.J. Nichols and A. Bewick, *J. Electroanal. Chem.*, **243**, 445 (1988)

77. S. Trasatti, in: *Electrocatalysis*, W.E. O'Grady, P.N. Ross and F.G. Will (eds.), The Electrochemical Society, Pennington, N.J. (1982) p. 73

78. A.G. Pshenichnikv, *Mat. Chem. Phys.*, **22**, 121 (1989)

79. S. Trasatti and O.A. Petrii, *Pure & Appl. Chem.*, **63**(5), 711 (1991)

80. G. Valette and A. Hamelin, *J. Electroanal. Chem.*, **45**, 301 (1973)

81. R. Parsons and F.R.G. Zobel, *J. Electroanal. Chem.*, **9**, 333 (1965)

82. L. Bai, L. Gao and B.E. Conway, *J. Chem. Soc., Faraday Trans.*, **89**(2), 235 (1993)

83. L. Bai, L. Gao and B.E. Conway, *J. Chem. Soc., Faraday Trans.*, **89**(2), 243 (1993)

84. G.G. Barna, S.N. Frank and T.H. Teherani, *J. Electrochem. Soc.*, **129**, 746 (1982)

85. B.E. Conway and L. Bai, *J. Chem. Soc., Faraday Trans.*, **81**(1), 1841 (1985)

86. J. O'M. Bockris and S. Srinvasan, *Fuel Cells: Their Electrochemistry*, Chapter 5, McGraw-Hill Book Company, N.Y. (1969)

87. R. de Levie, in: *Advances in Electrochemistry and Electrochemical Engineering.*, Vol.6, P. Delahay (ed.), Interscience, N.Y. (1964)

88. B.E. Conway and E. Gileadi, *Trans. Faraday Soc.*, **58**, 2493 (1962)

89. B.E. Conway and H. Angerstein-Kozlowska, *Acc. Chem. Res.*, **14**, 49 (1981)

90. P. Gu, L. Bai, L. Gao, R. Brousseau and B.E. Conway, *Electrochim. Acta*, **37**(12), 2145 (1992)

91. F.G. Will, *J. Electrochem. Soc.*, **112**, 451 (1965)

92. J. Clavilier, R. Faure, G. Guinet and R. Durand, *J. Electroanal. Chem.*, **107**, 205 (1980)

93. P.N. Ross, *J. Electrochem. Soc.*, **126**, 67 (1979)

94. A. Hubbard, *Acc. Chem. Res.*, **13**, 177 (1980)

95. J. Clavilier, D. Armand, S.G. Sun and M. Petit, *J. Electroanal. Chem.*, **205**, 267 (1986)

96. R. Adzic, A.V. Tripkovic and Vesovic, *J. Electroanal. Chem.*, **204**, 329 (1986)

97. B. Love, K. Seto and J. Lipkowski, *J. Electroanal. Chem.*, **199**, 219 (1986)

98. S. Schuldiner, M. Rosen and D. Flinn, *J. Electrochem. Soc.*, **117**, 1251 (1970)

99. K. Seto, A. Iannelli, B. Love and J. Lipkowski, *J. Electroanal. Chem.*, **226**, 351 (1987)

100. S. Trasatti, in *The Chemistry and Physics of Electrocatalysis*, J.D.E. McIntyre, M.J. Weaver and E.B. Yeager (eds.), The Electrochem. Soc., Princeton (1984)

101. L. Bai, D.A. Harrington and B.E. Conway, *Electrochim. Acta*, 32, 1713 (1987)

102. R. Parsons, *Chem. Rev.*, 90, 813 (1990)

103. H.L.F. Von Helmholtz, *Ann. Phys. Chem.*, 7, 337 (1879)

104. G. Gouy, *Ann. Phys.*, 6(9), 5 (1916)

105. D.L. Chapman, *Phil. Mag.*, 25, 475 (1913)

106. O. Stern, Z. Elektrochem., 30, 508 (1924)

107. D.C. Grahame, *Chem. Rev.* 47, 441 (1947)

108. M.A.V. Devanathan, J.O'M. Bockris and K. Müller, *Proc. Roy. Soc.*, London, A274, 55 (1963)

109. N.F. Mott and R.J. Watts-Tobin, *Phil. Mag.*, 7(8), 483 (1962)

110. M.W. Breiter, C.A. Knorr and W. Volkl, *Z. Elektrochem.*, 59, 681 (1955)

111. A.N. Frumkin and B. Slygin, *Acta Physicochim.*, URSS, 5, 819 (1939)

112. A. N. Frumkin, in: *Advances in Electrochemistry and Electrochemical Engineering*, P. Delahay and C. Tobias, (eds), Interscience, N.Y., 3 (1963), p. 287

113. M.W. Breiter, H. Kammermaier and C.A. Knorr, *Z. Elektrochem.*, 60, 37 (1956)

114. M.W. Breiter, in: *Symposium on Electrode Processes*, E. Yeager (ed), The Electrochem. Soc., J. Wiley and Sons, N.Y. (1961) p. 307

115. F.G. Will and C.A. Knorr, *Z. Elektrochem.*, 64, 258 (1961)

116. B.E. Conway, W.B.A. Sharp and H. Angerstein-Kozlowska, *J. Chem. Soc., Faraday Trans.*, I, 74, 1373 (1978)

117. E. Gileadi and B.E. Conway, in: *Modern Aspects of Electrochemistry*, Vol.3, Chapter 5, J. O'M. Bockris and B.E. Conway (eds), Butterworths, London, (1964)

118. E. Gileadi and B.E. Conway, *J. Chem. Phys.*, **39**, 3420 (1963)

119. E. Gileadi, E. Kirowa-Eisner and J. Penciner, in: *Interfacial Electrochemistry*, Chapter 7 and 8, Addison-Wesley Publishing Company, Inc. (1975)

120. H. Angerstein-Kozlowska, J. Klinger and B.E. Conway, *J. Electroanal. Chem.*, **75**, 45 (1975)

121. F. Ludwig, R.K. Sen and E. Yeager, *Electrokhimiya*, **13**, 847 (1977)

122. B.E. Conway, *Proc. Symposium on Electrode Materials*, The Electrochem. Soc., Princeton, N.J., **77** (1971) p. 441

123. B.J. Bowles, *Electrochim. Acta*, **10**, 717 (1965); **15**, 589 (1970)

124. H. Angerstein-Kozlowska, W.B.A. Sharp and B.E. Conway, *Proc. Symposium on Electrocatalysis*, M. Breiter (ed.), The Electrochem. Soc., N.J. (1974) p. 94

125. L. Angely, G. Bronoel and G. Peslerbe, *J. Electroanal. Chem.*, **96**, 183 (1979)

126. M.A.V. Devanathan and B. Selvaratnam, *Trans. Faraday Soc.*, 56, 1820 (1960)

127. L. Vracar and B.E. Conway, *J. Electroanal. Chem.*, **277**, 253 (1990)

128. S. Trasatti, in *Advances in Electrochemical Science and Engineering*, Vol.2, H. Gerischer and C.W. Tobias (eds.), VCH Publishers Inc., N.Y. (1992) p.1

129. F. Ephraim, *Inorganic Chemistry*, Gurney and Jackson, London (1942)

130. B. Baranowski and M. Smialowski, *J. Phys. Chem. Solids*, **12**, 206 (1959)

131. H.A. Kozlowska, *Acad. Pol. Sci., Series Sci. Chim.*, 7, 881 (1959)

132. N.A. Galktinowa, *Hydrogen-Metal Systems Data Book*, Ordentlich Publ. Co., Holon, Israel (1988)

133. J. van Fucht, F.A. Fuijpers and H. Bruning, *Phlips Res. Repts.*, **25**, 133 (1970)

134. H.F. Bittner and C.C. Badcock, *J. Electrochem. Soc.*, **130**, 193 (1983)

135. M.A. Fetcenko, S. Venkatesan, S.R. Ovshinsky and M. Hirota, *Proc. Intl. battery Association Conference*, Seattle, Washington (1990)

136. M. Fleischmann and S. Pons, *J. Electroanal. Chem.*, **261**, 301 (1989)

137. F.A. Lewis and T.B. Flanagan, *Trans. Faraday Soc.*, **55**, 1400 (1959)

138. A.N. Frumkin and N. Aladjalova, *Acta Physicochim.*, URSS, **19**, 1 (1944)

139. R.N. Iyer, H.W. Pickering and M. Zamanzadeh, *J. Electrochem. Soc.*, **136**, 2463 (1989)

140. O. Vosikovsky, M. Marecek and D.J. Ross, *Intl. J. Pressure Vessels and Piping*, **13**, 197 (1983)

141. E. Protopopoff and P. Marcus, *J. Electrochem. Soc.*, **135**, 3073 (1988)

142. E. Lamy-Pitara, L. Lghouzouani, Y. Tainon and J. Barbier, *J. Electroanal. Chem.*, **260**, 157 (1989)

143. P. Marcus and E. Protopopoff, *Surf. Sci.*, **17**, 533 (1985)

144. A. Slygin and B. Ershler, *Acta Physicochim.*, URSS **11**, 45 (1939)

145. J. O'M. Bockris and B.E. Conway, *Trans. Faraday Soc.*, **45**, 989 (1949)

146. S. Schuldiner and J.P. Hoare, *J. Chem. Phys.*, **26**, 1771 (1957)

147. P. Stonehart and G. Kohlmayr, *Electrochim. Acta*, **17**, 369 (1972)

148. E.P.M. Leiva, E. Santos and T. Iwasita, *J. Electroanal. Chem.*, **215**, 357 (1986)

149. A. Nidola and R. Schira, *J. Electrochem. Soc.*, **133**, 1653 (1986)

150. A.A. Kuznetsov and Yu.V. Fedorov, *Elektrokhimiya*, **18**, 828 (1982)

151. A. Nidola and R. Schira, in: *Advances in the Chlor-alkali and Chlorate Industry*, M.M. Silver and E.M. Spore (eds.), The Electrochem. Soc., Pennington, N.J. (1984) p. 206

152. D.E. Hall, J.M. Sarver and D.O. Gothard, in: *Electrochemical Engineering in the Chlor-Alkali and Chlorate Industries*, F. Hine, R.E. White, W.B. Darlington and R.D. Varjian (eds.), The Electrochem. Soc., Pennington, N.J. (1988), p. 184

153. J. Barbier, E. Lamy-Pitara, P. Marecot, J.P. Boitiaux, J. Cosyns and F. Verna, in *Advances in Catalysis*, Vol. 37, D.D. Eley, H. Pines and P.B. Weisz (eds.), Academic Press Inc., (1990) p. 279

154. C.H. Bartholomew and P.K. Agrawal, in *Advances in Catalysis*, Vol. 31, D.D. Eley, H. Pines and P.B. Weisz (eds.), Academic Press Inc., (1982) p. 135

155. E.B. Maxted, *Adv. Catal.*, **3**, 129 (1951)

156. J.W. Schultze and F.D. Koppitz, *Electrochim. Acta*, **21**, 327 (1976)

157. A.Q. Contractor and H. Lal, *J. Electroanal. Chem.*, **96**, 175 (1979)

158. C. Horanyi and E.M. Ritzmayer, *J. Electroanal. Chem.*, **206**, 297 (1986)

159. W. Heegemann, K.H. Meister, E. Bechtold and K. Hayek, *Surf. Sci.*, **49**, 161 (1975)

160. T.E. Fischer and S.R. Kelemen, *Surf. Sci.*, **69**, 1 (1977)

161. J. Oudar, C.M. Pradier, D. Vassilakis and Y. Berthier, *Catal Lett.*, **1**, 339 (1988)

162. J. Oudar, S. Pinol, C.M. Pradier and Y. Berthier, *J. Catal.*, **107**, 445 (1987)

163. J.O'M. Bockris, J. McBreen and L. Nanis, *J. Electrochem. Soc.*, **112**, 1125 (1965)

164. F.A. Lewis, in: *The Palladium Hydrogen System*, Academic Press, N.Y. (1967)

165. T.P. Radhakrishman and L.L. Shreir, *Electrochim. Acta*, **11**, 1007 (1966)

166. P.K. Subramanyam, in: *Comprehensive Treatise of Electrochemistry*, J.O'M. Bockris, B.E. Conway, E.B. Yeager and R.E. White (eds.), Chapter 8, Vol.4, Plenum Press, N.Y. (1981) p. 411

167. Z.A. Foroulis, *J. Electrochem. Soc.*, **128**, 219 (1986)

168 J. Stachurski, D. Pouli, G. Pokrzyk and J. Ripas, U.S. Patent 4,354, 915 (1982) (Hooker Chemical Co., Niagara Falls, N.Y.)

169. B.E. Conway and L. Bai, *Proc. 5th World Hydrogen Energy Conference*, Toronto, Canada, July (1984) 879

170. H.A. Kozlowska in *Comprehensive Treatise of Electrochemistry*, Vol. 9, Chapter 2, E. Yeager, J.O'M. Bockris, B.E. Conway and S. Sarangapani (eds.), Plenum Publ. Corp., N.Y. (1984)

171. G.J. Hills and D.J.G. Ives, in *Reference Electrodes*, D.J.G. Ives and G.J. Janz (eds), Academic Press, N.Y. (1961) p.35

172. B.E. Conway, H.A. Kozlowska, B. Barnett and J. Mozota, *J. Electroanal. Chem.*, **100**, 417 (1979)

173. A. Hamelin, *Comptes Rendues.*, **282**, 1013 (1976)

174. E.R. Gonzalez, L.A. Avaca, A. Carubelli, A.A. Tanaka and G. Tremiliosi-Filho, *Intl. J. Hydrogen Energy*, **9**, 689 (1984)

175. J.De Carvalho, G. Tremiliosi-Filho, L.A. Avaca and E.R. Gonzalez, *Intl. J. Hydrogen Energy*, **14**, 161 (1989)

176. A.J. Rudge, in *Industrial Electrochemical Processes*, Chapter 1, A.T. Kuhn (ed.), Elsevier Publishing Company, Amsterdam, (1971)

177. W.C. Schumb, R.C. Young and K.J. Radimir, *Ind. Eng. Chem.*, **39**, 244 (1947)

178. J.D. Bernal and R.H. Gowler, *J. Chem. Phys.*, **1**, 515 (1933)

179. B.E. Conway, J.O'M. Bockris and H. Linton, *J. Chem. Phys.*, 24, 834 (1956)

180. M. Eigen and L. de Maeyer, *Zeit. Elektrochem.*, **60**, 1037 (1956)

181. B.E. Conway, H.A. Kozlowska, W.B.A. Sharp and E.E. Criddle, *Anal. Chem.*, **45**, 1331 (1973)

182. F. Ludwig, R.K. Sen and E. Yeager, *Elektrokhimiya*, **13**, 847 (1977), see *Soviet Electrochemistry*, **13**, 717 (1977)

183. N. Pentland, J.O'M. Bockris and E. Sheldon, *J. Electrochem. Soc.*, **104**, 181 (1957)

184. P. Delahay, in *New Instrumental Methods in Electrochemistry*, R.E. Krieger (ed.), Huntington, N.Y. (1980)

185. Southampton Electrochemistry Group, in *Instrumental Methods in Electrochemistry*, John Wiley and Sons, N.Y. (1985)

186. B.L. Hulme, *Math. Comp.*, **26**, 881 (1972)

187. A. Lasia and A. Rami, *J. Electroanal. Chem.*, **294**, 123 (1990)

188. J.R. Macdonald (ed.), in *Impedance Spectroscopy*, Wiley, N.Y. (1987)

189. D.A. Harrington and B.E. Conway, *Electrochim. Acta*, **32**, 1703 (1987)

190. R. Armstrong and M. Henderson, *J. Electroanal. Chem.*, **39**, 81 (1972)

191. R. Durand, *Electrochim. Acta*, **24**, 1095 (1979)

192. G. Armstrong and J.A.V. Butler, *Trans. Faraday Soc.*, **29**, 126 (1933)

193. B.V. Tilak and B.E. Conway, *Electrochim. Acta*, **21**, 745 (1976)

194. B.V. Tilak, C.G. Rader and B.E. Conway, *Electrochim. Acta*, **22**, 1167 (1977)

195. L. Gao, J. Barber and B.E. Conway, *Proc. of 184th Electrochem. Soc. Meeting*, The Electrochem. Soc., New Orleans (1993)

196. L. Bai, *J. Electroanal. Chem.*, **355**, 37 (1993)

197. M. Boudart, *J. Amer. Chem. Soc.*, **72**, 3566 (1952)

198. N. Watanabe, M. Ishii and S. Yoshizawa, *J. Electrochem. Soc. Jap.* **29**, E180 (1961)

199. N. Watanabe, *Proc. Electrochem. Soc., Electrochemistry of Carbon* (1984) p.536

200. D. Devilliers, F. Lantelme and M. Chemla, *Electrochim. Acta*, **31**, 1235 (1986)

201. W.H. Smyrl, in *Comprehensive Treatise of Electrochemistry*, Vol.4, Chapter 2, J. O'M Bockris, B.E. Conway, E. Yeager and R.E. White (eds.), Plenum, N.Y. (1981)

202. R. de Levie, *J. Electroanal. Chem.*, **281**, 1 (1990)

203. W. Scheider, *J. Phys. Chem.*, **79**, 127 (1975)

204. L. Nyikos and T. Pajkossy, *Electrochim. Acta*, **30**, 1533, (1985)

205. J.C. Wang, *Electrochim. Acta*, **33**, 707, (1988), see also *Electrochim. Acta*, **34**, 987, (1989)

206. W.H. Mulder and J.H. Sluyters, *Electrochim. Acta*, **33**, 303, (1988)

207. D. Linden, in *Handbook of Batteries and Fuel Cells*, McGraw-Hill, N.Y., 1984

208. A.H. Thompson, *J. Electrochem. Soc.*, **126**, 608 (1979)

209. G.J. Hills and R. Payne, *Trans. Faraday Soc.*, **61**, 316 (1965)

210. M. Breiter, *J. Electroanal. Chem.*, **81**, 275 (1977)

211. T. Ohmori, *J. Electroanal. Chem.*, **157**, 159 (1983)

212. B.V. Tilak, C.G. Rader and S.K. Rangarajan, *J. Electrochem. Soc.*, **124**, 1879 (1977)

213. H. Siegenthaler and K. Juttner, *J. Electroanal. Chem.*, **163**, 327 (1984)

214. C.H. Giles and A.P. D'Silve, *Trans. Faraday Soc.*, **65**, 2516 (1969)

215. A.W. Adamson, *Physical Chemistry of Surfaces*, Wiley, N.Y., 4th edition, 1982

216. S.B. Brummer and A.C. Makrides, *J. Electrochem. Soc.*, **111**, 1122 (1964)

217. V.A. Vicente and S. Bruckenstein, *J. Electroanal. Chem.*, **82**, 187 (1977)

218. H. Angerstein-Kowzlowska, B.E. Conway, A. Hamelin and L. Stoicoviciu, *Electrochim. Acta*, **31**, 1051 (1986)

219. L. Gao, *Interface*, Vol.2, **3**, 58 (1993)

220. T. Biegler and R.W. Woods, *J. Electroanal. Chem.*, **29**, 269 (1971)

221. A.N. Frumkin, P. Dolin and B.V. Ershler, *Acta Physiochim. U.R.S.S.*, **13**, 747 and 802 (1940)

222. H. Angerstein-Kowzlowska, J. Klinger and B.E. Conway, *J. Electroanal. Chem.*, **75**, 45 (1977)

223. J. O'M. Bockris and S. Srinivasan, *Fuel Cells: Their Electrochemistry*, McGraw-Hill, N.Y. Chapter 5, 1969

224. C.M. Lacnjevac and M.M. Jaksic, *J. Res. Inst. Catal.*, Hokkaido University, Japan, **31**, 7, (1982)

225. D.F. Tessier and B.E. Conway, *Electrochim. Acta*, **30**, 1703, (1985)

226. J. O'M. Bockris and B.E. Conway, *Trans. Faraday Soc.*, **45**, 989 (1949)

227. S. Bhatia, B.C. Gerstein and T.S. King, *J. Catal.*, **134**, 572 (1992)

228. B.C.Wiegand and C.M. Friend, *Chem. Rev.*, **94**, No.4, 491 (1992)

229. G.S. Somorjai and D.W. Blakely, *Nature*, **258**, 580 (1975)

230. S.R. Keleman and T.E. Fischer, *Surf. Sci.*, **87**, 53 (1979)

231. Y.J. Kuo and B.J. Taturchuk, *J. Catal.*, **112**, 229 (1988)

232. F.W. Schapink, M. Oudeman, K.W. Leu and J.N. Helle, *Trans. Faraday Soc.*, **56**, 415 (1960)

233. R. Parsons, *Proc. Roy. Soc.*, **A261**, 79 (1961)

234. B.E. Conway, *Electrochemical Data*, Elsevier, Amsterdam, (1952)

APPENDIX

Procedures and Instructions for the Computer Simulations

Procedures for computer simulation of potential-relaxation transients are described in this section. The executing programs were implemented on the CMS mainframe computer at the University of Ottawa. They consist of an executing batch file, GAORUN EXEC; a compiled main program PDGAO TEXT; a main FORTRAN program KSUB FORTRAN (for the poison effects it was KSUBP FORTRAN); and an input data file INFO DAT. To gain admission to the mainframe system, a terminal connected to the main-computer is required. In the present work, the connection was realized using a software called "Kermit", implemented on IBM PC. In the directory of Kermit, you type:

c: > kermit > **kermit**

#call 3301

vt100

cms "your account number or i.d."

password

now, you are in CMS system, type:

filel

Xedit "files you want to edit"

The INFL DAT file contains all the pre-set rate-constants, other parameters and experimental data. On line 3, the first number (130 here) means the number of experimental data. Line 4 to 10 are parameters, $p(1)=k_1$, $p(2)=k_{-1}$, $p(3)=k_2$, $p(4)=V_{t=0}$, $p(5)=k_3$, $p(11)=C_{dl}$, $p(12)=q_1$,

p(13)=g and p(14)=θ_p. On line 11, it indicates status of parameters, 1 means free approximation and 0 means fixed parameter. Line 12 and below are for experimental data.

File "INFL DAT"

```
OCPD
    ZZRR K        R       -0  00.0D-1  +00  -10
 130  34 190  50  +1   0  +0   1  +2   0
7.40000000D-11 8.30000000D-11 2.10000000D-12-0.25000000D-00 8.70000000D-13
  1.00000D-06   1.00000D-08   1.00000D-11   1.00000D-11   0.00000D 00
  2.50000D-05   2.10000D-04   3.30000D+00   5.30000D-01   0.00000D 00
  0.00000D-00   0.00000D 00   0.00000D 00   0.00000D-00   0.00000D 00
0.00000000D+00 0.00000000D-00 0.00000000D-00 0.00000000D+00 0.00000000D-00
0.00000000D+00 0.00000000D+00 0.00000000D+00 0.00000000D-00 0.00000000D+00
0.00000000D+00 1.00000000D+00 0.00000000D+00 0.00000000D+00
11101000001100000000000000000000
```

0.5520000000000E-05	-0.2500000000000E+00	
0.1050000000000E-04	-0.2500000000000E+00	
0.1560000000000E-04	-0.2500000000000E+00	
0.2060000000000E-04	-0.2500000000000E+00	Experimental data
0.2560000000000E-04	-0.2500000000000E+00	
0.3060000000000E-04	-0.2490000000000E+00	
0.3570000000000E-04	-0.2490000000000E+00	
.....	.....	

When INFL DAT file is edited, you can start running the program by typing **GAORUN** under "Ready" promote. The batch file GAORUN EXEC tells how to run the programs step, by step automatically. In the case of the poison effect work, modify all "KSUB" into "KSUBP" in the GAORUN EXEC file.

When you want to calculate a theoretical potential-relaxation transient for given parameters, input the parameters into file "INFL CALC". Change INFL DAT into INFL CALC in the file of GAORUN EXEC.

The simulation parameters (rate-constants) can be found in the generated file "PDGAO PNTOUTL". Theoretically simulated potential-relaxation data (time vs potential) can found in the file "PDGAO AUXPNTL" under the line "model data ...". Edit and save the data in a file that you prefer.

file "GAORUN EXEC"

```
/*execute pdgao...cjc 1992.4*/
/*trace all*/
'EXEC FORTVS KSUB(OPT(2)'
fortvsrc=rc
'GLOBAL TXTLIB VLNKMLIB VFORTLIB'
'FILEDEF INFL DISK INFL DAT'
'FILEDEF INFLOUT DISK  INFL OUT'
'FILEDEF AUXPNTL DISK  PDGAO AUXPNTL (LRECL 133'
'FILEDEF PNTOUTL DISK  PDGAO PNTOUTL (LRECL 133'
'FILEDEF OUTIN DISK  PDGAO OUTIN (LRECL 133'
'FILEDEF AUXPTL1 DISK  PDGAO AUXPTL1'
'FILEDEF LINOUT DISK  PDGAO LINOUT'
'FILEDEF LVOUT DISK  PDGAO LVOUT'
if fortvsrc=0 then 'LOAD KSUB PDGAO'
else exit rc
'START'
'ERASE LOAD MAP A'
'ERASE KSUB LISTING A'
'ERASE KSUB TEXT A'
'ERASE PDGAO OUTIN A'
'ERASE PDGAO LINOUT A'
'ERASE PDGAO LVOUT A'
'ERASE FILE AUXPNT1 A'
```

From the simulation parameters, the Tafel relation, C_ϕ vs η and the θ_H vs η relations can be calculated according to the definitions. FORTRAN programs were written for this purpose. Input all kinetic parameters into TAFEL FORTRAN (in case of the poison effect, it is the POI FORTRAN) file; then run the file "TAFRUN EXEC" for the associated programs.

Data transfer can be realized between CMS and IBM PC through Kermit. Under "Ready" status in CMS, type

micro

kermit

Kermit-CMS>**send OCT0101 DAT** (the data file to be transferred)

^]C

MS-Kermit>**receive**

transferring ....

MS-Kermit>**c**

Kermit-CMS>**ex**

For more information on CMS commands, type **help cms** for detailed instructions on the CMS system.